Manipulating the Coupling between Electronic and Spin Degrees of Freedom in Molecules

D.Phil. Thesis



Michael Christian Slota

Wolfson College

Lead Supervisor: Prof. Dr. Lapo Bogani

Co-Supervisor: Prof. Dr. Arzhang Ardavan

Oxford, Michaelmas Term 2017

OxfordMaterials

Abstract

The miniaturisation of semiconductors is running into physical limitations. In order to further enhance computational powers, reaching the atomic or molecular level is both necessary and inevitable. At the nanometre scale, the quantum properties of materials become important. These can be used for qubits in quantum computers, which are able to process information significantly faster than traditional counterparts. One approach towards such novel nanoelectronic devices is realised via molecular magnetic materials. Single-molecule magnets, which represent the smallest possible molecular magnetic structures, are currently being tested in such devices. However, the physics of these materials is not yet completely understood. The magnetic property of electrons, known as the electron spin, plays a crucial role here. It is furthermore very sensitive to its surroundings. Interactions with neighbouring nuclear spins, for instance, lead to decoherence, which translates to a loss of stored quantum information. In order to promote the development of new elements for nanoelectronics or qubits, it is therefore essential to unravel the couplings of the spins and their surroundings, and learn how to control and manipulate them.

The present work focuses on how light, as an ultra-clean technique, can be used to manipulate the molecular spin states, and how magnetic centres interact when chemically attached to a graphene nanoribbon. We employ state-of-the-art electron spin resonance techniques and SQUID magnetometry to investigate the effect of light on a new cobalt valence tautomer, where we find an enhanced blocking temperature of a metastable light-excited state. Furthermore, we examine an Fe_3Cr-based single-molecule magnet, where light causes a change in the giant spin. We then progress to graphene nanoribbons, which offer an interesting semiconducting backbone for magnetic molecules. Through a comprehensive analysis of spin-spin couplings in nitronyl-nitroxide graphene nanoribbons, we eventually prove the existence of an edge state, which allows for two-qubit applications.

Contents

1 Motivation **1**

2 Theory and Concepts **5**

2.1 Molecular magnetic nanomaterials 5

2.1.1 Single-Molecule Magnets 5

2.1.2 Spin Hamiltonian model 8

2.1.3 Slow relaxation and quantum tunnelling of magnetisation . 11

2.1.4 Requirements of SMMs 15

2.1.5 Quantum coherence and quantum computation 16

2.2 Photoswitching of molecular magnets 18

2.2.1 Spin crossover 18

2.2.2 Charge transfer 20

2.2.3 Photoisomerisation 22

2.2.4 Further notable light-effects in molecules 23

2.3 Graphene nanoribbons 25

2.3.1 Introduction 25

2.3.2 Structure 27

2.3.3 Band structure of AGNRs 29

2.3.4 Edge state and band structure of ZGNRs 30

2.3.5 Cove-type GNRs and further structures 33

2.3.6 Spin-orbit coupling and Rashba-effect in graphene and graphene nanoribbons 34

2.3.7 Fabrication 38

3 Experimental Methods **43**

3.1 Electron spin resonance spectroscopy 43

3.1.1 Basic principles 43

3.1.2 CW spectroscopy 44

3.1.3 Theoretical description of pulsed ESR 46

3.1.4 FID-detected ESR 53

3.1.5 Measurement of spin-spin dephasing T_m 54

3.1.6 Measurement of spin-lattice relaxation T_1 58

3.1.7 DEER spectroscopy 60

3.1.8 ELDOR-detected NMR (EDNMR) 62

3.1.9 HYSCORE 66

3.1.10 Bruker Elexsys Setup 72

3.2 SQUID magnetometry 77

3.2.1 Static SQUID magnetometry 77

3.2.2 AC SQUID magnetometry 79

3.3 Setup development to investigate light-induced effects 83

3.3.1 Low-temperature collimation setup for SQUID magnetometry 83

3.3.2 CW-ESR under continuous irradiation of light 86

3.4 Broadband torque-detected ESR (TDESR) 87

3.4.1 Magnetic anisotropy 87

3.4.2 Torque magnetometry 89

3.4.3 Basic principle of TDESR 90

3.4.4 TDESR setup 92

3.4.5 Combination of TDESR with photoexcitation 95

4 Magnetic bistability in a new cobalt valence tautomer **97**

4.1 Overview of the project 97

4.2 Synthesis and DFT calculations 99

4.2.1 Synthesis 99

4.2.2 DFT calculations 99

4.3 The valence tautomeric mechanism 102
4.4 Characterisation before photoirradiation 104
4.4.1 SQUID magnetometry 104
4.4.2 ESR spectroscopy 109
4.5 Investigation of photomagnetic properties 115
4.5.1 SQUID magnetometry 115
4.5.2 ESR spectroscopy 121
4.5.3 Investigation of backswitching 126
4.5.4 Comparison of the critical temperature 129
4.6 Outlook and Perspectives 130
4.7 Summary 131

5 Photoswitching of an Fe_3Cr-based SMM via spin-forbidden transitions 133

5.1 Overview of the project 133
5.2 Molecular structure and the spin-forbidden process 135
5.2.1 Molecular structure and spin Hamiltonian 135
5.2.2 The photoswitching effect 137
5.3 Broadband TDESR 139
5.3.1 Experimental results 139
5.3.2 Simulation of the spectra 144
5.3.3 Fitting of the spectrum 146
5.3.4 Discussion on the photo-effects and the axial anisotropy barrier 148
5.4 Photomagnetic characterisation via SQUID magnetometry 151
5.4.1 Static magnetometry 151
5.4.2 Dynamic magnetometry 153
5.5 Outlook and perspectives 164
5.6 Summary 167

6 Magnetic edge states and coherent manipulation in graphene nanoribbons 169

6.1 Overview of the project 169

6.2 Structure and synthesis 170

6.2.1 Bottom-up fabrication 170

6.2.2 Theoretical calculations on spin injection effects and band structure 172

6.3 Electron spin resonance characterisation 175

6.3.1 Spin Hamiltonian 175

6.3.2 CW and FID-detected ESR 177

6.3.3 Spin-orbit effects 184

6.3.4 Spin-lattice relaxation 184

6.3.5 Spin-spin relaxation 189

6.3.6 Investigation of hyperfine interactions 195

6.3.7 Coherent manipulation using DEER spectroscopy 201

6.4 Outlook and perspectives 205

6.5 Summary 208

7 Conclusion 211

7.1 Outlook 214

List of figures 219

List of tables 219

Bibliography 243

Acknowledgement 245

Declaration of Authorship 247

1 Motivation

Over recent decades, the miniaturisation of semiconductors has made significant progress, which has led to unprecedented computational power. The manufacturing of microelectronic structures on a length scale of tens of nanometers has enabled potent and highly efficient electronic devices. Looking back ten years ago, the use of smartphones as universal daily accompaniments was a concept unthought of, while, nowadays, it is becoming increasingly difficult to imagine a life without them. However, the miniaturisation of silicon nanostructures is fast approaching the end of the road. Therefore, scientists and engineers are working together in seeking alternative materials that would lead to a further reduction of manufacturing processes [1]. To meet the challenges of the future, the development of transistors on a single-molecule level is becoming increasingly important, as it represents the ultimate form of miniaturisation. At the molecular scale, it is the spin property of electrons that determines the conductive behaviour. This leads to interesting quantum phenomena and to physics that differs from that of bulk systems [2].

In molecular spintronics, a young field arising from the combination of molecular electronics and single-molecule magnets (SMMs), the question of how molecular magnetic spin centres in nanostructures can be controlled is being tackled, with the goal of creating new devices on the nanoscale. Achievements include the development of molecular nanotransistors [3, 4], switches [5] and even the electronic read-out of nuclear spin states on the single-molecule level [6]. SMMs are molecular structures with a metallic core, which act as tiny magnets below a certain blocking temperature [7, 8]. The origin of molecular magnetism is the spin or angular

momentum of unpaired electrons, and we therefore refer to the molecular magnetic centres as 'spin centres'. Representing molecular assemblies, nanomagnets can be functionalised and therefore deposited on conducting surfaces such as gold, carbon nanotubes or graphene [2] using appropriate anchor groups.

SMMs have a fascinating ability: their physical properties can be tailored by varying the spin centres and the surrounding ligands. This allows for a control of magnetisation not only via magnetic fields or temperature [7], but also via pressure [9–11], electric fields [12, 13], or even visible light [14–16]. The use of light is particularly appealing because it allows ultra-clean and ultra-fast control. It directly affects the electronic and spin degrees of freedom, and therefore represents a potentially interesting way to perform quantum logic operations. Other means, such as electrical contacting, directly manipulate the electronic surrounding of SMMs in unwanted ways, often leading to degradation or even loss of SMM behaviour [2, 17, 18]. Thus, the design of robust SMMs is a pressing concern in the field [19, 20]. On the contrary, no direct electric manipulation is necessary when using light as external stimulus, which leads to lower requirements for the robustness of SMMs. All in all, the great tunability of SMMs makes them components of choice for the creation of novel molecular spintronic devices and observations of yet unknown coupling phenomena at cryogenic temperatures.

A potential material for the integration of such magnetic centres are graphene nanoribbons (GNR). In contrast to graphene, a two-dimensional material with fascinating electronic and mechanic properties [21] for which its first experimental investigators were awarded a Nobel Prize, GNRs are confined to one dimension. This leads to a band-gap, making GNRs an interesting nano-sized substitute for current semiconductors. From a theoretical point of view, GNRs have attracted much attention in the last twenty years, yet experimental evidence has remained scarce due to the insufficient purity of fabricated GNRs. However, as a result of recent and novel developments in the bottom-up synthesis technique, it is now possible to synthesise GNRs of high purity and atomically-precise structure, where the sensitive nature of spin-spin interactions is conserved. Consequently, theories

on spin-spin interactions can finally be tested. Using the latest developments in electron spin resonance spectroscopy (ESR), spin states can be directly manipulated on a nanosecond time scale, and interesting coupling phenomena resolved. Finally, we gain access to quantum coherence times and can assess potential applications for quantum operations [22]. The challenging task of combining ESR with molecular spintronics could open up a new horizon for spin manipulation and quantum computing.

In this work, we tackle the question of how light and microwaves can be used to manipulate spin states in molecules and molecular assemblies. We begin with a general theoretical introduction to build up the framework of the thesis. We discuss the properties of SMMs, how to model their physical behaviour using the spin Hamiltonian and discuss quantum coherence phenomena. Since light as an external stimulus plays an important role in this research project, we present an overview on how light can manipulate the states in magnetic molecules. As an interesting backbone, we then give an introduction to graphene nanoribbons. In consideration of the experimental techniques developed for this work, a chapter is dedicated to the experimental background. We explain the different ESR techniques and the instrumental developments used to perform measurements under irradiation of light. Three main research projects are then presented in detail. We begin with the investigation of a new cobalt valence tautomeric complex, which can be switched using light. We shall see how this shows enhanced properties when compared to similar complexes. Then, we progress to the photoswitching properties of an Fe_3Cr-based SMM, and show how to investigate a spin-forbidden transition which manipulates the overall spin state. Finally, we investigate how a chain of magnetic radicals, grafted on a graphene nanoribbon, can interact with each other and with the substrate. We conclude with an examination of the intriguing properties of the material and present clear evidence for the existence of a magnetic edge state in GNRs. This latter observation is the demonstration of theoretical predictions made twenty years go [23], yet unobserved.

2 Theory and Concepts

2.1 Molecular magnetic nanomaterials

The integration of Single-Molecule Magnets (SMMs) and other nanomagnetic materials into new environments, such as molecular cages [24] or nanoelectronic devices [25], has revealed fascinating quantum phenomena [2, 7]. For a better understanding of the research projects and modelling, we will give an overview of the basic properties and appealing features of molecular magnets, which can be exploited for molecular spintronics and quantum computation. We will discuss the bulk properties, highlighting how they become affected by environmental effects, when single molecules are considered.

2.1.1 Single-Molecule Magnets

Single-molecule magnets represent magnetic materials, where the magnetic hysteresis is intrinsically associated to single molecules [7], and, in contrast to ferromagnets, long-range cooperative exchange interactions are not required. SMMs represent the ultimative miniaturisation of magnetic materials, as every single molecule behaves as a tiny magnet, yielding a fruitful ground for molecular spintronics [25] and quantum computation [26]. Like superparamagnets, SMMs retain their magnetisation for long periods of time below a certain blocking temperature, T_B, which can exceed many hours at sufficiently low temperatures [27]. Usually, T_B is defined as the temperature where, after the removal of an external magnetic field, the relaxation of the magnetisation is comparable to experimental time scales [7].

Above T_B, thermal fluctuations drive the system into a paramagnetic equilibrium state. The thermal relaxation time τ, which corresponds to the characteristic time for a spin-flip (Néel relaxation), can be generally expressed as [27]

$$\tau = \tau_0 \exp\left(\frac{U_{\text{eff}}}{k_B T}\right) , \tag{2.1}$$

where τ_0 denotes the inverse spin-flip attempt frequency (typically $10^{-9} - 10^{-10}$ s), U_{eff} the magnetic anisotropy barrier, k_B the Boltzmann constant and T the system temperature.

The unique feature of SMMs is, decidedly, their monodispersity. In contrast to superparamagnetic nanoparticles, every magnetic molecule acts as a magnet by itself. Fabricated nanoparticles show a distribution of sizes, which is why stochastic behaviour is observed and many efforts are being undertaken to narrow down the distribution [28, 29]. Furthermore, as SMMs are constructed via bottom-up approaches, the structural compositions are known and the atomic positions are well-defined in geometry, which is a monumental advantage for the integration into nanoelectronic devices and the interpretation of the phenomena.

The first SMM, a Mn_{12}Ac-complex $[Mn_{12}O_{12}(OAc)_{16}(H_2O)_4]$ with a blocking temperature of 3.1 K, was discovered in the early 90s [30, 36]. It consists of a magnetic centre that is formed by several exchange-coupled metal ions, which are coordinated by organic ligands. In this case, a set of eight Mn^{IV}-ions with a spin of $s = 2$ show antiferromagnetic coupling with four Mn^{III}-ions with $s = 3/2$. The result is a large spin state of $S = 10$ creating a strong uniaxial magnetic anisotropy. Carboxyl groups ($RCOO^-$) and oxygen ions (O^{2-}) are employed as linkers. Physicists and chemists worked together to model the behaviour and created an abundant family of new molecular magnetic materials (see Fig. 2.1).

Through functionalisation, the properties of SMMs can be tailored to display desired features. By substituting parts of the organic shell with appropriate ligands, SMMs can be deposited on conducting surfaces such as gold or carbon nanotubes [25]. Moreover, covalent binding to defective sites or reactive groups are possi-

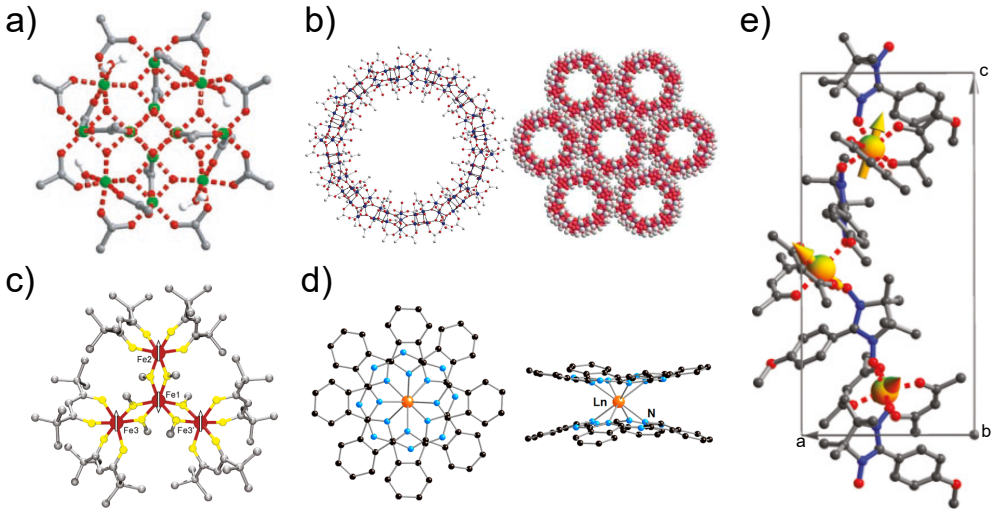

Fig. 2.1: Selected structures of molecular magnets. (a) The archetypal $Mn_{12}Ac$ cluster with $S = 10$ (from Ref. [25, 30]). (b) Mn_{84}-torus and hexagonal packing in tube structure (from Ref. [31]). (c) $Fe_4L_2dpm_6$-cluster (H_3L = tripodal ligand R–$C(CH_2OH)_3$, Hdpm = dipivaloylmethane) with exchange-coupled iron ions ($s = 5/2$ each) yielding an $S = 5$ ground state (from Ref. [32]). (d) The archetypal lanthanide-based SMM $LnPc_2$ (Ln = Tb or Dy, Pc = phtalocyanine) with only one metal centre (from Refs. [33, 34]). Due to strong spin-orbit coupling of lanthanide ions, no exchange-coupling is necessary for SMM behaviour. This sub-class of SMMs is also referred to as Single-Ion-Magnets (SIMs). (e) Assembly of $Co(hfac)_2$(NIT-PhOMe) molecules to a single-chain magnet (SCM) as a magnetic nanowire (hfac = hexafluoroacetylacetonate, NIT-PhOMe = 2-(4'-p-methoxyphenyl)-4,4,5,5-tetramethylimidazoline-1-oxyl-3-oxide) (from Ref. [35]).

ble. This remarkable property enables the direct integration into nanoelectronic circuits. Furthermore, magnetic field and temperature are not the only external stimuli that manipulate the behaviour of SMMs. By inserting the appropriate ligands, photons are able to control the spin state of SMMs [14, 15], which could be exploited for quantum logic operations. Further stimuli imply the use of pressure [9, 10] or electric fields [12, 13]. The control of magnetic properties via light is further reviewed in Chapter 2.2.

2.1.2 Spin Hamiltonian model

The fascinating properties of magnetic molecular materials are a result of the different magnetic effects and spin-spin interactions, which are also responsible for the crystal-field splitting of an SMM. It is described by the spin Hamiltonian model, which is a summation over the interaction Hamiltonians [7, 37] given by

$$\mathcal{H} = \mathcal{H}_{\mathrm{Z}} + \mathcal{H}_{\mathrm{CF}} + \mathcal{H}_{\mathrm{JJ}} + \mathcal{H}_{\mathrm{dd}} + \mathcal{H}_{\mathrm{HF}} + \mathcal{H}_{\mathrm{NZ}} + \mathcal{H}_{\mathrm{NQ}}\,, \tag{2.2}$$

with

$$\mathcal{H}_{\mathrm{Z}} = \mu_B \boldsymbol{B} \cdot \mathbf{g} \cdot \boldsymbol{S} \qquad \text{(Zeeman effect)} \tag{2.3}$$

$$\mathcal{H}_{\mathrm{CF}} = \sum_{k\geq 2,\,|q|\leq k} B_q^k \hat{\boldsymbol{O}}_q^k \qquad \text{(Crystal-field interaction)} \tag{2.4}$$

$$\mathcal{H}_{\mathrm{J}} = \sum_{i\neq j} \boldsymbol{S}_i \cdot \mathbf{J}_{ij} \cdot \boldsymbol{S}_j \qquad \text{(Exchange coupling)} \tag{2.5}$$

$$\mathcal{H}_{\mathrm{d}} = \sum_{i\neq j} \boldsymbol{S}_i \cdot \mathbf{D}_{\mathbf{ij}}^{\mathrm{dip}} \cdot \boldsymbol{S}_j \qquad \text{(Magnetic dipole coupling)} \tag{2.6}$$

$$\mathcal{H}_{\mathrm{HF}} = \sum_{i} \boldsymbol{S} \cdot \mathbf{A}_i \cdot \boldsymbol{I}_i \qquad \text{(Hyperfine coupling)} \tag{2.7}$$

$$\mathcal{H}_{\mathrm{NQ}} = \sum_{i\neq j} \boldsymbol{I}_i \cdot \mathbf{P}_{\mathbf{ij}} \cdot \boldsymbol{I}_j \qquad \text{(Nuclear quadrupole interaction)} \tag{2.8}$$

$$\mathcal{H}_{\mathrm{NZ}} = \sum_{i} \mu_n g_{n,i} \boldsymbol{B} \cdot \boldsymbol{I}_i \qquad \text{(Nuclear Zeeman effect)} \tag{2.9}$$

The Zeeman term describes the interactions of a spin $\boldsymbol{S}$ with a magnetic field $\boldsymbol{B}$, where $\mathbf{g}$ denotes the g-tensor of the magnetic centre and μ_B the Bohr magneton. The crystal-field (CF) term is a result of the electrostatic Coulomb interactions of the electrons of unfilled orbitals with the electrostatic potential of the ligands. Here, the parameter k describes the order of the CF term. It can be shown that it is sufficient to consider terms up to the sixth order [37]. For transition metal complexes, lower-order terms have a much larger influence than higher-order terms, while for lanthanide complexes even higher-order terms are as significant as lower-order ones. The CF terms with even k are responsible for the crystal-

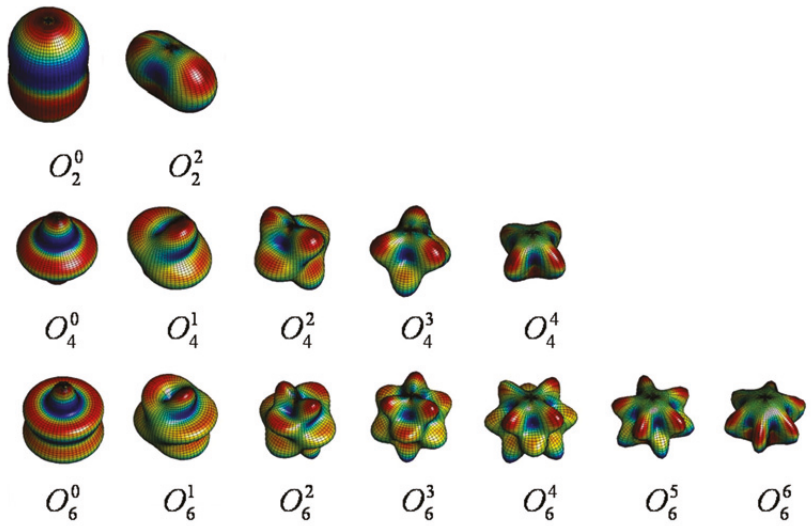

Fig. 2.2: Spherical representation of the crystal-field parameters. The geometric representation visualises the spherical harmonics contained in the CF Hamiltonian, which follow the symmetry of the molecule. The q-fold symmetry can be well seen from the visualisation. With increasing order k, the tesseral harmonics become more complex. Figure adapted from Ref. [38].

field splitting, and therefore determines the anisotropy barrier height. Since the barrier scales with the crystal-field parameters, large values are the most important ingredient for SMM behaviour. However, the CF parameters strongly depend on the environment of the spin centre, which is the crucial point why many SMMs lose or alter their magnetic properties when deposited on surfaces. Furthermore, it has been shown, that tiny changes in the surrounding or magnetic centre can have a vast impact on magnetic properties, even totally inverting anisotropy axes [39, 40] (see Fig. 2.3). The second-order approximation of the CF Hamiltonian is given as [7]

$$\mathcal{H}_{\mathrm{CF}} = DS_z^2 + E(S_x^2 - S_y^2)\,, \tag{2.10}$$

where $D = 3B_0^2$ is commonly referred to as the axial anisotropy parameter, and $E = B_2^2$ as the transverse anisotropy term. Higher-order terms have minor influences on transition metal ions [7, 41], but considerable effects on lanthanides [37, 42]. In Mn_{12}Ac-clusters, these are responsible for state-mixing and thus quan-

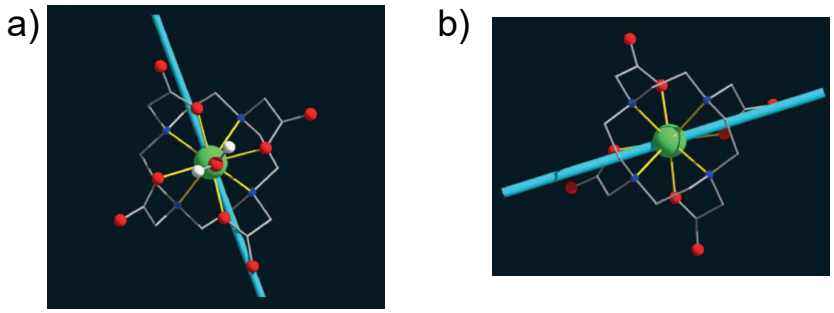

Fig. 2.3: Calculations of environmental effects on magnetic properties of a LnDOTA-complex. The preferred orientation of magnetisation is denoted by the blue easy-axis, here exemplarily for a LnDOTA-complex. Removing the central water molecule results in a 90° rotation of the easy-axis. Figures adapted from Ref. [39].

tum tunneling of magnetisation [7]. The number and kind of higher-order terms strongly depend on the symmetry of the SMM [37]. A spherical representation of the CF-terms is depicted in Fig. 2.2, which shows the relationship between the molecular geometry and the CF parameters.

The exchange-interaction Hamiltonian incorporates the exchange-coupling tensor $\mathbf{J}$, which can be reduced to a sum of isotropic exchange (Heisenberg-type [43]), anisotropic exchange and antisymmetric exchange (Dzyaloshinskii-Moriya interaction [44, 45]). Usually, the isotropic term $-J_{ij}\boldsymbol{S_i}\cdot\boldsymbol{S_j}$ with $J_{ij} = -\mathrm{Tr}(\mathbf{J_{ij}})/3$ dominates and produces, depending on the sign of J_{ij}, either parallel or antiparallel coupling. The topology of the intramolecular couplings in $Mn_{12}Ac$ produces a total ground spin state $S = 10$ [30, 36]. Anisotropic exchange $\boldsymbol{S_i}\mathbf{D_{ij}}\boldsymbol{S_j}$ with $D_{ij}^{\alpha\beta} = (J_{ij}^{\alpha\beta} + J_{ij}^{\beta\alpha})/2 - \delta_{\alpha\beta}\mathrm{Tr}(\mathbf{J_{ij}})/3$ and antisymmetric exchange $\mathbf{J_{DM}}(\boldsymbol{S_i}\times\boldsymbol{S_j})$ with $J_{\mathrm{DM}} = (J_{ij}^{\beta\gamma} + J_{ij}^{\gamma\beta})/2$, where α, β, γ represent Cartesian coordinates, are comparatively small in many cases (strong exchange limit), and can be treated as perturbations [7]. Magnetic dipole interactions are described via the dipolar coupling tensor $\mathbf{D_{ij}^{dip}}$, which can be reduced to a scalar value d_{ij} where the orientational dependence is accounted by dipolar field vectors.

The last term, the electron-nuclei interaction term, can usually be reduced to

hyperfine coupling. This interaction is comparably small (splitting in mK region). The main part of the coupling arises from magnetic dipole-dipole interactions between the nuclei j with nuclear spin $\boldsymbol{I_j}$, described by the tensor $\mathbf{A_{ij}}$. Furthermore, the coupling of the orbital momentum of the electron to the nuclei also contributes to the hyperfine coupling, which is also known as pseudo-hyperfine coupling [46]. Hyperfine interactions plays an important role in microwave spectroscopy and decoherence mechanisms (see Sec. 2.1.5). For nuclear spins with $I \geq 1$, quadrupolar interactions, where $\mathbf{P_{ij}}$ denotes the quadrupole tensor, add to the hyperfine structure. The nuclear Zeeman effect (similar to the standard Zeeman effect but with nuclear g_n-factor and nuclear magneton μ_n) may play a role in some cases.

It should be noted that the interaction with the environment also strongly depends on the nature of the electronic states within the metal ion [37]. Hereby, electron-electron interactions within the ion and spin-orbit coupling (for lanthanide ions usually) play an important role. This leads to a shift in energies and to higher-order interaction patterns. These interactions are well described in the framework of the Wyborne formalism, whose discussion goes beyond the scope of this work. For the interested reader we here refer to Ref. [37].

2.1.3 Slow relaxation and quantum tunnelling of magnetisation

The magnetic blocking originates from the slow relaxation of magnetisation, a phenomenon first observed on SMMs in 1991 [47]. Intriguingly, both classical and quantum physics play a simultaneous role. The energy diagram (double-well potential) of the crystal-field splitting is shown in Fig. 2.4 for $Mn_{12}Ac$. The ground multiplet with $S = 10$ splits into $2S + 1$ states, denoted by the magnetic quantum number m_s. At sufficiently low temperatures, only the lowest lying state is occupied. Depending on the magnetic field, the system can be polarised in $m_s = +S$ or $m_s = -S$. The magnetisation can then be inverted via three pathways.

Firstly, it can be inverted thermally. When increasing the temperature of a spin ensemble, excited spin states are getting populated obeying a Boltzmann

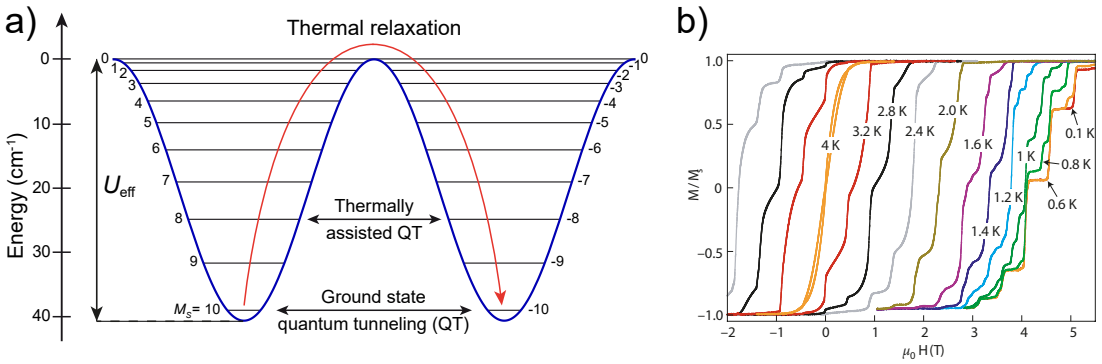

Fig. 2.4: Slow relaxation of magnetisation. (a) Relaxation mechanisms in Mn_{12}Ac-SMMs. At very low temperatures, only the lowest lying state is occupied, and magnetic reversal is thermally blocked. (b) Magnetic hysteresis of Mn_{12}Ac-SMMs. The characteristic steps in the hysteresis loop appear when two energy levels are in resonance when sweeping the magnetic field. Due to the Zeeman-effect, a magnetic field shifts the states of both sides in opposite directions. In resonance, quantum tunneling of magnetisation is possible. The appearance of hysteresis is strongly dependent on the field sweep rate. Figure adapted from Ref. [25].

distribution. In an SMM, phonon-induced transitions lead to population of states on the counter side of the energy barrier via spin-phonon interactions. Here, each phonon excites a transition with $\Delta m_s = 1$, and, consequently, when several phonons excite the spin, relaxation takes place when the highest state at the top of the barrier is reached. This process is also known as Orbach relaxation [7], where the the anisotropy barrier corresponds to the activation energy. Additionally, higher-order transitions with $\Delta m_s = 2$ may also appear [7]. If the thermal energy is larger than the anisotropy barrier U_{eff}, the thermal fluctuations dominate the system and the SMM behaves as an usual paramagnet.

Secondly, inversion takes place via quantum tunnelling of magnetisation as first observed by Friedman *et al.* in 1996 [48]. In fact, the energy diagram shown in Fig. 2.4 is only partially correct. Due to all terms in the spin Hamiltonien that contain S_+ and S_- operators, the m_s states are not pure eigenstates, but are

admixtures of different states. For $Mn_{12}Ac$ these are mixtures with $\Delta m_s = \pm 4$ at the first order. At higher orders, the $|\pm 10\rangle$ states are thus mixed, with a small degeneracy lifting, which creates the barrier for quantum tunnelling. The steps in magnetic hysteresis curves of SMMs are a typical hint of quantum tunnelling of magnetisation (Fig. 2.4b) and can be understood as follows. Under the influence of a magnetic field, the spin doublet degeneracy is lifted due to the Zeeman effect, as depicted in Fig. 2.5. When two spin states were to cross in energy at distinct magnetic fields, they show an avoided level-crossing signature and a non-linear field dependence, Fig. 2.5b. At such avoided level-crossings, where the symmetry condition contained in the crystal-field parameters is fulfilled, quantum tunnelling takes place. However, in order to see those steps in the hysteresis curve, enough time must be given for the spin-flip to happen, i.e. the sweep rate of the magnetic field must be slow compared to the quantum tunnelling process. More precisely, it must fulfill the following condition [7].

$$\hbar \frac{\mathrm{d}}{\mathrm{d}t} \frac{1}{\Delta E(t)} \ll 1 \,, \tag{2.11}$$

where $\Delta E(t)$ corresponds to the energy difference between excited and ground state in a time-dependent magnetic field. On the contrary, if a fast sweep rate is chosen, the spin state becomes trapped in its ground state, leading to a suppression of the quantum tunnelling effect, and the molecule remains in its original state even at higher fields. This phenomenom is described by the Landau-Zener-Stückelberg theory [7].

As a third possibility, thermally assisted quantum tunnelling can also take place, when transition between excited states are allowed by symmetry. This behaviour shows clearly that in molecular magnetism classical and quantum behaviour occur in parallel, which makes SMMs fascinating objects for scientists.

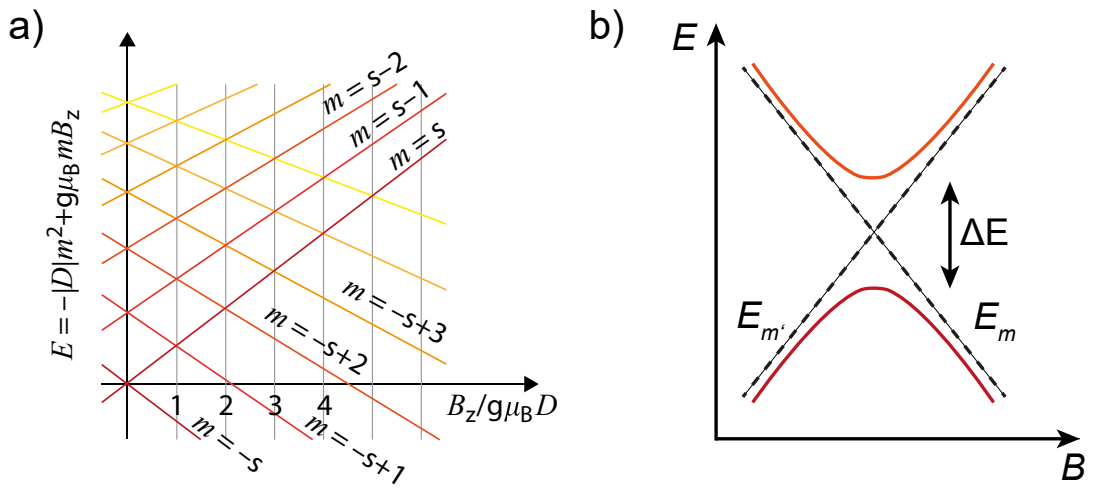

Fig. 2.5: Splitting of SMM spin states in a magnetic field. (a) The application of a magnetic field removes the degeneracy of doublet states. The energy scales linear with a magnetic field applied in z-direction for a purely axial system. (b) Avoided level crossing schemes. The energies of states E_m and $E_{m'}$ that scale in opposite direction with magnetic field do not cross each other, but come as close as ΔE. Figure adapted from Ref. [7].

2.1.4 Requirements of SMMs

In order to behave as an SMM, the anistropy barrier must be sufficiently large. In the simplest approximation for transition metal ions, it is given by $U_{\text{eff}} = |D|S^2$, where D is the axial anisotropy parameter [7, 33] (see next section). The D value depends on the electrostatic interactions between the magnetic centre and the organic ligands. For negative values, a large spin projection is preferred, resulting in a strong easy-axis anisotropy.

To obtain larger anisotropy barriers and thus higher blocking temperatures, scientists tried to maximise the spin by synthesising huge exchange-coupled clusters. However, it has been found that a large spin state usually comes together with a small axial anisotropy parameter [33]. The Mn_{19}-cluster with a record spin of 83/2 only shows $U_{\text{eff}} = 4\,\text{cm}^{-1}$ [49], while Mn_{12}Ac with $S = 10$ shows $U_{\text{eff}} = 51\,\text{cm}^{-1}$ [30, 36]. This is due to the fact that in such large clusters, the single anisotropy terms of the ions cancel out each other [33]. Therefore, scientists started to find ways to increase single-ion anisotropy.

Lanthanide ions show a strong single-ion anisotropy due to their unquenched orbital momentum. Ishikawa *et al.* were the first to show a single-molecule magnet with only one central lanthanide ion [34] (Fig. 2.1d). Not a long time ago, the highest blocking temperature achieved with lanthanides was 14 K [50], which is still far away from room temperature, and anisotropy barriers as large as 1815 K [51]. Recently, an SMM with a magnetic hysteresis at 60 K was reported [52], which is a giant step, showing there is still ample room for improvements. Nevertheless, despite the intense research, the strongest drawback of SMMs continues to be their low blocking temperatures.

2.1.5 Quantum coherence and quantum computation

In modern computers, information is stored and processed in the form of two states, "1" and "0". However, imagining storing information in more than two ways, for example as any superposition of "1"s and "0"s (i.e. $a\,|1\rangle + b\,|0\rangle$) as qubits, would greatly enhance computational power, and even overcome current encryption technology with ease [8, 53]. As theoretically demonstrated by Leuenberger and Loss [26], SMMs are able to perform Grover's quantum search algorithm, enabling storage of 2^{2S+1} numbers, thus having some potential applications for quantum computation. Recently, the experimental implementation of Grover's algorithm in $TbPc_2$-SMMs has been demonstrated [54].

In order to perform quantum logic operations, the phase relationship must be maintained for a reasonable duration (coherence time T_2) to allow finishing a computation without any errors. Investigation of decoherence mechanisms, such as electron-nuclei or dipole-dipole interactions [55, 56], is crucial for the rational design of molecular materials with long coherence times. Pulsed ESR gives direct access to the coherence times, so that decoherence sources can be studied profoundly.

In the last years, the development of qubits and quantum computers has made significant progress. Recently, Intel presented a superconducting 17-qubit chip, operating at 20 mK [57]. Moreover, IBM has presented a working quantum computer with 50 qubits, with coherence times as large as 90 µs [58]. Using an array of superconducting qubits, it was possible to calculate the electronic structure of molecular hydrogen via quantum algorithms, and obtain its energy potential [59]. Furthermore, quantum error detection protocols have been successfully integrated on a 4-qubit device [60]. Looking at these latest developments, we can expect to see further experimental realisations of quantum computations and, accordingly, interesting results in the near future.

Quantum coherence in SMMs

The first observations of quantum coherence on SMMs were published in 2000 on Fe_8 and Mn_{12} clusters [61]. However, in this case, quantum coherence was not measured via pulsed ESR. Early calculations yielded a lower limit for the coherence time of about 1 ns in a manganese-based dimer [62]. However, a large step towards possible application of SMMs as quantum logic elements was achieved in 2007 [63]. Via pulsed ESR, quantum coherence was observed in Cr_7Ni-clusters reaching a phase-memory time of 3 µs at low temperatures [63]. This result demonstrates that coherence times can be actually much larger. The basic pulse scheme for determining the phase-memory time is shown and explained in Ch. 3.1. In subsequent years, many follow-ups based on both transition metal and lanthanide ions have been reported [64–72], where phase-memory times between hundreds of nanoseconds and 15 microseconds have been observed.

Due to the possibility of controlling and manipulating molecular centres individually, SMMs are interesting objects for integration into quantum computation. Their mesoscopic nature together with their large magnetic moment enables easier control than atomic objects. Alternative approaches make use of quantum dots [73–75], superconducting qubits [76], entangled states in trapped atomic ions [77] and nitrogen-vacancy centres in diamonds [78, 79], where addressability or the maintenance of quantum behaviours are still important issues [8]. Via pulsed ESR, the state of SMMs can be controlled and environmental perturbations investigated.

The integration of SMM qubits in devices is an important issue for quantum technology. However, control mechanisms are not well developed yet and require innovative approaches. Therefore, integrating pulsed ESR in electronic nanodevices could enable a revolution for quantum computation. Furthermore, potential candidates are organic radicals, with coherence times as large as milliseconds [80]. As organic systems, these can be grafted to other organic systems such as graphene, yielding interesting possibilities as shall be seen later.

2.2 Photoswitching of molecular magnets

In this section we will clarify the most prominent mechanisms where light influences the magnetic state of a molecule. In the past, research focused on three primary mechanisms, where the spin state of a molecule is manipulated by a spin-crossover (SCO), charge-transfer process (CT) or photoisomerisation, also known as photochromic complexes. Here, we will give a theoretical introduction of the processes. Additional information can be found in Ref. [14, 81, 82]. At the end of this chapter, we will discuss further niche photoswitching mechanisms, which have not attracted much attention, yet still have great potential for the field of molecular spintronics.

2.2.1 Spin crossover

A spin transition, where the magnetisation becomes either enhanced or lowered, can occur in octahedral transition metal complexes with d^{4-7} configuration. The octahedral crystal-field partially removes the degeneracy of the five d-orbitals into a set of two and three degenerated orbitals, named as e_g and t_{2g}, respectively. By minimising Coulomb repulsion forces, t_{2g}-orbitals are lower in energy for octahedral symmetry. Depending on the crystal-field strength, the ground state can be either a low-spin (LS) or a high-spin (HS) state. In the LS state, first the t_{2g}-orbitals are filled with electrons leading to partial or complete cancellation of magnetic moment due to Pauli's principle (Fig. 2.6). In contrast, in the HS state all Coulomb repulsive forces dominate over Pauli's principle, and thus all orbitals are first singly occupied leading to an increased magnetisation. A temperature-driven crossover between these two states may appear when the pairing energy lies between the energies of the HS and LS states. Usually, the complex shows a HS state at high, i.e. room temperature, and undergoes the LS transition when cooling down. In cases where intermolecular interactions are strong, temperature hysteresis effects can be observed and the HS-LS-transition becomes abrupt, as depicted in Fig. 2.6.

External stimuli such as pressure or light are able to drive the LS-HS-transition

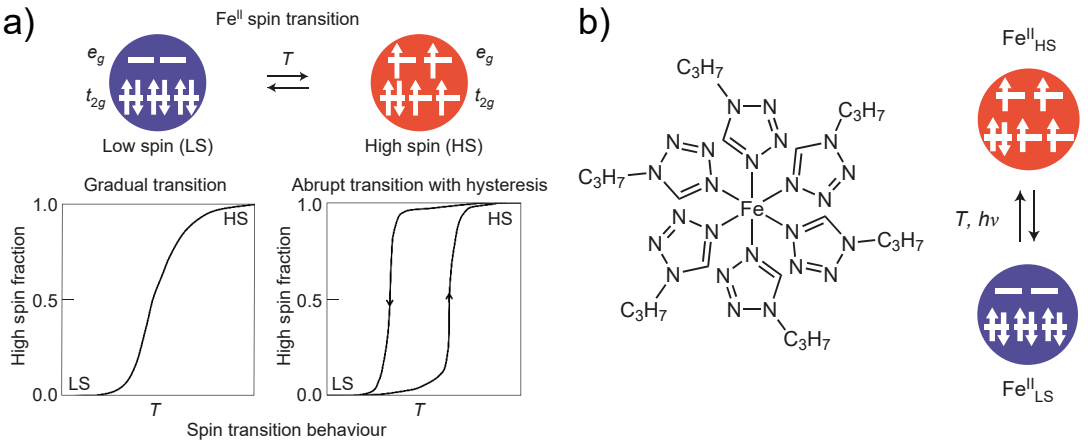

Fig. 2.6: Spin-crossover process. (a) Spin-crossover of an iron-based complex. In the LS state, spins pair up, while in the HS state single occupation is preferred. The HS-LS transition can be thermally induced and either shows a gradual transition or an abrupt transition with a hysteresis. (b) SCO-complex $[Fe^{II}(1\text{-propyltetrazole})_6]^{2+}$. Figures adapted from Ref. [81].

[81, 83]. By irradiating a SCO complex at sufficiently low temperatures, an SCO complex turns from the LS to the HS state, and relaxes either thermally described by an Arrhenius law, or via temperature-independent quantum tunnelling phenomena [84]. This effect, typically observed in complexes based on Fe^{II} or Fe^{III}-ions [85, 86], is also known as light-induced excited spin-state trapping (LIESST) [87]. The spin change can either be detected using magnetometric techniques or ESR spectroscopy, where microwaves probe spin states.

The spin-crossover process is coupled with a change of the unit cell volume. This is due to the fact that the higher-lying e_g states have anti-bonding character. Moreover, this also means that the LIESST-effect can be quenched in high-pressure environments. In fact, such a mechanical change has been observed in bilayer structures [88].

Furthermore, spin-state switching has also been observed in iron-based SMMs, and even SMM-behaviour can be switched on and off via the use of different wavelengths [15, 89]. The tristability process is explained in Fig. 2.7. Potentially, the magneto-optical Kerr effect (MOKE) could be used to read the spin state in

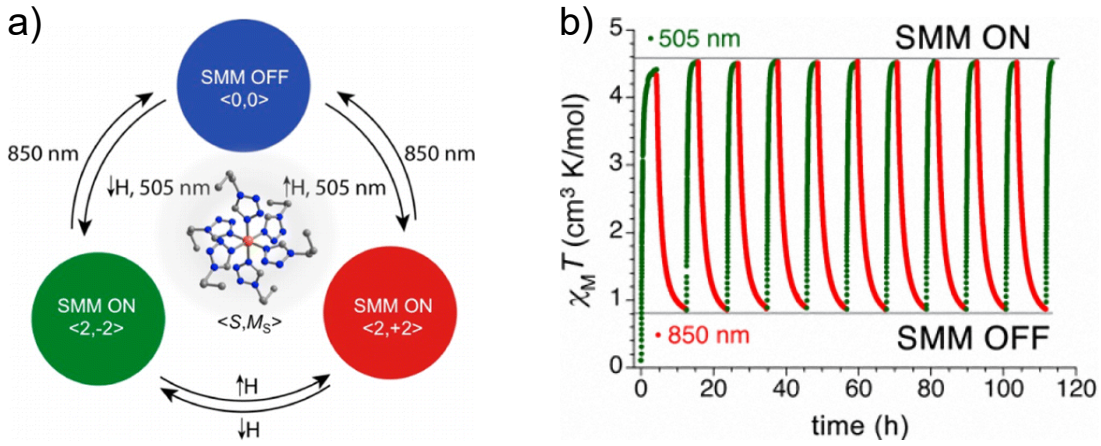

Fig. 2.7: Tristability in an iron-based SMM. (a) SMM-behaviour can be switched on and off using the appropriate wavelength. Irradiation at 850 nm creates an $S = 0$ state and therefore the SMM-behaviour vanishes. This effect can be reversed via illumation at 505 nm. (b) The susceptibility-temperature product indicates the switching behaviour, and it is completely reversible without degradation even after many hours. Figures adapted from Ref. [15].

such a system, while a short-wavelength and long-wavelength laser allows to write the spin state [15, 27]. The magneto-optical Kerr effect describes the phenomenon where the polarisation of light, like for example from a laser, gets rotated by an angle θ_K when it hits a magnetic surface. The turning angle depends on the magnetisation of that surface, and is usually of the order of 1° [27]. Confining light to the dimensions of a molecule is an on-going field of research [15, 90].

2.2.2 Charge transfer

In charge transfer complexes, a light-induced electron transfer between the metal centre and the surrounding may cause the magnetic state to change. In this case, the charge transfer is coupled to an LS-HS transition of the central metal ion. Charge transfer processes are usually classed based on which kind of orbitals take place in the redox process. A charge transfer between the metal centre and the coordinating redox-active ligand is known as valence tautomerism [91], for instance. Often, catechol and semiquinone redox-ligands are used in valence

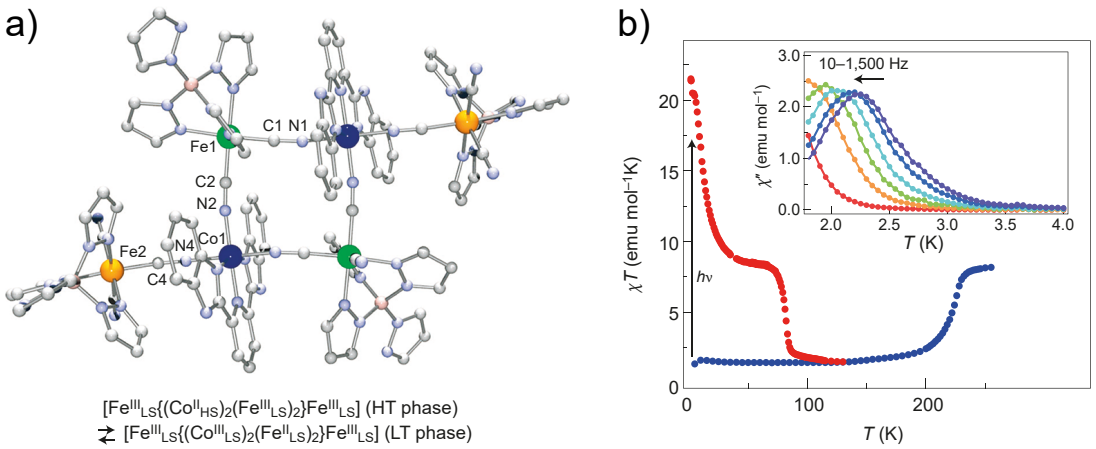

Fig. 2.8: Photoswitching via charge-transfer. (a) Molecular structure and the HS-LS mechanism of an Fe-Co-based charge-transfer complex. (b) Determined χT at different temperatures. The molecule shows an HS state at room temperature, and LS at cryogenic temperature. After irradiation at low temperatures, χT increases (red curve) and the molecule shows an out-of-phase magnetisation, which indicates SMM behaviour. Figures adapted from Ref. [81] after Ref. [93].

tautomeric complexes [92]. Furthermore, valence tautomerism is not necessarily controllable with light and usually observable in cobalt-based complexes.

The first investigations on charge-transfer-based photoswitchable magnetic systems were performed on FeCo Prussian blue analogues, where two metal centres are connected via cyanide bridges. Here, the spin-state change happens via a metal-to-metal charge transfer, thus changing both oxidation and spin states. A more advanced version of this mechanism is shown in Fig. 2.8, where SMM-behaviour in the photoexcited state [93] was observed. When cooling down from room temperature, the molecule goes from an HS into an LS state, which can be switched back with 808 nm light, similar to SCO complexes. When warming up afterwards, the light-excited meta-stable state can be maintained until approximately 80 K. Interestingly, after irradiation, the molecule shows an out-of-phase magnetisation in an alternating magnetic field, which indicates SMM behaviour.

2.2.3 Photoisomerisation

Some molecules change their molecular structure under irradiation of light, which can be accompanied with a spin-state transition. This phenomenon is known as photoisomerisation. In contrast to SCO or charge-transfer photoswitchable molecules, compounds exhibiting photoisomerisation show large critical temperatures above 200 K. Until this, the metastable photoexcited state can be maintained and the switching remains reversible at different wavelengths. Furthermore, these photochromic molecules show a completely different absorption pattern in the two states, leading to a colour change. A prominent group represents compounds based on diarylethene showing an open and a closed form [95], shown in Fig. 2.9a. Ultraviolet light (365 nm) switches the molecules from the open to the closed isomer, while green light (>500 nm) has the reverse effect. The combination of diarylethenes with Mn_4-SMMs has led to a molecule with properties that can be controlled via light [96]. In this photochromic Mn_4-SMM-chain, intermolecular interactions can be tuned through irradiation. Moreover, other molecular groups may completely revert the magnetic properties. Via trans-cis transitions

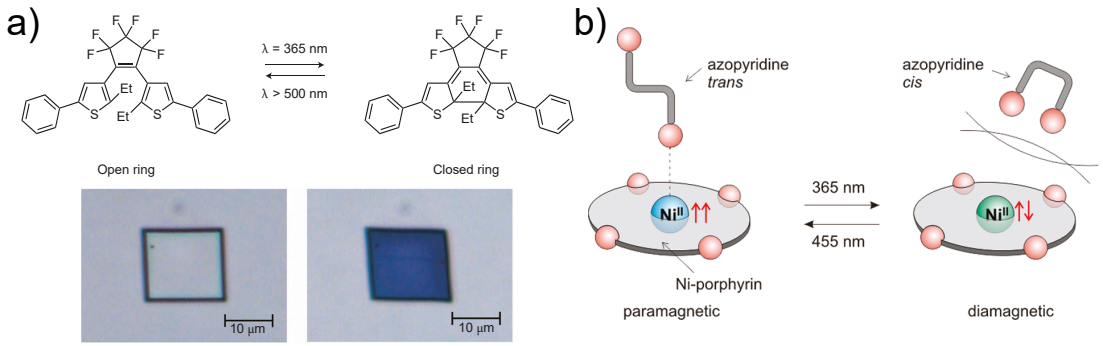

Fig. 2.9: Photoswitching via isomerisation. (a) Molecular structure of a diarylethene compound. Using light, diarylethenes can be switched to an open or closed version. Furthermore, the visible aborption spectrum changes drastically, as can be seen in the different colours of the two states. Figure adapted from Ref. [81] after Ref. [93]. (b) Photoswitching of a Ni^{II}-porphyrin. Figure adapted from Ref. [94].

of azopyridine groups, Ni^{II}-porphyrins can be switched from a paramagnetic to a diamagnetic state as depicted in Fig. 2.9b [94].

2.2.4 Further notable light-effects in molecules

There are numerous other photoswitching phenomena that have potential application for photoswitchable molecules. Further effects imply an interconversion of a radical σ-dimer to a π-radical pair, $(\sigma_2^+)^2 \leftrightarrow (\pi^+)(\pi^-)$. As has been shown in Ref. [97], a sulphur-bridged bisdithiazolyl radical σ-dimar with $S = 0$ dissociates into two π-radicals, each of which carrying a spin of 1/2 und irradiation of light, yielding unprecedentedly high LIESST temperatures of about 242 K. Another interesting effect consists of spin-forbidden transitions (SFT) in chromium-based complexes, with lifetimes in the milliseconds to seconds range [98]. Investigations on the SFT-mechanism in an Fe_3Cr-based SMM form one part of the thesis, discussed in Ch. 5.

Progressing beyond the scope of photoswitchable molecules, one of the most prominent light-effects is photosynthesis, which remains a chief natural process impacting daily life. The absorption of a photon initiates an electron transfer from a donor to an acceptor group, and spin physics plays an essential role here. Understanding these processes will promote the development of similar artifical systems, which could then be used as molecular switches with interesting applications for molecular spintronics [99]. One example for such a donor-acceptor complex, together with ESR spectroscopy results, is shown in Fig. 2.10 [100]. Further effects of light also exist, but go well beyond of the scope of the present work. The interested reader may find more thought-provoking effects in Refs. [14, 81].

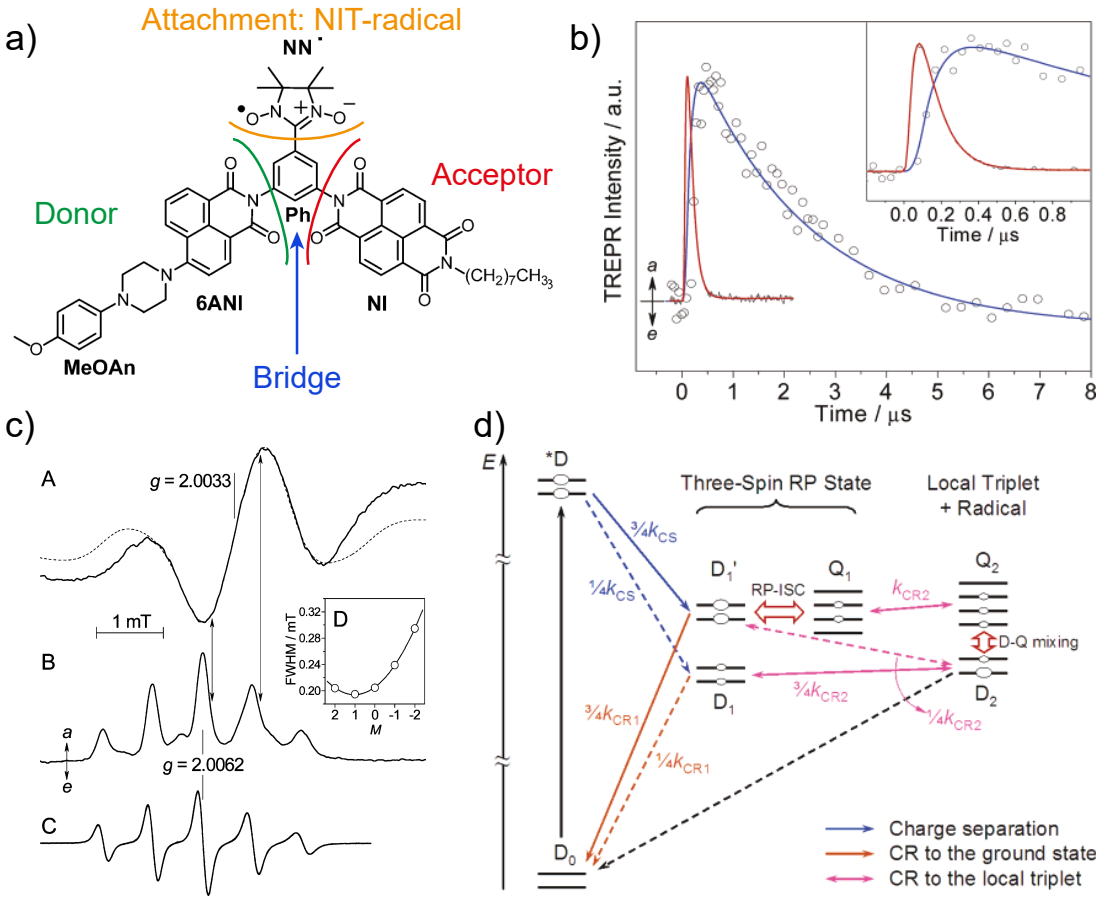

Fig. 2.10: Donor-bridge-acceptor nitronyl-nitroxides (D-B-A-NIT). (a) Chemical structure of the D-B-A-NIT complex. Via excitation with 416 nm light, a radical pair is generated, and the electron travels through the bridge-molecule to the acceptor. On its way, it perturbs the attached nitronyl-nitroxide molecule. (b) Transient ESR signal after excitation with a laser pulse. The blue curve is a pure signature of the NIT-radical, as the radical-pair (RP) signal (red) decays much faster. (c) X-band ESR-spectrum of D-B-A-NIT in toluene (A) 60 ns and (B) 320 ns after laser pulse (absorptive type), and (C) before laser excitation (derivative type). The evolution shows the distortion generated by the quasi flowing electron. (d) Energy level diagram of the molecule, resulting from exchange interactions within the triradical (CR: charge recombination). Figures adapted from Ref. [100].

2.3 Graphene nanoribbons

2.3.1 Introduction

Graphene is considered as the miracle nanomaterial of our future and it has found application in nanotechnology [21]. It can be used in photodetectors [101], reinforcing agents in biodegradable nanocomposites [102], single-molecule DNA sequencing [103] or transparent electrodes as replacements for InSbO [104], for instance. Being flexible and conductive, graphene also finds application in conductive plastics and electric batteries [105]. One of its main advantages is that it represents the ultimate miniaturised form of a conducting layer: a two-dimensional honeycomb network of carbon atoms whose π-orbitals generate a delocalised electron gas and form a zero-bandgap semiconductor, or semi-metal. This type of conductor shows the presence of point-like connection points between the valence and conduction bands, called Dirac points. When the chemical potential is at the Fermi energy, the conductivity of the material is thus at its lowest, while by shifting the chemical potential to higher or lower energies we can have transport via either hole or electron carriers [21]. One key characteristic of graphene is that the energy band structure, in proximity of the Dirac points, is linear in the wavevector k, contrarily to the energy dispersions of most solids, which have a quadratic dependence. This makes electrons behave in a relativistic manner, and produces very high mobilities in the material. On the other hand, the absence of a band gap creates considerable problems in the creation of switchable graphene devices such as field-effect-transistors.

One proposal to overcome such issues is to open a band-gap by confining graphene to one dimension, i.e. creating a graphene nanoribbon. Graphene can actually be considered as the basis material for carbon allotropes. As shown in Fig. 2.11, the structures of zero-dimensional fullerenes, one-dimensional carbon nanotubes, one-dimensional graphene nanoribbons or three-dimensional graphite structures, can all be obtained by manipulating the graphene lattice. In fact,

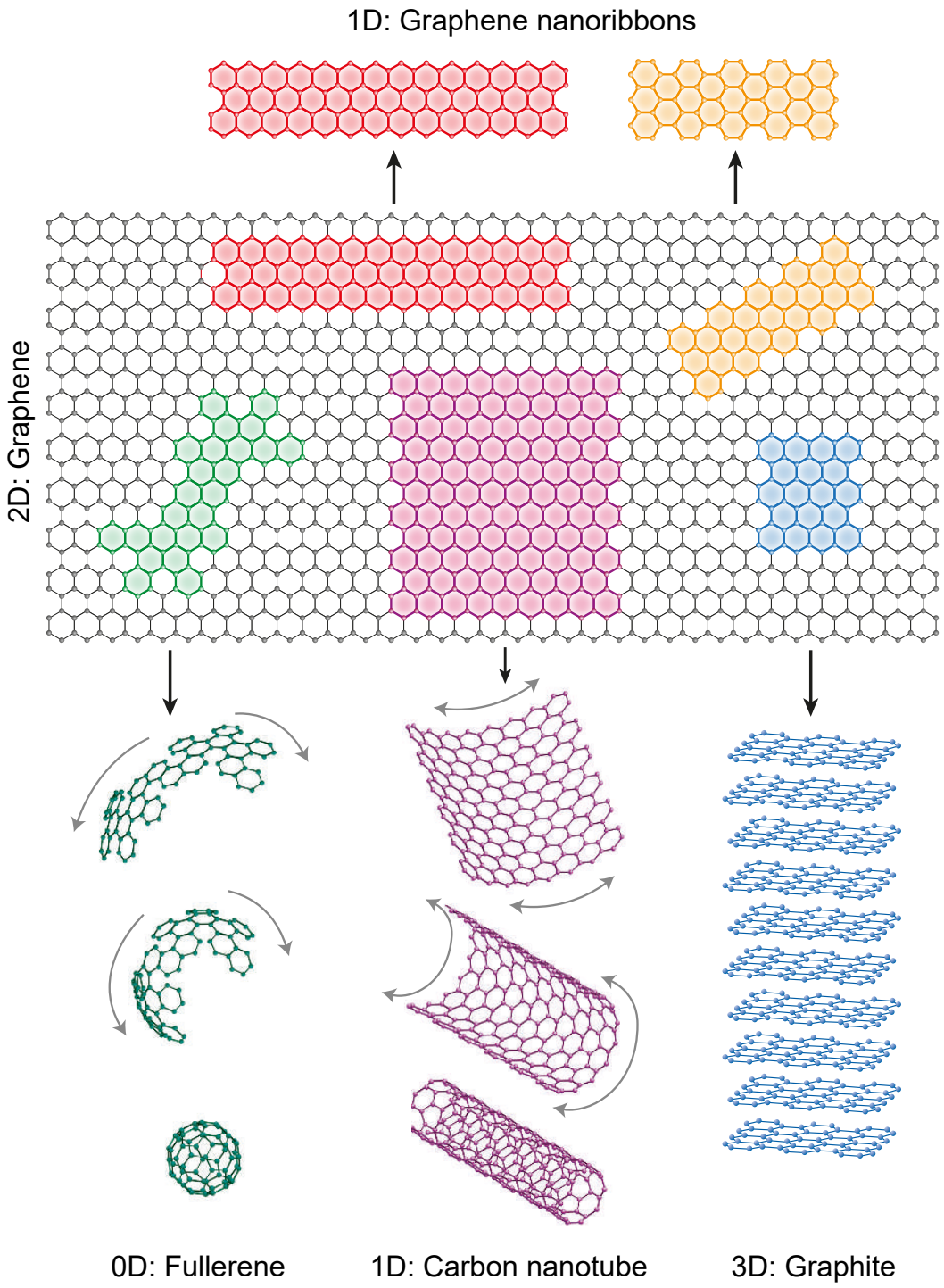

Fig. 2.11: Graphene as base for other carbon materials. The structure of graphene nanoribbons is found in graphene itself, while pieces of graphene can be rolled to 0D fullerenes or 1D carbon nanotubes, or stacked to 3D graphite. Figures partially adapted from Ref. [21].

graphene nanoribbons (GNRs) were not shown in a similar figure in Ref. [21] from 2007. Since then, synthetic approaches have improved significantly and it has become possible to synthesise flat ribbons of graphene, with well-defined edges [106]. The additional confinement has dramatic effects on their physical properties. For example, some quasi-onedimensional GNRs feature a band gap leading to real semiconducting properties [107], and the existence of a spin-polarised edge-state that is delocalised along the edges of zigzag-type GNRs [23, 108]. Here, we will provide the theory needed to understand the experiments performed in this work.

2.3.2 Structure

The carbon atoms of graphene form a honeycomb lattice with a lattice constant of $a = 2.46\,\text{Å}$ (Fig 2.12a). Each carbon atom is surrounded by three neighbours. Therefore, three valence electrons are sp^2-hybridised and form σ-bonds. The remaining valence electron sits in a p_z-orbital. While the hexagonally-placed σ-bonds enable the outstanding elastic properties [109], the π- and π^*-electrons are delocalised and form a two-dimensional electron gas, which is responsible for the conductive and optical properties [110]. The resulting band structure is shown in Fig. 2.12b. In graphene, two neighbouring sites are not equivalent, and the honeycomb lattice is spanned by two triangular sublattices A (blue) and B (green), as shown in Fig. 2.12a. The corresponding Brillouin zone shows two inequivalent points K and K', known as Dirac-points, which lead to the so-called valley degeneracy. At the Dirac-points, the valence band and conduction band show a linear dispersion with no band gap, which causes graphene to be a gapless semiconductor.

When graphene is confined to one dimension, a different situation emerges. Predominantly, one distinguishes between armchair-GNRs and zigzag-GNRs, denoted as AGNRs and ZGNRs, respectively (Fig. 2.12c and d). Both types can show semiconducting properties and direct band gaps. In the case of AGNRs, quantum confinement leads to the band gap, while for ZGNRs spin-ordered edge states create a staggered sublattice potential causing a band gap [111]. Importantly, the band gap scales with the inverse of the width of the ribbons [112].

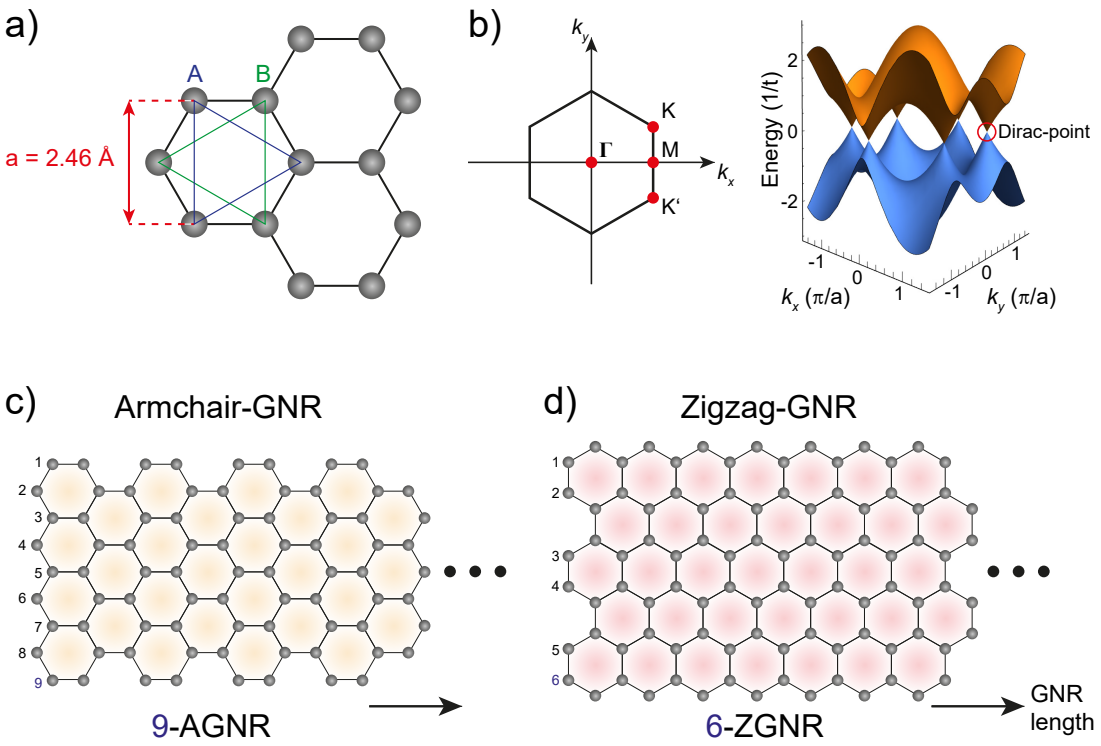

Fig. 2.12: Graphene and possible GNR structures. (a) Honeycomb-lattice of graphene. (b) Brillouin-zone and band structure of graphene. (c) Armchair-GNR structure. The direction of growth is indicated by the arrow. (d) Zigzag-GNR structure. Hydrogens are omitted for clarity.

2.3.3 Band structure of AGNRs

The electronic properties of an AGNR depend on its belonging to one of the three different types, which structurally differ in the number N_a of carbon atoms across the ribbon, as shown in Fig. 2.12c. In the following we therefore introduce the notation N_a-AGNR. N_a-AGNRs are grouped into the types $N_a = 3p$, $n = 3p + 1$ and $n = 3p + 2$, where p represents an integer that can be deduced from the number of carbon atoms across the ribbon. Theoretical tight-binding calculations

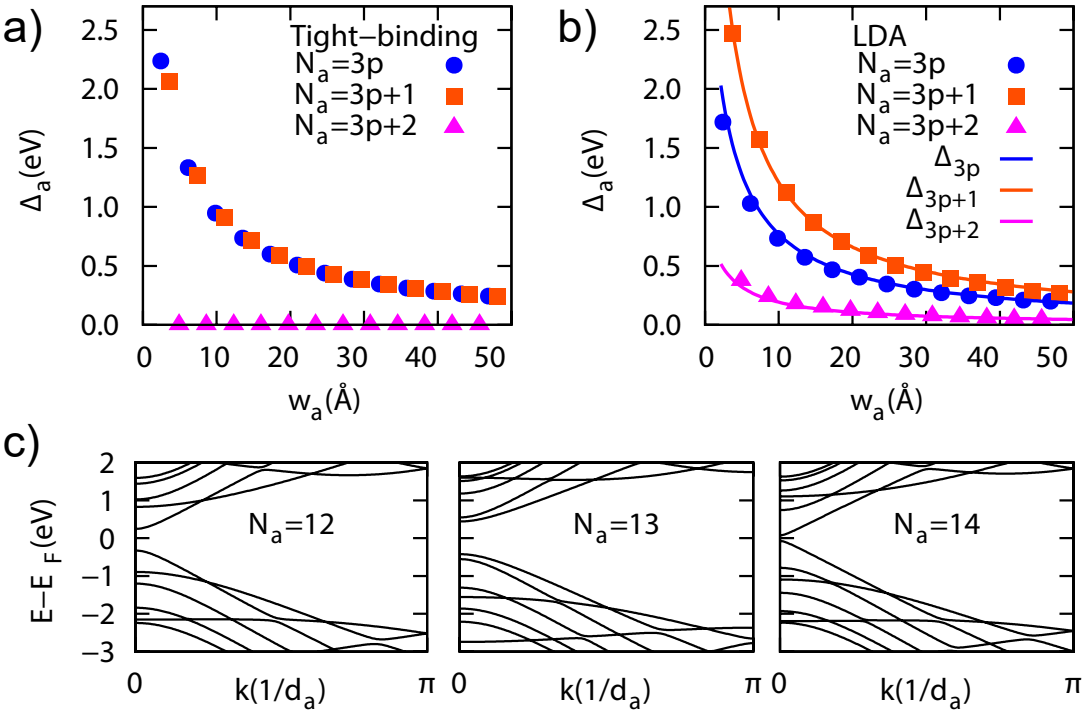

Fig. 2.13: AGNR band gaps and band structure. (a) Band gaps Δ_a for different widths w_a and types of AGNRs. Results were obtained using a tight-binding approach with $t = 2.7\,\text{eV}$ as nearest neighbour hopping integral between π-electrons. (b) Band gaps Δ_a obtained via first-principles calculations, explained in detail in Ref. [111]. In contrast to the tight-binding model, the first-principles calculations predict semiconducting behaviour for $3p + 2$-AGNRs. c) Exemplary first-princinples band structure for the three different AGNR types, where k represents the normalised wavevector and E_F the Fermi energy. Figures adapted from Ref. [111].

show that $3p$- and $3p+1$-AGNRs show semiconducting behaviour with a band gap in the 0.1-2.5 eV regime (Fig. 2.13) [111, 112], which is the typical range for common semiconductors. As can be seen from Fig. 2.13a, the band gap for AGNRs scales with the inverse of the width. Intriguingly, tight-binding calculations suggest that $3p+2$-AGNRs are nearly metallic with an almost vanishing band gap. In contrast to that, first-principles calculations predict semiconducting properties for $3p+2$-AGNRs [111]. However, experiments proved a nearly metallic behaviour as predicted by the tight-binding model [113].

2.3.4 Edge state and band structure of ZGNRs

The particular feature that differentiates ZGNRs from other types is the existence of a perfectly spin-polarised [23]. Tight-binding calculations yield a degenerate flat band structure for $k = \pi$ around the Fermi energy E_F, which is absent for graphene. Via analysis of charge density distributions at that flat band, it was found that it corresponds to a state localised along the edges of the ZGNR [23, 114]. Towards the centre of the GNR, its localisation fades exponentially. However, prior to this thesis, experimental evidence on the edge state and its polarisation was, at best, scarce [115], making its existence mainly theoretical. In Ch. 6 we will show our approach to experimentally prove its existence and how to find its signatures.

More interestingly, the edges are spin-polarised in opposite direction. The spins at the two edges couple antiferromagnetically across the ribbon, and ferromagnetically along the edges, which yields interesting possibilities for spintronic applications such as perfect spin filters [116, 117]. The spin-polarisation of the edges has been investigated on a theoretical level: early models often included Hartree-Fock or *ab initio* calculations [118–121], based on mean-field theory, newer ones employed an effective fermionic theory, as shown and detailed in the literature [122, 123]. All methods agree in providing the same spin-polarisation.

Using first-principles calculations based on DFT, Lee *et al.* calculated the energies and densities of states of the different possible spin orientations: paramagnetic

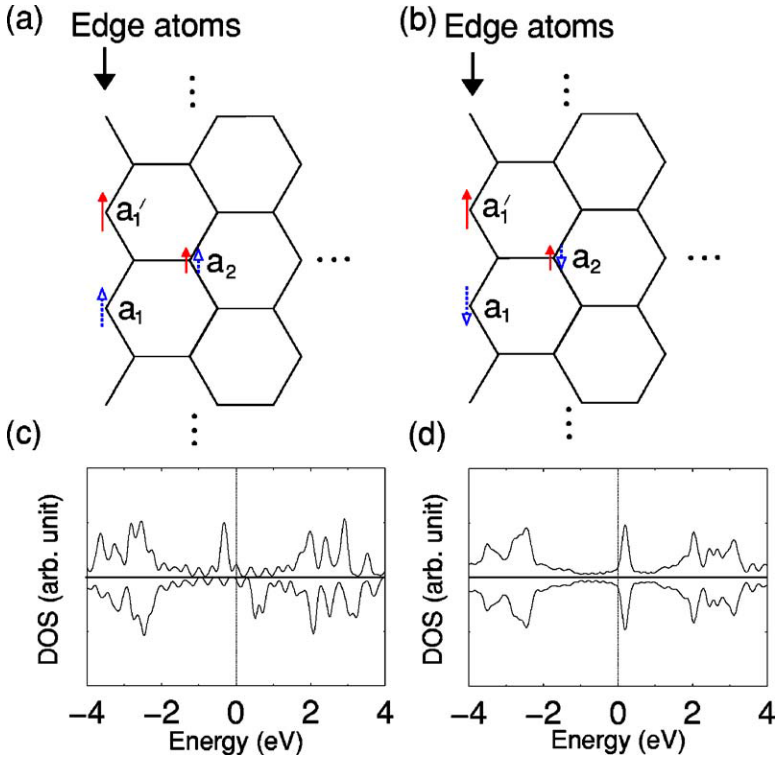

Fig. 2.14: Ferromagnetic and antiferromagnetic polarisation of the edge state. a) and b) show the case for ferromagnetic and antiferromagnetic orientation of the spins on the edges. A local magnetic moment is denoted by the red arrow, and its tail by the blue dotted arrow. The corresponding projected densities of states is shown in c) and d). Figure adapted from Ref. [121].

edges, ferromagnetic edges with either ferromagnetic or antiferromagnetic coupling across the ribbon, and antiferromagnetic edges [121]. They found that the configuration with ferromagnetic edges and antiferromagnetic coupling across the ribbon has the lowest energy. Furthermore, they give an intuitive picture on why it is favoured over a full antiferromagnetic state, which is illustrated in Fig. 2.14. First, Fig. 2.14a shows the ferromagnetic (FM) case with ferromagnetic edges at sites $a_1(a_1')$ (FM case). The polarisation at site a_2 is a result of the polarised π-orbitals on the edges. Second, Fig. 2.14b shows the case for antiferromagnetic (AFM) edges. The FM case leads to constructive contributions to the spin at a_2, while the AFM configuration is destructive at a_2. The corresponding densites of states, depicted in Fig. 2.14c and d, show that the FM configuration leads to an exchange splitting

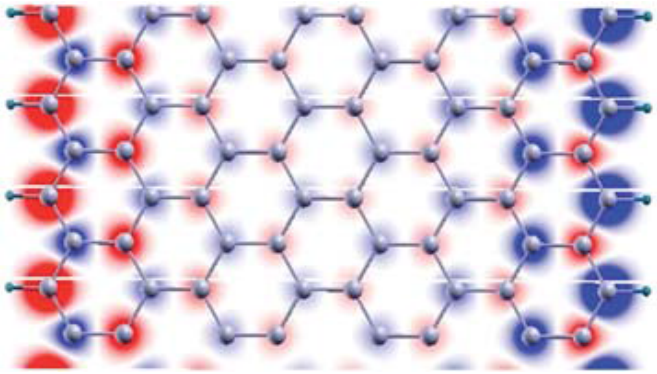

Fig. 2.15: Edge-state delocalisation of GNRs. The spin-polarised edge-state is delocalised along the edges of the backbone. The different colours represent different spins. Figure adapted from Ref. [112] after Ref. [124].

between the 'down' and 'up' spin-orientations of the π-orbitals at the Fermi level, which is absent in the AFM case due to the destructive interference. As a result, the total energy of the FM state is lower than the AFM state [121].

The formation of spin-polarised edge states is responsible for the semiconducting properties of ZGNRs [111]. The two different spin species occupy different sublattices, as illustrated in Fig. 2.15. Therefore, the magnetic ordering in ZGNRs creates staggered sublattice potentials that, in honeycomb lattices, lead to an energy gap for electrons [125], and, consequently, explain why ZGNRs are semiconducting. In the end, it is the difference of the respective exchange energy potentials that explain the band gap [111].

Band gaps for different widths of ZGNRs are shown in Fig. 2.16a. Except for very narrow ZGNRs, the band gap scales with the inverse width, w_z, of the ribbon. This is due to the fact that with increasing width, the staggered sublattice potential loses in strength towards the middle axis. This is a direct result of the exponential decay of localisation towards the ribbon center. Similarly, one can define ZGNRs via their number of carbon atoms on a line across the ribbon, as depicted in the example of 6-ZGNR in Fig. 2.12d. Compared to AGNRs, the band gap is slightly smaller and falls into the 0.1-0.7 eV regime, as shown in Fig. 2.16a.

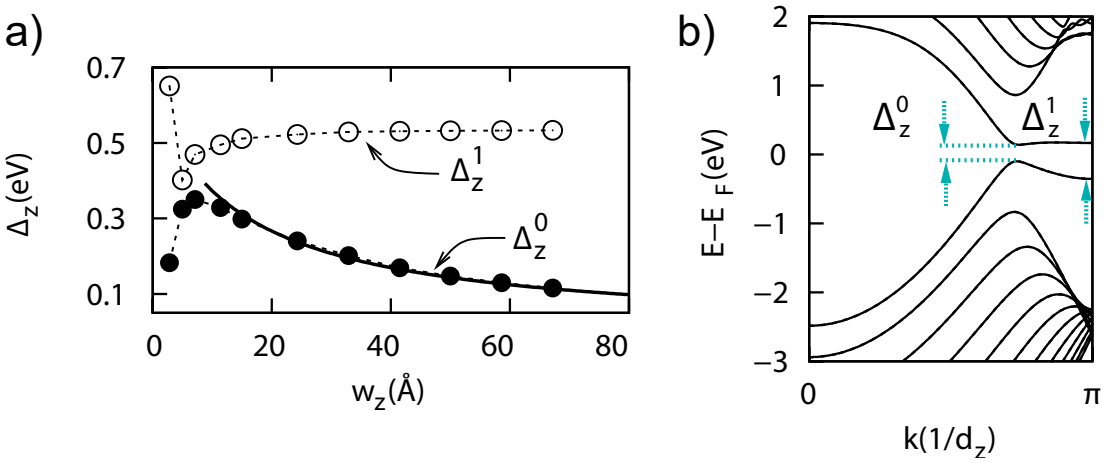

Fig. 2.16: ZGNR band gaps and band structure. (a) Band gaps for different widths of ZGNRs. The two curves correspond to different wavevectors, Δ_z^0 for the direct band gap, and Δ_z^1 the energs splitting for $k = \pi$. (b) ZGNR band structure where k denotes the normalised wavevector and E_F the Fermi energy. The k positions for Δ_z^0 and Δ_z^1 are indicated. Figures adapted from Ref. [111].

2.3.5 Cove-type GNRs and further structures

Advances in bottom-up fabrication techniques have enabled graphene nanoribbon structures beyond armchair and zigzag-type, such as cove-type [106] (CGNR), chiral [126] or chevron-type GNRs [127], depicted in Fig. 2.17. Even more structures are possible, thoroughly discussed in Ref. [128], and they can be functionalised with different groups [106]. The edges of these novel GNRs follow AGNRs or ZGNRs, or a mixture of both. In Ch. 6, we will present a detailed characterisation of a functionalised cove-type GNR. Its edge has a zigzag-type character, and the classification of CGNRs is the same as for ZGNRs (Fig. 6.1d). Theoretical calculations predict an edge state, same as for ZGNRs [129]. Although the capes on the edges can vary in position and distance, the different structures seem to maintain band gaps and edge state properties [129]. Therefore, the edge state theory explained in the previous section can be applied to CGNRs as well. Furthermore, band gaps of CGNRs seem to be comparable to other AGNRs. The band gap of a 4-CGNR was found to be slightly smaller than that of an AGNR of similar width [130].

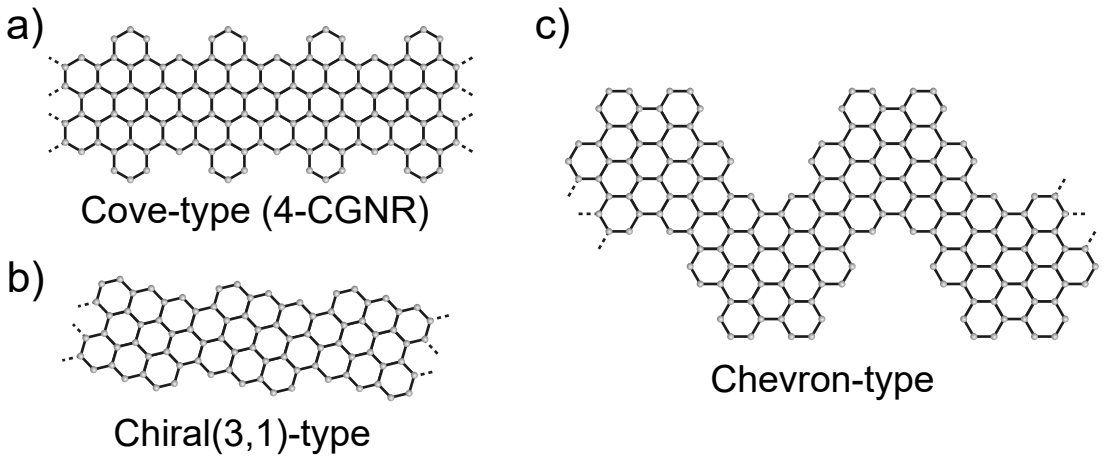

Fig. 2.17: Small selection of further GNR structures. (a) Cove-typ GNR [106], (b) chiral(3,1)-type GNR [126], (c) chevron-type GNR [127]. Further potential structures can be found in Ref. [128].

2.3.6 Spin-orbit coupling and Rashba-effect in graphene and graphene nanoribbons

The quantum mechanical state of electrons is defined by the spin and orbital momentum, amongst others. Often, spin and orbital momentum are not separate quantities, but are coupled to each other. The resulting spin-orbit coupling is usually more important in heavier atoms, and, for example, responsible for the enormous magnetic moments found in lanthanide SMMs [33]. As carbon atoms represent relatively light atoms, spin-orbit coupling is usually found to be small for graphene-based systems. In fact, it was found that curvature induces strong spin-orbit coupling in graphene nanotubes or fullerenes [131].

The role of intrinsic spin-orbit coupling in graphene, which arises from its hexagonal lattice, is described via the following Hamiltonian [132–134]:

$$\mathcal{H}_{SO,\mathrm{int}} = \Delta_{SO}\alpha_i\sigma_i S_i \tag{2.12}$$

with Δ_{SO} the intrinsic spin-orbit interaction, $\alpha_i = \pm 1$, which describes the states at the K or K', also known as valley degree of freedom, σ_i represents the Pauli matrices related to the pseudospin [135], which is a consequence of the two sub-

lattices A and B of graphene, and S_i the spin operators. The pseuospin represents an additional degree of freedom, described in the Dirac theory of graphene. In the case of intrinsic spin-orbit coupling, only $i = z$ is relevant for graphene [132–134].

Furthermore, electron spins in graphene can be affected by the Rashba-effect [136], which has consequences for the band gaps and the magnetic edges in graphene nanoribbons [137]. The Rashba-term appears in cases where the in-plane mirror symmetry is broken [134, 137], e.g. via the application of a perpendicular electric field or when graphene is interacting with a substrate. It is defined as [136]:

$$\Delta_\alpha(\boldsymbol{S} \times \boldsymbol{p}) \cdot \boldsymbol{e_z}\,, \tag{2.13}$$

where Δ_α corresponds to the coupling constant, $\boldsymbol{p}$ to the electron momentum and $\hat{\boldsymbol{e}}_{\boldsymbol{z}}$ to the unit vector along the z-direction. For graphene, it has been shown that Eq. 2.13 can be written as [132, 137]:

$$\mathcal{H}_R = \Delta_R(\pm\sigma_x S_x - \sigma_y S_y)\,, \tag{2.14}$$

where Δ_R denotes the Rashba coupling constant. We can then write down the total spin-orbit Hamiltonian as:

$$\mathcal{H}_{SO} = \mathcal{H}_{SO,\text{int}} + \mathcal{H}_R\,. \tag{2.15}$$

Interestingly, spin-orbit coupling has an important effect for the band structure of graphene. If there is no Rashba-effect, i.e. $\Delta_R = 0$, intrinsic spin-orbit coupling leads to an energy gap $2\Delta_{SO}$, and the dispersion relation becomes [132]:

$$E(\boldsymbol{k}) = \pm\sqrt{(\hbar v_F \boldsymbol{k})^2 + \Delta_{SO}^2} \tag{2.16}$$

with v_F the Fermi velocity and $\boldsymbol{k}$ the wavevector. On the contrary, if the Rashba-effect is larger than the intrinsic spin-orbit coupling, the gap vanishes and graphene becomes a gapless semiconductor. In the intermediate case, where $\Delta_R < \Delta_{SO}$, the band gap shrinks to $2(\Delta_{SO} - \Delta_R)$.

Graphene Nanoribbons

Spin-orbit coupling can have interesting effects on graphene nanoribbons. Kane *et al.* used a second neighbour tight-binding model to calculate the band structure of a zigzag-type graphene nanoribbon including intrinsic spin-orbit coupling [132]. It is reported that in the case of vanishing spin-orbit coupling, the edge state band becomes flat for $k/d_z \to \pi$ [114], as can also be seen in Fig. 2.16b. As a result, the zigzag edge density of states at the Fermi energy is increased. Otherwise, the edge state band can traverse the gap and connect K and K' points [132].

Without Rashba spin-orbit coupling, each wavevector k_x (see Fig. 2.12) has two degenerate spinors [137], corresponding to $k_y = \pm k$. The resulting wavefunction is a superposition of these spinors. As an example, the resulting conduction band structure is shown in Fig. 2.19a for a 4-ZGNR. When Rashba spin-orbit coupling is introduced, each k_x now has four degenerate states [137], defined as $k_y = \pm k_1$ and $k_y = \pm k_2$, and the wavefunction consists of a superposition of four spinors. Fig 2.19b shows this degeneracy in the case of graphene. As a results, the band structure changes as illustrated in Fig. 2.19c. Using these results, one can calculate the spin polarisation of a graphene nanoribbon under the influence of Rashba spin-orbit coupling (Fig. 2.19d). It shows that Rashba spin-orbit coupling leads to a spin-polarisation of the edges. Furthermore, the spatial distribution of the spin-polarisation $\langle S_z \rangle$ within the ribbon depends on the state, which is shown for a few different wavevectors k_x in Fig. 2.19d. Depending on the wavevector, the edges can a stronger stronger or weaker spin-polarisation. This is a direct consequence of Rashba spin-orbit interaction. However, when Rashba spin-orbit coupling is not present, the spatial distribution of the spin-polarisation within the ribbon is the same for all states [137, 138], which is the case we have presented in the previous section.

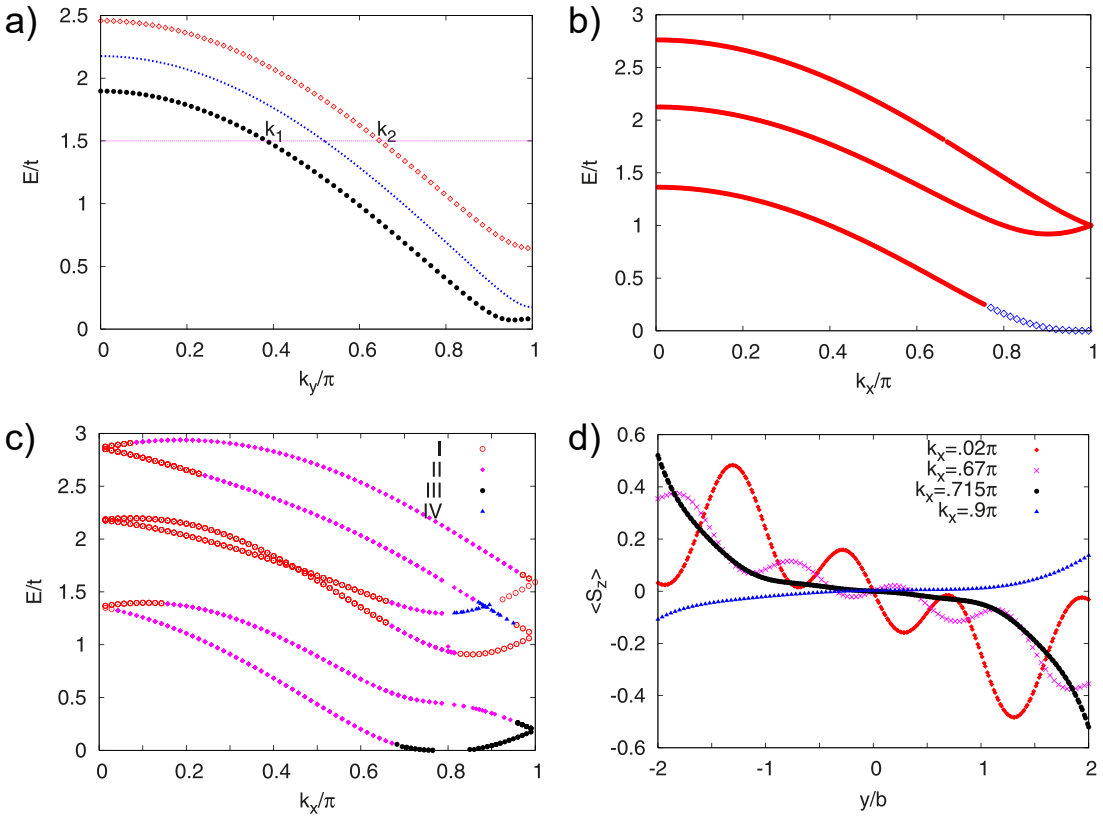

Fig. 2.18: Rashba spin-orbit effects on the band structure of a ZGNR. (a) Graphene band structure for $k_x = 0.6\pi$ without (blue) and with a Rashba spin-orbit coupling of $\lambda_R = 0.2t$ (black and red), where t corresponds to the hopping integral of the tight-binding Hamiltonian. The energy E is given in terms of t. The graph shows the fourfold degeneracy at $k_y = \pm k_1, \pm k_2$. (b) Band structure of the conduction bands of a 4-ZGNR without Rashba spin-orbit coupling. The edge band is marked with blue diamonds, where k is imaginary. (c) Band structure of a 4-ZGNR with Rashba spin-orbit coupling ($\lambda_R = 0.4t$). The different regions denote different values for k_1 and k_2: (I) both real, (II) and (III) one real, (IV) both imaginary. (d) Spin-polarisation $\langle S_z \rangle$ as a function of the Cartesian coordinate y across the ribbon, where $4b$ is the full width of the 4-ZGNR. Figures adapted from Refs. [137].

2.3.7 Fabrication

The fabrication of GNRs can be mainly divided into top-down and bottom-up approaches [139]. Top-down approaches imply the use of graphene flakes or sheets, and the removal of material until a GNR is formed. Lithography and etching techniques fall into this category [140, 141]. GNRs can also be created via chemical methods, such as by unzipping of multi-walled carbon-nanotubes [142] as depicted in Fig. 2.18a. Alternatively, GNRs can be fabricated via catalytic particles [143]. Metallic iron and nickel particles are able to cut C-C bonds in a hydrogen atmosphere while generating methane and other carbon-based byproducts. The produced GNRs are relatively wide, with a width at the order of 10 nm, or slightly below [143]. However, this fabrication technique is difficult to control and yields GNRs with indeterminable shapes.

For the study of physical properties, it is essential to have a well-defined structure. In fact, bottom-up approaches enable a high-precision structure. By using well-defined molecular precursors, GNRs of controlled shapes are obtained [106, 128, 144]. Ref. [128] gives an excellent overview on the different fabrication methods, which we outline in the following.

In general, the synthetic approaches can be split into three categories. The first one is based on solution-mediated techniques, such as A_2B_2-type Suzuki, AA-type Yamamoto and AB-type Diels-Alder polymerisation, with different limitations. Drawbacks of the A_2B_2 Suzuki polymerisation are the requirements of two different monomers, which may potentially lead to stoichiometric problems, and limited molecular weights of the polyphenylene precursors, which constraints GNR lengths to less than 30 nm. The AA-type Yamamoto polymerisation is more efficient in this respect. It requires only one dihalogenated monomer, so that stoichiometric problems are absent. Furthermore, it allows for wider and longer GNRs. Via this technique, lengths of more than 100 nm for Chevron-type GNRs are reported [127]. In most cases, however, lengths are shorter than 50 nm. The most advantageous method is the AB-type Diels-Alder polymerisation. Without the need of expensive

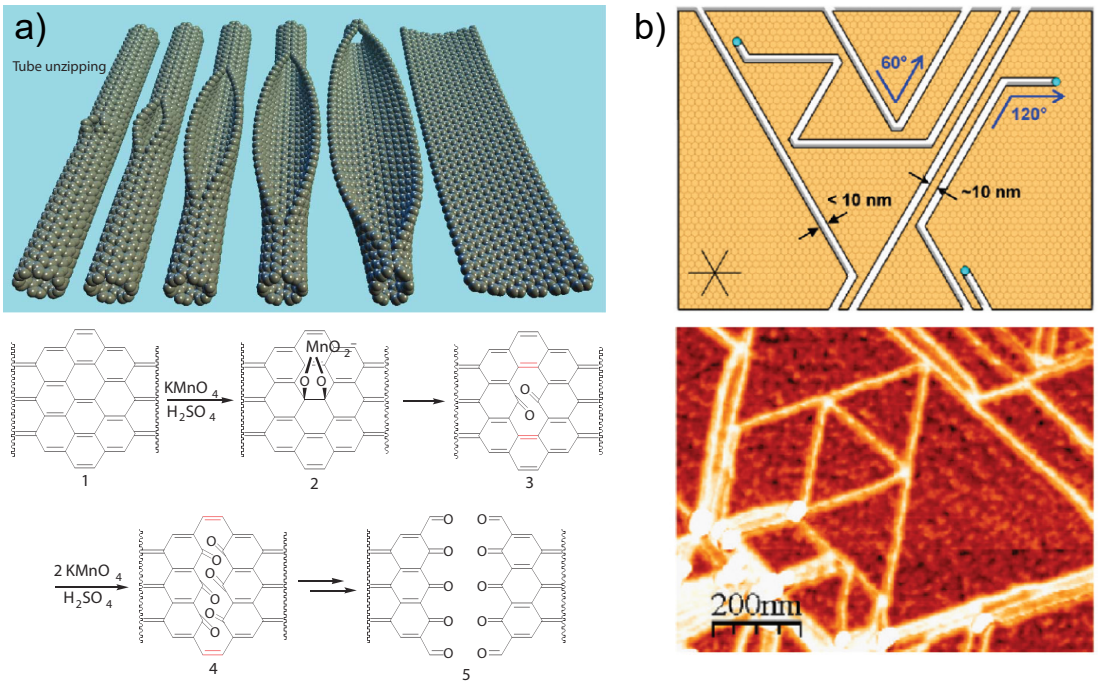

Fig. 2.19: Top-down fabrication of GNRs. (a) Unzipping of carbon nanotubes via chemical reactions. Figures adapted from Ref. [142]. (b) Fabrication via catalytic particles. Figures adapted from Refs. [139, 143].

metal catalysts, lengths of more than 600 nm are possible [145]. This is possible via an appropriate choice of the precursor, where steric repulsion avoids the formation of undesired C-C bonds. It is, nowadays, the method of choice therefore.

When one is interested in the physical characterisation of single GNRs, the mere solution-mediated methods may not be the right way, as the produced GNRs may suffer from aggregation effects [128]. Furthermore, placing them on surfaces may lead to undesired results due to surface contamination. Surface-assisted methods under ultra-high vacuum (UHV) conditions, where GNRs are grown on a metal surface, are able to solve this issue. In the first step, the polyphenylene precursors are fabricated from dihalogenated monomers via surface-assisted coupling of aryl halides. Via annealing at high temperatures, surface-catalysed cyclodehydrogenation of the polyphenylene produces the GNRs on the surface (Fig. 2.20a). As shown by STM measurements, lengths of up to 100 nm can be obtained via this technique [146]. Furthermore, N-doped monomers can be used

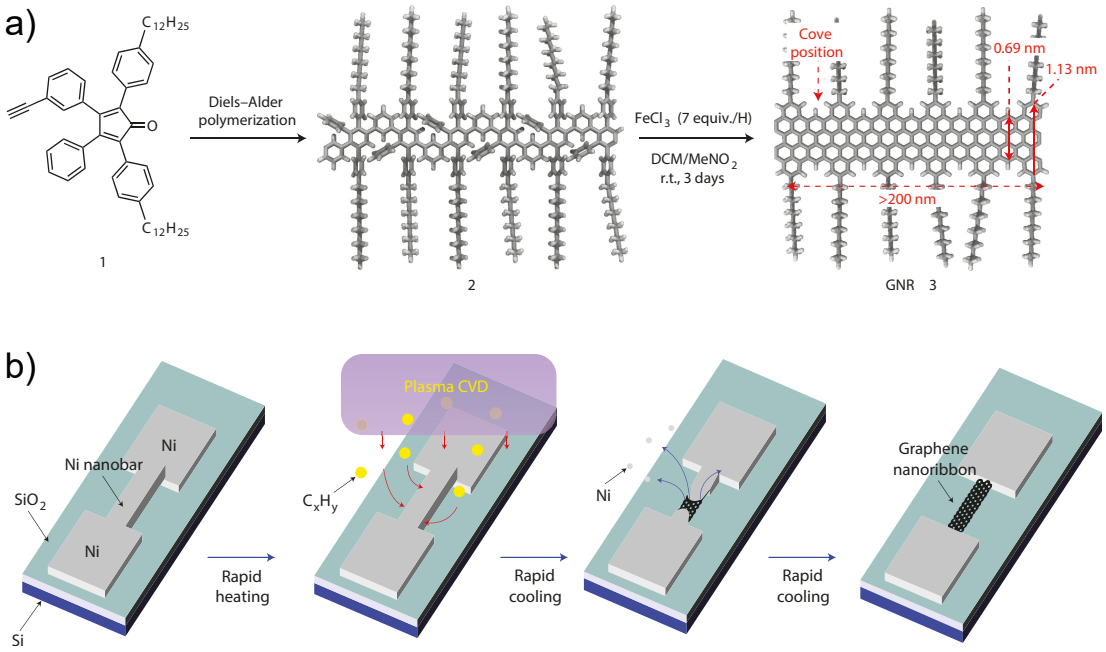

Fig. 2.20: Bottom-up fabrication of GNRs. (a) GNR bottom-up synthesis using a molecular precursor (1), which reacts first to polyphenylene (2) and later graphitised via cyclodehydrogenation to the GNR. Figure adapted from Ref. [106]. (b) Conversion of a Ni nanobar using chemical vapour deposition. First, a Ni structure is evaporated on a substrate. CVD is performed after heating up to 700 °C. During the cooling process, the GNR is formed rapidly with a typical width of about 23 nm. Figure adapted from Ref. [149].

to create N-doped GNRs [147]. Such GNRs show n-type conducting properties, and Bronner *et al.* showed that their band gap is not altered much by doping [147]. Such surface-GNRs can be extracted via the argon-bubbling technique. However, the required setups to perform the synthesis under UHV conditions are complex and expensive, and, furthermore, the produced quantities are rather small due to the slow process [128]. One workaround is the fabrication of GNRs using chemical vapour deposition (CVD) conditions, demonstrated in Ref. [148]. Other than that, the fabrication is similar to the one in UHV environment.

As the last bottom-up method we mention the synthesis of GNRs encapsulated in carbon nanotubes (CNTs) [150, 151]. Here, the synthesis happens via thermal or electron-beam polymerisation of appropriate aromatic precursors within single-

walled CNTs. While the GNRs produced via this method show rather smooth edges and widths, their quality is worse compared to the other bottom-up approaches discussed above. Furthermore, the removal of the CNTs is troublesome [128].

Moreover, CVD represents another bottom-up technique [149]. Here, GNRs are grown between two electrodes as depicted in Fig. 2.20b. Amongst these techniques, the direct molecular synthesis is possibly more versatile for the investigation of GNR properties, such as edge states, especially when narrow GNRs in the sub-10-nm regime are required.

There are further techniques that combine top-down with bottom-up approaches, such as the epitaxial growth on SiC sidewalls [152]. These, and others, are thoroughly discussed in Ref. [139].

3 Experimental Methods

In this chapter we will discuss all experimental techniques that are presently being employed. We begin with a general introduction into electron spin resonance techniques (ESR) and explain all pulse sequences that have been used in this work. Since ESR allows for a quantitative analysis of the spin Hamiltonian parameters, we utilise it to gain a comprehensive picture on the couplings in different materials such as graphene nanoribbons or molecular nanomagnets. The second section deals with SQUID magnetometry and the development of a setup which allows measurements under controlled irradiation of light. In some samples, light excites a molecular system into a long-lived state with different magnetic properties, which can be quantitatively investigated using the setups developed in this work. The last section presents the torque-detected electron spin resonance technique (TDESR), which represents an ESR method that merges the fields of torque magnetometry and ESR. The torque magnetometer is far more sensitive compared to a SQUID magnetometer, and allows the detection of sensitive light-induced effects.

3.1 Electron spin resonance spectroscopy

3.1.1 Basic principles

We consider a spin-1/2-system without nuclear spin I. The Zeeman effect (Eq. (2.3)), splits $m_s = +1/2$ and $m_s = -1/2$ states as shown in Fig. 3.1 in an external field. Since $m_s = +1/2$ has a lower energy, it has a higher population than the excited state, following the Boltzmann distribution. According to the magnetic dipole

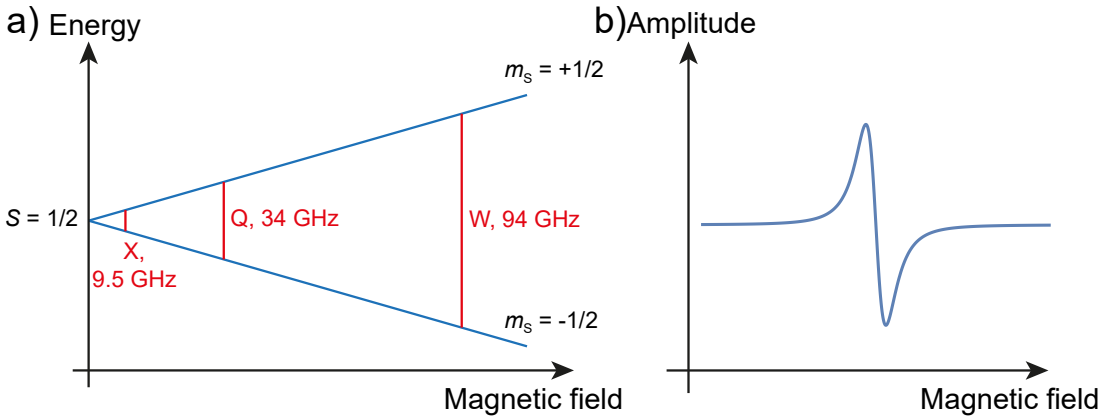

Fig. 3.1: Energy splitting of a spin-1/2-system in a magnetic field. (a) The energy splitting scales linearly with the magnetic field when it is parallel to the quantisation axis. The red lines show the transition frequencies. W-band experiments demand magnetic fields approximately ten times stronger compared to X-band experiments. The stronger splitting increases the resolution via a larger population difference, and further separation of g-orientations in disordered powder samples. (b) Typical derivative absorption signal of an ESR experiment.

selection rules $\Delta S = 0$ and $\Delta m_s = 0, \pm 1$ [153], the system can be excited by an absorption of a photon. This energy lies in the microwave regime for typical magnetic fields.

Frequencies widely used in ESR spectroscopy lie in the X-band (9.5 GHz), Q-band (34 GHz) and W-band (94 GHz) regimes. To fulfill the resonance condition, the field is swept. For a free electron with $g = 2.0023$, resonance at those frequencies appears at 0.3390 T, 1.213 T and 3.354 T, respectively. If the system is continuously irradiated with microwaves at, or close to, resonance, the population between these two states oscillates. This phenomenon is known as Rabi oscillation [154].

3.1.2 CW spectroscopy

In a continuous-wave (CW) ESR experiment, the microwave absorption at a fixed frequency is continuously recorded while sweeping the magnetic field. It might

not perhaps be intuitive to show an absorption spectrum as its first derivative, but it has several advantages. The common CW measurement technique contains a phase-sensitive detection which improves the overall sensitivity and makes an ESR signal more discernible from noise or interference sources in the environment [155]. It reduces both noise originating from the microwave diode and the baseline drift originating from the DC electronics.

The idea of CW spectroscopy is to modulate the applied magnetic field by an amplitude ΔB and a frequency in the 10-100 kHz regime. Ideally, the modulation amplitude is smaller than the linewidth of the signal. If it is set too large, the lines will get distorted and features will be lost. The field modulation translates into a sinusoidal modulation of the ESR signal, and its amplitude is proportional to the slope of the actual ESR absorption line. A lock-in amplifier, which in the ESR community is better known as a signal channel or phase sensitive detector, generates a DC signal that is proportional to the modulated ESR amplitude. Therefore, typical ESR spectra are given as their first derivative. The lock-in amplifier is synchronised with the frequency of the field modulation. It filters out any other frequencies or phases in the spectrum that do not match. This allows for the suppression of noise and interference effects, and therefore leads to an enhanced signal-to-noise ratio (SNR). By increasing the time constant, i.e. by slowing down the response time of the instrument, one can improve the SNR, but this also results in a slow measurement. Moreover, we take multiple scans to increase the SNR.

In the end, one has to find the optimum of all the parameters that affect the spectrum. The modulation amplitude must not be too large in order to not suppress narrow ESR features, but, at the same time, large enough to provide a good SNR. A large time constant distorts the spectrum, and might even cause the resonance frequency to spuriously change. It is advised to use a time constant that is short, about one order of magnitude less, compared to how long it takes to sweep past spectral features. Furthermore, field-dependent signal saturation plays an

important role and should be avoided. Spectra should be acquired at a microwave intensity, where a linear response is obtained. Power-swept measurements can be used to find the optimum microwave intensity. Moreover, the SNR can be enhanced strongly at lower temperatures. However, the spin dynamics decelerate at the same time as the spin-lattice relaxation time T_1 increases (see Sec. 3.1.6), so that fields need to be swept more slowly in order to avoid distortion. Lastly, the modulation frequency needs to be adjusted so that narrow features will not get lost due to Heisenberg's uncertainty principle.

In fact, finding a phase-stable optimum for all these parameters can be a time-consuming task, and especially challenging at higher frequencies. If a sample shows a measurable free-induction-decay (FID), i.e. it shows an echo after using microwave pulses, it is more convenient to obtain an FID-detected field-swept ESR spectrum, which will be explained in Sec. 3.1.4.

3.1.3 Theoretical description of pulsed ESR

Access to the spin dynamics of magnetic clusters is achieved via time-domain experiments such as pulsed ESR. Furthermore, performing quantum operations is quite similar to pulse ESR techniques, as both work with pulses of variable lengths and phases that match the energy difference between the states involved [22]. In this section, we will discuss a basic quantitative description of pulsed ESR, and how $\pi/2$ and π-pulses affect the spin dynamics of a coupled spin system. We will adhere to the density operator formalism thorougly discussed in Ref. [156]. Since a full description goes well beyond the scope of this thesis, for a more in-depth analysis we shall refer to Ref. [156]. The following example has been adapted from Ref. [156] and extended. It should intuitively illustrate the effect of pulses on spin dynamics. The description is valid when the quantisation-axis is, per definition, parallel to the z-axis. In this frame, the polarisation of microwaves, i.e. the direction of the microwave magnetic field component $\boldsymbol{B_1}$, is either $\pm x$ or $\pm y$.

For the derivation of the spin dynamics after the application of a microwave

pulse, we define a time-dependent density operator $\sigma(t)$, with t the time. Here, all relevant coupled spins, such as electron spins coupled to nuclear spins, are described via a density matrix $\sigma(t)$ that includes the time-independent probabilities p_k to find the system in a distinct state k. For example, in the case of a spin-1/2 system, two spin states $m_s = \pm 1/2$ are allowed. Then, the density operator is described via a 2×2 matrix, where the diagonal elements correspond to the probabilities to find the ensemble in one of these states, while the off-diagonal elements describe coherences. Mathematically, $\sigma(t)$ is defined as

$$\sigma(t) = \sum_k p_k \left|\psi_k(t)\right\rangle \left\langle\psi_k(t)\right| , \tag{3.1}$$

where the sum goes over all spin states k. The wavefunctions $\psi_k(t)$ are the only time-dependent variables here. By assuming pure states, no coherences are present and σ is diagonal.

From textbooks on quantum mechanics we furthermore know that the time evolution of a spin species is described via the Schrödinger equation:

$$\frac{\mathrm{d}}{\mathrm{d}t}\left|\psi(t)\right\rangle = -\mathrm{i}\mathcal{H}(t)\left|\psi(t)\right\rangle , \tag{3.2}$$

where $\mathcal{H}(t)$ describes, in general, a time-dependent Hamiltonian of a system. In order to solve the Schrödinger equation, we first take the first time-derivative of Eq. 3.1, and then insert Eq. 3.2 in there. We then obtain:

$$\begin{aligned}\frac{\mathrm{d}}{\mathrm{d}t}\sigma(t) &= -\mathrm{i}\sum_k p_k \left(\mathcal{H}(t)\left|\psi_k\right\rangle\left\langle\psi_k\right| - \left|\psi_k\right\rangle\left\langle\psi_k\right|\mathcal{H}(t)\right) \\ &= -\mathrm{i}\left(\mathcal{H}(t)\sigma(t) - \sigma(t)\mathcal{H}(t)\right) \\ &= -\mathrm{i}\left[\mathcal{H}(t), \sigma(t)\right] ,\end{aligned} \tag{3.3}$$

also known as the Liouville-von-Neumann equation. Here, we use the standard commutator relationship $[A, B] = AB - BA$, where A and B are quantum operators. In order to solve this differential equation, we make the assumption that $\mathcal{H}$ is

time-independent, which is generally valid for spin Hamiltonians. Via integration of the differential equation, one finds the solution of Eq. 3.3 as:

$$\sigma(t) = \exp(-\mathrm{i}\mathcal{H}t)\sigma(0)\exp(\mathrm{i}\mathcal{H}t) \tag{3.4}$$

$$= U(t)\sigma(0)U(t)^{\dagger}\,, \tag{3.5}$$

where the operator $U(t) = \exp(-\mathrm{i}\mathcal{H}t)$ is known as the propagator. It can be shown by inserting that Eq. 3.4 solves the differential equation in Eq. 3.3. in The propagation of the density operator is only valid for unitary operators that fulfil $U^{-1} = U^{\dagger}$. In fact, rotary operators are unitary and fulfil this equation. Spin rotations can therefore be described using this formalism.

In the quantum mechanical picture, the application of a microwave pulse leads to a perturbation of the spin Hamiltonian. A pulsed ESR experiment that consists of a series of microwave pulses can then be described via a series of time intervals, where each one is described by a different time-independent Hamiltonian [156]. Therefore, each time interval can be described via the propagator formalism in Eq. 3.5. In a pulse sequence, these propagators can be applied subsequently via the product operator formalism [156].

We now move on to the application of such propagators, and see how they affect quantum mechanical operators. The time-evolution of one product operator A under the influence of the other B, for example, can be calculated using this formalism. The final operator C is then defined as

$$C = \exp(-\mathrm{i}\phi B)A\exp(\mathrm{i}\phi B)\,, \tag{3.6}$$

or in short

$$A \xrightarrow{\phi B} C\,, \tag{3.7}$$

where ϕ corresponds to a phase, and B is a normalised operator. By using the

Baker-Hausdorff formula, this relationship can be simplified as

$$A \xrightarrow{\phi B} A\cos\phi - \mathrm{i}\,[B, A]\sin\phi\,. \tag{3.8}$$

Eventually, we can move on to describe mathematically how microwave pulses affect the time propagation of a spin manifold. Manipulations on an electron spin are described by the spin operators S_x, S_y and S_z. For a spin-1/2-system, these operators are known as Pauli spin matrices, in the $|S, m_s\rangle$ basis defined as:

$$\frac{S_x}{\hbar} = \frac{1}{2}\begin{pmatrix} 0 & 1 \\ 1 & 0 \end{pmatrix}, \quad \frac{S_y}{\hbar} = \frac{1}{2}\begin{pmatrix} 0 & -\mathrm{i} \\ \mathrm{i} & 0 \end{pmatrix}, \quad \frac{S_z}{\hbar} = \frac{1}{2}\begin{pmatrix} 1 & 0 \\ 0 & -1 \end{pmatrix}. \tag{3.9}$$

These act on spin systems in the $|S, m_s\rangle$ basis as follows:

$$S_\pm\,|S, m_s\rangle = \hbar\sqrt{S(S+1) - m_s(m_s \pm 1)}\,|S, m_s\rangle\ , \tag{3.10}$$

$$S_z\,|S, m_s\rangle = \hbar m_s\,|S, m_s\rangle\ , \tag{3.11}$$

where $S_\pm = S_x \pm \mathrm{i}S_y$ and $[S_i, S_j] = \mathrm{i}\hbar\varepsilon_{ijk}S_k$ with ε_{ijk} as the Levi-Civita symbol. Similar relations are valid for the nuclear spin I. Intuitively, these operators act like rotation operators in the rotating frame of a spin system. We now consider a coupled spin-1/2 system with $S = 1/2$ and $I = 1/2$. At the beginning of a pulsed experiment, spins are polarised in equilibrium along the z-axis by applying an external magnetic field. By dropping constants and the identity operator, which is justified as they are invariant in an ESR experiment, one finds $\sigma_{\mathrm{eq}} = -S_z$ in equilibrium [156]. Using the discussed formalism, we can mathematically describe the application of a $\pi/2$-pulse about the x-axis as:

$$\sigma_{\mathrm{eq}} = -S_z \xrightarrow{\pi/2S_x} S_y\,, \tag{3.12}$$

since $[S_x, S_z] = -\mathrm{i}S_y$. This means that the spins polarised along the negative z-axis are rotated by 90° about the x-axis in the S_x, S_y, S_z coordinate system.

Hence, this operation creates a coherent superposition on nuclear transitions with $\Delta m_I = 0$.

Now that the spins are polarised in the y-direction, they begin to precess in the xy-plane while being subjected to the magnetic fields of the nuclei. In the case of isotropic hyperfine coupling, the propagation Hamiltonian is defined as

$$\mathcal{H}_0 = \Omega_S S_z + a_{\text{iso}} S_z I_z \,, \tag{3.13}$$

where Ω_S corresponds to the offset precession frequency $\omega_S - \omega_{\text{mw}}$, with ω_S the Larmor precession frequency of the spin and ω_{mw} the frequency of the microwaves, and a_{iso} stands for the isotropic hyperfine coupling constant. Successive application of the Hamiltonian yields

$$\begin{aligned} S_y \quad & \xrightarrow{\Omega_S S_z} \cos(\Omega_S t) S_y - \sin(\Omega_S t) S_x & (3.14) \\ & \xrightarrow{a_{\text{iso}} S_z I_z} \cos(\Omega_S t) \cos\left(\frac{a_{\text{iso}}}{2} t\right) S_y - \sin(\Omega_S t) \sin\left(\frac{a_{\text{iso}}}{2} t\right) 2 S_y I_z \\ & - \sin(\Omega_S t) \cos\left(\frac{a_{\text{iso}}}{2} t\right) S_x - \cos(\Omega_S t) \sin\left(\frac{a_{\text{iso}}}{2} t\right) 2 S_x I_z \,. & (3.15) \end{aligned}$$

As can be seen from the result, the application of a $\pi/2$-pulse in the first instance creates in-phase coherences described by the terms evolving with S_x and S_y. In addition to that, a part is transferred into anti-phase components, described by $S_x I_z$ and $S_y I_z$, which represent rather abstract quantities that cannot be detected [156].

In a time-resolved ESR esperiment, information on spin dynamics is contained in spin-echos. A spin-echo is generated by refocusing a set of spins after a free precession time. For example, the simplest way to create such an echo is via the Hahn-echo sequence, explained later in Sec. 3.1.5. The measured quantities are

the expectation values given by [156]

$$\begin{aligned}\langle S_x \rangle (t) &= -\sin(\Omega_S t) \cos\left(\frac{a_{\text{iso}} t}{2}\right) \\ &= -\frac{1}{2}\sin\left(\left(\Omega_S + \frac{a_{\text{iso}}}{2}\right) t\right) - \frac{1}{2}\sin\left(\left(\Omega_S - \frac{a_{\text{iso}}}{2}\right)\right) , \end{aligned} \tag{3.16}$$

$$\begin{aligned}\langle S_y \rangle (t) &= \cos(\Omega_S t) \cos\left(\frac{a_{\text{iso}} t}{2}\right) \\ &= \frac{1}{2}\cos\left(\left(\Omega_S + \frac{a_{\text{iso}}}{2}\right) t\right) + \frac{1}{2}\cos\left(\left(\Omega_S - \frac{a_{\text{iso}}}{2}\right)\right) . \end{aligned} \tag{3.17}$$

This means that when the coherence is preserved, the electron spins evolve under the influence of hyperfine parameters with a fast and a slow component. As we shall see later, in experiments involving a $\pi/2$-pulse couplings to nuclei can be observed and determined, such as in the Hahn-echo sequence.

Another important pulse of time-resolved ESR experiments is the π-pulse. The effect of a π-pulse can be immediately seen from Eq. 3.8: it corresponds to the negation operation.

The case presented here is valid for isotropic hyperfine coupling. In most cases, however, the hyperfine coupling is anisotropic and the equations become lengthy, especially in combination with nuclear spins larger than 1/2, which is the case for nitrogen. We will therefore neglect a purely mathematical description of the pulse sequences used throughout this work, and instead quantitatively discuss the relevant information contained in the data.

For non-selective pulses, i.e. pulses with a large bandwidth, which excite all

allowed transitions with $\Delta m_s = 1$, we can summarise their effect as follows [156]:

$$S_x \xrightarrow{\phi S_x} S_x \tag{3.18}$$

$$S_y \xrightarrow{\phi S_x} \cos(\phi)S_y + \sin(\phi)S_z \tag{3.19}$$

$$S_z \xrightarrow{\phi S_x} \cos(\phi)S_z - \sin(\phi)S_y \tag{3.20}$$

$$S_x \xrightarrow{\phi S_y} \cos(\phi)S_x - \sin(\phi)S_z \tag{3.21}$$

$$S_y \xrightarrow{\phi S_y} S_y \tag{3.22}$$

$$S_z \xrightarrow{\phi S_y} \cos(\phi)S_z + \sin(\phi)S_x \tag{3.23}$$

The same relationships are valid for nuclear spins. In the case of selective pulses, where a distinct part of the spectrum is excited, the transition amplitude has to be taken into account additionally in order to calculate the effective flip angle. The effective flip angle then scales with the relative amplitude of the chosen transition, which has an immediate effect on the formulae, presented in Ref. [156]. The electron coherence transition is now probed most effectively when the effective flip angle is $\pi/2$. Interestingly, the application of a selective π-pulse creates, so-called, two-spin order proportional to $2S_zI_z$. To understand this, we consider a spin system in equilibrium in a magnetic field. Then, states with parallel and antiparallel orientation of nuclei and electron spins are populated. These will later be defined as state 1 and 2 in Fig. 3.7. After the π-pulse, an antiparallal state 1 goes into a state 3 (Fig. 3.7), resulting in population of states where electron and nuclear spins are oriented parallel, thus creating the two-spin order. This means that nuclear polarisation is being created with different orientation in the two m_s manifolds [156].

Keeping this theoretical formalism in mind, we will proceed with the description of pulse sequences used in this work. We will employ a more qualitative picture of the pulse models to intuitively demonstrate how the pulse sequences affect the spin dynamics of the systems. Extensive calculations can be found elsewhere [156].

3.1.4 FID-detected ESR

Free-induction-decay-detected (FID-detected) ESR, as illustrated in Fig. 3.2, allows the obtaining of a field-swept absorption spectrum without the need of a long calibration procedure. This technique is based on a single, long FID-optimised pulse, which brings the equilibrium magnetisation into a non-equilibrium state with transverse components. If the magnetic field is set along the z-axis, the spins precess around the z-axis as well. During the coherence time T_2, they generate an exponentially decaying ESR signal in the transverse detection direction, the so-called FID. A long pulse creates a long FID-signal, which persists after the receiver protection switch. Furthermore, the FID-signal is proportional to the oscillator strength. The resulting spectrum comes very close to the integral of the corresponding CW measurement [157]. In contrast to the complicated CW tuning procedure, it is enough to overcouple the resonator and to calibrate the FID-optimised pulse.

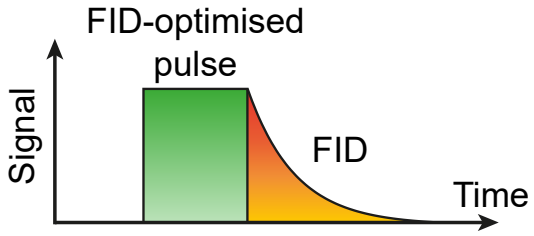

Fig. 3.2: FID-detection pulse scheme. A spin ensemble produces an FID after application of an FID-optimised pulse. The vertical axis corresponds to a general signal intensity, the horizontal axis to the time line.

3.1.5 Measurement of spin-spin dephasing T_m

The measurement of the phase-memory time T_m is done via a Hahn-echo sequence, depicted in Fig. 3.3. In the rotating wave approximation, i.e. in the framework of a rotating coordinate system, a $\pi/2$-pulse turns an oriented spin into the xy-plane. During the following free precession in the xy-plane, the spins interact with their environment and start to dephase. A π-pulse after the time τ adds a phase to the spins, which causes them to recombine and produce a spin-echo after the time 2τ. The π-pulse has the same power as the $\pi/2$-pulse but with a doubled pulse duration.

If the phase-memory time was infinitely long, all spins would point in the same direction after 2τ. However, magnetic interactions such as hyperfine coupling or the rotation of methyl groups cause the spins to get out of phase. Therefore, not all spins recombine after 2τ and the echo intensity is reduced. Phenomenologically, the signal decay follows a stretched exponential law, $\propto \exp\left(-2\tau/T_m\right)^x$, where the stretch parameter x contains information on the dephasing patterns, thoroughly discussed in Ref. [158].

During the free precession, spin-flips of coupled partners such as neighbouring nuclei give rise to a modulation of the exponential decay [156]. This effect is known as electron spin echo envelope modulation, ESEEM, and gives useful information on what causes dephasing. In order to understand this phenomenon, we consider an $S = 1/2$, $I = 1/2$ system. Following the example presented in Ref. [46], we can then write down the spin Hamiltonian $\mathcal{H}_S$ in terms of angular frequency units, considering the electron and nuclear Zeeman effect and the hyperfine interaction, as follows [46]:

$$\mathcal{H}_S = \omega_S S_z + \omega_I I_z + A S_z I_z + B S_z I_x \,, \tag{3.24}$$

where ω_S, ω_I correspond to the angular Larmor frequencies in a given magnetic field and S_i, I_i are the spin operators for electron spins and nuclear spins, respectively. Here, we chose a coordinate system where the electron is located in the origin, and the nuclei in the xz-plane. Then, $A = A_{zz}$ and $B = \sqrt{A_{zx}^2 + A_{zy}^2}$,

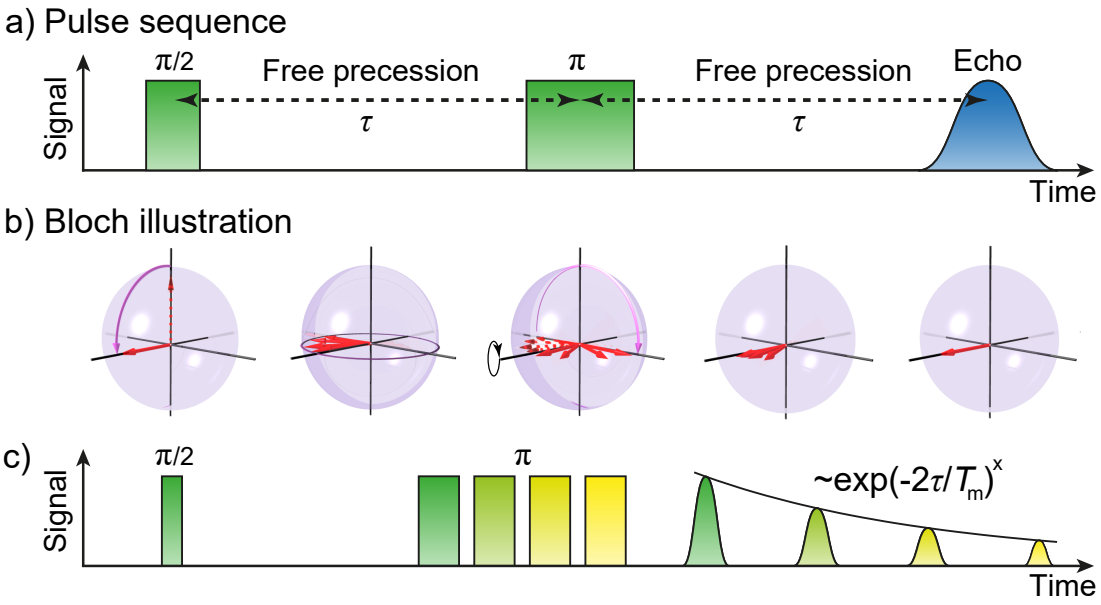

Fig. 3.3: Hahn-echo pulse sequence. (a) Hahn-echo pulse sequence to determine T_m. (b) Bloch sphere illustration of the effect of the pulses on the spin system. A $\pi/2$-pulse turns an oriented spin into the xy plane, while a π-pulse inverts a spin orientation. (c) Echo decay with increasing free evolution time τ.

in literature referred to as the secular and pseudo-secular hyperfine coupling, respectively [46]. Via a unitary transformation U, the spin Hamiltonian can be diagonalised. In this example, U is defined as [46]:

$$U = \exp\left(-\mathrm{i}\left(\xi I_z + \eta 2 S_z I_y\right)\right) , \tag{3.25}$$

with

$$\xi = \frac{\eta_\alpha + \eta_\beta}{2} , \tag{3.26}$$

$$\eta = \frac{\eta_\alpha - \eta_\beta}{2} . \tag{3.27}$$

$$\eta_{\alpha,\beta} = \arctan\left(-\frac{\pm B/2}{\pm A/2 + \omega_I}\right) , \tag{3.28}$$

$$\tag{3.29}$$

To understand the Hahn-echo sequence, we will use the formalism introduced in Sec. 3.1.3. We first transform the Hamiltonian into its eigenbasis using Eq. 3.25,

and obtain [46, 156]

$$\mathcal{H}_S^d = \omega_S S_z + \frac{\omega_+}{2} I_z + \omega_- S_z I_z \,, \tag{3.30}$$

with

$$\omega_\pm = \omega_{12} \pm \omega_{34} \,, \tag{3.31}$$

$$\omega_{12} = \left(\omega_I + \frac{A}{2}\right) \cos\eta_\alpha - \frac{B}{2} \sin\eta_\beta \,, \tag{3.32}$$

$$\omega_{34} = \left(\omega_I - \frac{A}{2}\right) \cos\eta_\alpha + \frac{B}{2} \sin\eta_\beta \,, \tag{3.33}$$

where ω_{12} and ω_{34} correspond to the angular nuclear frequencies for the two orientations of the electron spin (see also Fig. 3.7).

The application of a $\pi/2$-pulse is described in Eq. 3.12. Starting from there, we apply the transformation U and use Eq. 3.8. We obtain:

$$S_y \xrightarrow{\xi I_y + \eta 2 S_z I_y} \cos(\eta) S_y - \sin(\eta) 2 S_x I_y \,. \tag{3.34}$$

Since the matrix elements S_y and $2S_xI_y$ are nonzero, this equation shows that after the application of the $\pi/2$-pulse, nuclear spins are taking part in the evolution of the electron coherence during the time τ.

An ESR-allowed transition is characterised by a change of the magnetic electron quantum number $|\Delta m_s| = 1$, while the nuclear quantum number does not change, $\Delta m_I = 0$. We define the corresponding angular transition frequency as $\omega_{13} = 2\pi\nu_{13}$ (see also Fig. 3.7). After the $\pi/2$-pulse, the electron spins freely evolve in the xy-plane, and thus gain a phase $(\omega_{13} - \omega_{\mathrm{mw}})\tau$ in the rotating frame after the time τ, where ω_{mw} corresponds to the angular microwave frequency. However, the application of the subsequent π-pulse does not necessarily only flip the electron spins, but can also flip nuclear spins, caused by a redistribution of the electron coherences amongst all the electron spin transitions [46, 156]. This effect is also known as branching. Consequently, the ESR-forbidden transition with $|\Delta m_I| = 1, |\Delta m_s| = 1$ gains a phase $(\omega_{14} - \omega_{13})\tau = \omega_I \tau$ relative to the ESR-allowed

transition. Under variation of τ, this leads to a modulation of the echo intensity, where its frequency corresponds to the nuclear spin transition frequency. The modulation of the echo amplitude V can be calculated from the expectation value of the S_y operator:

$$V_{\mathrm{mod}} = -\langle S_y \rangle = 1 - \frac{k}{4}[2 - 2\cos(\omega_{12}\tau) - 2\cos(\omega_{34}\tau) + \cos(\omega_-\tau) + \cos(\omega_+\tau)], \quad (3.35)$$

with

$$k = \sin^2 2\eta\,. \quad (3.36)$$

The echo amplitude consists of three parts. First an unmodulated part with amplitude $1-k/2$, second, a modulated signal with frequencies $\omega_{12,34}$ and amplitude $k/2$, and, third, a modulated signal with combination frequencies $\omega_\pm$ and half amplitude $k/4$. These frequencies can be obtained from a fit of the Hahn-echo decay over 2τ.

In the final experiment, we may encounter unwanted echoes and FID signals. In this work, we carried out 2-step or 16-step phase cycling to compensate for these effects.

3.1.6 Measurement of spin-lattice relaxation T_1

Access to the spin-lattice relaxation time T_1 is enabled via saturation recovery or Picket-Fence sequences [156]. In the simplest case, a short, high-power microwave pulse saturates a given spin transition, and the signal recovery is measured via continuous microwave irradiation at a very low power. A more advanced technique is inversion recovery, where a π-pulse first flips oriented spins. After a variable time-delay t, the number of relaxed spins, i.e. spins oriented along $+z$-direction, is measured via a Hahn-echo sequence at a fixed evolution time τ. The measured echo signal recovery M against the relaxation time t follows an exponential law,

$$M(t) = M_0 \left(1 - \left(\exp\left(-t/T_1\right)\right)\right) , \tag{3.37}$$

where M_0 describes the saturation signal. However, all these techniques suffer from spectral diffusion or spin diffusion which overlap with the spin-lattice relaxation curve. These processes are related to magnetisation exchanges at the time scale of T_1 [156]. Spectral diffusion is often caused by molecular tumbling, nuclear spin flips or cross relaxation [159, 160]. In the inversion recovery technique spectral diffusion effects contribute to the echo signal when the inhomogeneous linewidth of the ESR signal is larger than the pulse excitation bandwidth. In this case, Eq. 3.37 needs to be expanded with a sum of exponentials accounting for all processes.

If spectral diffusion is present, a dependence on the excitation pulse duration is observed. With longer pulses, these can be reduced or even removed. The echo-detected saturation recovery (Fig. 3.4b) uses a long initialisation pulse at a low amplitude which reduces spectral diffusion effects greatly [159, 161]. In contrast, in stimulated-echo decay experiments (Fig. 3.4c) spectral diffusion effects can be enhanced. This technique can be therefore used for a more in-depth investigation of spectral diffusion and coupling partners.

A more effective way to suppress spectral diffusion can be achieved with the Picket-Fence pulse sequence [162], shown in Fig. 3.5. A series of π-pulses first

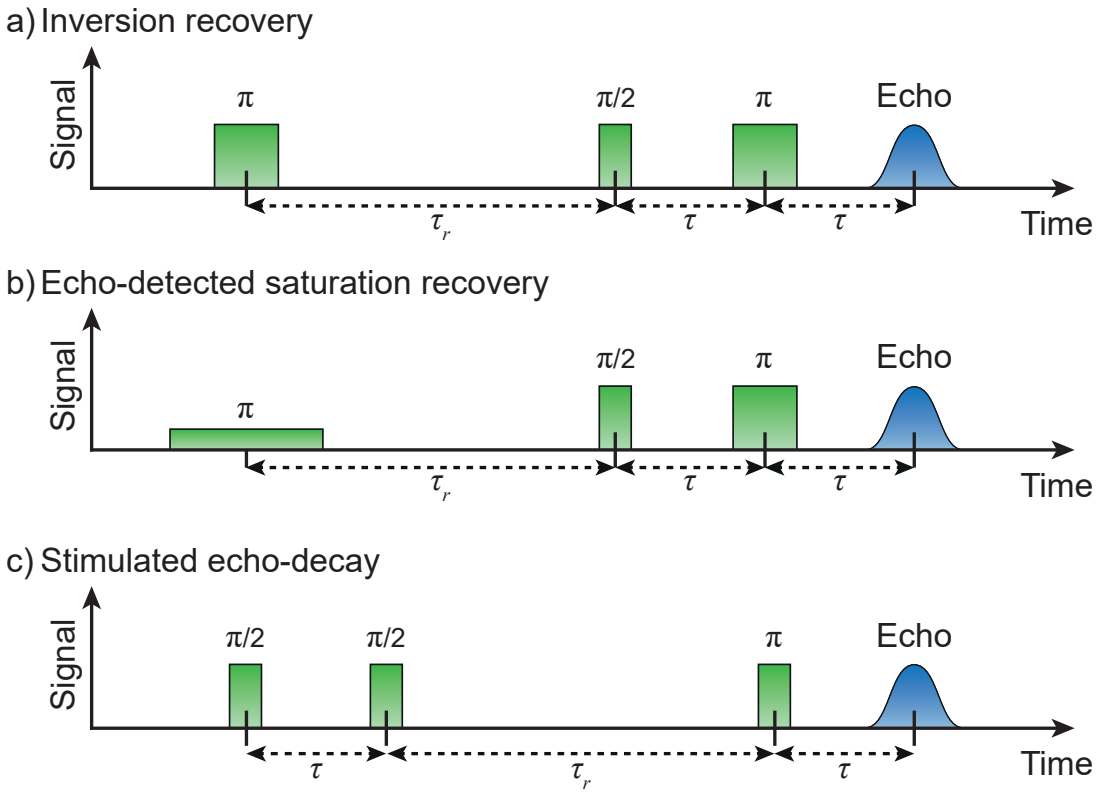

Fig. 3.4: Saturation recovery sequences. (a) Inversion recovery sequence. A π-pulse flips the magnetisation first. After a time-delay τ_r, a Hahn-echo sequence is used to measure the echo signal intensity. (b) Echo-detected saturation recovery technique. The pulse sequence is similar to inversion recovery, but uses a long, low-intensity π-pulse to saturate the spins. (c) Stimulated echo-decay sequence. The inversion pulse is split into two $\pi/2$-pulses.

demagnetises the system. The relaxation back to its original oriented state is then measured via a Hahn-echo sequence. This method will be the most widely technique used throughout this work to determine T_1. Due to the nature of this experiment, residual spectral diffusion processes can be detected on a time scale smaller than T_1, which allows for the identification of the spin-lattice relaxation time. Furthermore, we used a four-step phase-cycling procedure to remove unwanted echoes and FIDs.

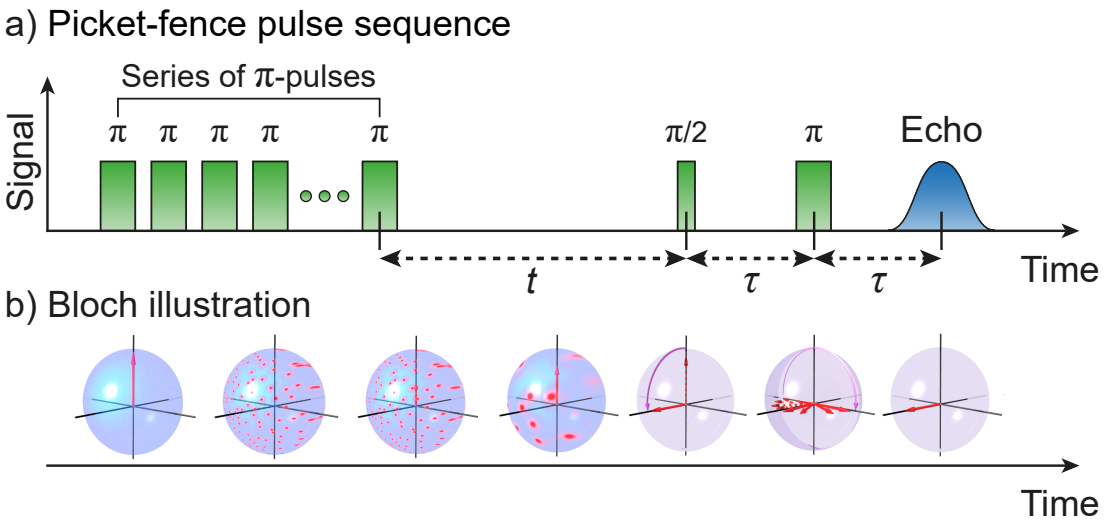

Fig. 3.5: Picket-fence pulse sequence. (a) Picket-fence pulse sequence to determine T_1. (b) Bloch sphere illustration of the effect of the pulses on the spin system. A series of π-pulses first demagnetise the system. After a variable time t the recovered spin signal is detected via a Hahn-echo seqeuence (Fig. 3.3).

3.1.7 DEER spectroscopy

Double-electron-electron-resonance (DEER) spectroscopy, in literature sometimes referred to as ELDOR (electron-electron double resonance), is a useful technique to investigate the coupling between two spins [163, 164]. It can be employed to study effects of spin-spin interactions in the time-domain, or to determine coupling energies originating from dipolar or exchange interactions. The principle of DEER spectroscopy is depicted in Fig. 3.6. At the observer frequency ν_1 (probe) a distinct spin species is initialised with a Hahn-echo sequence, and precesses mainly in the xy-plane. The initialisation sequence removes the instrumental dead-time. After a delay t, a π-pulse at the pump frequency ν_2 flips the polarisation of a second spin species. Another π-pulse at ν_1 reverts the evolution at the observer frequency, which leads to an echo after $2\tau_2 + 2\tau_1$. By varying t, the phase on the observer spins can be changed, which results in a modulation of the signal. Its modulation frequency can be obtained via fast Fourier transformation (FFT), and corresponds to the coupling energy between the two spin systems.

The main limitation in DEER spectroscopy is the phase-memory time. The

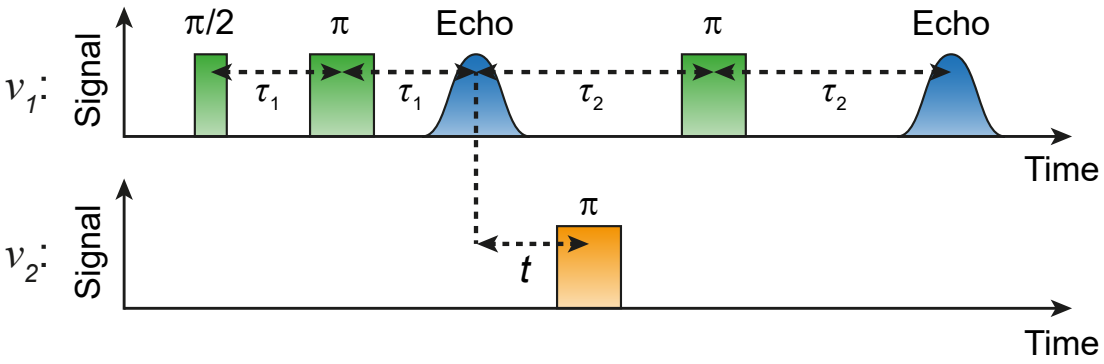

Fig. 3.6: DEER pulse sequence. The DEER technique uses two frequencies ν_1 and ν_2, defined as the observer and the pump frequency, respectively. After a Hahn-echo sequence at the observer frequency, a π-pulse flips spins at the pump frequency. Using another π-pulse at ν_1, an echo is registered after $2\tau_2$.

whole sequence can only be run if $2\tau_2 + 2\tau_1 \leq T_m$, which imposes an upper limit on t. Therefore, T_m sets a lower limit for the least detectable coupling energy.

We treat all DEER data using the Matlab software package DeerAnalysis [165]. It is used to phase and zero the data, and to subtract the background, which in the end yields a normalised time-domain and frequency-domain spectrum. The intermolecular background usually follows an exponential function, $\propto \exp\left(-kt^{D/3}\right)$, where D corresponds to the overall dimensionality of the system and k to a decay constant. In most cases, the intermolecular background is three-dimensional, as we will be dealing with either dissolved or powder samples, which represent a homogeneous distribution, and thus $D \approx 3$.

3.1.8 ELDOR-detected NMR (EDNMR)

A first estimate on possible couplings between electrons and nuclei can be obtained from the Hahn-echo sequence, where the frequency of modulations might correspond to nuclear spin excitation. However, it is not a very sensitive technique to gain hyperfine couplings, and, in most cases, an unwanted artefact thereof. ELDOR-detected NMR, more commonly known as EDNMR, gives a more sensitive insight into electron nuclei-couplings, and, in favourable cases, coupling strengths can also be obtained [46, 166–168].

The EDNMR pulse sequence is shown in Fig. 3.9. To explain the effect of the sequence, we consider an $S = 1/2$, $I = 1/2$ system as depicted in Fig. 3.7a. We describe our system by the two quantum numbers $m_s = \pm 1/2$ and $m_I = \pm 1/2$, which results in four possible states $|\alpha, b\rangle$, $|\alpha, a\rangle$, $|\beta, b\rangle$ and $|\beta, a\rangle$, which describe the possible spin orientations as depicted in Fig. 3.7. In the following, we will abbreviate these states as 1-4, respectively. Due to the Zeeman effect, a magnetic field removes the degeneracy, which results in four states with different energies. In equilibrium, state 1 and 2 are close together in energy and thus majorly populated. Due to the selection rules $|\Delta m_s| = 1$ and $|\Delta m_I| = 0$, the spin-allowed transitions are $1 \rightarrow 3$ and $2 \rightarrow 4$, while $1 \rightarrow 4$ and $2 \rightarrow 3$ are spin-forbidden due to a change of both the nuclear and the electron spin, and are therefore less likely to happen

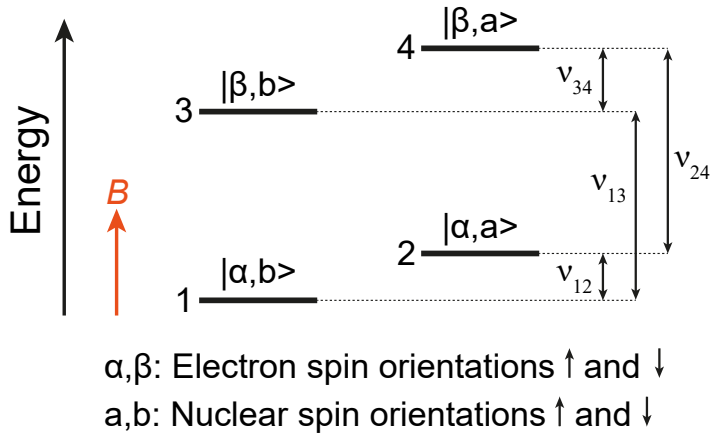

Fig. 3.7: Energy splitting of an S=1/2, I=1/2 system. A magnetic field B removes the degeneracy into a four-fold level splitting.

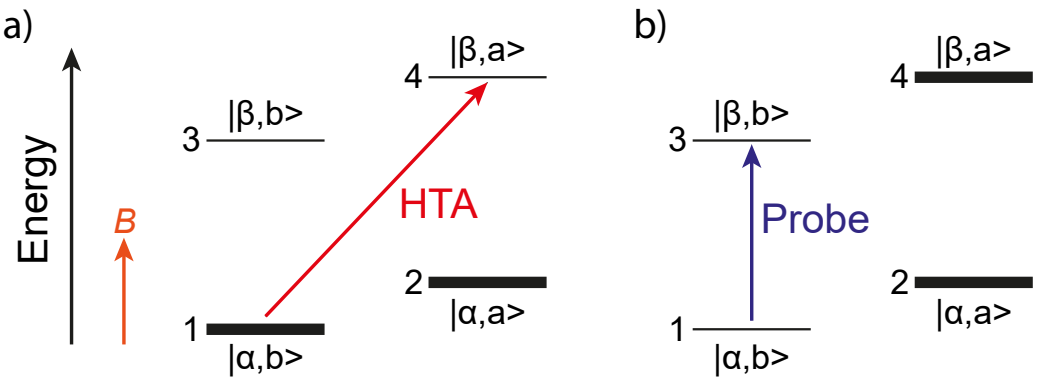

Fig. 3.8: EDNMR pump and probe pulse setting for a S=1/2, I=1/2 system. (a) In equilibrium, state 1 and 2 are populated as indicated by the thick lines. The HTA-pulse drives the spin-forbidden transition $1 \rightarrow 4$ and changes the population of states as indicated in (b). The probe frequency, ν_1, is swept and drives allowed transitions such as $1 \rightarrow 3$.

in experiments. In fact, we can drive such spin-forbidden transitions using long microwaves pulses, i.e. with a pulse duration of at least several 100 ns in our setup.

The idea of the EDNMR experiment is to use a high-turning-angle (HTA) pulse of varying frequency relative to the excitation frequency of an allowed ESR transition. In the experiments of the thesis, the HTA pulse is Gaussian-shaped. The HTA pulse, set to frequency ν_2, is calibrated to achieve a turning angle close to π for the spin-forbidden transition, obeying $|\Delta m_s| = 1$ and $|\Delta m_I| = 1$. As a consequence, the allowed transitions with $|\Delta m_s| = 1$ and $\Delta m_I = 0$, which are more likely to happen, are overrotated, so that we end up in a polarisation-transferred state as depicted in Fig. 3.8. The difference of the turning angles is due to the different transition strengths of allowed and forbidden transitions. After the polarisation transfer, the states 1 and 3 have equal populations, as well as 2 and 4. After a time-delay τ after the HTA-pulse, we apply a soft FID-optimised pulse (Fig. 3.9), set at the frequency ν_1 to drive either of the allowed transitions, and measure the FID.

In order to find hyperfine transitions, we fix the field and the probe frequency ν_1, and sweep the pump frequency ν_2 of the HTA pulse, and measure the inte-

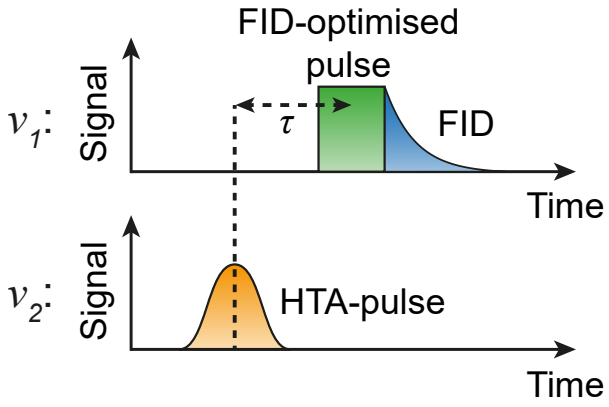

Fig. 3.9: EDNMR pulse sequence. Like DEER spectroscopy EDNMR uses two frequencies ν_1 and ν_2 as observer and pump-frequencies. A Gaussian-shaped high-turning-angle-pulse, HTA, overrotates allowed transitions. A NMR signal peak is observed, when $\Delta\nu$ corresponds to a nuclear spin resonance frequency.

grated FID intensity in dependence of ν_2. When sweeping through the resonance frequencies of the spin-forbidden transitions $\nu_{1\to4}$ and $\nu_{2\to3}$, the signal intensity goes through a dip due to the polarisation transfer and the thereof resulting lower transition probabilities of the allowed transitions [46]. At this condition, the difference frequency $\Delta\nu = \nu_2 - \nu_1$ corresponds to a nuclear transition frequency $\nu_{1\to2}$ or $\nu_{3\to4}$, as can be seen from Fig. 3.8. Thus, in the analysis of EDNMR spectra, we plot the difference frequency $\Delta\nu$ rather than the actual frequency against the integrated FID signal intensity. In this work, we will show the EDNMR spectra as their first derivative so as to improve the visualisation of overlapping peaks.

In the frequency spectrum, one will identify nuclear transitions that follow the selection rules $\Delta m_I = \pm1$ (single quantum transition, SQ) or $\Delta m_I = \pm2$ (double quantum transition, DQ). Furthermore, a combination of two single quantum transitions of two coupled nuclei is possible. An example for an EDNMR spectrum is depicted in Fig. 3.10. In this example, we consider an electron coupled to one ^{15}N nuclei with nuclear spin $I = 1/2$. The dips correspond to reductions of the ESR signal intensity when on resonance with a nuclear transition. At W-band frequency, the Larmor frequency ^{15}N is approximately 15 MHz. Hyperfine interactions cause a shift of the resonance frequency. By probing the different transitions $1 \to 3$ and

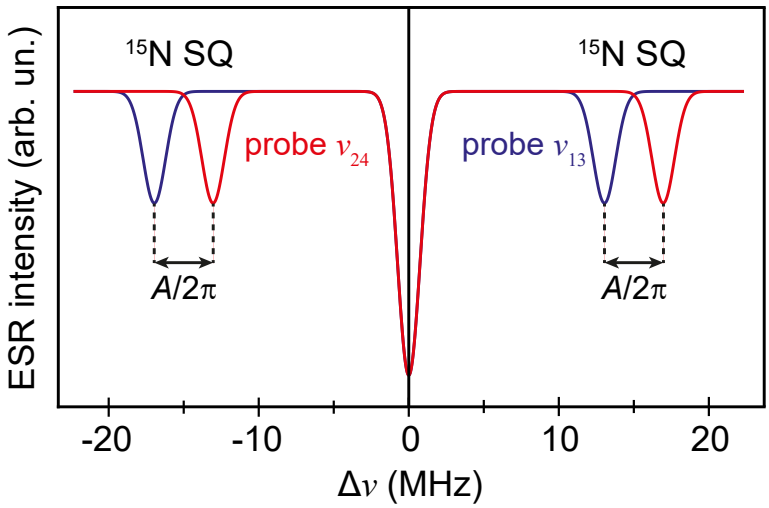

Fig. 3.10: Example of a W-band EDNMR spectrum. The example represents the case for an electron coupled to a ^{15}N nuclei with $I = 1/2$. By probing the different possible transitions $1 \rightarrow 3$ (blue) and $2 \rightarrow 4$ (red), which are depicted in Fig. 3.7, the hyperfine coupling A can be obtained from the relative shift of the nitrogen SQ dips. The central dip around zero frequency represents the central hole, which is a result of a spectral overlap of probe and pump pulses, where the HTA pulse drives the ESR transition. Example after Ref. [46].

$2 \rightarrow 4$ (Fig. 3.7) we can obtain the hyperfine coupling strength A by determining the spectral shifts, as depicted in Fig. 3.10. Moreover, from the asymmetry of the spectrum one can determine the coupling regime. Strong coupling to nuclei, i.e. $|A| > 2\nu_I$, can be concluded if spectral features only appear on either side of the spectrum, i.e. either for $\Delta\nu < 0$ or $\Delta\nu > 0$. Features on both sides, which is the case in this example, result from weak coupling [167]. An in-depth discussion on the mathematical description of EDNMR, as well as the esperimental HTA parameters, can be found in Refs. [46, 167].

Furthermore, a Voigtian lineshape occurs when $\nu_2 \approx \nu_1$. This so-called central hole can be fitted and subtracted from the data, and at the same time yields the zero-frequency calibration for the spectrum. In practice, this means that at Q-band frequency no reliable information can be obtained in the range $-3\,\mathrm{MHz} \leq \Delta\nu \leq 3\,\mathrm{MHz}$. Since nuclear nitrogen transitions are close to this range, no reliable

information on hyperfine couplings to nitrogen atoms can be obtained at Q-band frequency. For nuclear transitions that are in this frequency regime, higher microwave frequencies are necessary.

3.1.9 HYSCORE

Information on hyperfine couplings can also be obtained via hyperfine sublevel correlation spectroscopy (HYSCORE) [156, 170]. In contrast to other hyperfine spectroscopic techniques, two time variables t_1 and t_2 are tuned here. This allows us to deconvolve a one-dimensional hyperfine spectrum, where different hyperfine interactions overlap, into two dimensions with distinct features.

As the HYSCORE pulse sequence is more complex, we will visualise the effect of the pulses on the density matrix, depicted in Fig. 3.11. A mathematical description is presented at the end of the section. We will adhere to the notation in Ref. [169]. The HYSCORE pulse sequence is shown in Fig. 3.12. We start with a polarised system at equilibrium, where the density matrix is diagonal. By applying a $\pi/2$-pulse, we convert the polarisation into electron coherence, in the same way as a Hahn-echo experiment (Sec. 3.1.3). After a time-delay τ, in which the spins freely

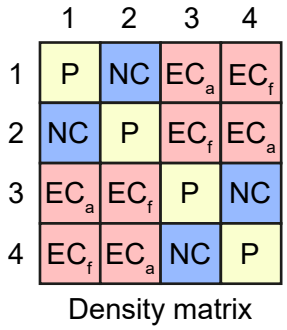

Fig. 3.11: Definition of the density matrix terms. The density matrix is pictorially shown for an $S = 1/2$, $I = 1/2$ system, with P the polarisation, NC the nuclear coherence, and EC_a and EC_f the electron coherences for allowed and forbidden transition, respectively. The numbers 1-4 correspond to the states defined in Fig. 3.7. Picture based on Ref. [169].

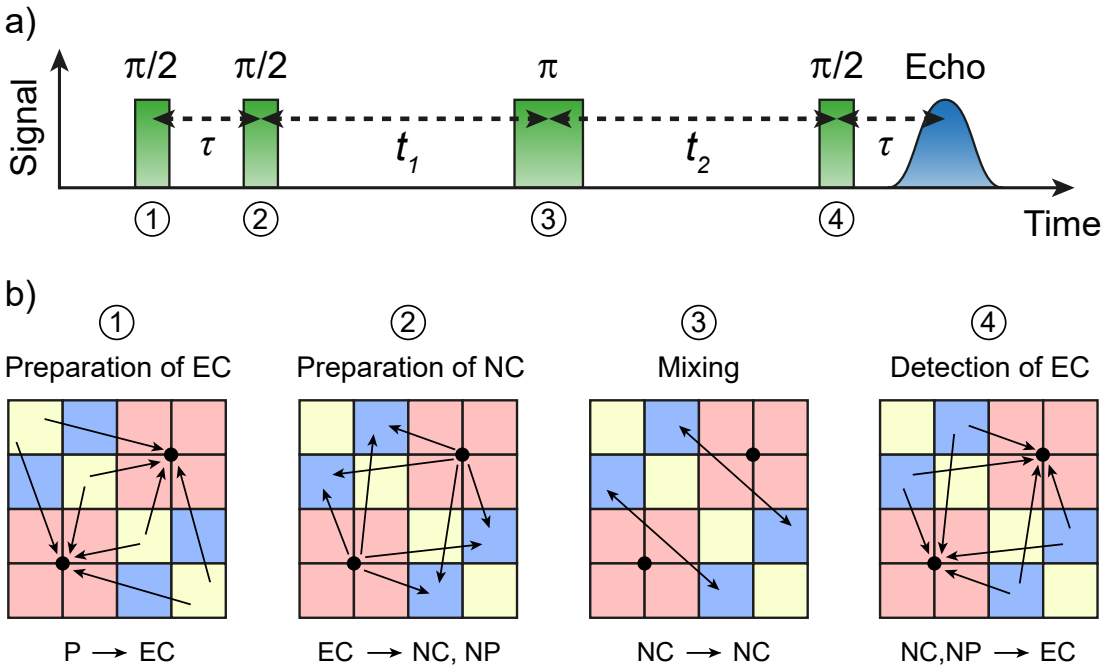

Fig. 3.12: HYSCORE pulse sequence. (a) The HYSCORE pulse sequence starts with two $\pi/2$-pulses, where the first one generates electron coherence (EC), and the second one nuclear spin coherence (NC) together with nuclear polarisation (NP), as shown in the pictorial representation of the density matrix in (b). The arrows in (b) denote the transfer of polarisations and coherences. After a free evolution time t_1, a π-mixing pulse interchanges the nuclear spin coherences. To generate an electron spin echo, a $\pi/2$-pulse after t_2 restores the electron spin coherence, thus generating an echo after τ. Representation based on Ref. [169].

evolve, we apply a second $\pi/2$-pulse. It can be shown via transfer coefficients [156, 169] that a second $\pi/2$-pulse creates nuclear coherence, which is the crucial point of this experiment. Therefore, during the following time t_1, nuclear spins freely evolve with their corresponding nuclear Larmor frequencies. Since electron coherence contributes to nuclear coherences, destructive interference occurs for certain values of τ, and therefore τ must be well chosen in the experiment to maximise the signal output. After t_1, a π-pulse interchanges the nuclear spin phases between electron spin species α and β, and the nuclear spins freely evolve for another time t_2. In the case of an $S = 1/2$, $I = 1/2$ system, this mixing pulse interchanges nuclear spins rotating at frequencies ν_{12} and ν_{34}, as depicted

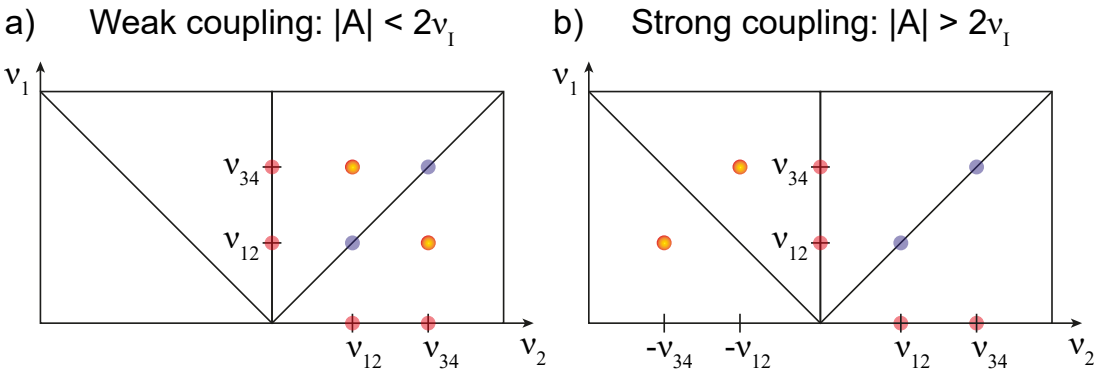

Fig. 3.13: Example spectrum of a HYSCORE experiment. The spectrum is obtained after FFT of the two-dimensional time-domain signal, so that the ν_1-axis corresponds to the FFT of t_1 and the ν_2-axis to the FFT of t_2. The example corresponds to an $S = 1/2$ with $I = 1/2$ system. The interesting peaks are at (ν_{12}, ν_{34}) and (ν_{34}, ν_{12}), since the hyperfine coupling can be estimated from their relative distance. Sketch adapted after Ref. [156].

in Fig. 3.12b. After t_2, a $\pi/2$-pulse restores electron coherence, which produces a measurable echo after τ. In contrast to the Hahn-echo experiment, this sequence is not directly limited by the electron phase memory time, but by the nuclear one $T_{m,n}$ [169]. Typically, $T_{m,n}$ has the same order of magnitude as T_1.

The time-domain data is then analysed via a fast Fourier transformation (FFT), so that a detailed spectrum is obtained where the corresponding transitions can be identified. Typical spectra are shown in Fig. 3.13. In the weak coupling regime, i.e. $|A| < 2\nu_I$ with ν_I the hyperfine-free nuclear Zeeman frequency of the corresponding free nucleus, peaks at (ν_{34}, ν_{12}) and (ν_{12}, ν_{34}) in the first quadrant are observed. Since the transition frequencies ν_{12} and ν_{34} are shifted relative to ν_I by the hyperfine tensor $\mathbf{A}$, the hyperfine coupling constants can be extracted. In the strong coupling regime, $|A| > 2\nu_I$, cross-peaks appear in the second quadrant. For intermediate coupling, $|A| \approx 2\nu_I$, peaks in both quadrants are observed.

Furthermore, measurement artefacts might appear in the spectrum. Peaks along the axes (red) are associated with interchanges of nuclear coherences and two-spin orders, and should be disregarded. Diagonal peaks (blue) are due to an imperfect

mixing pulse, which result from an incomplete flip angle that does not flip all spins. Subsequently, as the nuclear coherence path is not changed, peaks at (ν_{12}, ν_{12}) and (ν_{34}, ν_{34}) occur. To reduce this behaviour, pulses with large bandwidths are used, i.e. pulses are set as short as possible. Moreover, in order to suppress electron-coherence to nuclear-coherence transfer, and vice versa, a four-step phase-cycling procedure is carried out.

The HYSCORE spectrum contains all possible combinations of transitions for nuclei with $I > 1/2$. This is particularly important when dealing with nitrogen atoms present in nitronyl-nitroxide radicals. Therefore, we will avoid analysing single peaks in a spectrum, and instead consider complete HYSCORE simulations using EasySpin [171].

Mathematical description of HYSCORE

The obtained two-dimensional HYSCORE time-domain signal is described via the following formula [169, 172]:

$$V(\tau, t_1, t_2) = 1 - \frac{k}{4}(V_{\mathrm{I}} + V_{\mathrm{IIa}} + V_{\mathrm{IIb}} + V_{\mathrm{IIIa}} + V_{\mathrm{IIIb}}) \tag{3.38}$$

with k the modulation depth, which can be mathematically deduced from hyperfine-coupling constants as

$$k = \sin^2 \eta = \sin^2 \left(\frac{\eta_\alpha - \eta_\beta}{2} \right) , \tag{3.39}$$

where η, as in Eq. 3.27, is defined as:

$$\eta_{\alpha,\beta} = \arctan \left(-\frac{\pm B/2}{\pm A/2 + \omega_I} \right) , \tag{3.40}$$

with hyperfine couplings $A = A_{zz}$, $B = (A_{zx}^2 + A_{zy}^2)^{1/2}$ and ω_I the nuclear Larmor frequency, as defined earlier. Furthermore, we introduce the nuclear transition

frequencies and their combinations:

$$\omega_\alpha = \omega_{12} = \left(\omega_I + \frac{A}{2}\right)\cos\eta_\alpha - \frac{B}{2}\sin\eta_\beta\,, \tag{3.41}$$

$$\omega_\beta = \omega_{34} = \left(\omega_I - \frac{A}{2}\right)\cos\eta_\alpha + \frac{B}{2}\sin\eta_\beta\,, \tag{3.42}$$

$$\omega_\pm = \omega_{12} \pm \omega_{34}\,. \tag{3.43}$$

The individual V-terms in Eq. 3.38 can then be derived as [169, 172]:

$$V_\mathrm{I} = 3 - \cos(\omega_\beta\tau) - \cos(\omega_\alpha\tau) - \sin^2\eta\cos(\omega_+\tau) - \cos^2\eta\cos(\omega_-\tau)\,, \tag{3.44}$$

$$V_\mathrm{IIa} = C_\alpha(\tau)\cos\left(\omega_\alpha\left(t_2 + \frac{\tau}{2}\right)\right) + C_\beta(\tau)\cos\left(\omega_\beta\left(t_2 + \frac{\tau}{2}\right)\right)\,, \tag{3.45}$$

$$V_\mathrm{IIb} = C_\alpha(\tau)\cos\left(\omega_\alpha\left(t_1 + \frac{\tau}{2}\right)\right) + C_\beta(\tau)\cos\left(\omega_\beta\left(t_1 + \frac{\tau}{2}\right)\right)\,, \tag{3.46}$$

$$\begin{aligned} V_\mathrm{IIIa} = {} & C_c(\tau)\cos^2\eta\left[\cos\left(\omega_\alpha t_1 + \omega_\beta t_2 + \omega_+\tau/2\right)\right. \\ & \left. + \cos\left(\omega_\beta t_1 + \omega_\alpha t_2 + \omega_+\tau/2\right)\right]\,, \end{aligned} \tag{3.47}$$

$$\begin{aligned} V_\mathrm{IIIb} = {} & -C_c(\tau)\sin^2\eta\left[\cos\left(\omega_\alpha t_1 - \omega_\beta t_2 - \omega_-\tau/2\right)\right. \\ & \left. + \cos\left(\omega_\beta t_1 - \omega_\alpha t_2 - \omega_-\tau/2\right)\right]\,. \end{aligned} \tag{3.48}$$

Here, the C_α, C_β and C_c-terms are responsible for blind spots in the spectrum. These are dependent on τ, which is why the experiment needs to be optimised by choosing the right τ values. The V_I-term explains the generation of nuclear polarisation, NP, from the preparation part of the HYSCORE sequence (Fig. 3.12). Since τ is a fixed time in our experiment, it will not contribute to the modulation of our signal and is thus not in the interest of HYSCORE. The second term, V_IIa, arises from NP to NC transfer due to the π mixing pulse. It thus causes a modulation during the following time t_2. The choice of τ changes the phase of the modulation. V_IIb describes the inverted case, where the mixing pulse creates NP from a NC state. Therefore, the modulation depends on t_1, and τ adds a phase. Since this phenomenon creates peaks along the diagonal line in the FFT, they are not considered in HYSCORE. This means that the only relevant terms are V_IIIa

and V_{IIIb}.

The term V_{IIIa} describes the case where NC first evolves during t_1, and then after the mixing pulse, the different m_s states become exchanged, and NC evolves during t_2 under a different frequency. This term describes the weak hyperfine-coupling case, since $\eta \to 0$ for weak coupling and thus $\cos^2 \eta \approx 1$, and peaks therefore appear on the right quadrant in the FFT, as shown in Fig. 3.13. However, in the case of strong hyperfine coupling where $\eta \to \pi/2$, this term vanishes and V_{IIIb} comes into play. Consequently, peaks appear in the left quadrant. Since τ is fixed, τ-terms only add a phase to the modulation.

In the case where an electron is coupled to several nuclei i, a product rule applies to the echo amplitude [169]:

$$V_{\mathrm{tot}}(\tau, t_1, t_2) = \frac{1}{2}\left[\prod_i V_i^{\alpha\beta}(\tau, t_1, t_2) + V_i^{\beta\alpha}(\tau, t_1, t_2)\right] . \tag{3.49}$$

Coupling to several nuclei has an important consequence: when writing down the terms in the same way as above, the modulation will contain combination frequency terms of the different nuclei involved. Depending on the resulting dominant combinations, one can identify the signs of the hyperfine coupling from the HYSCORE spectrum [169].

3.1.10 Bruker Elexsys Setup

X-band (E680 and EMX(plus))

ESR measurements were carried out on a Bruker Elexsys E680 and EMX(plus) for X-band, Bruker Elexsys E680 for W-band, and Bruker Elexsys E580 for Q-band frequencies. A schematic overview of the most important parts of the spectrometer is given in Fig. 3.14. Microwaves are generated by a Gunn diode, which emit at 9-10 GHz in the Elexsys system. It is actually not a typical diode made of p- and n-conduction materials, but contains only n-doped components, which causes it to conduct in both directions. At a threshold voltage, it shows a negative differential conductance and oscillates at a given frequency, that can be used to generate the microwaves in an electronic oscillator. Since the Gunn diode needs to be driven at fixed conditions to be stable, an attenuator is used to vary the microwave power. The circulator directs the microwaves in the respective direction. Incoming microwaves at port 1 are directed to the cavity in which the sample is located in a magnetic field B. The reflected microwave power at port 2 is then directed to the detector diode via port 3. Detection is performed by a Schottky barrier diode, which absorbs incoming microwaves. At low powers, the produced current is proportional to the incoming microwave intensity, whereas at higher powers it is proportional to the square root of the intensity. Since the electrical power scales with the square of either voltage or current, the high power regime is the one we utilise, as it will give a linear response. Therefore, the detector is additionally fed by the reference arm ensuring an operation in this regime. An integrated phase-shifter ensures that the reference arm is in-phase with the reflected microwave power. Furthermore, the cavity is located in a cryostat, which allows control of the temperature between 3 K and 300 K with the use of liquid helium. Except for the cavity, all components sit in the microwave bridge. Magnetic fields are generated with a water-cooled electromagnet and can be set as large as 1.45 T.

The cavity, which is either a rectangular or circular hollow box, serves as an amplifier. When critically coupled at the resonance condition, no microwaves are

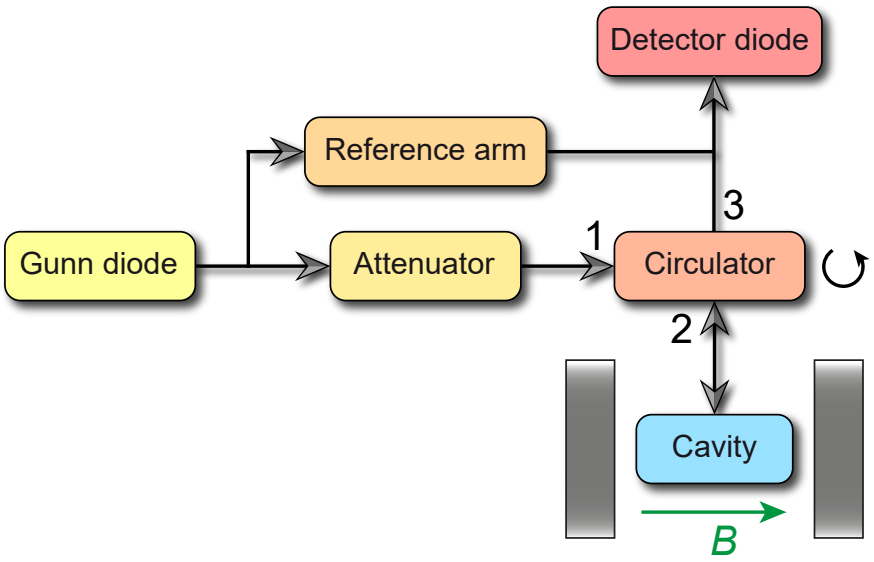

Fig. 3.14: Schematic setup of a Bruker Elexsys system. The function of the ESR setup is described in the main text.

reflected, since the dissipative energy loss rate in the cavity matches the coupling loss rate. A cavity is classed by the quality factor Q, defined as

$$Q = \frac{2\pi \times (\text{energy stored})}{\text{dissipated energy per cycle}} = \frac{\nu_{\text{res}}}{\Delta\nu}\,. \tag{3.50}$$

The sensitivity of the instrument scales with the Q-factor. When more energy is stored, rather than lost, small signals are better resolved. Energy can be lost via the walls in which microwaves create currents, for example. In the end, the system measures the quality factor by dividing the resonance frequency with the width at half intensity $\Delta\nu$. Inside the cavity, electric and magnetic fields are out-of-phase. This means that locations where the electric field component of the standing microwaves shows a maximum, the magnetic field component is minimal. For electrically conductive materials, the quality factor gets lowered at high electric fields due to non-resonant absorption. Since the magnetic field component drives ESR transitions, in literature known as magnetic dipole transitions with $\Delta m_s = \pm 1$, we want to place our sample at maximum magnetic fields. Microwaves are coupled into the resonator via a hole, the iris, which affects the intensity of reflected microwaves. By changing the size of the iris, the impedance of the resonator and

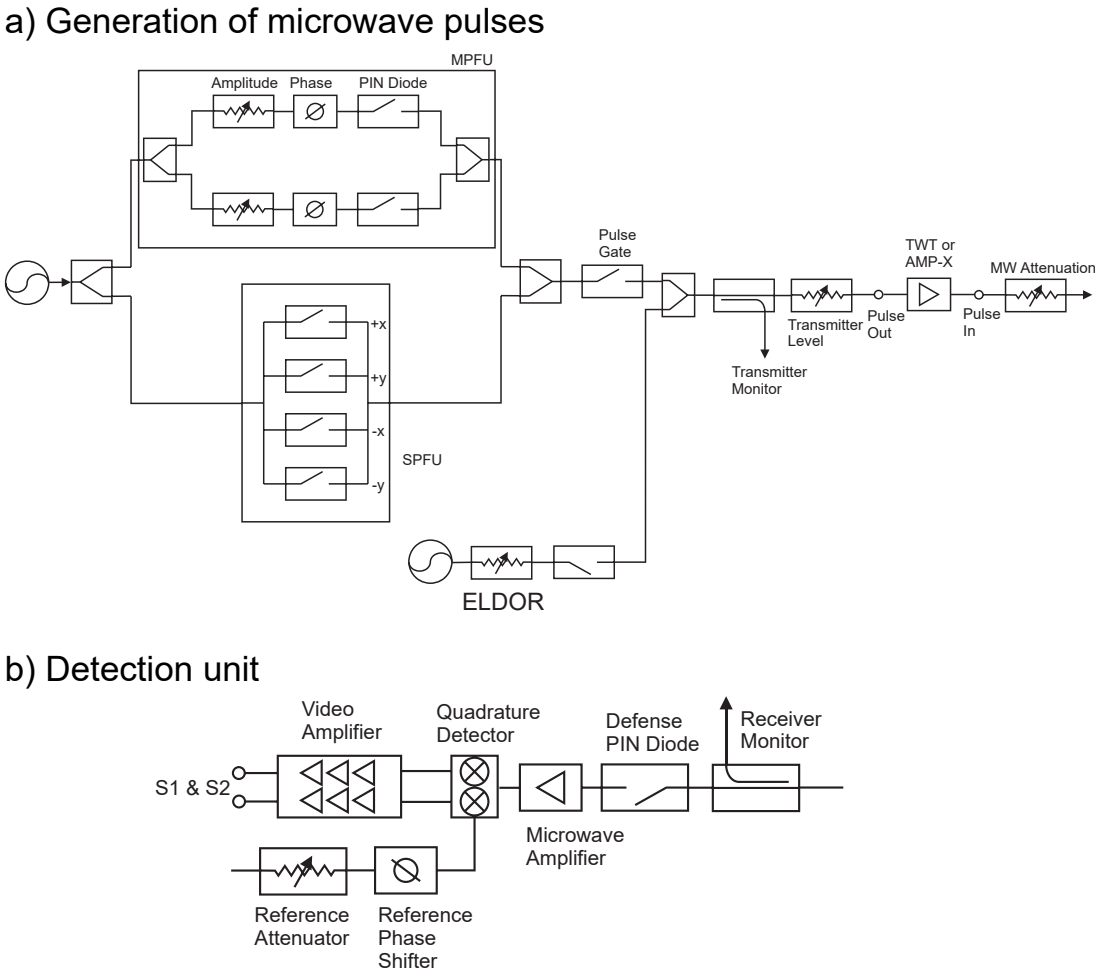

Fig. 3.15: Schematic setup of the pulsed unit of the Bruker Elexsys system. (a) Pulse excitation unit represented in a block diagram. (b) Pulse detection unit. Figure adapted from Ref. [173].

the waveguide can be matched or varied.

The quality factor decreases when a sample absorbs microwaves. This is due to the losses inside the cavity, which changes the impedance, so that the resonator is no longer critically coupled. In this case, microwave power gets reflected giving rise to an ESR signal.

Pulsed ESR

For pulsed measurements at X-band frequency, we overcouple the resonator by lowering Q intentionally to about ~ 100 in order to minimise the ring-down time and thus the deadtime. Microwave pulse durations are controlled via PIN-diodes,

which can be turned on to allow microwaves to pass through them for a desired pulse length. Pulses are furthermore amplified by a TWT (Travelling Wave Tube). Their phases can be controlled in four ways, $+x$, $-x$, $+y$ and $-y$. To control the power of the pulses, a fraction gets directed to a transmitter monitor (TM). The power is controlled via the transmitter level, which is an attenuator.

FIDs and echoes are detected via amplification of the outcoming microwaves. In order to avoid destructive oversaturation of both the detector and the amplifier caused by resonator ring-down and reflection of high-power pulses, an additional PIN-diode blocks the latter by generating a defense pulse. For calibration purposes, some power of the reflected microwaves is measured as the receiver monitor signal RM. Detection is performed in quadrature. This means that both transverse magnetisation components in the rotating frame are measured. The output of the quadrature detector is given in two channels, a real one and an imaginary one. By phasing the signal, we store all relevant information in the real channel and process it thereon. The data is further amplified and filtered by the video amplifier. These signals are amplified as long as the signal does not show any distortions, and the bandwidth is set to 200 MHz.

W-band (E680)

The generation of W-band frequencies is performed via the intermediate frequency unit (IF). An up-converter mixes the frequency of a different Gunn diode operating at 84.5 GHz with the X-band output at 9.5 GHz (IF signal). Via sum frequency generation, we arrive at 94 GHz in the W-band regime. Potential difference frequency signals are suppressed by the microwave electronics. Similar to Fig. 3.14, the W-band microwaves travel into the cavity via the circulator. The reflected signal is then down-converted to the X-band frequency, and measured with the X-band setup. This method has one primary advantage: all operating electronics optimised for X-band frequency can also be used also for W-band measurements. The cavity is cylindrical with typical dimensions of about 3 mm. The magnet

system consists of superconducting coils that generate fields up to 6 T. Additionally, an electromagnet with a limited range allows for a more accurate field sweep around the main field set by the superconducting magnet.

Q-band (E580)

The generation of Q-band frequencies on the E580 works in a similar fashion to W-band. Here, microwaves of a local oscillator at 25 GHz are mixed with the 9.5 GHz X-band frequency. The Q-band cavity dimensions are in the 1 cm regime. Magnetic fields are generated with a water-cooled electromagnet.

3.2 SQUID magnetometry

3.2.1 Static SQUID magnetometry

To determine the magnetic moment of our samples, we used a Superconducting Quantum Interference Device magnetometer (SQUID) MPMS XL-7, manufactured by QuantumDesign. It is a very sensitive instrument which can detect magnetic moments with up to 10^{-8} emu accuracy, and, under ideal conditions, even 10^{-9} emu. The measurements can be run automatically via measurement sequences, where a software controls all operations of the SQUID. In the following section, we give a brief description on how the SQUID works. The interested reader can find more details about SQUID magnetometry in Refs. [174, 175].

The basic setup of a SQUID is shown in Fig. 3.16. Both the superconducting magnet and the radiofrequency (RF) SQUID, which represent the heart of the

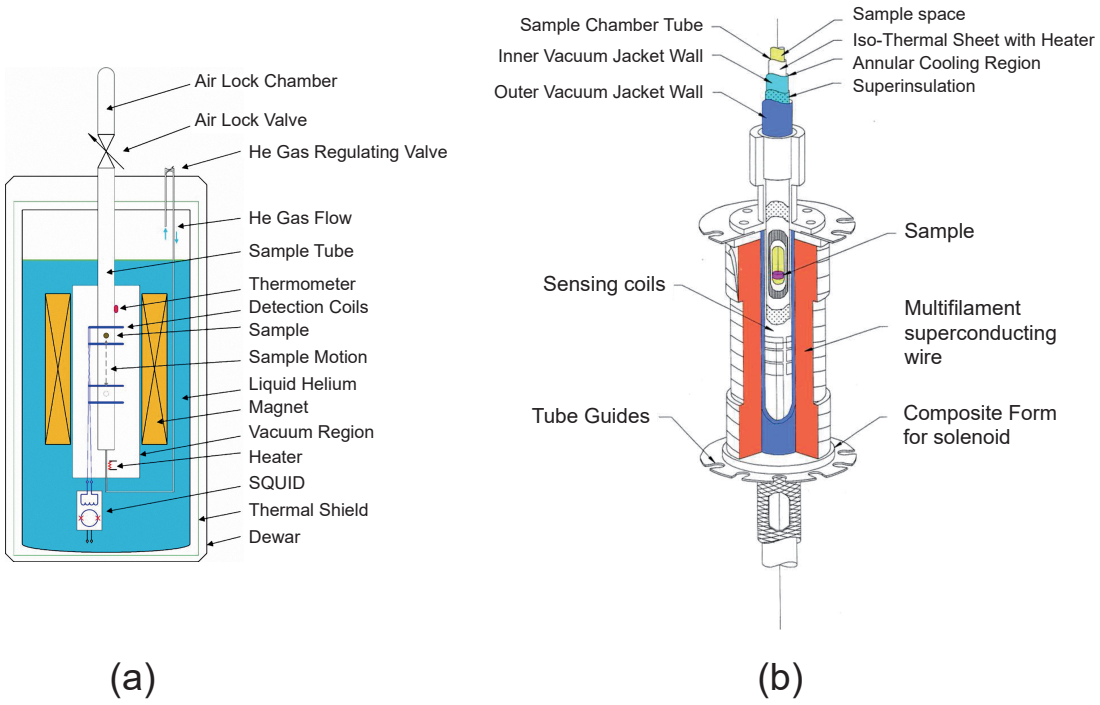

Fig. 3.16: Schematic setup of a MPMS XL-7 SQUID magnetometer. Figure (a) shows the cooling system and the main electric components of the SQUID. A zoom-in of the detection unit around the sample space is shown in (b). Figure adapted from Ref. [175].

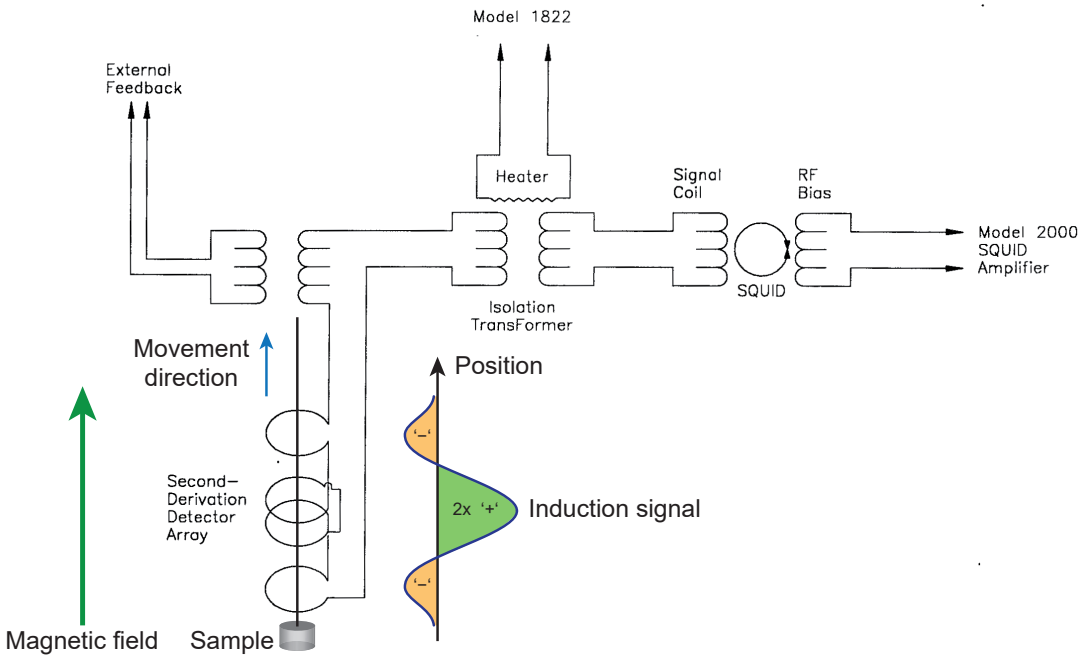

Fig. 3.17: Function of the MPMS XL-7 SQUID magnetometer. A magnetised sample is pulled through a second-derivative pick-up coil and produces a current, which perturbs the SQUID. This perturbation is compensated by an external current, which is proportional to the magnetic moment and thus the measured quantity. Figure adapted from Ref. [175].

magnetometer, are immersed in liquid helium. The magnet can be swept between -7 T and 7 T with an accuracy of 0.2 G below 0.6 T, and 2 G above 0.6 T. The magnetic field is collinear with the sample holder, and points to the top. The temperature of the sample chamber can be swept between 1.8 K and 400 K.

The measurement procedure is displayed in Fig. 3.17. Our samples were prepared in the form of loose powder in a gelatin capsule with low magnetic background. By pulling the magnetic sample through the second-derivative pick-up coil, we generate an induction signal as depicted. The clockwise windings produce a positive signal, while the counterclockwise windings a negative one. This particular orientation allows us to cancel ambient magnetic fields and their gradients. The generated current perturbs the RF SQUID. Instead of measuring this distortion, an external feedback current is added to keep the RF SQUID at a stable field. Therefore, the feedback current is the measured quantity in this system, which is

proportional to the magnetic moment. By fitting the induction signal, the magnetic moment of the sample is determined. Moreover, the heater is used to bring the RF SQUID into the normal conducting state to remove trapped currents that arise from field sweeps and imperfect coil windings.

3.2.2 AC SQUID magnetometry

AC SQUID magnetometry is a sensitive technique which gives access to the dynamic susceptibility of a sample, and thus to magnetic relaxation times. In AC magnetometry, an alternating magnetic field is applied to the sample via an AC coil. The AC coil is situated in the helium chamber in between the main magnet and the detection coil unit, so that AC fields are concentric with the main field. Thus, the magnetic field H can be written as

$$H = H_0 + h\cos\omega t\,, \tag{3.51}$$

with H_0 the static external field, h the amplitude of the oscillating field, ω the oscillation frequency and t the time. The AC field, usually at the order of a few Oe, causes the magnetic moment to oscillate.

In the following, we will consider the effect of the oscillating field in the example of a spin-1/2 system [7]. The time-dependent population of the two possible $m_s = \pm 1/2$ states, p_1 and p_2, is given as [7]

$$\frac{p_1}{p_2} = \exp\left(-\frac{g\mu_B(H_0 + h\cos\omega t)}{k_B T}\right)\,, \tag{3.52}$$

with g the g-factor, μ_B the Bohr-magneton, k_B the Boltzmann-constant and T the temperature.

Thermal relaxation, τ, plays an important role in AC magnetometry. When the field-oscillations are slower than the thermal relaxation time of the system, the magnetic moment follows the external field oscillations. In this case, i.e. $\omega\tau \ll 1$, the measured complex susceptibility $\chi = \chi' + \mathrm{i}\chi''$ can be identified as the isothermal

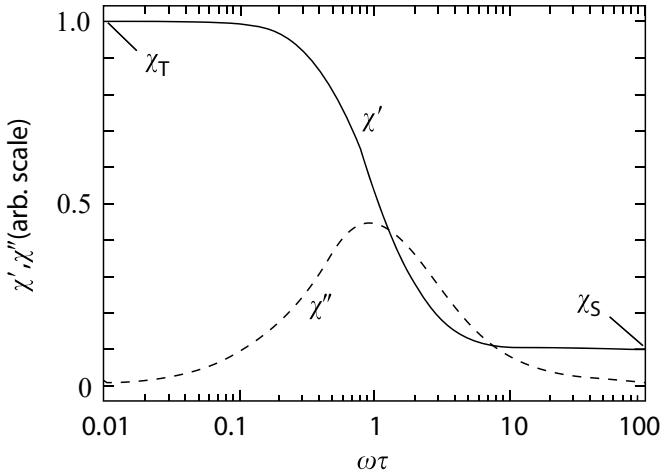

Fig. 3.18: Frequency-dependence of the dynamic magnetic susceptibility. In the low or in the high frequency regime, the imaginary part χ'' vanishes and the real magnetic susceptibility is constant in frequency. In the intermediate regime where the frequency is close to the thermal relaxation time of the system, the out-of-phase component χ'' gives a signal and shows a peak when in resonance. Figure adapted from Ref. [7].

susceptibility χ_T. In the opposite case, where $\omega\tau \gg 1$, the susceptibility reaches its adiabatic limit χ_S since no exchange of magnetic energy with the environment is happening. If $\omega\tau \approx 1$, the magnetic moment partially follows the external oscillations. Then, the dynamic susceptibility is a complex function given as [7, 176]:

$$\chi(\omega) = \chi_S + \frac{\chi_T - \chi_S}{1 + \mathrm{i}\omega\tau}\,, \tag{3.53}$$

which yields for the real and imaginary part

$$\chi' = \frac{\chi_T - \chi_S}{1 + \omega^2\tau^2}\,, \tag{3.54}$$

$$\chi'' = \frac{(\chi_T - \chi_S)\omega\tau}{1 + \omega^2\tau^2}\,. \tag{3.55}$$

While the real part corresponds to the magnetic susceptibility as obtained from DC measurements when in the isothermal limit, the imaginary part describes energy losses in the sample. When $\omega \ll \tau$, the magnetic moment of a sample is able to

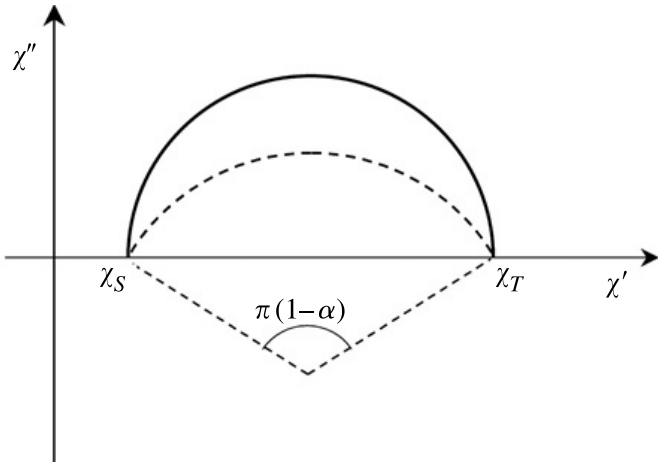

Fig. 3.19: Argand diagram of the dynamic magnetic susceptibility. In an Argand diagram, the imaginary susceptibility is plotted against the real one. Each relaxation process corresponds to a half-circe. In cases where a distribution of relaxation times is present, the opening angle of the half-circle becomes smaller, $\pi(\alpha - 1)$. Figure adapted from Ref. [7].

follow the oscillations of the AC coil. However, when $\omega \approx \tau$, the magnetic moment follows the oscillations out-of-phase. Therefore, χ' and χ'' are also known as in-phase and out-of-phase components of the magnetic susceptibility, respectively. The exact frequency dependence of these terms is further explained in Fig. 3.18.

Sometimes, the relaxation is not characterised by a single process, but via a distribution of relaxation times $G(\tau)$. In this case, Eq. 3.53 is modified and becomes [7, 177]:

$$\chi(\omega) = \chi_S + \frac{\chi_T - \chi_S}{1 + (\mathrm{i}\omega\tau)^{1-\alpha}}\,, \tag{3.56}$$

where α is a measure for the aforementioned distribution of relaxation times.

Typically, AC susceptibility data are analysed via an Argand diagram [7], where the imaginary susceptibility is plotted against its real counterpart. An example is shown in Fig. 3.19. In an Argand diagram, each relaxation process appears as a half-circle. When several relaxation paths or mechanisms are present, this representation allows distinguishing between them. The peak of a half-circle corresponds to the resonance frequency, from which one can identify the characteristic

relaxation time via $\tau = \omega^{-1}$ [7]. In the case when $\alpha \neq 0$, the half-circle is shifted as depicted in Fig. 3.19.

The extraction of the relaxation times is particular interesting in the studies of SMMs. By investigating the temperature dependence of τ, important parameters such as the anisotropy barrier D can be extracted [7]. This will be explained and demonstrated in Ch. 5.

3.3 Setup development to investigate light-induced effects

An essential part of this work was the development of a fibre-optical setup for the MPMS XL-7 and the Elexsys systems, which allows us to investigate how ultraviolet (UV), visible or infrared (IR) light affects the magnetic properties of a molecular system. Although existing commercial options provide a way to perform experiments under light irradiation, they share a setback: no real information is given on the actual light intensity arriving at the sample. In consequence, such options can mainly be used for qualitative analyses with little room for optimisation. However, for quantitative studies, knowing the intensity is crucial. We want to overcome this issue with a fibre-optical setup where beam paths are known and can be adjusted to the sample requirements. Furthermore, low-temperature studies under light irradiation suffer from generation of heat, which is due to the excitation of phonons. By knowing the experimental parameters of the home-built system, we are consequently able to control the heating effect, enabling us to optimise our results. In the following, the here developed setups will be introduced.

3.3.1 Low-temperature collimation setup for SQUID magnetometry

The developed low-temperature collimation setup consists of a fibre-coupling part and a low-temperature part. Two systems have been designed, one for coupling of laser light into a single-mode fibre, and one for coupling of incoherent light of a Xenon light source into a thick-core fibre, where the latter is commercially available. Both designs are shown in Fig. 3.20.

Lasers have the advantage of being monochromatic, thermally-stable sources with negligible warm-up times and temperature drifts. Coupling into a single-mode fibre with about 5 µm core diameter can be done via the beamwalk technique: with the two-axis mirror **1** we align the beam through aperture **1**, and with mirror

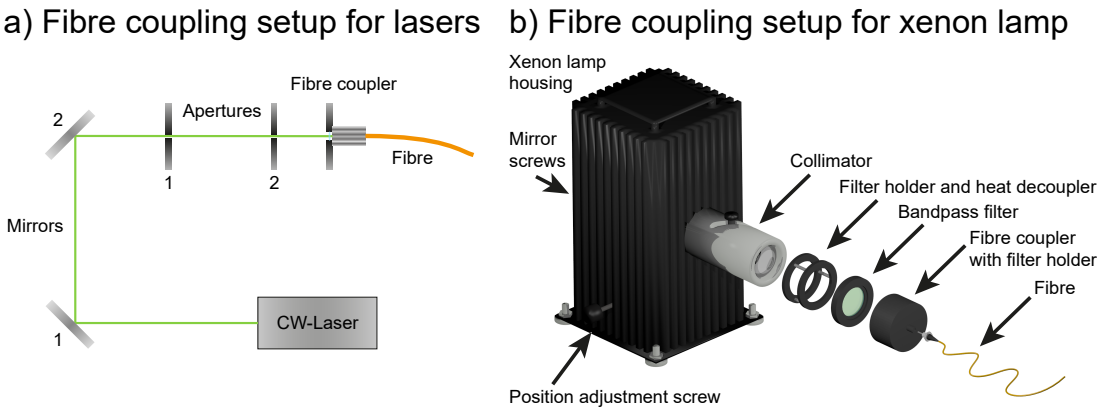

Fig. 3.20: Fibre-coupling units. (a) Fibre-coupling unit to couple a CW-laser into a single-mode fibre. (b) Fibre-coupling unit to couple light from a white light source (xenon lamp) into a multimode thick-core fibre.

2 through aperture **2**. Via iterative repetitions, we ensure that the beam passes parallel into the fibre coupler (FiberPort PAF-X by Thorlabs), which contains a lens that can be aligned perpendicular to it, and a fibre connector that can be turned around its direction. For optimal coupling of lens and connector, succeeding in a maximised light output, we must first align the position of the lens and then the fibre connector to the focal point of the lens. We perform these steps at the lowest necessary power. The intensity of the laser can either be changed with the driver, or by using neutral density (ND) filters. If the fibre coupler is completely misaligned, it might help to use an external light source connected to the other end of the fibre and adjust the beam direction so that it comes out straight from the fibre coupler. We achieve efficiencies of typically 80 %, depending on the quality of the beam shape.

With the xenon light source we are not restricted to certain wavelengths, since xenon arc lamps emit between 200 nm and 2500 nm. The xenon lamp, model LS1002, and the fibre coupling parts shown in Fig. 3.20 were manufactured by LOT-QuantumDesign. Using dielectric filters with a bandwidth of 40 nm, we select the desired wavelengths. The intensity is adjusted by using a set of ND filters. Since we are dealing with a point-source, we couple the light into a thick-core fibre with 1 mm core diameter by varying the position adjustment screws, the

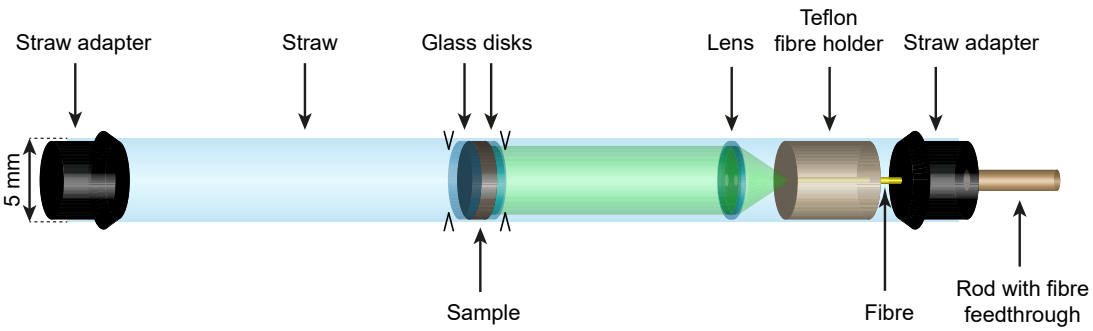

Fig. 3.21: SQUID sample holder for measurements under irradiation of light. The light is guided through the hollow sample rod and held by a Teflon fibre holder. The lens collimates the outcoming beam. For standard measurements, samples are fixed in a thin plastic straw by making holes that bulge the plastic.

mirror screws and the position of the collimator iteratively. A disadvantage of xenon lamps is the typically long warm-up time. After approximately two hours, the setup becomes thermally stable.

The fibre then goes through the sample rod into the sample space as shown in Fig. 3.21. It is losely held by a Teflon cylinder in a plastic straw to allow for thermal compression at low temperatures. Furthermore, it must be placed roughly 8 cm above the sample to avoid additional background effects. Using a lens with a short focal length of 7.5 mm, the light is collimated and directed to the sample. The sample itself is fixed by creating holes into the straw with a needle. The straw then bulges inside and provides support for the sample. When using pellet samples, two glass disks provide additional support against cracking. For some mechanisms, pressed pellets quench light-induced excitations since volume changes often arise. Therefore, it is advisable to use powder samples if no expected transitions are observed. In this case, a small amount of thin powder is well-spread in a gelatin capsule. Before placing the sample rod into the SQUID, the light intensity hitting the sample is measured.

3.3.2 CW-ESR under continuous irradiation of light

CW-ESR measurements under continuous irradiation of light were performed on the Bruker EMXplus system. The fibre goes into the resonator space and is fixed with Teflon tape in an open NMR tube, as shown in Fig. 3.22. We prepare the sample as loose powder in an open capsule, and fix it on the open NMR tube. The fibre is placed at a height where the light cone ideally illuminates the entirety of the sample, which is usually a few millimetres depending on the numerical aperture. In contrast to the procedures required for SQUID measurements, the proximity of fibre and sample here will not interfere with one another, eliminating the concern of background signals.

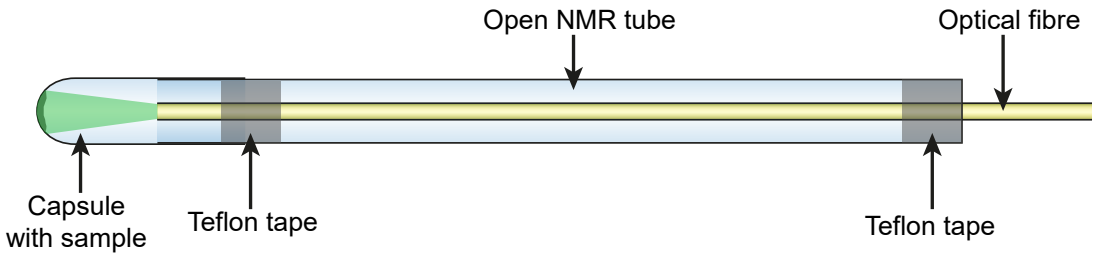

Fig. 3.22: ESR EMX sample holder for measurements under irradiation of light. Light from the fibre coupling unit goes via a fibre into the sample space. The fibre is fixed inside an open NMR tube via Teflon tape.

3.4 Broadband torque-detected ESR (TDESR)

Torque-detected ESR, TDESR, is a sensitive technique that detects ESR signals indirectly via the generation of a torque. When in resonance with microwaves, the population of the spin states change, which affects the overall magnetisation of a sample. In anisotropic crystals this creates a torque except when the magnetic field is aligned parallel to one of the magnetic main axes of the crystal. The primary advantage of this technique is its high sensitivity combined with a broadband approach, where magnetic field and frequencies can be swept independently and continuously, thus providing a detailed spectroscopic resolution. Furthermore, it gives access to a broad excitation regime inaccessible with the Elexsys systems. This section briefly introduces magnetic anisotropy, which is the basic requirement for the detection of a torque, and proceeds with the theory of torque magnetometry. The torque magnetometer was developed and thoroughly tested by Fadi El Hallak at the University of Stuttgart. Eric Heintze subsequently extended the TDESR-setup by facilitating the excitation of a sample with light. This allows for a detailed high-frequency ESR investigation of photoexcited states.

3.4.1 Magnetic anisotropy

The key ingredient for torque magnetometry is magnetic anisotropy, which describes the property of a sample to show a magnetic moment that depends on the orientation of an external magnetic field. Mathematically, the magnetic response is described by the magnetic susceptibility tensor χ. There are different physical phenomena which contribute to the magnetic anisotropy. For macroscopic ferromagnets, for example, magnetic anisotropy is strongly influenced by the shape of the magnet. In the samples under study in this work, intrinsic effects dominate and magnetic anisotropy is defined via the crystal-field splitting and accordingly via the population of the different magnetic states explained in Ch. 2.

The magnetisation of a molecule is obtained from thermodynamic laws. The

molar magnetisation M_α parallel to the Cartesian coordinate α is defined as [178]:

$$M_\alpha = \frac{N_A k_B T}{\mu_0} \frac{\partial \ln Z}{\partial H_\alpha} , \tag{3.57}$$

with N_A the Avogadro constant, k_B the Boltzmann constant, T the temperature, μ_0 the vacuum permeability, H_α the magnetic field and Z the partition function. The partition function is defined as the Boltzmann-weighted sum over all magnetic states i,

$$Z = \sum_i \exp\left(-\frac{E_i}{k_B T}\right) , \tag{3.58}$$

where E_i describes the energy difference to the ground state obtained from the diagonalisation of the spin Hamiltonian. The magnetic susceptibility is commonly defined as $\partial M/\partial H$. Using this definition the susceptibility can thus be obtained via

$$\chi_{\alpha\beta} = \frac{N_A k_B T}{\mu_0} \frac{\partial^2 \ln Z}{\partial H_\alpha H_\beta} , \tag{3.59}$$

with α and β being Cartesian coordinates. It is convenient to give the susceptibility in its diagonalised form with the three main susceptibilities χ_{xx}, χ_{yy} and χ_{zz}. When $\chi_{zz} > \chi_{xx} \approx \chi_{yy}$, the molecule shows easy-axis anisotropy, which means it can be easily magnetised along the easy-axis and harder magnetised in the plane perpendicular to the easy-axis. This type of anisotropy is also known as Ising anisotropy. Furthermore, when $\chi_{xx} \approx \chi_{yy} > \chi_{zz}$, the molecular spins prefer an orientation perpendicular to the quantisation axis z. This means that it has one hard-axis and two easy-axes; this type is known as xy-type anisotropy. If there is no clear dominance of one term, so that the molecule has one easy axis, one intermediate axis, and a hard axis, the anisotropy is of Heisenberg-type.

In order to provide an intuitive picture for the correlation between the magnetic state and the magnetic anisotropy, we introduce the semiclassical vector-model shown in Fig. 3.23. We consider an $S = 6$ system, which is the spin ground state of the Fe_3Cr molecule investigated in Ch. 5. Assuming dominating second-order anisotropy described by the B_0^2 crystal-field parameter, the states are split into

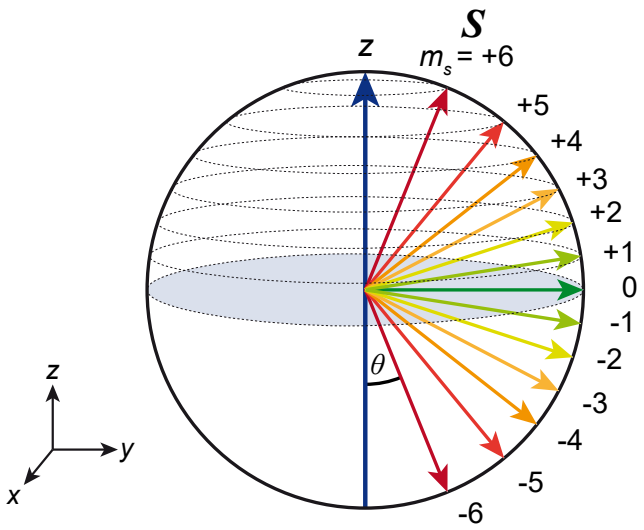

Fig. 3.23: Semiclassical vector-model for the spin orentiation. Depending on the spin state, spins prefer either to align along the quantisation axis z and thus giving rise to an easy-axis anistropy, or to align in the xy-plane which is known as easy-plane anisotropy.

$2S+1$ pseudo doublets. The spins $\boldsymbol{S}$ are, depending on the m_s state, oriented as depicted in Fig. 3.23. When we apply a magnetic field in z-direction, the spins precess about the z-axis with their Larmor frequency, and the projections to the z-axis determines the magnetic moment of the spins. The angle θ between quantisation axis and spin orientation is then given by

$$\cos\theta = \frac{|m_s|}{\sqrt{S(S+1)}}\,. \tag{3.60}$$

A ground state of $m_s = \pm 6$ gives rise to an easy-axis anisotropy, as the spins are largely aligned close to the z-axis. On the contrary, a low ground state of $m_s = 0$ gives rise to an easy-plane anisotropy.

3.4.2 Torque magnetometry

A magnetic torque arises from non-collinearity between the magnetic moment of a sample and the external field. This non-collinearity can only be found for samples that show magnetic anisotropy. When applying an external field to an

anisotropic sample, where the field direction is not parallel to any of the three magnetic main axes, the molecular frame is no longer identical to the frame of the external magnetic field. In this case, off-diagonal components in the susceptibility tensor appear, leading to a magnetisation that is not parallel to the external field.

Distinctively, the potential energy in a magnetic field, $U_{\mathrm{mag}} = -\boldsymbol{M} \cdot \boldsymbol{B} = -MB\cos\theta$, is minimised when the magnetisation $\boldsymbol{M}$ is parallel to the magnetic field $\boldsymbol{B}$ at $\theta = 0°$. The resulting torque τ_M can thus be obtained via

$$\tau_M = \frac{\mathrm{d}U_{\mathrm{mag}}}{\mathrm{d}\theta} = MB\sin\theta\,. \tag{3.61}$$

A more general expression is obtained by using the cross-product formalism, which yields

$$\boldsymbol{\tau_M} = \boldsymbol{M} \times \boldsymbol{B} = (\chi\boldsymbol{B}) \times \boldsymbol{B}\,. \tag{3.62}$$

As can be seen from this equation, the torque scales quadratically with the magnetic field in the linear regime, i.e. for fields far away from saturation. Here, the susceptibility tensor frame and the experimental one share a universal coordinate system. It can now be intuitively understood that the torque vanishes when the magnetic field is parallel to the easy axis of the system, which represents the lowest possible potential energy. However, the torque also vanishes when the magnetic field is parallel to the hard axis. In this case, an equal equilibrium number of spins are oriented parallel and antiparallel to a given orientation of the easy axis. Therefore, any resulting torque becomes cancelled out overall.

3.4.3 Basic principle of TDESR

The magnetisation of a system depends on the population of the spin states described by Eqs. 3.57 and 3.58, where the partition function describes an equilibrium condition at a given temperature. When in resonance with a microwave field, an excited state becomes populated, where the actual averaged population depends on the microwave intensity. In this non-equilibrium condition, the overall

magnetisation increases or decreases, and, accordingly, the torque changes. By recording this change, one can perform an ESR experiment, where either the microwave frequency or the magnetic field is swept.

To quantify the torque, Eq. 3.61 requires a modification that takes the population of the involved states into account. The total torque τ_{tot} of a spin ensemble that follows a Boltzmann distribution pattern can be written as

$$\tau_{\mathrm{tot}} = \sum_i \tau_i \frac{\mathrm{e}^{-E_i/k_B T}}{Z}\,, \tag{3.63}$$

where τ_i corresponds to the torque generated by spin specimen that populate the magnetic state $i = m_s$. Population is taken into account via the exponential term, and normalised by dividing with the partition function Z. In an ESR experiment, resonant microwave irradiation modulates the population between the initial state i and the final state f, which now has to be included in the torque. To deal with this, we describe the fractional population change via the parameter δ. Therefore, Eq. 3.63 becomes

$$\tau_{\mathrm{tot}}(\delta) = \frac{1}{Z}\left[\left((1-\delta)\mathrm{e}^{-\frac{E_i}{k_B T}} + \delta \mathrm{e}^{-\frac{E_f}{k_B T}}\right)\tau_i + \left((1-\delta)\mathrm{e}^{-\frac{E_f}{k_B T}} + \delta \mathrm{e}^{-\frac{E_i}{k_B T}}\right)\tau_f\right] + \tau_r\,, \tag{3.64}$$

where τ_r corresponds to the torque of the remaining Boltzmann-populated states that are not in resonance with the microwave field. At sufficiently low temperatures, these do not play a role as they are not populated. In saturation, one finds $\delta = 0.5$ which corresponds to an equal population of ground and excited state.

When showing the ESR resonances, we plot the difference with and without irradiation, i.e. $\tau(\delta) - \tau(0)$. This allows us to remove any background effects and torques originating from higher excited states. Under ideal conditions, where temperature and microwave power do not drift, this will give an absorption-like ESR-spectrum with either Lorentzian and Gaussian-shaped absorptive features.

3.4.4 TDESR setup

The TDESR measurements were carried out in collaboration with Eric Heintze at the University of Stuttgart. The TDESR setup, shown in Fig. 3.24, is based on the cantilever torque magnetometer (CTM) developed by Fadi El Hallak and thoroughly described in this work [179]. A crystal sample is placed on a flexible CuBe cantilever of either 25 µm or 80 µm thickness (Fig. 3.24a). The cantilever is spaced from the conductive base plate. This configuration represents a parallel-plate capacitor, where the capacitance C depends on the distance d between the plates as follows:

$$C = \frac{\varepsilon A}{d}\,, \tag{3.65}$$

with ε the permittivity of the medium in between the plates and A the surface area of the plates. A torque changes the distance, which again modifies the capacitance ΔC. Therefore, we detect a torque by measuring the changes in the capacitance. In the first order, the capacitance scales linearly with distance changes, as can be seen from the Taylor series expansion:

$$\Delta C = C(d_0 + \Delta d) - C_0 = C_0 \left(-\frac{\Delta d}{d_0} + \frac{(\Delta d)^2}{d_0^2} - \frac{(\Delta d)^3}{d_0^3} + \dots \right). \tag{3.66}$$

To detect the torque, a sensitive measurement device with attofarad resolution is required. In order to meet this requirement, we used an Andeen Hagerling AH2550A capacitance bridge. It provides a resolution of 0.8 aF, and measures capacitances up to 1.5 µF. To balance out the impedances, the bridge operates with an AC voltage of 15 V and 1 kHz. The capacitance is then obtained either repetitively, or averaged.

The CuBe-alloy is known to be a stable material that can be well-handled at liquid helium temperatures. By placing spacers of about 30 µm in thickness, the distance between the cantilever and the support can be tuned, and the cantilever fixed by two screws on top. For the calibration process it is crucial to choose the right amount of spacers and cantilever thickness, as large torques can excessively

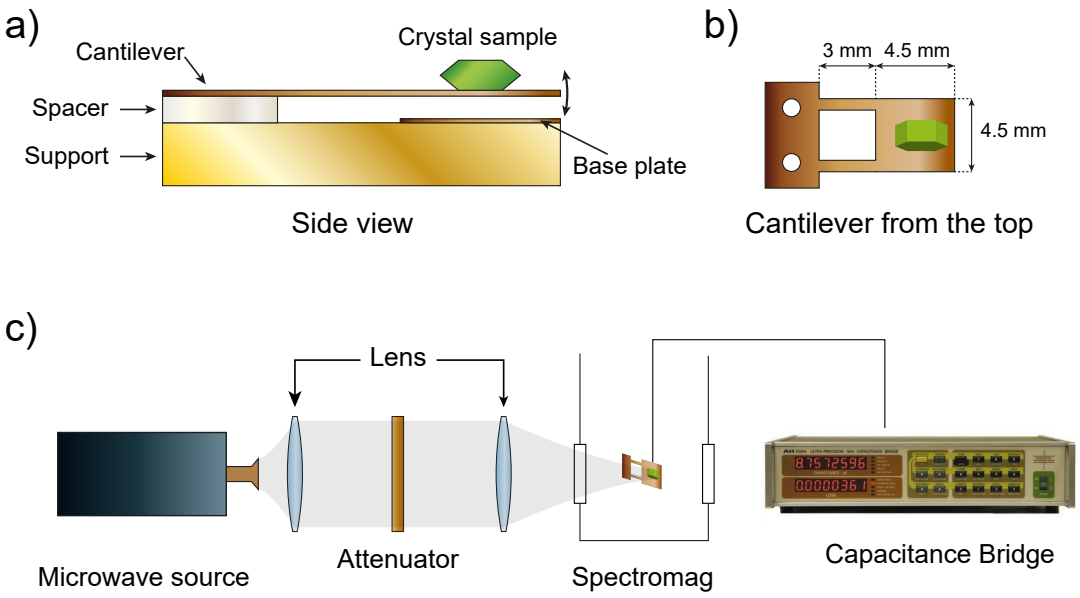

Fig. 3.24: TDESR setup. (a) Side view of the mount. The CuBe cantilever is placed on spacers to adjust the distance between the cantilever and the conductive base plate. The support provides general rigidity for the setup. (b) Top view of the cantilever. The sample is fixed using vacuum grease, which freezes at cryogenic temperatures. To create a long lever, the sample is mounted at the end of the cantilever. The two thin arms decrease the rigidity and therefore increase the torque sensitivity. (c) TDESR setup. Microwaves are generated via tunable backword-wave oscillators and hit the sample using microwave optics. The sample is located in a Spectromag that provides a cryogenic environment and generates magnetic fields. Torque is read out via a capacitance bridge.

bend the cantilever leading to a nonlinear response, or even short cut with the base plate. On the other hand, if the cantilever thickness is too large, the torque signal might be lost in the noise floor. The top view of the cantilever is displayed in Fig. 3.24b. The crystal sample is fixed with Apiezon N vacuum grease. It is important to know the orientation of the magnetic main axes of the crystal, as these should not be aligned parallel to the magnetic field. In favorable cases, point symmetry enables us to find them. For low symmetry crystals, such as triclinic ones, these main axes must be determined first. The whole sample stage can be rotated via a stepper motor along a horizontal axis to align the sample in the

field, and also to perform angle-dependent magnetometry measurements. The magnetic field is generated via a superconducting split-coil magnet inside the Oxford Instruments Spectromag. It generates fields up to ±7 T. Furthermore, the Spectromag provides a cryogenic environment for the sample stage which allows for temperatures down to 1.8 K with liquid helium.

The spectroscopic part is depicted in Fig. 3.24c. Microwaves are generated by backward-wave oscillators (BWOs), which represent coherent and tunable sources. With a set of different BWOs, we cover a range of 30 - 1500 THz, where resolutions of up to 10^{-6} can be achieved. Furthermore, the microwaves are highly linearly polarised ($> 99\%$). Inside the BWO, electrons are accelerated in an evacuated tube by a high voltage of up to 6 kV. These electrons are attracted by the anode and travel on a periodic comb-like structure. Via electric fields, their velocity becomes modulated and electrons get bunched when passing this structure. Additionally, magnetic fields are used to collimate the electron beam. The continuous acceleration and deceleration leads to an emission of microwaves that leave the BWO in the opposite direction, giving the source its name. The frequency of the microwaves can be tuned by varying the acceleration voltage. However, the power is also frequency-dependent, and, therefore, the resulting spectrum must be normalised relative to the output power, which can be obtained via a Golay cell.

The emitted microwaves are then collimated and focused onto the sample via lenses made of Teflon, polytheylene or quartz. These are located on a rail, which allows calibrating the Gaussian beam. Using the same set of lenses, the beam diameter is about 3 mm. In regimes where no frequency-trippler is used, the microwave radiation may be large and thus requires attenuation. Having the advantage of an almost perfectly linearly polarised source, polarisation-dependent measurements can be carried out. By tuning the polarisaton, the selection rules of magnetic-dipole transitions can be varied, giving a more detailed spectroscopic picture on the nature of the states. The Spectromag has a Mylar window on each

side, which are transparent to microwaves. In order to calibrate the microwave beam direction, an aperture with same size as the cantilever is mounted. By lifting the cantilever part, we can then use the aperture to direct the beam towards the sample position by maximising the power measured with a Golay cell behind the Spectromag. Furthermore, for a given manual calibration of the BWO, we measure the frequency-dependent output power in order to normalise the spectrum and to account for possible microwave heating effects of the cantilever. As the external magnetic field direction is horizontally fixed, we can irradiate the sample either in Voigt or in Faraday geometry, i.e. either field parallel or perpendicular to the propagation direction of the microwaves.

3.4.5 Combination of TDESR with photoexcitation

Combining light-excitation with TDESR enhances the capabilities of the setup. The spectral sensitivity of high-frequency and high-field ESR can be used to acquire detailed insight into the crystal-field splitting of photomagnetic systems. In contrast to the Elexsys system, we are not limited to certain frequencies. In Ch. 5 we will present the use of this setup exemplarily on an Fe_3Cr-based SMM and perform spectroscopy on its photoexcited state. Currently, this method is limited to continuous-wave operation.

The setup was developed by Eric Heintze at the University of Stuttgart as part of his thesis [180]. Having the option of four windows in the Spectromag allows us to use the TDESR setup described in the previous section, and irradiate the sample using the third window. The experimental geometry is depicted in Fig. 3.25. As a light source we utilise a commercial laser diode. Its intensity can be controlled via the corresponding driver module or via ND filters. A lens is used to focus the beam onto the crystal sample. As photoexcitation inevitably leads to excitation of phonons during the relaxation process, we can use the resulting heating effect for calibration. With increasing temperature, the magnetisation of an easy-axis, and, accordingly, the resulting torque, decreases. By maximising this

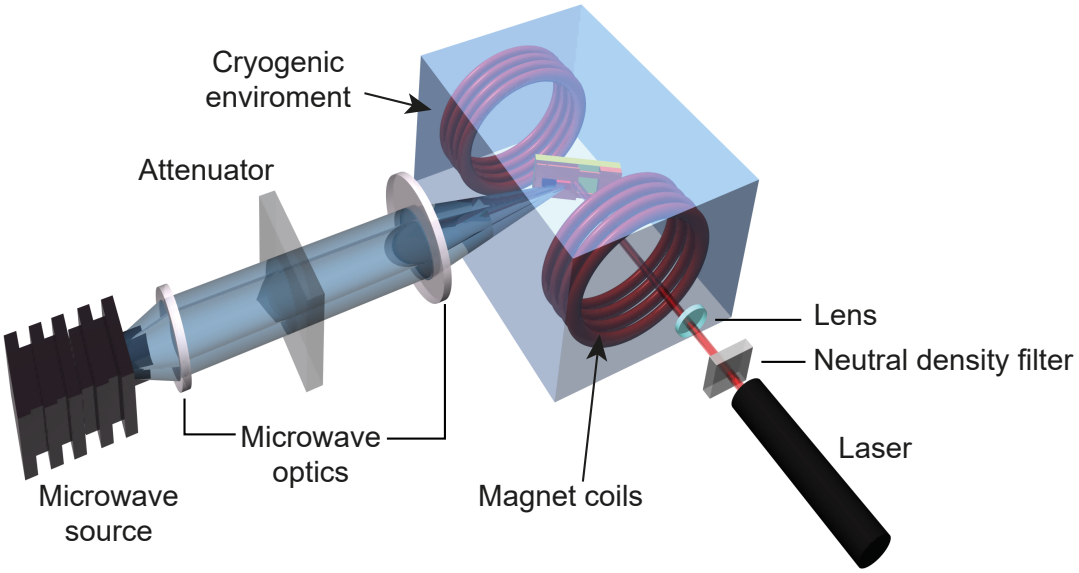

Fig. 3.25: Extension of the TDESR setup with a laser. Using the TDESR setup shown in Fig. 3.24c and simultaneously irradiate the sample with a laser enables spectroscopy of photoexcited states. Scheme modified and adapted from Ref. [180].

laser-induced effect, we can therefore centre the beam position. Quantification of the heating effect can be achieved in the following way. First, by measuring the baseline with the laser. Then, with the laser switched off, by finding the right temperature which corresponds to this baseline.

4 Magnetic bistability in a new cobalt valence tautomer

4.1 Overview of the project

Combining the photoswitching properties of magnetic molecules, which show valence tautomerism (VT) or spin crossover, with molecular nanomagnets, could lead to novel and interesting possibilities for the field of molecular spintronics. The ability to control the magnetic properties of building blocks via light is certainly fascinating, as it represents a non-invasive and clean method without the need of electrical manipulation. In many cases, electrical contacting results in deterioration of the magnetic properties [2]. This problem could be overcome with the use of photoswitchable nanomagnets.

Established synthetic methods present one option in the design of photoswitchable nanomagnets. For example, bipyridine and bipyrimidine ligands are common building blocks in molecular nanomagnets [181–184]. By using bipyrimidine as the bridging ligand between a molecular nanomagnet and a photoswitchable counterpart one could motivate a new class of molecular switchable clusters, outlined later in this chapter.

In this study we characterise the photoswitching properties of a new cobalt valence tautomeric complex, $Co(3,5\text{-dbbq})_2(\mu\text{-bpym})$, that uses bipyrimidine (bpym) as stabilising ligand. It is part of the broad family of Co-catecholate/semiquinone compounds which are known to display VT [185–193]. The photoswitching process is based on an intramolecular charge transfer explained in Ch. 2. The role of the bpym ligands is passive, and mainly affects the energy barrier for relaxation in Co-VT complexes, as we shall see later. Moreover, as the bpym ligand features

nitrogen atoms on each side, one can motivate grafting an SMM on the side that is not attached to the Co ion. This may allow the emergence of intriguing coupling phenomena, which can potentially be controlled with light. Furthermore, we are interested in how small changes of the electrostatic environment at Co affect the photoswitching properties. We will compare our results with the properties of a similar, already reported complex [187], which uses 3,6-dbbq instead of 3,5-dbbq ligands. We used SQUID magnetometry and ESR spectroscopy to investigate the photoswitching properties of the complex. The results shown in this chapter have been published in Ref. [194]. Contents and all figures from Ref. [194] are reproduced with the permission from the Royal Society of Chemistry.

4.2 Synthesis and DFT calculations

4.2.1 Synthesis

The synthesis, carried out by Dr. Ralph Hübner, follows routines already reported in literature [194, 195]. At first, a mixture of 0.25 mmol $Co_2(CO)_8$ and 0.55 mmol 2,2'-bipyrimidine (μ-bpym) was stirred for 10 min in 20 mL toluene. After that, 2 mmol 3,5-dbbq (3,5-di-tert-butyl-1,2-benzoquinone) in 15 mL toluene was added and the whole mixture was stirred for 3 h. Then, it was concentrated under reduced pressure and stored overnight in a fridge at 4 °C. The blue precipitate was filtered and washed using hexane. The end product, $[Co(3,5\text{-dbbq})_2(\mu\text{-bpym})]$, is schematised in Fig. 4.2. The metal ion is surrounded by one μ-bpym ligand, and, depending on the oxidation state, by either two semiquinone ligands or one semiquinone and one catecholate group, abbreviated as 3,5-dbbq. In the following, we will use the term semiquinone (SQ) when we refer to the oxidised state of the catecholate ligand (Cat), while quinone represents the oxidised state of semiquinone. These are depicted in Fig. 4.1.

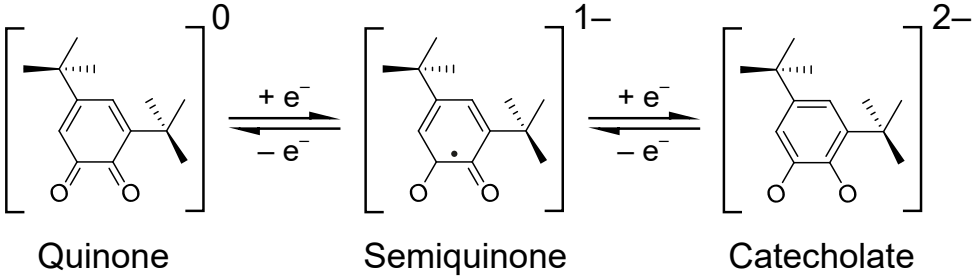

Fig. 4.1: Oxidation states of the quinone ligand. Quinone reduces to semiquinone, which again reduces to catecholate.

4.2.2 DFT calculations

DFT calculations, conducted by Ralph Hübner, were carried out at the B3LYP level [196]. A 6-31G* basis set was assigned to all atoms, and the calculations were performed using Spartan'14 program packages [197]. Tab. 4.1 shows the atomic bond lengths in the LS and HS state. Typically, bond lengths obtained via DFT

calculations come close to results from X-ray diffraction methods, and thus DFT calculations represent a legitimate way to gain an idea on bond length changes after the VT mechanism.

The DFT calculations show that in the HS state, the bond lengths between the central cobalt-ion and the surrounding O and N atoms are increased by about 0.19 Å on average. This can be explained by the fact that in the HS state, e_g orbitals are taking part in the bonding to neighbouring atoms. Since these have antibonding character, bond lengths increase leading to a larger unit cell volume. When external pressure is applied on the Co-VT samples, the ligands are coming closer to the central Co(III)-ion. As a result, the crystal-field interaction becomes stronger, and the splitting between the t_{2g} and e_g-orbitals increases [198]. In this case, the population of the energetically lower lying t_{2g}-orbitals is favored, which leads to a LS configuration.

We note, however, that it may not be entirely appropriate to perform DFT calculations on this complex. Originally, DFT calculations, based on the Kohn-Sham equation, are supposed to handle non-degenerated ground states. On the contrary, in the case of our octahedral Co-VT complex, the cobalt-ion has three degenerate t_{2g}-orbitals. Efforts have been made to also deal with this case. Moreover, DFT calculations on high-spin systems often lead to erroneous results, since usually only Fermi correlations are taken into account in the exact exchange, but not Coulomb correlations [199]. Nevertheless, workarounds are available and thoroughly discussed in Refs. [199, 200]. These imply nontrivial modifications to the exchange energy calculations to obtain the correct energy splitting of the different multiplets e_g and t_{2g}. In the end, it is important to find the correct admixture of exact and local exchange in hybrid functionals such as B3LYP. It has been shown that about 20 % admixture of exact exchange into the B3LYP function provides good results [200]. The discussion on how to find the right admixtures and workarounds, however, goes well beyond the scope of this thesis. The interested reader can find an in-depth discussion in Ref. [200], and in references therein. Via such adjustments to the exchange correlations, satisfying results are obtained.

Tab. 4.1: Bond lengths of LS-Co^{III} and HS-Co^{II} from DFT calculations.

Bond	LS-Co^{III} (Å)	HS-Co^{III} (Å)
Co – N(1)	1.968	2.140
Co – N(2)	1.961	2.145
Co – O(1)	1.873	2.060
Co – O(2)	1.856	2.049
Co – O(10)	1.864	2.059
Co – O(20)	1.877	2.050
O(1) – C(1)	1.324	1.290
O(2) – C(6)	1.317	1.288
C(1) – C(2)	1.423	1.438
C(2) – C(3)	1.391	1.385
C(3) – C(4)	1.424	1.431
C(4) – C(5)	1.387	1.383
C(5) – C(6)	1.408	1.415
C(1) – C(6)	1.438	1.472
O(10) – C(11)	1.339	1.290
O(20) – C(16)	1.331	1.288
C(11) – C(12)	1.415	1.440
C(12) – C(13)	1.401	1.381
C(13) – C(14)	1.412	1.435
C(14) – C(15)	1.397	1.379
C(15) – C(16)	1.398	1.420
C(11) – C(16)	1.430	1.470

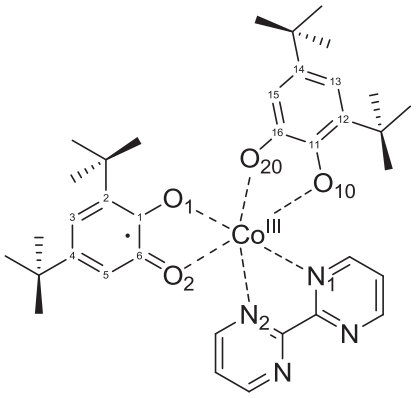

Fig. 4.2: Numbering of the atoms in the Co-VT complex.

4.3 The valence tautomeric mechanism

The VT mechanisms implies an electron transfer between the ligands and the Co-ion that results in a change of spin states in both the metal centre and its surrounding ligands. This interconversion process between Co^{III}(Cat) and Co^{II}(SQ) is depicted in Fig. 4.3 and formulated as follows:

$$[Co^{III}(\mu\text{-bpym})(Cat)(SQ)]^{LS} \rightleftharpoons [Co^{II}(\mu\text{-bpym})(SQ)_2]^{HS}\,. \tag{4.1}$$

At room temperature, the molecule is in an entropy-favoured HS state. The d^7 orbitals of the Co^{II}-ion are occupied as $t_{2g}^5 e_g^2$. This yields a 3/2 net spin, as shown in Fig. 4.3. Furthermore, the SQ ligands carry a spin of 1/2 each since one electron sits in a singly-occupied π^{*1}-orbital. As the semiquinone spins couple either antiferromagnetically or ferromagnetically, the overall spin state in the HS configuration can be 1/2 or 5/2. The molecule undergoes a thermally-reversible HS to LS transition when cooling down below the transition, or crossover, temperature $T_{1/2}$, which is approximately 200 K [14]. One electron moves from the Co^{II}-ion to a SQ group, thus leaving a d^6 configuration in the Co^{III}-ion and forming a Cat group with $S = 0$ and π^{*2}. The d^6 (t_{2g}^6) configuration favours an LS population, i.e. spins pair up in the t_{2g} orbitals. Since the Cat orbitals are filled, the resulting net spin state is 1/2 arising from the remaining partially-filled π^*-orbital of the SQ ligand. The transition temperature strongly depends on the electrostatic potential created by all atoms and varies with the different types of ligands.

Although it is commonly accepted that complexes of the family studied in this work are supposed to show valence tautomerism [14], we should not exclude the possibility that a spin crossover from HS-Co^{II} to LS-Co^{II} may take place instead. The d^7 LS-Co^{II} has the configuration $t_{2g}^6 e_g^1$, carrying a net spin of 1/2 due to the unpaired electron residing in the e_g-orbital. Both semiquinones can then couple either ferro- or antiferromagnetically as discussed above, leading to either a total spin of 3/2 or 1/2. Magnetometric techniques likely will not be able to tell us

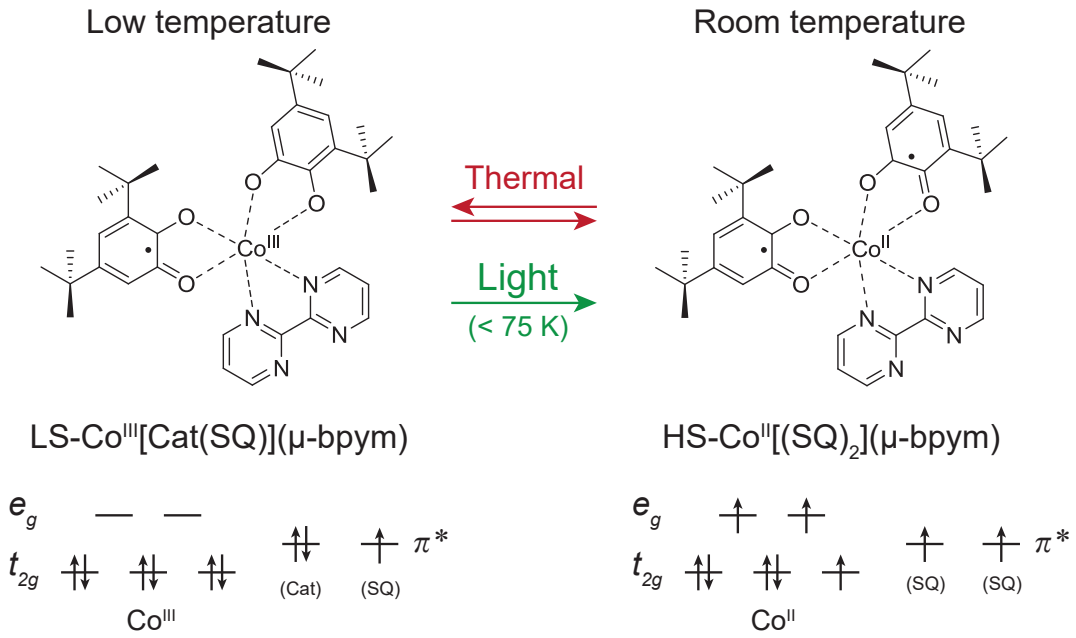

Fig. 4.3: Valence tautomerism in $[Co(3,5\text{-dbbq})_2(\mu\text{-bpym})]$. The molecule is in a high spin state at room temperature. When cooling down, one electron moves from the *d*-orbital of the Co^{II}-ion to the SQ ligand, which results in low-spin configuration. This effect is thermally reversible, and, with light, can be reversed below the LIESST temperature T_{LIESST}.

which of the two mechanisms are taking place, if the ground spin state is 3/2. Hence, in this study we will utilise ESR spectroscopy to conclude the states of the system. If the compound shows a LS-Co^{II} state at low temperatures, we can expect to see wide spectral features, with a total linewidth at the order of 100 mT. Furthermore, ESR spectra of LS-Co^{II} show a rich hyperfine spectrum due to the large cobalt nuclear spin of 7/2 [201]. Moreover, powder measurements on Co^{II} show a big variation of the g tensor, with values ranging between 1.8 and 3 [201–204], which are characteristic for d^7 systems [202, 205, 206]. The enhancement of g is due to second-order spin-orbit coupling [204]. On the contrary, if the ground state is LS-Co(III), we can expect a narrow ESR spectrum, with a linewidth at the order of 1 mT, from the semiquinone ligand. Typically, organic radicals show linewidths below 10 mT, and a g-values close to 2, as can also be seen later in Ch. 6.

It has been shown that the interconversion process can be reversed by photoexcitation below the light-induced excited spin-state trapping (LIESST) temperature T_{LIESST} [14], and thus offers an interesting experimental ground for the study of photoinduced effects on spin centres. Furthermore, it is reported that the interconversion process causes a contraction of the coordination sphere [187]. We note that T_{LIESST} has a double definition. Since LIESST complexes show similar photoexcitation characteristics in a $\chi_m T$-T-diagram, it is commonly accepted to define T_{LIESST} as the corresponding critical temperature, where one can trap the system in a photoexcited state for a reasonable time, for Co-VT complexes. We therefore stick to this notation.

Factors that influence T_{LIESST} should be found in the electrostatic environment of the metal ion. It is favourable to achieve large critical temperatures without the need of excessive cooling. In this work, we investigated how a small change in the crystal-field can affect the magnetic bistability and thus T_{LIESST}, which shall hopefully be beneficial to the design of molecules with desired properties.

4.4 Characterisation before photoirradiation

4.4.1 SQUID magnetometry

We started with a SQUID characterisation of a pellet sample made from crystalline material (5 mm diameter, 7.0 mg) to determine $T_{1/2}$. In order to avoid cracking, the pellet was sandwiched in between two glass platelets with 1 mm thickness, as shown in Fig. 3.21. The magnetic moment was recorded between 2 K and 300 K at a field of 5000 Oe both while cooling down and warming up. The temperature sweep rates were set to 0.5 K/min below 100 K, and 2.5 K/min above. The diamagnetic background of the glass platelets was measured independently and subtracted from the data.

It is convenient to regard the product of the molar magnetic susceptibility χ_m and the temperature T, since the $\chi_m T$-value is temperature-independent

for a purely paramagnetic system. The results are shown in Fig. 4.4. At 300 K, $\chi_m T$ reaches 2.41 emu K/mol, which corresponds to an effective moment of $\mu_{\text{eff}} = \sqrt{8\chi_m T} = 4.39\,\mu_B$. Such a value can be expected for Co^{II} in octahedral environment [178]. However, even at 300 K $\chi_m T$ does not reach saturation. In the following we will carry out an analysis on how the spin states relate to the determined magnetic moment. Pure spin-3/2 systems show $\mu_{\text{eff}} = \mu_B g\sqrt{S(S+1)} = 3.87\,\mu_B$ for $g = 2$, while spin-1/2 systems have $\mu_{\text{eff}} = 1.73\,\mu_B$. A ferromagnetic interaction between the semiquinones and the Co^{II}-ion ($7.33\,\mu_B$), even if it was in a low-spin configuration ($5.19\,\mu_B$), would exceed the measured value by far and can thus be excluded. An antiferromagnetic coupling between the semiquinones and the Co^{II}-ion in either configuration would lead to a smaller magnetic moment, $\mu_{\text{eff}} = 1.73\,\mu_B$. As none of the combinations matches the value measured, we can exclude that ferromagnetic coupling between the seminquinones take place, and suggest antiferromagnetic coupling instead. On the contrary, $\mu_{\text{eff}} \approx 4.5\,\mu_B$ is a typical value for pure HS-Co^{II} systems [185], so that we conclude that the paramagnetic properties are dominated by a HS-Co^{II}-ion, and the SQ ligands couple antiferromagnetically. We relate the found larger value to spin-orbit interactions, and reduced orbital momenta contribute to the magnetic moment [207, 208]. Therefore, Co^{II}-ions should not be treated with a spin-only model, and in the following we will see how the raised magnetic moment can be deduced, as demonstrated in Ref. [207].

High-temperature behaviour

The ground term of HS-Co^{II} is a ^4F-term, which is split by about 19 000 cm^{-1} from the first excited state ^4P. Due to the large separation, ^4P is not populated at room temperature, and only contributes via second-order spin-orbit coupling [207, 209]. In octahedral crystal-fields, the ^4F-term is split into $^4T_{1g}$, $^4T_{2g}$ and $^4A_{2g}$, separated by about 9000 cm^{-1} from each other. Thus, at room temperature, the triplet $^4T_{1g}$ with $L = 1$ is the only populated multiplet. Due to spin-orbit coupling, the $^4T_{1g}$-term is split into three multiplets $J = 1/2, 3/2, 5/2$, in this

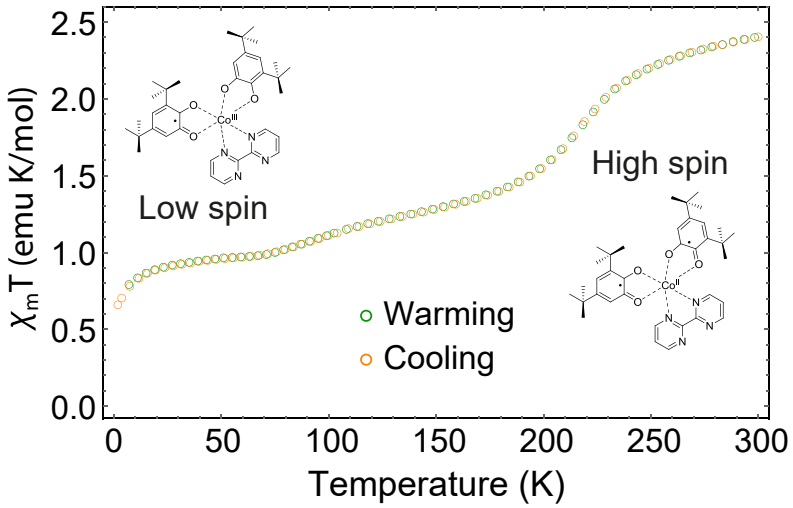

Fig. 4.4: SQUID characterisation of Co(3,5-dbbq)$_2$(μ-bpym) without irradiation. The graph shows the temperature dependence of the molar susceptibility of the VT. At 215 K, the molecule changes its spin configuration between high spin and low spin.

energetic order. By considering the orbital momentum, the Zeeman Hamiltonian becomes

$$\mathcal{H}_{\mathrm{Z}} = (-\alpha L + g_e S)\mu_B B\,, \tag{4.2}$$

where α corresponds to the total orbital reduction parameter [207]. The parameter $\alpha = \kappa A_\alpha$ has two contributions κ and A_α of different origins. The parameter κ, which ranges between 0 and 1, arises from the covalency of bonds between metals and ligands [207]. With increasing covalency, κ becomes lowered. The parameter A_α stems from admixtures between the $^4T_1$ states of the ^4F ground multiplet and the $^4T_1$ states of the excited ^4P multiplet, since they share the same symmetry relationships. With increasing ligand-field strengths, the admixtures becomes larger and, consequently, the orbital reduction increases. Values for A_α can be determined via electronic spectra, which is why one will find these two different parameters independently in literature. As a consequence of the orbital reduction, the spin-orbit coupling Hamiltonian becomes

$$\mathcal{H}_{\mathrm{SO}} = -\alpha\lambda \boldsymbol{L}\boldsymbol{S}\,. \tag{4.3}$$

Furthermore, the spin-orbit coupling parameter λ can be reduced compared to the free-ion value. The reduction depends on the covalency of the metal-ligand bonds, and is generally enhanced for heavier atoms from the third row and beyond, while it is minimally influenced by second row atoms such as nitrogen or oxygen.

In the end, the effective magnetic moment in saturation, i.e. at large temperatures, and at liquid-helium temperatures does not significantly depend on λ. It merely changes the slope of the temperature dependence. On the contrary, the reduction parameter α greatly influences the effective magnetic moment. Typical values for α range between 1 and 1.5 [207]. Hence, the magnetic moment of HS-Co^{II}-ions ranges between $5.22\,\mu_B$ and $4.65\,\mu_B$ at room temperature, as can be calculated from the Hamiltonian [207]. Our non-saturation value of $4.5\,\mu_B$ comes very close, and it can be estimated that it will fall into that regime at larger temperatures. Therefore, we conclude our room temperature magnetic properties to be due to HS-Co^{II} spin species.

Low-temperature behaviour

When cooling down, we observe a significant decrease between 190 K and 240 K, with its inflection at $T_{1/2} = 215\,\mathrm{K}$, followed by a more gradual decrease until it reaches a shoulder-shaped plateau at 70 K with $\chi_m T = 0.97\,\mathrm{emu\,K/mol}$ ($2.79\,\mu_B$). This observation indicates a phase transition from HS-Co^{II} to LS-Co^{III}, where the magnetic properties are now dominated by one SQ-radical. In contrast to reported Co-VT complexes [187], the value of the plateau does not correspond to the theoretical value of $0.38\,\mathrm{emu\,K\,mol^{-1}}$ ($1.73\,\mu_B$) for a typical spin-1/2 system. We expect this value when the magnetism is solely due to the SQ-radicals, since the LS configuration of Co^{III} is diamagnetic. However, from the SQUID data alone we should not exclude the possibility of an HS-LS spin-crossover process, which would yield a spin-1/2 ground state as well. As will be seen later from ESR results, we can tentatively exclude that spin-crossover is happening.

There is no possible combination of effective magnetic moments of states that

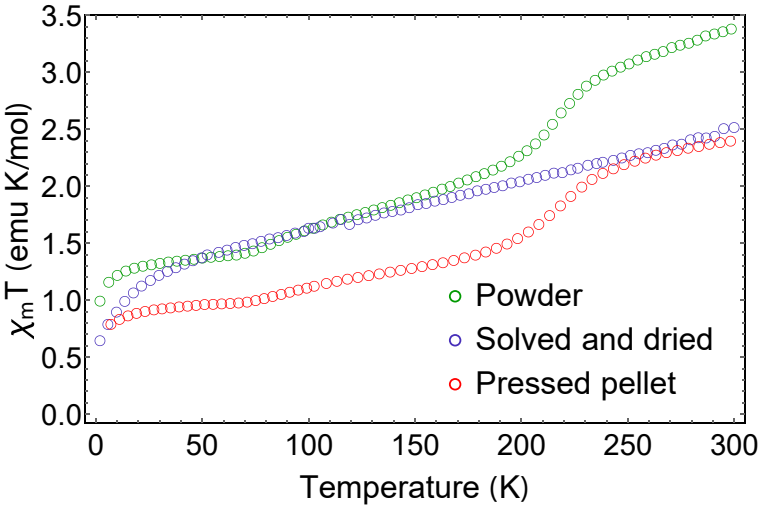

Fig. 4.5: $\chi_m T$ for different sample preparations. The powder data shows intriguingly high values, probably because of mass uncertainty. Furthermore, the VT effect is enhanced because of the smaller internal pressure compared to the pellet sample. A first dissolved sample in dichloroethane and later dried on a glass platelet shows deterioration of the signal, where no VT features can be observed.

is able to explain the measured behaviour, assuming that the sample has a pure ground state. From the data it seems that the HS-LS conversion is incomplete and we might have to deal with residual HS-Co^{II} impurities. In fact, the possible presence of HS-Co^{II} impurities leading to higher magnetic moments has already been observed and discussed [185], although to a lesser extent than observed here. These could potentially couple ferromagnetically with the SQ π^*-electrons [186]. Furthermore, rearrangements of charge distributions may happen at long timescales [185]. Fast charge transfer processes between the quinone ligands may appear resulting in a distribution pattern of semiquinone and catecholate ligands amongst the sample, resulting in different magnetic moments depending on temperature sweep rates [185]. A faster temperature sweep rate with fewer data points could possibly reduce this problem. When reducing the temperature below 10 K, another sharp drop of $\chi_m T$ can be observed, where $\chi_m T$ falls below 0.9 emu K mol^{-1}. We attribute this observation to antiferromagnetic interactions between the spins of the SQ-radicals as discussed for a similar Co-VT complex in Ref. [185].

Throughout this experiment, we did not observe any thermal hysteresis. Even after several temperature sweeps between 2 K and 300 K, the cooling-down and warming-up curves overlap and no deterioration of the magnetic moment was observed. We therefore conclude that the VT process is fully reversible in our complex.

Dependence on sample preparation

One intriguing observation was found in the magnetisation data of loose crystalline powder (mass $m = 2.9\,\mathrm{mg}$ prepared in a gelatin capsule), shown in Fig. 4.5. It is theoretically possible that the increased values are due to magnetic torques in the magnetic field, as the sample was not fixed firmly inside the capsule. More likely, however, are errors in the determination of mass. Due to the low mass, we can estimate an error of up to 30 % (1 mg). In fact, not shown here, rescaling the powder data overlaps with the pellet data very well. To create a thinner and more homogeneous sample, we dissolved the complex in dichloroethane and dried a droplet of the solution on the glass platelet. However, the VT feature vanished completely. This observation agrees with the fact that VT is a very sensitive mechanism, which is greatly influenced by the molecular environment [210–212]. The most likely explanation for this is that the sample did not survive the solution process. We assume that the sample had undergone a chemical reaction in that solvent, or dissociated and did not recrystallise after drying the sample.

4.4.2 ESR spectroscopy

Magnetometric measurements often suffer from background effects as practically all parts of a samples contribute to a total magnetic moment. In contrast, ESR spectroscopy represents a more selective method, where we may conveniently record the LS-HS conversion by measuring the spin signal. Owing to their fast spin-lattice relaxation times at room temperature, HS-$Co^{II}(SQ)_2$ is ESR-silent and thus undetectable. On the contrary, spin signals from semiquinones can be

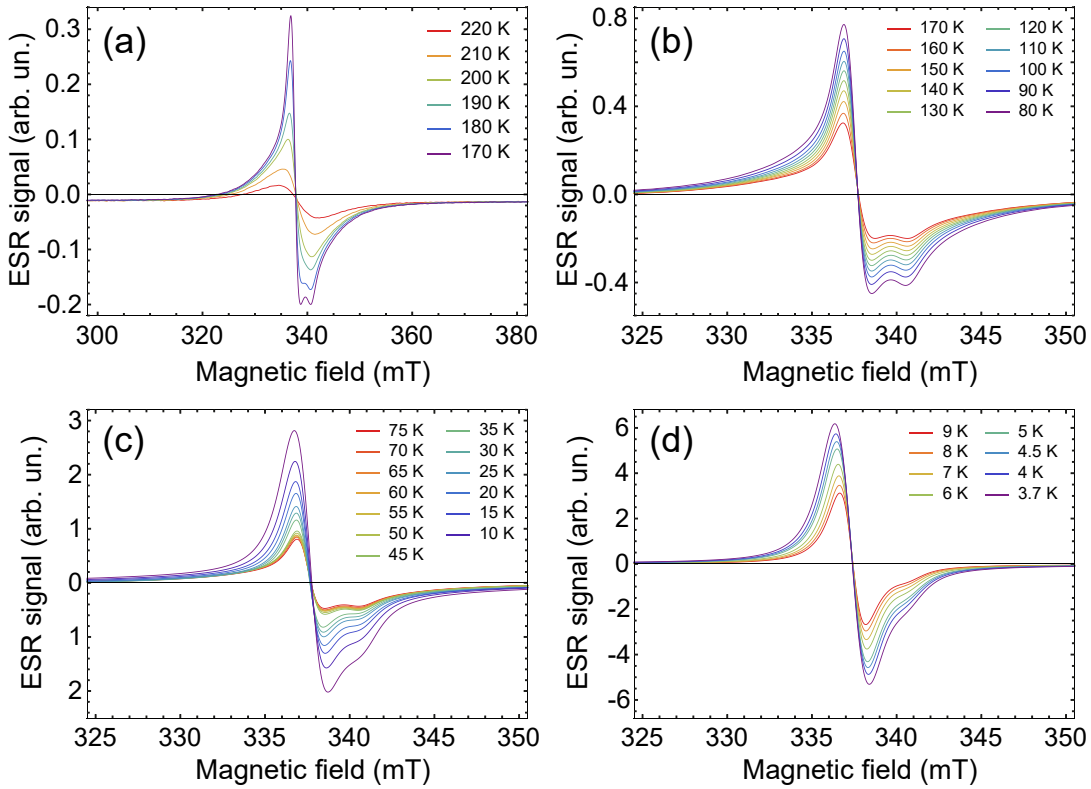

Fig. 4.6: ESR spectra of the Co-VTs between 220 K and 3.7 K. All measurements were taken at the same microwave power. The first signature of SQ can be obtained at 260 K, which is not shown here since a smaller attenuation would have been necessary to obtain a signal above the noise floor.

measured, if present, and thus determine the conversion process happening in our complex.

ESR spectroscopy was conducted at X-band frequency (9.48 GHz) between 3 K and 300 K on the Bruker EMX system. The sample (mass $m \approx 0.2$ mg) was prepared in an open 4 mm diameter polycarbonate capsule, as depicted in Fig. 3.22. The temperature-dependent ESR spectra are shown in Fig. 4.6. At room temperature, the sample does not show any ESR signatures. When cooling down, the first ESR feature appears at 260 K at a field of 3385 G ±10 G, which can be fitted with an isotropic g-value $g_{\text{iso}} = 2.006(6)$. Since we find g-values that are close to 2 and linewidths that are at the order of 2 mT, we attribute the measured spectra to transitions within the SQ-Cat ligand, which can only be present in the LS state. Hence, we can conclude that our complex shows valence tautomerism,

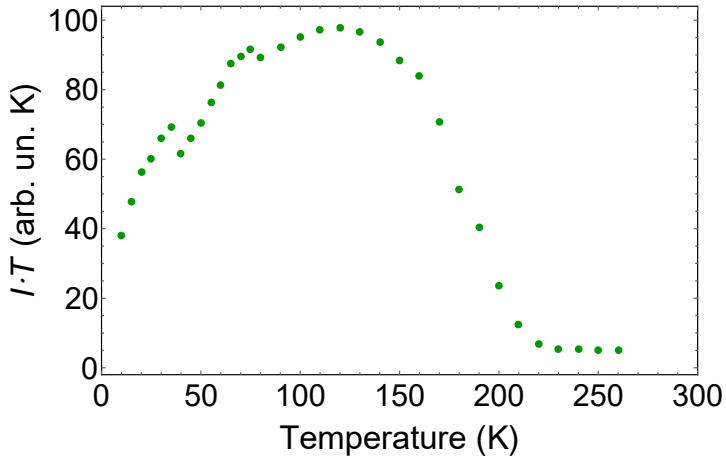

Fig. 4.7: ESR-intensity temperature product against temperature. Overall, the signal becomes stronger with decreasing temperature. The interconversion, starting at 260 K and reaching a maximum between 100 K and 150 K, can be well observed. The kink around 40 K likely stems from recalibration of the apparatus.

and not spin crossover. When cooling down to 170 K, the signal increases due to the formation of catecholate groups and splits up into two minima, where the first one corresponds to a resonance at 3376 G ±1 G. Interestingly, the intensity of the first minimum increases relative to the second minimum when cooling down to 3.7 K. No spin-1/2 signal can be observed at room temperature which indicates a complete HS state.

In Fig. 4.7 the ESR intensity I was multiplied with the temperature T, and displayed against T. The diagram indicates a broad interconversion process in agreement with our SQUID results. When cooling down from room temperature, the interconversion begins significantly at around 230 K and peaks at 120 K. The measurements may thus suggest a lower $T_{1/2}$ of about 175 K. For spin-1/2 species and temperatures above 4 K, the intensity scales with the inverse temperature [213], assuming Boltzmann population of states. A non-zero constant horizontal line would therefore indicate pure Boltzmann behaviour. One could claim that, within experimental errors, this is the case between 60 K and 80 K, which would then fall in line with SQUID results, but it is not very convincing. Similar to the $\chi_m T$ curve, IT decreases upon further decreasing the temperature. The reduction

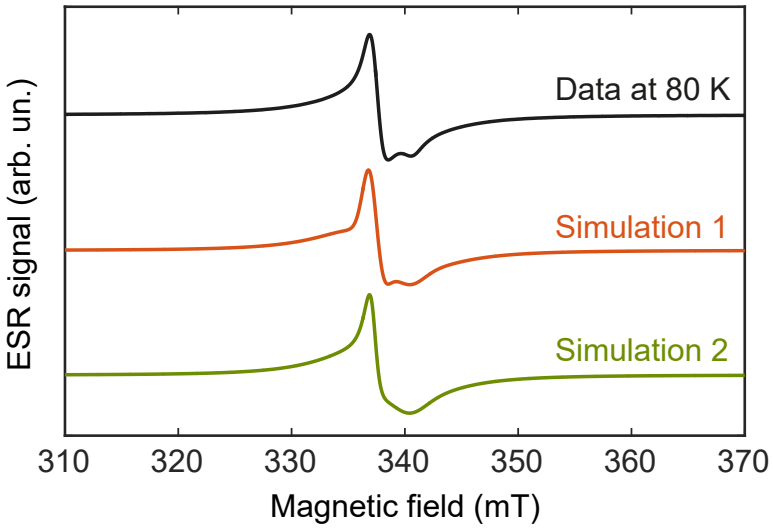

Fig. 4.8: Simulation of the Co-VT ESR spectrum at 80 K. The black line represents the measured ESR spectrum. The orange curve shows a simulation with Gaussian broadening of the central peak, while a Lorentzian line shape function was used for the simulated curve in green. In both simulations, the broad background signal was reproduced with a Lorentzian function.

below 60 K can be attributed to antiferromagnetic exchange interactions between the radical spins, as it has been observed for many similar valence tautomeric complexes, and is discussed in Ref. [185]. Overall, the ESR observations agree with our measurements obtained on the SQUID magnetometer, although we determined $T_{1/2}$=215 K for the HS-LS interconversion before.

Low-temperature data can be fitted with g-anisotropy and a g_z-strain of 0.015, which corresponds to a Gaussian distribution of g_z. An exemplary simulation of the 80 K ESR spectrum is given in Fig. 4.8. We simulated the spin-1/2-signal both with a Gaussian and a Lorentzian lineshape, displayed with an orange and green curve, respectively. The simulations were performed with $g = (2.0088(12), 2.0088(12), 1.989(12))$. Main error is the uncertainty of the magnetic field. Intriguingly, in the simulation we had to include an additional Lorentzian-shaped lineshape with $g_{\mathrm{iso}} = 2.0023(12)$ and 6 mT linewidth, which we ascribe to unresolved hyperfine couplings from the metal ion and impurities. The Lorentzian lineshape function is able to describe the broadening more accurately. However, the Gaussian lineshapes

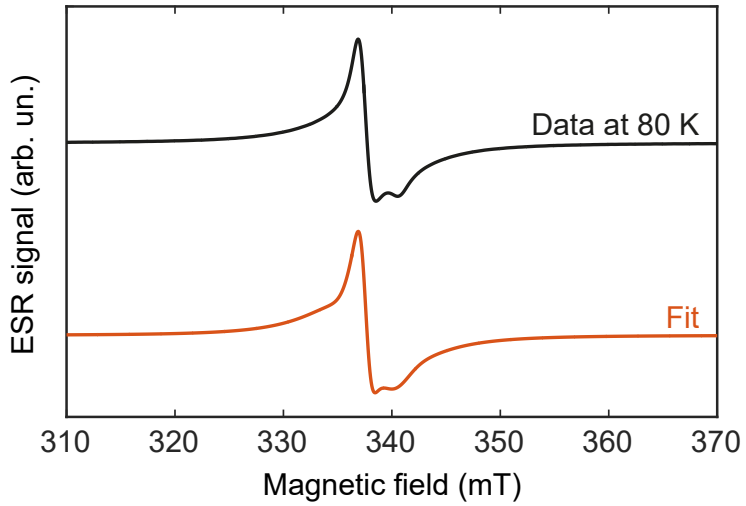

Fig. 4.9: Fitting of the Co-VT ESR spectrum at 80 K. The black line represents the measured ESR spectrum. The orange curve shows the best fit with Gaussian broadening of the central peak and additional Lorentzian background.

are able to resolve the two local minima. A Voigtian function, which corresponds to a convolution of a Gaussian and Lorentzian lineshape function, did not improve the quality of the simulation. Since we are interested in spectral features, we concluded that the Gaussian lineshape is the best choice for a fit of the spectrum, shown in Fig. 4.9. The fit reproduces our spectrum very well. Using the simulation parameters as starting values, we obtain $g = (2.0113(12), 2.0071(12), 1.9904(12))$ and 0.58 mT ± 0.09 mT peak-to-peak linewidth. Main error here is the field uncertainty of the X-band magnet, which turned out to be larger than the error of the fit. Furthermore, strains, which correspond to a distribution of the corresponding spin Hamiltonian parameters, of the g-tensor were obtained as $g_{\text{strain}} = (0.0119(2), 0.0045(6), 0.0167(2))$. The isotropic g-value can be calculated as $g_{\text{iso}} = \sqrt{(g_x^2 + g_y^2 + g_z^2)/3} = 2.0028(12)$, which comes close to the value of the free electron. For the additional isotropic Lorentzian signal we determined $g_{\text{iso}} = 2.0040(12)$ and 5.81 mT ± 0.01 mT linewidth. Moreover, both signals have a similar temperature dependence, when we correct for the Boltzmann population of states. However, we cannot rule out that impurities lead to the observation of a second minimum, which flatten out at temperatures below 10 K. At those

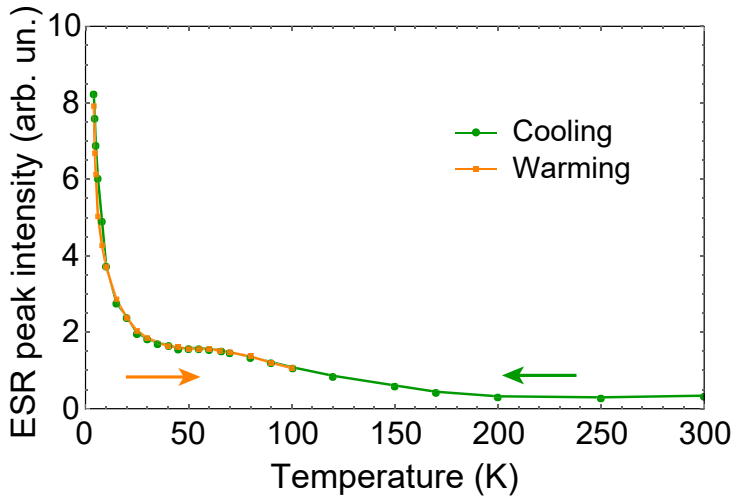

Fig. 4.10: Temperature dependence of the ESR signal intensity. The intensity was obtained from summing the peak maxima and minima. Both the warming up and cooling down curves overlap, which indicates that no thermal hysteresis is present.

temperatures, the ESR signal shape can be described by isotropic Lorentzian functions.

To gain an idea on possible light-switching mechanisms, the intensity is displayed against the temperature in Fig. 4.10. Since all spectral components show a similar temperature dependence, it is valid to analyse the peak maxima and minima. The temperature dependence looks similar to the $\chi_m T$ curve. Below 260 K, the signal intensity starts to increase until it reaches a plateau at around 70 K. Below 50 K, when the interconversion is complete, the intensity shows an exponential increase that we ascribe to the Boltzmann population of states. Furthermore, we did not observe any notable differences between warming up and cooling down, in agreement with our SQUID results.

4.5 Investigation of photomagnetic properties

It is reported that, after cooling down, Co-VT complexes show a photoswitching effect, where visible light excites the complex back to its original HS state [14]. This phenomenon can only be observed below a blocking temperature T_{LIESST} and is accompanied with an expansion of the coordination-sphere [187]. After excitation, the photoexcited metastable HS state can be maintained for a long time, a duration which can range between several minutes to several days, depending on the temperature [188]. The related thermal relaxation mechanism can be described via an Arrhenius law:

$$\tau = \tau_0 \exp(\Delta / k_B T)\,, \tag{4.4}$$

with τ the relaxation time, τ_0 the inverse attempt frequency, Δ the energy barrier, k_B the Boltzmann constant and T the temperature. As we shall see, the relaxation time does not get infinitely long for $T \to 0$. Temperature-independent relaxation via quantum tunnelling plays a role and sets the upper limit for the relaxation time at low temperatures. In the following, we will demonstrate how we investigated the photoswitching via SQUID magnetometry and ESR spectroscopy, and how we analysed relaxation effects.

4.5.1 SQUID magnetometry

All measurements under irradiation of light were carried out using the setup described in Sec. 3.3. For this experiment, we used a green (532 nm) diode laser with 15 mW maximum output power. Although the choice of this particular wavelength was made for economic reasons, Co-VTs typically absorb all wavelengths in the visible regime. Behind the single-mode fibre ending, the light shows a perfect Gaussian profile. Before inserting the sample holder into the magnetometer, we measured the light intensity that hits the sample. We then ranged the intensity between 0.2 mW and 5.4 mW by using a set of ND filters.

In the scope of photomagnetic measurements, low conversion efficiencies are

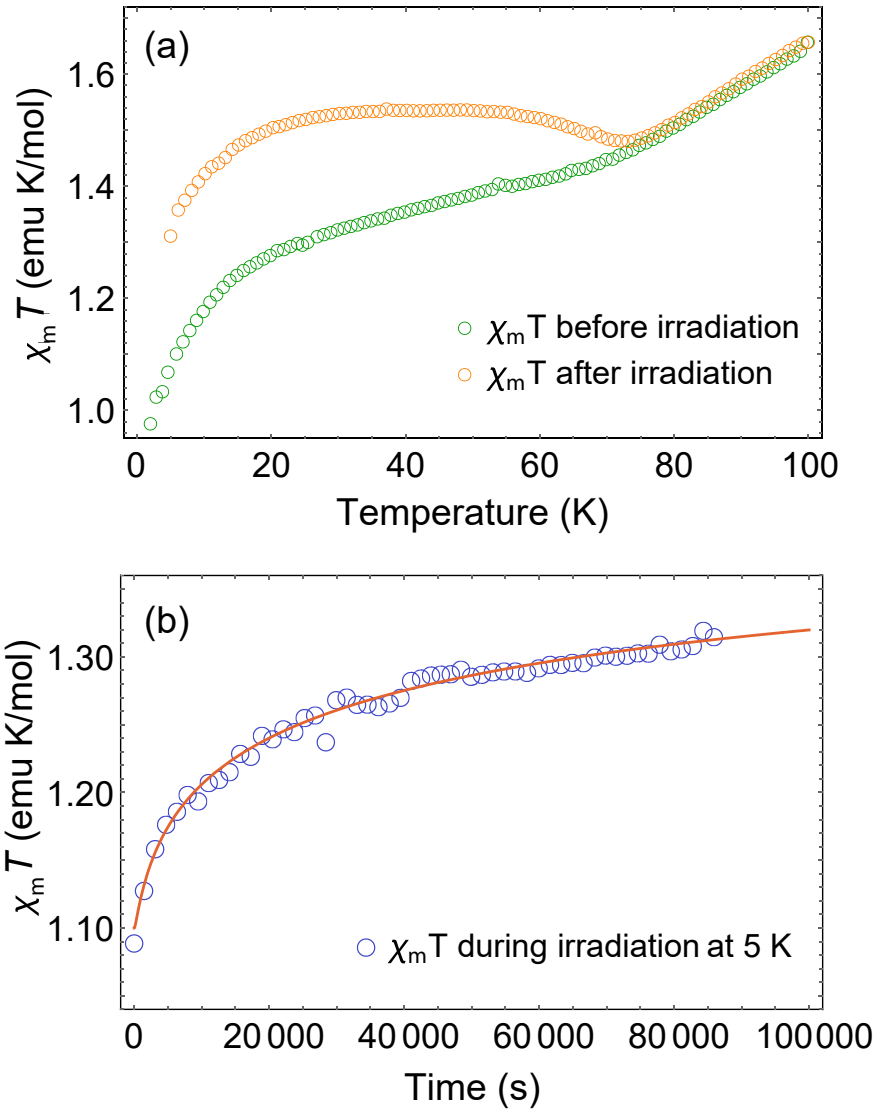

Fig. 4.11: Photomagnetic properties of the Co-VT complex. (a) Temperature dependence of $\chi_m T$. After irradiation at 532 nm for 24 h at 5 K, the magnetic moment increases due to a LS-to-HS transition. (b) Time-evolution of $\chi_m T$ during light irradiation at 5 K.

a common issue. Our sample itself shows a very dark, black colour. Therefore, its extinction coefficient is relatively large. In order to maximise the conversion efficiency, thin samples are of crucial importance. We therefore attempted to make the pellet as thin as possible, and careful handling was required in order to avoid cracking. Due to its defined shape, quantitative measurements can best be carried out on a pellet sample. However, owing to the large pressure of 1.9 kbar applied during its production, the VT mechanism is partially quenched. The large internal

strain may compress the unit cell volume. If the expansion of the coordination sphere during the photoexcitation is not strong enough to compete with the strain, the interconversion cannot take place. A different approach involves dissolving and drying a droplet of solution on a glass platelet. However, as discussed before, it is reported that Co-VT complexes deteriorate in solution [186, 214]. This method is therefore not advisable. We found best conversion efficiencies on powder samples. In the sample preparation process, we gently pressed the powder ($m = 2.9\,\mathrm{mg}$) in the gelatin capsule, which formed a dust-like layer. However, the determination of the the mass can be troublesome. Furthermore, rearrangements, especially at higher temperatures, may take place in the magnetic field, and yield higher spurious susceptibilities. Possible rearrangements at low temperatures are less likely as the powder sample is less magnetic in the LS state. Furthermore, owing to the small mass, errors in the weighing process cannot be excluded. Therefore, a quantitative magnetisation analysis will not be presented for the powder sample.

After continuously recording the magnetic moment while cooling down to 5 K, we irradiated the sample at 532 nm wavelength for 24 h at a magnetic field of 5000 Oe. Overall, $\chi_m T$ increases by about 20 % from 1.10 emu·K/mol to 1.31 emu·K/mol, which corresponds to an efficiency of 20 %. After the irradiation, we recorded the magnetic moment while warming up at a rate of 0.5 K/min. As shown in Fig. 4.11a, the photoexcited state can be observed up to about 75 K. The critical temperature T_{LIESST}, defined as the temperature where $\partial^2\chi_m/\partial^2 T = 0$ [215], can thus be obtained as 68 K. This value falls in the range of typical critical temperatures, between 38 K and 80 K, of Co-VT complexes [91]. More interestingly, the value is about 25 K higher than the one of the similar Co-VT complex, reported in Ref. [187], which is coordinated with 3,6-tert-butyl instead of 3,5-tert-butyl. This result underlines the sensitive nature of the VT process. A possible explanation for the higher T_{LIESST} will be given in Sec. 4.5.4 using DFT calculations. In conclusion, the photomagnetic measurements demonstrate that the complex undergoes a long-lived transition into a metastable HS-state at low temperatures.

Relaxation dynamics

Fig. 4.11b displays the time evolution of the magnetic moment during the irradiation. Even after 24 h of illumination, the photostationary limit has not been reached, indicating a long-lived photoexcited state. Since the increase of the magnetic moment $M(t)$ reaches a saturation point where relaxation and excitation are in equilibrium, the time evolution is phenomenologically described by a stretched exponential law, given as

$$M(t) = M_0 \exp(-(t/\tau_I)^\beta) \,. \tag{4.5}$$

Here, M_0 describes the starting magnetic moment before irradiation, τ_I the relaxation time and β the stretching exponent. It has been shown that this model well describes the relaxation of Co-VT complexes [216–218], and furthermore also SMMs [219] and spin glasses [220]. Intuitively, the stretching exponent can be understood as a distribution of relaxation times, which can be caused by heating, for instance. Heating is due to the excitation of phonons, which result from the absorption of light. Depending on how well the machine handles the resulting heat load, this leads to a significantly higher sample temperature, which is about 0.5 K per mW light power on the MPMS XL-7. After switching off the light source, the magnetic moment jumps to a higher value because of thermalisation. A more likely reason for the distribution of relaxation times can be found in variations of the internal strain. As the LS-HS interconversion process comes along with a change in volume, it can result in a distribution of strains and therefore less sharp relaxation behaviour.

The solid line in Fig. 4.11b represents the best fit of Eq. 4.5. For the fit we neglected the datapoints during the first 4.5 minutes of irradiation due to initial thermal instabilities in the sample chamber and nonlinear response after turning on the light source. At 5 K we determined a lifetime of $\tau_I = 25\,800 \pm 5000$ s, which corresponds to 7.2 h, and a critical exponent of $\beta = 0.48$. The measurement

during irradiation was corrected for the heating effect, which we estimated to $\Delta T = 2.45\,\mathrm{K}$ at 5.4 mW light power. The heating was derived from the fact that the last $\chi_m T$-value during irradiation has to match with the $\chi_m T$-value after switching off the light source.

Dependence on sample geometry

In principle, a complete photoconversion is desirable. The best conversion efficiency was obtained on a thin powder sample, owing to its high surface-to-volume ratio. The light penetration depth $I(z)$ is described by the Lambert-Beer law:

$$I(z) = I_0 \exp(-\varepsilon z)\,, \tag{4.6}$$

where z describes the depth, ε the extinction coefficient and I_0 the intensity. Due to a large ε, thin samples are desired. Fig. 4.12 shows the results on a pressed pellet sample. Measurements at a comparable laser intensity, but 90 min irradiation duration, yielded conversion efficiencies of about 5 %. On the one hand, a pellet offers a worse surface-to-volume ratio than a powder sample, and, as absorption mainly happens close to the surface, large parts of the sample remain unchanged. On the other hand, the lower yield can be explained by the internal pressure of the pellet, which can be as large as 1.9 kbar, which was applied in the fabrication process. Thus, the VT mechanism becomes partially quenched.

Nevertheless, pellet samples offer the possibility to investigate the effect of laser intensity displayed in Fig. 4.12b. The increase of $\chi_m T$ at 20 K scales nonlinearly with the laser power due to the Lamber-Beer law. As can be seen, laser powers beyond 2 mW only marginally increase the conversion. The maximum applied laser intensity that could be handled by the system was 5.4 mW. Higher powers result in strong heating of the sample and are thus counterproductive. Therefore, improvements in conversion can only be achieved via ideal sample preparation.

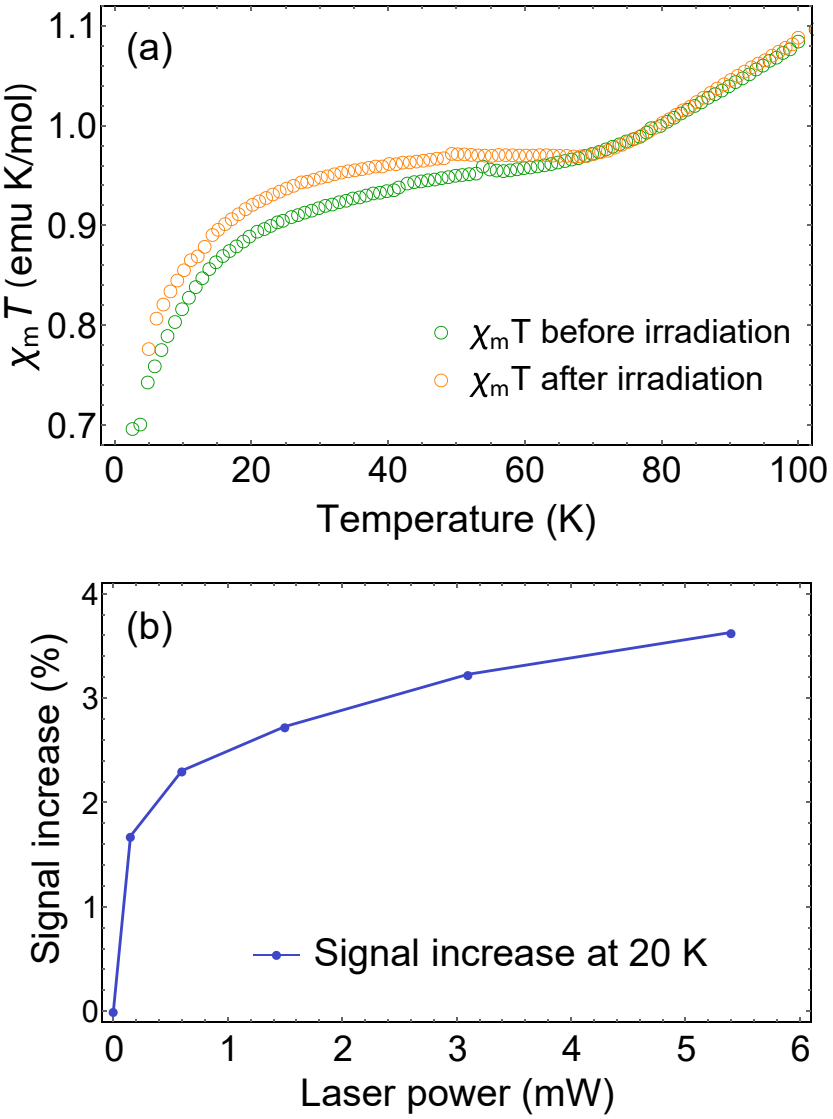

Fig. 4.12: Photomagnetic properties of the pellet sample. (a) Temperature dependence of $\chi_m T$ versus temperature. After irradiation at 532 nm for 90 min at 5 K, the magnetic moment increases due to an LS-to-HS transition. The increase is significantly worse compared to the powder sample (b) Dependence of the increase of $\chi_m T$ at 20 K for different laser powers.

Further observations

After the photoexcitation at 5 K, one can observe a kink in the $\chi_m T$ curve around 12 K when warming up. In fact, this kink is also visible in the 3,6-tert-butyl derivate [187], but it has not been discussed yet, and its origin is unclear.

The most advantageous property of the sample is its full thermal reversibility. After re-heating to room temperature, and cooling down again to 5 K, the sample shows its original magnetic behaviour. Therefore it survives temperature cycles, favourable for nanoelectronic devices. However, we noticed that the magnetic moment is not fully stable in time. Leaving the sample in the external magnetic field for several days might change its magnetic moment by up to 10 %. This effect is also reversible. By warming up to room temperature and removing the external field, the sample slowly regains its initial magnetic moment. This phenomenon could be attributed to the different trapping patterns of the charged ligands, as it has been discussed in Ref. [185].

4.5.2 ESR spectroscopy

Generally, ESR spectroscopy features a higher sensitivity compared to the SQUID magnetometer, and the setup shows a better thermal stability. For measurements under irradiation, we used the same setup and sample preparation described in Sec. 4.4.2. In contrast to SQUID measurements, we can bring the fibre close to the sample, so that no collimation optics are required. Therefore, the fibre was fixed at a distance of 4 mm from the powder sample ($m \approx 0.2$ mg). In order to conduct wavelength-dependent studies, we illuminated the sample with the LOT-QuantumDesign xenon lamp. To come close to the SQUID results, a 532 nm bandpass filter with 10 nm bandwidth was used. For wavelength-dependent investigations, a set of bandpass filters between 400 nm and 850 nm in 50 nm increments and 40 nm bandwidth was available. Prior to inserting the sample into the ER 4102ST resonator, the intensity after the fibre was calibrated with various filters after a 2 h warm-up time. For comparison, the power at 532 nm was approximately

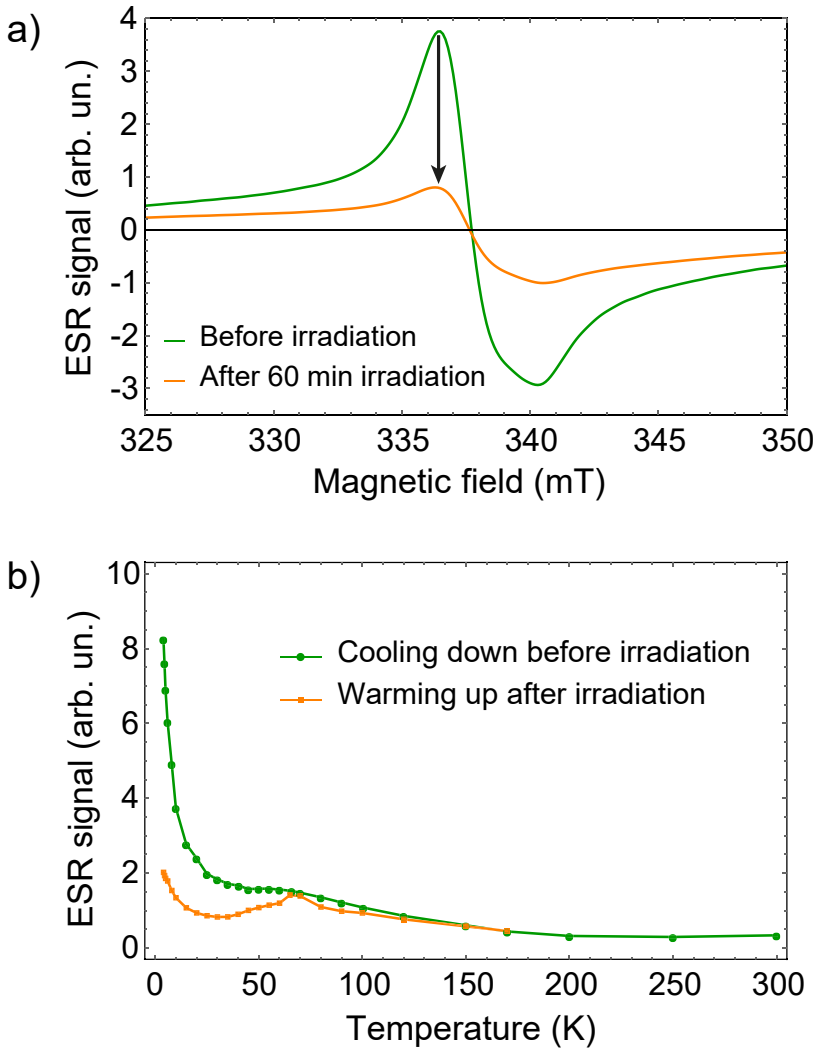

Fig. 4.13: ESR signal before and after irradiation. (a) The spin-1/2 ESR signal decreases upon illumination (532 nm, 1.5 mW, 3.5 K) since the HS-state is ESR-silent. (b) The diagram shows the ESR signal intensity against the temperature before (green) and after (orange) irradiation at 3.5 K. The curve after irradiation goes back to the original ground state one at 70 K, which we identify as the critical temperature T_{LIESST} for the LS-HS interconversion.

1.5 mW. Furthermore, the capsule was well contacted with the quartz glass tube in order to ensure good thermal conductivity. Since the cooling power of the ESR910 cryostat is naturally stronger than the one of the SQUID, light-induced heating can be better handled and is thus neglected here.

The sample was irradiated for 60 min at 532 nm at a chosen temperature of 3.5 K, where the glass cryostat shows a strong thermal stability. Since the HS-

state is ESR-silent [218], we can take the signal decrease upon illumination as a measure for the LS-HS conversion. The evolution of the ESR-signal intensity during irradiation is shown in Fig. 4.13. The signal-strength decrease indicates a conversion efficiency of 75 %, much higher than obtained after 24 h irradiation on the SQUID magnetometer (at 5.4 mW). We attribute the higher efficiency to the greater overall surface-to-volume ratio of the powder sample, as less sample is required due to the greater ESR sensitivity.

When warming up after blocking the light, the ESR signal decreases until 25 K and from thereon increases until 70 K, where it retrieves its original signal intensity before illumination. With increasing temperature, the ESR signal follows its original path as also observed on the SQUID magnetometer. The decrease until 25 K is partially due to depopulation of states explained by the Boltzmann distribution. Additionally, antiferromagnetic interactions discussed in the SQUID analysis section might play a role. When increasing the temperature further, thermal relaxation competes with the experimental time scale leading to a growing amount of LS-species.

Relaxation dynamics

In order to gain an understanding for the relaxation processes in the sample, we measured the time evolution of the ESR signal at different temperatures, displayed in Fig. 4.14 and Fig. 4.15. The sample was first illuminated for 60 min, and then the signal recovery was recorded in the subsequent 60 min. To account for both thermal assimilation and relaxation after switching off the light, the relaxation behaviour needs to be fitted with a sum of two exponentials:

$$I(t) = I_0 - I_1(0)\exp(-t/\tau_1) - I_2(0)\exp(-t/\tau_2)\,, \tag{4.7}$$

where I_0 corresponds to the saturation ESR signal, and τ_i to the characteristic relaxation times for the two processes involved, and their corresponding parts

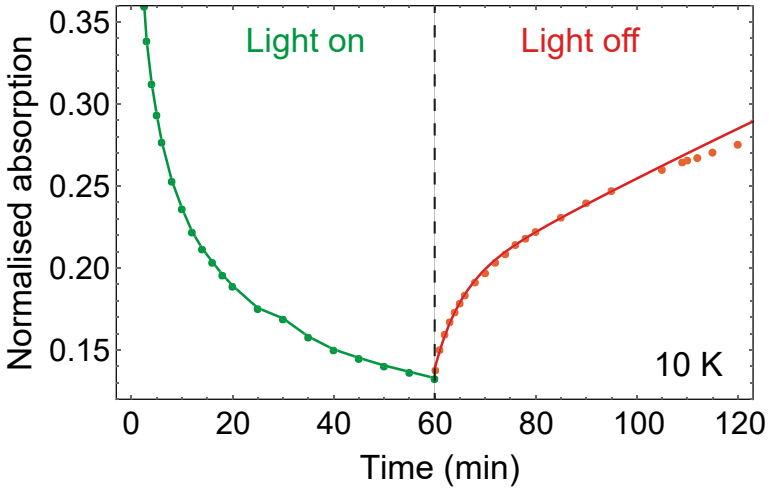

Fig. 4.14: Normalised ESR signal strength during and after irradiation at 10 K and 532 nm. The shown fit after switching off the light is based on a sum of two exponentials.

in the relaxation process $I_i(0)$. By fitting we found that one τ_i-value, τ_2, lies in the $10^2 - 10^3$ s regime, which we identify as the thermalisation constant. This allows us to identify the other, significantly longer τ_i-value, τ_1, as the characteristic relaxation time of the HS-LS backconversion.

By assuming that thermal relaxation (Eq. 4.4) plays the dominant role, we plotted τ_1 against the inverse temperature 1/K in a logarithmic diagram Fig. 4.15b. For thermal relaxation, the model follows a non-horizontal line, where its slope corresponds to the energy barrier. In Fig. 4.15b we can identify two regimes, a high temperature regime that follows the Arrhenius law, and a low temperature regime below 20 K, which is nearly temperature-independent. By fitting Eq. 4.4, we determined an energy barrier of $\Delta = 65.14\,\mathrm{K} \pm 8.25\,\mathrm{K}$ and an inverse attempt frequency of $\tau_1(0) = 1005\,\mathrm{s} \pm 391\,\mathrm{s}$. The found energy barrier comes close to T_{LIESST} determined via SQUID magnetometry. Furthermore, we attribute the low-temperature relaxation to quantum tunnelling relaxation, which sets the upper limit for relaxation. Here we find a tunnelling rate of $3.46{\cdot}10^{-5}\,\mathrm{s}^{-1}$, which corresponds to a lifetime of $28\,900\,\mathrm{s} \pm 100\,\mathrm{s}$. The lifetime roughly agrees with the value determined via SQUID magnetometry. Reported values for the quantum

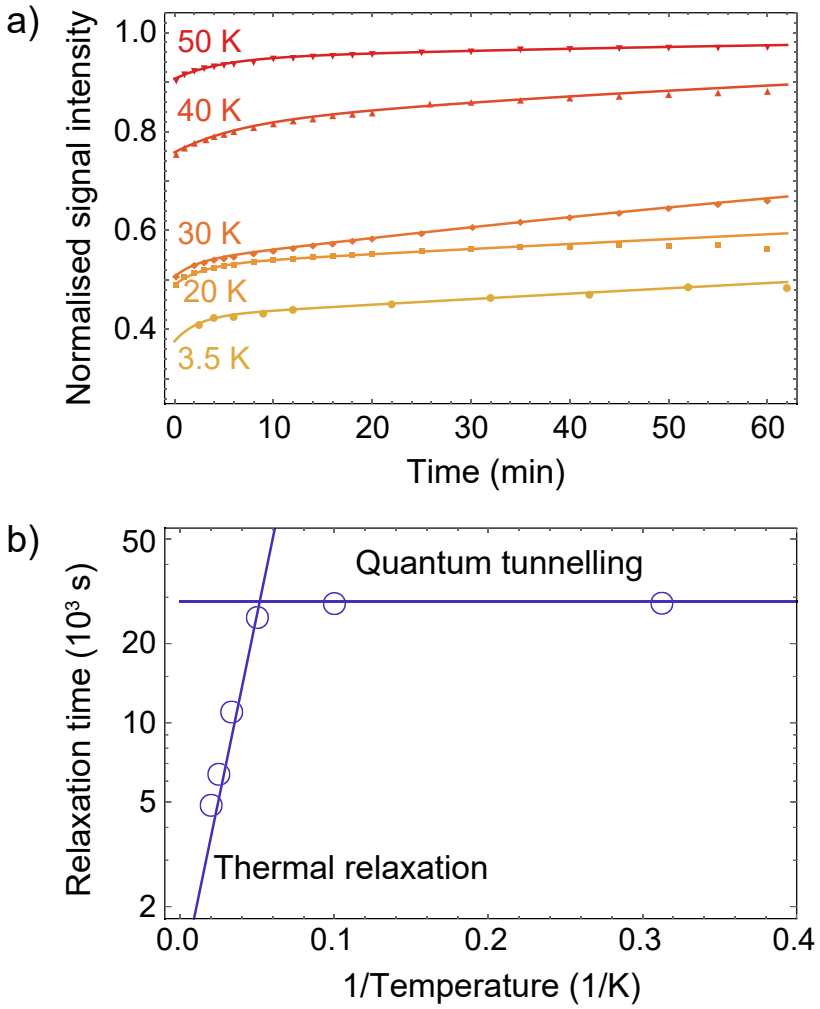

Fig. 4.15: Relaxation behaviour of the photoexcited HS-state. (a) Relaxation for different temperatures after 60 min irradiation at 532 nm. The curves correspond to a double-exponential fit to account for thermal assimilation and relaxation. The exctracted relaxation times are displayed against the inverse temperature in (b). We identify a thermal relaxation regime at higher temperatures that follows an Arrhenius law, and a temperature-independent low-temperature regime which we ascribe to quantum tunnelling induced relaxation.

tunnelling barriers for Co-VT complexes fall in the 10^4-10^5 s regime [217], which means that our complex competes with state-of-the-art possibilities.

4.5.3 Investigation of backswitching

There are reports on possible photoinduced backswitching mechanisms using blue or UV light [91, 221]. While 532 nm light drives the metal-to-ligand charge-transfer (MLCT), infrared light such as 850 nm could possibly reverse it (LMCT). Our Co-VT shows wavelength-dependent absorption bands (Fig. 4.16). Using the xenon lamp and the same setup, we therefore investigated what happens when we irradiate the sample at wavelengths other than 532 nm. The general idea is to first bring the system into the HS state at cryogenic temperatures using 532 nm light, and, subsequently to change the wavelength. The result after such a sequence is shown in Fig. 4.17b. We conducted the experiment at a temperature of 3.75 K to ensure a long relaxation time. In order to prepare the HS-state, we irradiated the powder for 70 min at 532 nm and 1.5 mW, and arrived at 86% conversion. For maximum effects, we chose to illuminate with the highest available power at 850 nm, 7.0 mW. In fact, we did not observe any backswitching, but, instead, the conversion was enhanced even further. As can be seen from Fig. 4.17, the efficiency rises up to 97.5% after 30 min. Such a high conversion rate has not yet been reported so far. The UV/Vis/NIR spectrum displayed in Fig. 4.16 shows a similar absorption efficiency for 532 nm and 850 nm light. However, the intensity of the infrared light was about 5 times higher, which contributes to the higher yield. In fact, it is favourable to use larger powers at potential de-excitation wavelengths. Otherwise, a decrease in HS species due to quantum tunnelling or thermal relaxation can be misinterpreted as being caused by the infrared light. Overall, this result indicates that the compound cannot be switched back at near-infrared wavelengths.

Using this as a new starting point, we then irradiated the sample at 400 nm. The idea is to check whether 400 nm light also drives the LS→HS transition, or whether it is able to induce backswitching from HS to LS. Due to poor emission

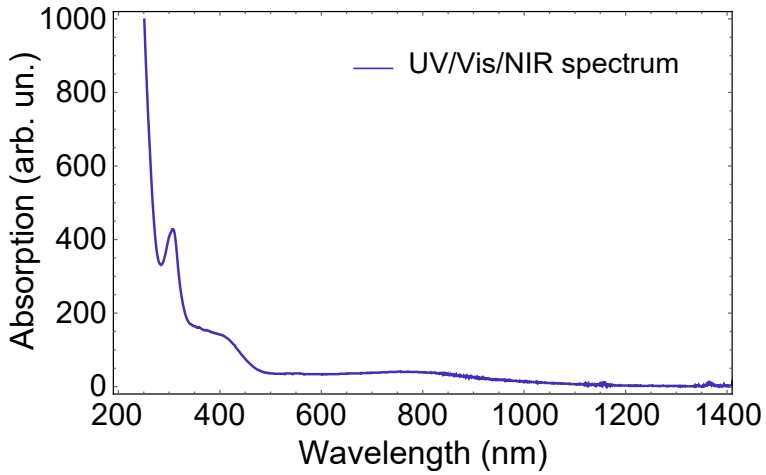

Fig. 4.16: UV/Vis/NIR spectrum of our Co-VT complex. The spectrum shows a broad absorption band in the visible regime, on which we can perform wavelength-dependent studies. The data was obtained by Ralph Hübner on an UV 160 (Shimadzu) spectrometer at room temperature between 200 nm and 1500 nm. The sample was prepared in a quartz glass HELMA cuvette of 10 mm thickness.

of xenon lamps at lower wavelengths, the maximum attainable power was 2.0 mW. During illumination, one can observe an increase in LS-species. It has to be carefully interpreted, since at such a large HS-fraction relaxation competes with the excitation process. When turning off the light source, the de-excitation happens faster, as the relaxation curve is steeper than in the case of irradiation with blue light. This can also be seen in the sudden kink after switching off the light source at 77 min in Fig. 4.17b. We identify two reasons for the generation of LS-species using blue light. First, the lower power is not large enough to maintain the nearly 98% conversion obtained at 7.0 mW infrared light. Second, it could be that the interconversion happens less likely at lower, and more likely at higher, wavelengths, which can be seen in the stronger HS-population with near-infrared light. It is likely that electronic absorptions of different origins compete in the blue region, a phenomenon which may be related to the cobalt-ion. A third possibility for the generation may be the lower penetration depth of blue light. In conclusion, we are not able to switch the Co-VT back to its original LS-state using light.

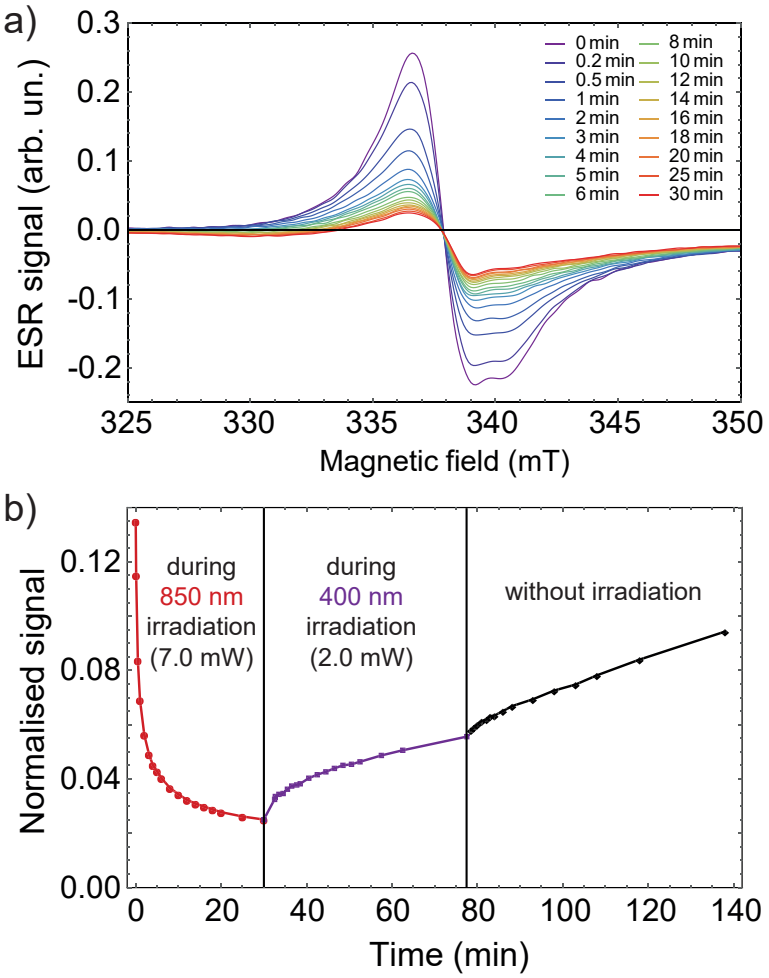

Fig. 4.17: Time evolution of the ESR signal with and without light at different wavelengths. (a) ESR signal during irradiation at 850 nm and 3.75 K for 30 min. (b) Evolution of the ESR signal strength when first irradiating at 850 nm for 30 min, then at 400 nm for another 30 min, and finally when turning off the light source.

4.5.4 Comparison of the critical temperature

Our Co-VT complex shows a much higher critical temperature T_{LIESST} than its 3,6-dbbq derivate reported in Ref. [187]. The reason for this can be found in the higher activation energy barrier for thermal relaxation. Using DFT calculations, we want to investigate the molecular changes that happen in the interconversion process, so that we can better understand the higher energy barrier.

The upper group in Tab. 4.1, which corresponds to the coordinating atoms, shows a drastic bond length change of 0.184 Å on average. In contrast, the 3,6-tert-butyl analogue shows an expansion of 0.16 Å in its coordination sphere. The larger bond length change in our sample could be related to a larger energy barrier for thermal relaxation and thus explain the approximately 25 K higher value of T_{LIESST} found in our Co-VT.

4.6 Outlook and Perspectives

Having characterised all properties of the shown Co-VT, the next step would certainly entail either device integration or chemical grafting to known magnets. Providing two additional nitrogen-binding sites is very advantageous for chemical engineering. By combining an SMM with our Co-VT-complex as exemplarily depicted in Fig. 4.18, one could think of using the photoactive property of the Co-VT to change the overall magnetic state. As we have seen in Ch. 2.1, small changes in the environment of the SMM can have significant effects on the magnetic properties. For instance, the relaxation dynamics and magnetic anisotropy can be affected. However, the synthesis is likely a challenging part. Since SMMs have already been tested in nanospintronic devices, combining Co-VT with SMM could yield new possibilities of control, where light is used as a non-invasive and clean technique. The here employed investigations work well and can be used as a basis to investigate photoswitching effects in SMMs, which are presented in the next chapter.

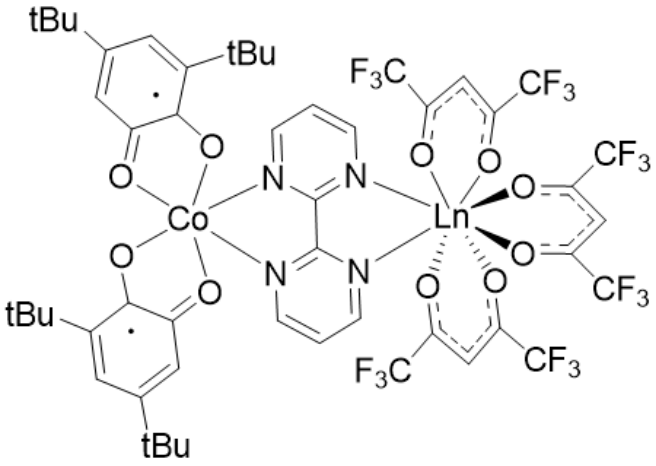

Fig. 4.18: A Co-VT-SMM complex. Using bipyrimidine as bridging ligand, one could graft a bipyrimidine-based SMM on the investigated Co-VT complex. The synthesis of this molecule could open the way for a new family of photoswitchable molecules.

4.7 Summary

In this study we have presented a full magnetic characterisation of a new cobalt valence tautomeric complex. We used SQUID magnetometry and ESR spectroscopy to fully characterise the dark and photomagnetic properties. The complex undergoes a high-spin to low-spin transition when cooling down from room temperature. This interconversion can be reversed at cryogenic temperatures using visible light, and maintained below a critical temperature. A different choice of the coordinating ligands led to a T_{LIESST} of 68 K, which is approximately 25 K higher than that of an already reported similar complex [187]. This is an important result and shows the relevance of molecular engineering in the design of new materials. We attributed the larger T_{LIESST} to a larger increase of the unit cell volume after the interconversion.

The relaxation from the metastable, photoexcited high-spin state to its low-spin equilibrium state shows two different regimes. Between the critical temperature and approximately 20 K, the relaxation is best described by the Arrhenius law, which means that in this regime thermal relaxation drives the system into its ground state. However, the relaxation time does not increase indefinitely exponentially when lowering the temperature, but hits a barrier at about $2.8 \cdot 10^4$ s, which cannot be overcome. This temperature-independent behaviour below 20 K is typical for relaxation via a quantum tunnelling processes.

A common issue is the usually low efficiency of photoswitchable complexes, which we have overcome by improving the sample preparation. We investigated the three types: powder sample, pressed pellet and sample dried from a dichloroethane solution. Strongest conversions were achieved on powder samples due to their large surface-to-volume ratio. Nearly 98 % excitation at 850 nm was reached without the need of a high-power pulsed laser source. Light absorbed by materials gets exponentially damped within the material, and thus best results were obtained on thin samples. Furthermore, larger light intensities improve the efficiency until a certain point, where the improvements per mW become minimal. Moreover, larger

light intensities develop an unwanted heating effect which, in the extreme case, heats up the sample into the thermal relaxation regime. Therefore, maximising the surface-to-volume ratio is key. In potential two-dimensional nanodevices that can be controlled with light, the surface-problem is naturally solved and high efficiencies can thus be expected.

Some sources report the possibility that after photoexcitation with green light, backswitching from high-spin to low-spin is possible via infrared light. However, our investigations have clearly shown that this is not the case for our sample. In fact, studies on backswitching must be carefully interpreted, as the excitation is in competition with relaxation processes.

Having a functional building block that could be grafted on single-molecule magnets, we now rely on the synthetic possibilities for further research. Being able to fabricate photoswitchable single-molecule magnets for nanospintronics would open up a new generation of nanodevices. Furthermore, the present investigation has shown that the here developed fibre-optical setup can be well employed for studying photoactive properties of materials, and, generally, how ESR and SQUID magnetometry together give a comprehensive picture. The gained knowledge was essential to interpret the spin-switching properties of an SMM presented in the next chapter.

5 Photoswitching of an Fe_3Cr-based SMM via spin-forbidden transitions

5.1 Overview of the project

In the previous study we performed a detailed investigation of the photomagnetic properties of a paramagnetic cobalt valence tautomer with a relatively high critical temperature. However, for nanospintronic applications, it is favourable to have a system with a quasi-permanent magnetic moment, such as SMMs. To achieve this goal, one may attempt the grafting of the Co-VT onto a molecule that shows SMM behaviour. Alternatively, one could introduce metallic ions into an SMM that have the possibility to show a photoexcited state of decent lifetime.

In this study, we tackle the question how the photoactive properties of single metallic ions can be used to change the spin state of a single-molecule magnet, and, furthermore, how we can detect such changes with state-of-the-art magnetometric and spectroscopic techniques. As with the Co-VT, light offers a significant advantage. It refrains to introduce any manipulations on the crystal-field, while alternative means influence or even destroy SMM behaviour. The overlap of wavefunctions between electrodes and the molecule often results in a loss of SMM behaviour [38, 222, 223]. Here, we chose an Fe_3Cr-based SMM as model complex. It is obtained from the common Fe_4 derivate [224, 225], which does not lose its SMM behaviour when deposited on surfaces [226]. The Cr^{III}-ion is known to show a spin-forbidden transition (SFT) that can be excited using visible light. Thereby, the ion undergoes a spin state change from 3/2 to 1/2, and thus affects the overall magnetisation of the molecule. When talking about a spin-forbidden transition,

we actually mean a transition that is unlikely to happen because it is forbidden by first-order selection rules. SFTs are characterised by a rather slow relaxation, which usually ranges between milliseconds and seconds [98], while spin-allowed decays show relaxation times of less than microseconds.

In fact, the photoactive property of Cr^{III}-ions finds applications in lasers. The active gain medium in the ruby laser is a Cr^{III}-doped Al_2O_3 crystal, where the population inversion is realised via optical pumping of the corresponding transition with a white xenon light source. Many more SFT properties of Cr^{III}-ions are extensively discussed in literature [98, 227–229]. Furthermore, the SFT allows connecting two separated Hilbert spaces within one molecular qubit, which could allow the implementation of complex quantum computational schemes, when coherences can be maintained long enough [230]. Moreover, Fe_3Cr has already been successfully placed on surfaces [231], where it retained its SMM behaviour according to X-ray circular dichroism spectroscopy results, thus fulfilling one of the essential requirements for integration in nanodevices. Using light as an external stimulus could herald a new generation of photoswitchable nanodevices with coherent manipulation of spin states, where otherwise separated Hilbert spaces can be connected.

Here, we present a full characterisation of the photoexcited state of Fe_3Cr, performed in a collaborative project with Eric Heintze from the University of Stuttgart. The samples were provided by the group of Andrea Cornia from the University of Modena, and synthesised using reported methods [224, 225]. We start with the molecular structure, describe the spin Hamiltonian and the spin-forbidden process. We then progress to results on broadband TDESR on the photoexcited state. These measurements were carried out by Eric Heintze at the University of Stuttgart and explained in his thesis [180]. My own work, hereby, was the analysis of the measured data, the extraction of the photoeffect and the simulation of all curves, as acknowledged in [180]. Therefore, this section focuses on the simulation and data analysis. The TDESR results will then be compared

to SQUID photomagnetometry measurements, where we employed the same setup as for the investigation of the Co-VT. The SQUID measurements were carried out together with Eric Heintze, the data analysis shown in the following was carried out by myself, as acknowledged in his thesis [180]. Finally, we will give further perspectives on how this molecule can be successfully implemented in nanodevices.

5.2 Molecular structure and the spin-forbidden process

5.2.1 Molecular structure and spin Hamiltonian

In order to demonstrate the SFT mechanism of Cr^{III}-ions in SMMs, we performed measurements on the molecular cluster $[Fe_3Cr(L)_2(dpm)_6] \cdot (CH_2SMe)$ (Hdpm = dipivaloylmethane, H_3L = 2-hydroxymethyl-2-phenylpropane-1,3-diol), in the following abbreviated as Fe_3Cr. Its molecular structure is shown in Fig. 5.1. The molecule has a trigonal D_3 symmetry and crystallises in a $C2/c$ space group. Fe_3Cr clusters are obtained by changing the central Fe^{III}-ion with a Cr^{III}-ion as described in Refs. [224, 225]. However, not all central Fe^{III}-ions can be replaced in the fabrication process. Crystals contain Fe_4 admixtures in a 16:84 (Fe_4:Fe_3Cr) ratio.

In our complex, three Fe^{III}-ions ($S = 5/2$, $^4A_2$ ground state) are coupled antiferomagnetically to the central Cr^{III}-ion ($S = 3/2$, $^4A_2$ ground state) due to the oxygen bridges via p-orbitals. This phenomenon is also known as superexchange. These ions are coordinated to bulky ligands which ensure a good magnetic isolation between molecules. Therefore, as intra-cluster coupling is larger than the thermal energy k_BT, each molecular centre in a crystal can be considered as a giant spin. The resulting ground multiplet is thus $S = 6$, which is split into $2S + 1$ states. In contrast, Fe_4 shows a ground multiplet of $S = 5$. Higher excited multiplets with $S = 5$ and $S = 4$ are separated by 33 K and 67 K from the ground multiplet, respectively [232]. We can describe the splitting of the multiplets via

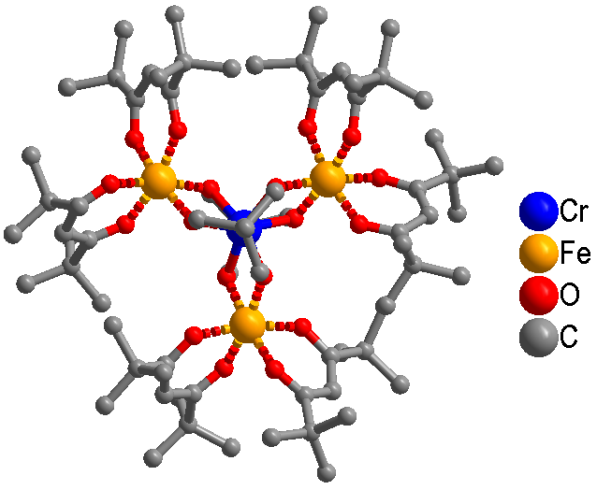

Fig. 5.1: Fe_3Cr structure. The Fe^{III}-ions couple ferromagnetically to each other, and antiferromagnetically to the Cr^{III}-ion. Crystallography performed by the Cornia group from the University of Modena.

the spin Hamiltonian for trigonal D_3 symmetry [37]:

$$H = \mu_B \boldsymbol{B} \cdot \mathbf{g} \cdot \boldsymbol{S} + DS_z^2 + B_0^4 O_0^4 + B_3^4 O_3^4 + B_3^6 O_3^6 + B_6^6 O_6^6 \,. \tag{5.1}$$

For transition metal clusters, the higher-order crystal-field terms B_q^k with $k \geq 4$ have a minor effect. Therefore, the crystal-field splitting is mainly determined by DS_z^2, leading to six degenerate pseudo doublets and one singlet state. The D values have been reported as -0.179 cm^{-1} and -0.418 cm^{-1} for Fe_3Cr and Fe_4, respectively [224]. These lead to energy barriers of 7 K and 15.6 K, respectively.

Due to the trigonal symmetry, the crystal-field parameter $E = B_2^2$ vanishes. Nevertheless, the system shows quantum tunnelling of magnetisation at zero-field [224]. A prerequisite for quantum tunnelling is the existence of mixed states with contributions of opposite magnetic quantum numbers. This means that the ground state $|m_s\rangle = |\pm 6\rangle$ is not a pure eigenstate. Mixing between $|+6\rangle$ and $|-6\rangle$ is due to the presence of crystal-field parameters with $\Delta m_s = q \cdot n$, where n is an integer. This condition is fulfilled by B_3^4, B_3^6 and B_6^6. However, the energy barrier for thermal relaxation is dominated by the lowest-order crystal-field parameter D.

Therefore, the relaxation time is given by

$$\tau = \tau_0 \mathrm{e}^{\frac{|D|S^2}{k_B T}} . \tag{5.2}$$

Via temperature-dependent AC SQUID magnetometry, where we apply an oscillating magnetic field and measure in-phase and out-of-phase magnetisations, we gain access to relaxation times τ. Then, the energy barrier can be extracted by fitting the temperature dependence of τ. However, this is only valid when the ground multiplet is largely populated. For a splitting of 33 K, >99 % population is achieved below 7 K.

5.2.2 The photoswitching effect

The photoactive property of Fe_3Cr is due to a spin-forbidden transition of the Cr^{III}-ion, which undergoes a transition from $S = 3/2$ to $S = 1/2$. As a consequence,

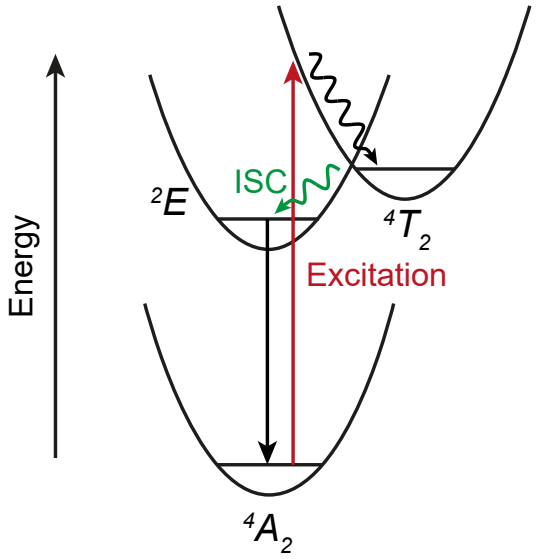

Fig. 5.2: Intersystem crossing (ISC) in Cr^{III}. By illuminating with red light, Cr^{III} gets excited into the $^4T_2$ state. Via radiation-free decay, the system relaxes within the excited state. Since there is an overlap of energies between the excited ^2E and $^4T_2$ state, the Cr^{III}-ion arrives at the ^2E state, and changes the molecular spin of Fe_3Cr from $S = 6$ to $S = 7$.

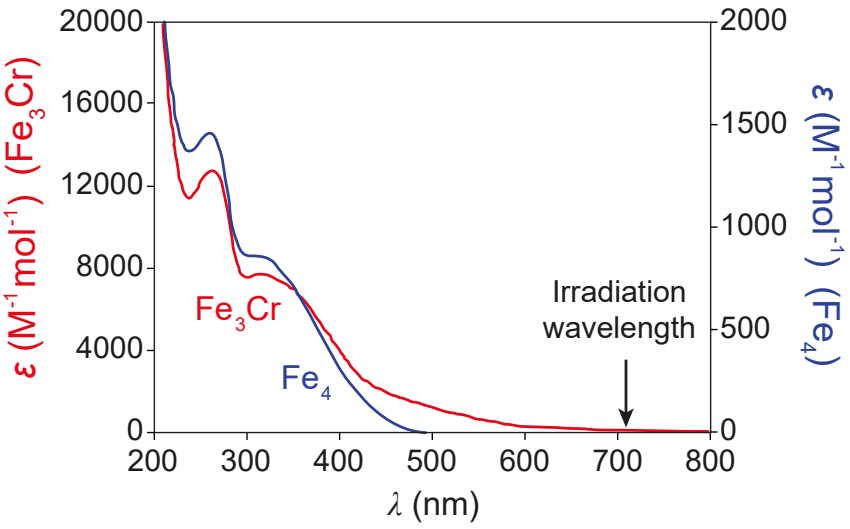

Fig. 5.3: UV/vis absorption diagram of Fe_3Cr and Fe_4. The irradiation wavelength 705 nm is indicated. The diagram was adapted from Ref. [224].

the spin state of the molecule increases from $S = 6$ to $S = 7$. In the group theory representation, this corresponds to the transition ${}^4A_2 \rightarrow {}^2E$. However, this SFT is difficult to drive directly due to its narrow excitation linewidth, and the corresponding small absorption profile. In fact, it is more effective to probe the spin-allowed transition ${}^4A_2 \rightarrow {}^4T_2$, as depicted in Fig. 5.2. After excitation, the system goes via a radiation-free transition to the ${}^2E$ state due to an energetic overlap of the different states. This phenomenon, also known as intersystem crossing (ISC), thus changes the molecular net spin. As the direct decay ${}^2E \rightarrow {}^4A_2$ is spin-forbidden, the system resides in the ${}^2E$-state for a long time. For Cr^{III}-ions, the relaxation time lies typically in the milliseconds regime [98], which allows us to conduct measurements with a continuous-wave laser instead of a pulsed laser source.

The UV/Vis absorption diagram for Fe_3Cr and Fe_4, taken from Ref. [224], is shown in Fig. 5.3. Both spectra share similar features in the deep UV-range below 300 nm. Cr^{III}-ions typically show broad absorptions at 352 nm and 396 nm. Furthermore, Fe_3Cr shows a broad absorption band between 500 nm and 800 nm. This broad feature is due to double excitations of Cr^{III} and Fe^{III}-ions, which can be

identified by both comparing the spectrum to the Fe_4 anologue and to typical Cr^{III} spectra [227, 229]. At higher wavelengths, in our case above 700 nm, the absorption is due to Cr^{III}-ions only, and the SFT is driven most efficiently. Therefore, we chose a 705 nm laser to excite the SFT.

5.3 Broadband TDESR

5.3.1 Experimental results

We started with broadband TDESR experiments with and without irradiation of light. Fitting and simulation of the spin Hamiltonian parameters (Eq. 5.1) will provide the numbers to fully understand our system. Using the W-band results reported in Ref. [232], we chose the appropriate BWO working in the frequency regime between 160 GHz and 260 GHz to allow for high-field measurements between 5.4 T and 7 T. The experiments were performed in collaboration with Eric Heintze from the University of Stuttgart, and the experimental details are described in his thesis [180]. Here, we will focus instead on the data analysis regarding the photoexcited state. The CuBe-cantilever thickness was chosen as 25 µm, and separated from the baseplate with a 30 µm spacer. A crystal sample was fixed with Apiezon N grease, with its easy-axis oriented a few degrees away from the magnetic field to ensure a measurable torque. The measurements were performed in Voigt geometry, meaning that the electric field component of incident microwaves is oriented nearly parallel to the easy-axis. Therefore, the energy splitting scales approximately linear with the external magnetic field. For measurements under irradiation of light, we set the laser power to 13 mW. All data presently shown were corrected for the frequency-dependent output power, temperature fluctuations during the measurement and the heating effect of the laser [180].

By varying both magnetic field and frequency, we arrive at the map shown in Fig. 5.4. We may clearly see the Zeeman splitting of the m_s sublevels. However,

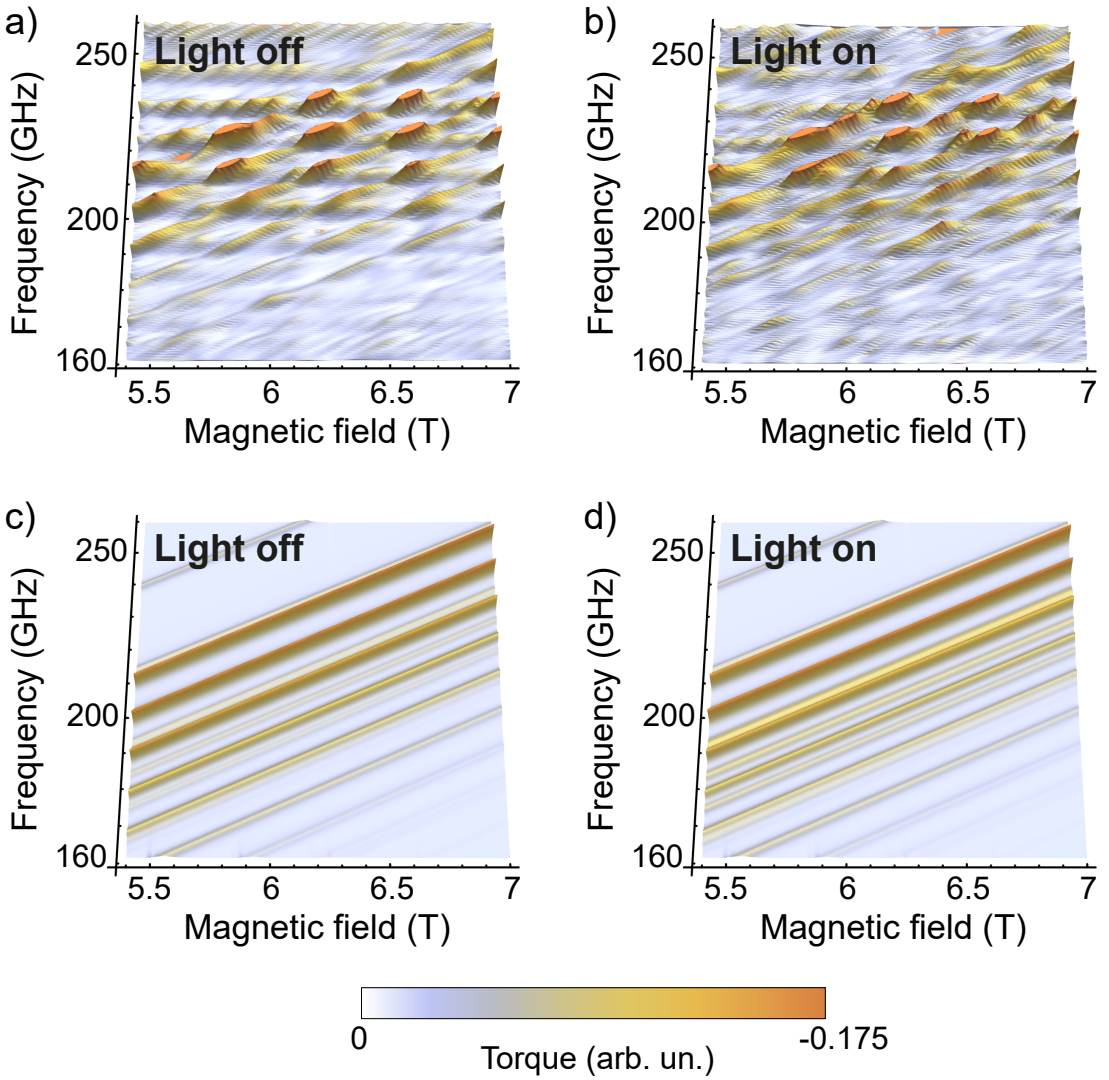

Fig. 5.4: TDESR measurement data and simulation for Fe_3Cr at 19.4 K. (a) Multifrequency multifield data without light and (b) during irradiation. The corresponding EasySpin simulations are shown (c) and (d), based on the extracted parameters in Tab. 5.1. Illustrations created in collaboration with E. Heintze [180].

at 19.4 K measurement temperature, the ground multiplet is not solely populated. Assuming Boltzmann population, the ground multiplet $S = 6$ is populated by 82.4%, first excited multiplet $S = 5$ by 15.0% and second excited multiplet $S = 4$ by 2.6%. This leads to additional satellite resonances that have to be taken into account. Although it would be possible to lower the temperature, we found that 19.4 K was very stable to operate at with the Spectromag. The whole spectrum is superimposed with a standing wave pattern, which originates from the fact that,

at these high frequencies, the microwave wavelengths are of the same order of magnitude as typical experimental dimensions. The standing wave frequency can be extracted as 10 GHz, which corresponds to a wavelength of 13 mm. In fact, this length matches with the distance between the cantilever and the inner sample chamber.

Zeeman-effect removal procedure and averaging of the spectra

As can be observed in the diagram, there are both certain fields and frequencies where the Zeeman lines are less distinct, which are due to standing waves and poor output powers at certain BWO voltages, i.e. BWO frequencies. In order to gain a comprehensive picture, we used a special averaging technique and Zeeman removal procedure, schematised in Fig. 5.5, which will be explained in the following.

In the chosen orientational regime, the magnetic field is nearly parallel to the quantisation axis, so that the Zeeman splitting scales linearly with the magnetic field at large fields. In the first step, we fit the field-dependent Zeeman resonance frequencies with a line and extract the slope. This slope is then subtracted in the two-dimensional datasets in Figs. 5.4a and b. As a result, the Zeeman lines now appear horizontally in a two-dimensional field-frequency diagram, i.e. the resonance frequency is now a fixed quantity against the magnetic field. This method projects the data on a new frequency axis, which we here call 'relative frequency'. Original field-dependent spectral features now appear at the same

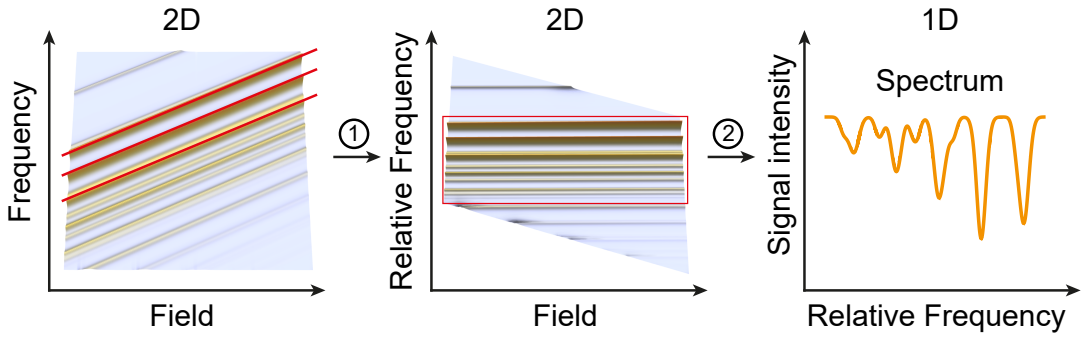

Fig. 5.5: Zeeman removal procedure. In the first step, the Zeeman slopes (red lines) are removed. In step 2, the resulting data (red rectangle) is averaged for the different field values to obtain a 1D spectrum.

corresponding resonance frequency for any given field. This allows us to treat the field-dependent data as if they were taken at one distinct field. However, differences can be found in the field-dependent signal strengths due to a stronger splitting of states at higher fields and the accompanied stronger population of lower lying states. This effect has been accounted for in our spectral simulations, which is discussed later. In the last step, we average over the field-dependent data and obtain one averaged data set. The resulting one-dimensional spectra are shown in Fig. 5.6.

Analysis of the averaged spectra

Without irradiation (Fig. 5.6a), five strong features highlighted by grey areas can be identified in the data. We assign these to magnetic dipole transitions with $|\Delta m_s| = 1$ within the ground multiplet. The strongest absorption that can be found at highest frequencies is due to the transition from $|6\rangle$ to $|5\rangle$, as the splitting between two energy levels scales linearly with the magnetic quantum number and, therefore, the population difference is maximal. Transitions at lower frequencies are then deduced from this, as indicated in the figure. Furthermore, additional features marked with diamonds appear at 13 GHz, 25 GHz, 35 GHz and 45 GHz. We assign these to contributions from the thermally-excited $S = 5$ multiplet. The corresponding transitions can be obtained in the same fashion. In the chosen field-regime, strongest contributions from Fe_4 are higher in energy than the ground multiplet transitions of Fe_3Cr, and are minimal otherwise. Therefore, all spectral features can be well identified.

Irradiating the sample shows an intriguing effect on the spectrum. New features may not be immediately visible because of mediocre excitation efficiency, so that a closer look is required. First, the peak at 40 GHz changes its intensity relative to the transitions at 51 GHz and 61 GHz. At the same time, new peaks at 34 GHz and 43 GHz arise. In order to determine the nature of these states, so as to understand what is happening during the irradiation process, modelling is required.

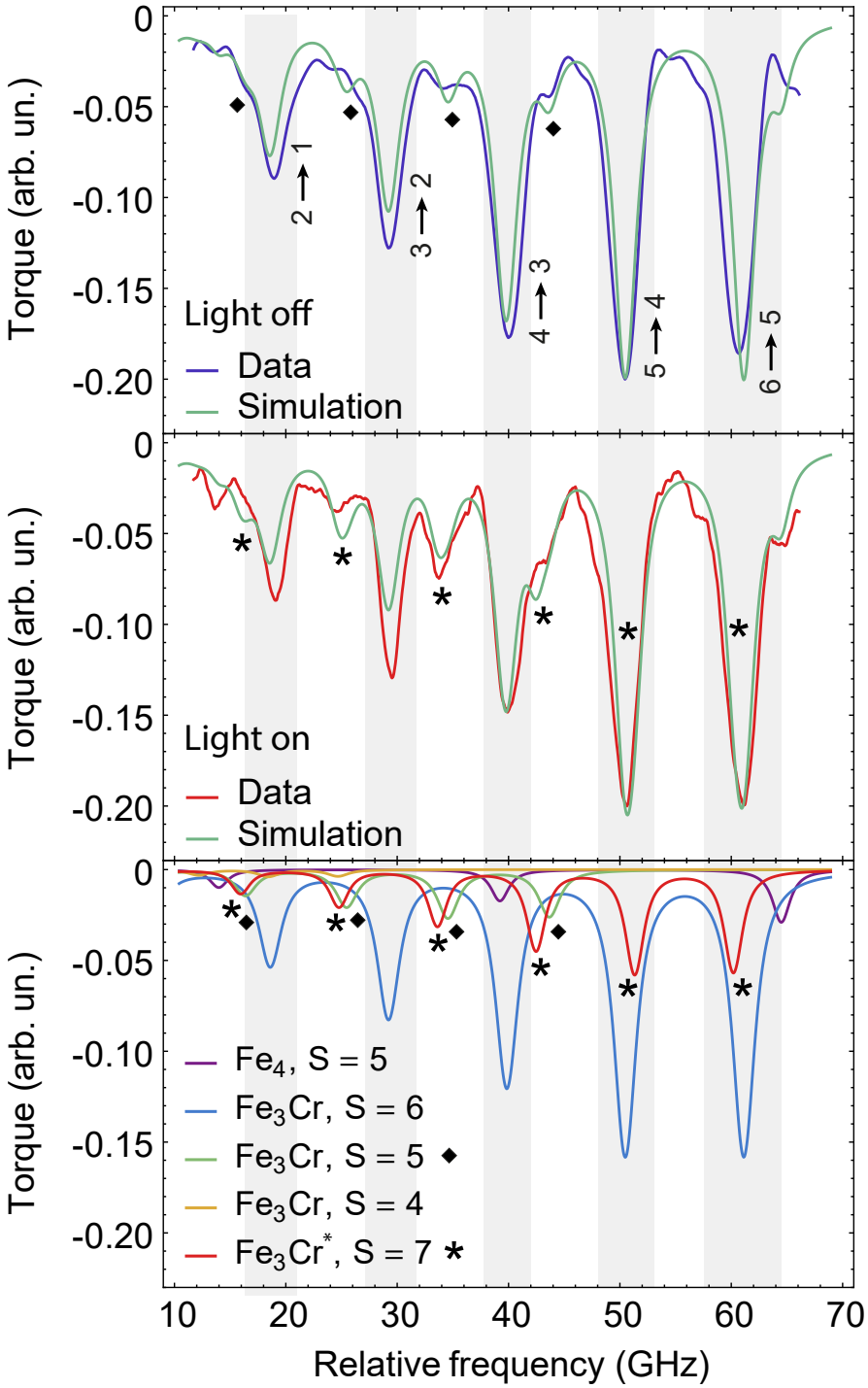

Fig. 5.6: Averaged and scaled TDESR-data on Fe_3Cr with and without light. The averaging and scaling technique is discussed in detail in the main text. (a) TDESR-data without irradiation. Simulation was performed via EasySpin. (b) TDESR-data and simulation on the photoexcited state. (c) Contributions from all states to the TDESR-signal with light. The diamonds and asterisks highlight the corresponding transitions. Illustrations created in collaboration with Eric Heintze [180].

5.3.2 Simulation of the spectra

Using the spin Hamiltonian (Eq. 5.1), we were able to reproduce the TDESR spectra. With EasySpin [171], simulations were performed by calculating the raw absorption spectrum with Lorentzian lineshapes. Spectra were first simulated for all fields, and then scaled and averaged together in the same manner as that of the measurement data. Rather than fitting, we adjusted the parameters within the Hamiltonian to find a best global set of variables that describes both spectra with and without light.

As starting values, we used the ones already published in Ref. [232]. Furthermore, we kept the Fe_4-values fixed from literature [32, 232] and $g = 2$. The found best set of parameters is given in Tab. 5.1, which we employed to reproduce the spectra. Overall, we found a reasonably good agreement between theory and experiment. The three peaks at 40 GHz, 51 GHz and 61 GHz of the spectrum without light can be well reproduced, while the lower are slightly underestimated. A reason for this observation could be the nonlinear response of the cantilever. At large torques, restoring forces increase, leading to smaller peaks than one would normally expect. More interestingly, for the case with light we could only fit the data by assuming contributions from a multiplet with $S = 7$. The SFT process predicts the spin-state change from $S = 6$ to $S = 7$, which is now proven by TDESR. Moreover, we found that the anisotropy parameter D changes from -0.178 cm^{-1} to -0.1482 cm^{-1}. This can be explained by the fact that the electrostatic interactions slightly change in the excited state. Moreover, we can explain this reduction via coupling of the single-ion anisotropies, which will we discussed in the next section. Eventually, the crystal-field interactions determine the anisotropy parameters. The given errors stem from uncertainties in the magnetic field and fitting standard errors, as discussed more in detail in the next section.

The contribution of all the single subspecies is given in the third panel of Fig. 5.6. From there we can finally understand the TDESR changes upon irradiation. Due to an overlap of transitions within the photoexcited $S = 7$ manifold with the peaks

Tab. 5.1: Simulation parameters for the Fe_3Cr TDESR spectra. The Gaussian linewidths are defined as FWHM. The asterisk denotes the photoexcited state.

	Fe_4	Fe_3Cr			
Spin state	$S = 5$	$S = 6$	$S = 5$	$S = 4$	$S = 7^*$
g_x	2.000	2.000 ± 0.001			
g_y	2.000	2.000 ± 0.001			
g_z	2.000	2.012 ± 0.001			
D (cm^{-1})	-0.422 ±0.004	-0.1780 ±0.0025	-0.1525 ±0.0036	-0.1050 ±0.0020	-0.1482 ±0.0036
Linewidth (MHz)	60	75	210	210	180
Population (light off)	16	68	13.5	2.5	-
Population (light on)	16	56.5 ± 1.2	11.1±0.25	2.1 ± 0.05	14.3 ± 1.5

at 51 GHz and 61 GHz, no relative intensity change can be observed. Only at lower frequencies, light-excited state features are located in between two main peaks, as D becomes decreased upon irradiation. At the same time, this conclusion means that the signal changes are not due to laser heating that results in a stronger population of the $S = 5$ manifold, which overlaps with the photoexcited transitions at lower frequencies. Furthermore, the $S = 4$ spin manifold has minimal effects on the spectrum. Its contribution is actually smaller than measurement errors, and will be neglected in the following. The $D_{S=4}$-value was kept fixed from Ref. [232], and its uncertainty was taken over.

From the simulations, we can also quantify the extent of light-absorption. All contributions have to be weighted with appropriate factors. We can safely say that spectral diffusion happens on a faster timescale than the de-excitation process. Therefore, Boltzmann distribution of states is maintained in the ground and thermally excited multiplets. From the global simulation we thus concluded an excitation efficiency of 14.3 %. The weighting of all the subspecies is depicted in Fig. 5.7.

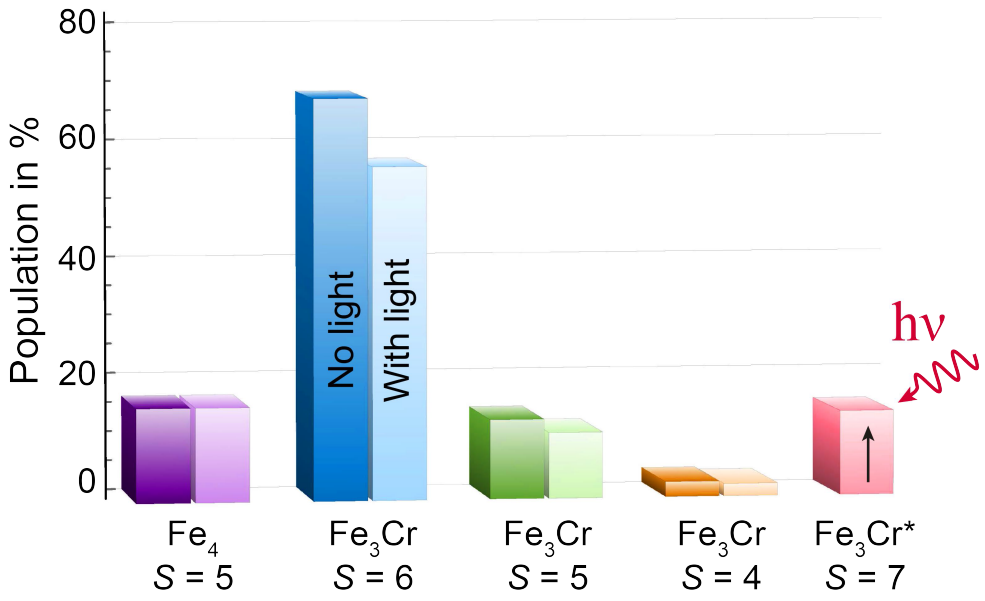

Fig. 5.7: Populations of states obtained from the simulation of the TDESR data. According to our simulations, we achieved an efficiency of 14.3 % at 13 mW laser power. Illustration created in collaboration with Eric Heintze [180].

5.3.3 Fitting of the spectrum

Using the simulation parameters as starting values, one could try fitting the resulting spectrum. This allows us estimate the errors of the found values, given in Tab. 5.1. However, the Hamiltonian is relatively large if we let all parameters of the different spin subspecies vary in the fitting process. In order to deal with the overparameterisation, we fixed the g values to the found values in Tab. 5.1, and neglect contributions from the second excited multiplet with $S = 4$ as well as from Fe_4 admixtures. We note, however, that a fit of the spectrum may lead to erroneous results and the simulations may describe the system better, which is the norm in ESR spectroscopy. This is due to background contributions, for example originating from standing waves, a nonlinear response of the cantilever, or even from irregularities in the helium flow around the torque setup, which altogether affect the measured TDESR signal intensities that a fit can overestimate. Although the here presented averaging technique allows to improve the handling of these

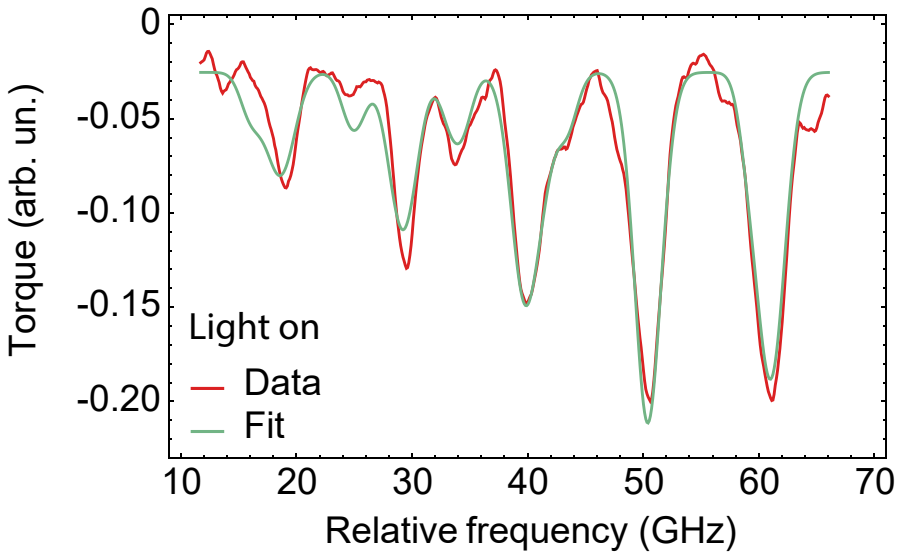

Fig. 5.8: Fit of the TDESR data obtained under irradiation of light. In the fit, contributions from the ground multiplet, first excited multiplet and photoexcited state are considered. The single contributions are similar to Fig. 5.6.

background effects, residual artefacts may still be present in the spectrum, which a mathematical fit potentially identifies as spectral contributions. Nevertheless, we can use the fit confidences to estimate errors in both our fit and simulation values.

The best fit is shown in Fig. 5.8. As best fitting parameters, we found $D = -0.1776 \pm 0.0025\,\mathrm{cm}^{-1}$ for the ground state and $D = -0.1511 \pm 0.0036\,\mathrm{cm}^{-1}$ for the first excited multiplet. In the photo-excited state, we found $D = -0.1451 \pm 0.0036\,\mathrm{cm}^{-1}$ and an excitation efficiency of $7.1 \pm 1.5\%$. The error bars of D were obtained from the standard deviations in the frequency-position of the single Lorentzian absorption lines. The found conversion efficiency is smaller than that from the simulation, which, on one hand, could be attributed to an overestimation of the background effects by the fit. However, due to overparameterisation, the fit produces a similar visual result, although with slightly a different population of the photoexcited state. Within the errors, the fit suggests a photoexcitation close to 10 %, which is sufficient to identify ESR transitions. We can take this value as the order of magnitude for the generation of the light-excited species here.

5.3.4 Discussion on the photo-effects and the axial anisotropy barrier

The magnetic anisotropy tensor $\mathbf{D}$ of the Fe_3Cr cluster can be obtained via projection of the anisotropies of the single ions $\mathbf{D}_i$ and their dipolar couplings $\mathbf{D}_{ij}$, as has been demonstrated in Refs. [224, 233]. In this section we want to find out whether we can explain the reduction of the anisotropy barrier in the photo-excited state via projection of the single-ion anisotropy tensors. This projection technique is well demonstrated in Ref. [234], and we will stick to the variable definitions of this reference. In the following we distinguish between peripheral ions, which couple ferromagnetically, and the central ion, which couples antiferromagnetically to each other. We introduce the index $i = 1$ for the central ion, and the indices $i = 2, 3, 4$ for the peripheral ones. The overall magnetic anisotropy for a tetranuclear cluster can then be expressed as [234]

$$\begin{aligned}\mathbf{D} &= \mathbf{D}_{\text{ion}} + \mathbf{D}_{\text{d}} \qquad (5.3)\\ &= d_1\mathbf{D}_1 + d_2\mathbf{D}_2 + d_3\mathbf{D}_3 + d_4\mathbf{D}_4 \\ &\quad + d_{12}\mathbf{D}_{12} + d_{13}\mathbf{D}_{13} + d_{14}\mathbf{D}_{14} + d_{23}\mathbf{D}_{23} + d_{24}\mathbf{D}_{24} + d_{34}\mathbf{D}_{34}\,, \qquad (5.4)\end{aligned}$$

where $\mathbf{D}_{\text{ion}}$ corresponds to single-ion anisotropy tensors and $\mathbf{D}_{\text{d}}$ the dipolar coupling tensors. Furthermore, d_i and d_{ij} define the corresponding projection coefficients. They can be calculated via reduced matrix elements, which is extensively presented in Ref. [234]. For a tetranuclear cluster, the direct calculation of the coefficients can become quite complicated. However, it is possible to use recurrence relationships to calculate these based on a stepwise dinuclear coupling [234]. In our case, we first couple two peripheral spins $\boldsymbol{S}_2$ and $\boldsymbol{S}_3$ to obtain the resulting spin $\boldsymbol{S}_{23} = \boldsymbol{S}_2 + \boldsymbol{S}_3$. Then we couple $\boldsymbol{S}_{23}$ with $\boldsymbol{S}_4$ and obtain $\boldsymbol{S}_{234}$. In the last step, we couple $\boldsymbol{S}_{234}$ with the central spin $\boldsymbol{S}_1$ antiferromagnetically, i.e. the total spin is $\boldsymbol{S} = \boldsymbol{S}_{234} - \boldsymbol{S}_1$. For this coupling scheme, the projection coefficients can

be derived as follows [234]:

$$d_1 = d_2^{(\mathrm{di})}(S_{234}, S_1, S)\,, \tag{5.5}$$

$$d_2 = d_1^{(\mathrm{di})}(S_{234}, S_1, S) d_1^{(\mathrm{di})}(S_{23}, S_4, S_{234}) d_1^{(\mathrm{di})}(S_2, S_3, S_{23})\,, \tag{5.6}$$

$$d_{12} = d_{12}^{(\mathrm{di})}(S_{234}, S_1, S) c_1(S_{23}, S_4, S_{234}) c_1(S_2, S_3, S_{23})\,, \tag{5.7}$$

$$d_{23} = d_1^{(\mathrm{di})}(S_{234}, S_1, S) d_1^{(\mathrm{di})}(S_{23}, S_4, S_{234}) d_{12}^{(\mathrm{di})}(S_2, S_3, S_{23})\,, \tag{5.8}$$

with

$$d_1^{(\mathrm{di})} = \frac{c_+ + c_-}{2}\,, \tag{5.9}$$

$$d_2^{(\mathrm{di})} = \frac{c_+ - c_-}{2}\,, \tag{5.10}$$

$$d_{12}^{(\mathrm{di})} = \frac{1 - c_+}{2} \tag{5.11}$$

$$\begin{aligned} c_+ = \frac{1}{Z_S} \big(&3[S_i(S_i+1) - S_j(S_j+1)]^2 \\ &+ S(S+1)[3S(S+1) - 3 - 2S_i(S_i+1) - 2S_j(S_j+1)]\big)\,, \end{aligned} \tag{5.12}$$

$$\begin{aligned} c_- = \frac{1}{Z_S} \big(&[4S(S+1)[S_i(S_i+1) - S_j(S_j+1)]] \\ &- 3[S_i(S_i+1) - S_j(S_j+1)]\big)\,, \end{aligned} \tag{5.13}$$

$$Z_S = (2S+3)(2S-1)S(S+1)\,, \tag{5.14}$$

$$c = \frac{S_i(S_i+1) - S_j(S_j+1)}{S(S+1)}\,, \tag{5.15}$$

$$c_1 = \frac{1+c}{2}\,, \tag{5.16}$$

$$c_2 = \frac{1-c}{2}\,. \tag{5.17}$$

The derivation of these coefficients, which represent scalar numbers, goes beyond the scope of this thesis. We therefore refer to Ref. [234] for further details. Using symmetry relations, we find that $d_2 = d_3 = d_4$, $d_{12} = d_{13} = d_{14}$ and $d_{23} = d_{24} = d_{34}$. We can therefore simplify Eq. 5.4 and evaluate the coefficients using $S_2 = S_3 =$

$S_4 = S_p = 5/2$ and $S_1 = S_c = 3/2$ for the ground state:

$$\begin{aligned}\mathbf{D}_{S=6} = {} & 0.02857\mathbf{D}_1 + 0.13878(\mathbf{D}_2 + \mathbf{D}_3 + \mathbf{D}_4) \\ & + 0.17347(\mathbf{D}_{23} + \mathbf{D}_{24} + \mathbf{D}_{34}) - 0.08095(\mathbf{D}_{12} + \mathbf{D}_{13} + \mathbf{D}_{14})\,. \end{aligned} \tag{5.18}$$

For the light-excited state, we obtain by keeping $S_p = 5/2$ and setting $S_c = 1/2$:

$$\begin{aligned}\mathbf{D}_{S=7} = {} & 0.10714(\mathbf{D}_2 + \mathbf{D}_3 + \mathbf{D}_4) \\ & + 0.13339(\mathbf{D}_{23} + \mathbf{D}_{24} + \mathbf{D}_{34}) - 0.02083(\mathbf{D}_{12} + \mathbf{D}_{13} + \mathbf{D}_{14})\,. \end{aligned} \tag{5.19}$$

The single-ion anisotropies and dipolar coupling energies of the ground state have been reported in Ref. [224]. Tancini *et al.* found for the peripheral ions $D_p = 0.656\,\mathrm{cm}^{-1}$ (easy-axis type), for the central ion $D_c = 0.470\,\mathrm{cm}^{-1}$ (hard-axis type) and a dipolar anisotropy of $D_{\mathrm{dip}} = -0.0132\,\mathrm{cm}^{-1}$. The projection coefficient for the chromium ion, 0.02857, leads to a contribution of $+0.0134\,\mathrm{cm}^{-1}$, nearly cancelling out the dipolar anisotropy [224]. Considering that we found $D = -0.178\,\mathrm{cm}^{-1}$ in our simulations, contributions from both the chromium ion and dipolar anisotropy are small and can be neglected. In the light-excited state, the dipolar anisotropy is of similar order of magnitude, but the projection coefficient for the peripheral ions becomes significantly reduced. We found a reduction factor of 0.772 leading to a new anisotropy barrier of $D_{S=7} = 0.772 D_{S=6} = -0.138\,\mathrm{cm}^{-1}$. This new found value comes relatively close to our simulation ($0.148\,\mathrm{cm}^{-1}$), and even closer to the fit ($0.145\,\mathrm{cm}^{-1}$), but slightly overestimates the reduction. In fact, we expect that the structure remains largely unaltered in the photoexcited state, which means that $|D_{S=6}|6^2 \approx |D_{S=7}|7^2$. The small difference between measured and theoretically predicted value could be explained via a small change of the orientation of the single-ion anisotropy tensors. We can conclude that our experiment comes close to expectations using the projection technique.

5.4 Photomagnetic characterisation via SQUID magnetometry

In order to confirm the TDESR observations, SQUID measurements under irradiation were performed. We used the same setup as for the Co-VT and irradiated a pressed pellet sample with the 705 nm laser. To distinguish between the different SQUID techniques, we introduce the term DC magnetometry for static measurements of magnetic moments, and AC magnetometry for dynamic measurements in an oscillating magnetic field.

5.4.1 Static magnetometry

At first, we measured the DC moment during irradiation. In contrast to the Co-VT, the lifetime of the photoexcited states is much shorter than the time to process a measurement, which takes about 10 s. Moreover, the spin-state change from six to seven does not have a large impact on the magnetic moment. Taking these arguments together, we do not expect to see a distinct spin effect in the DC data. The detection is furthermore hampered by the accompanied heating effect. However, this allows us to quantify the sample temperature by comparing the measured DC moment under irradiation with the temperature-dependent magnetic moment without light.

The results for different laser powers, ranging between 0 mW and 0.6 mW, is displayed in Fig. 5.9. Note that only in the case without light, the chamber temperature (x-axis) is identical to the sample temperature. We find that heating dominates, as the magnetic moment decreases during irradiation. The laser-power dependence, displayed in Fig. 5.9b, shows a nonlinear non-saturating behaviour. This means that at the chosen laser powers, only a fraction of the sample gets excited. Application of larger light intensities, however, results in a large heat load that cannot be handled by the SQUID, leading to large instabilities. This is due to the fact that the cooling power of the SQUID is lower in the low-temperature operation mode below 4.2 K.

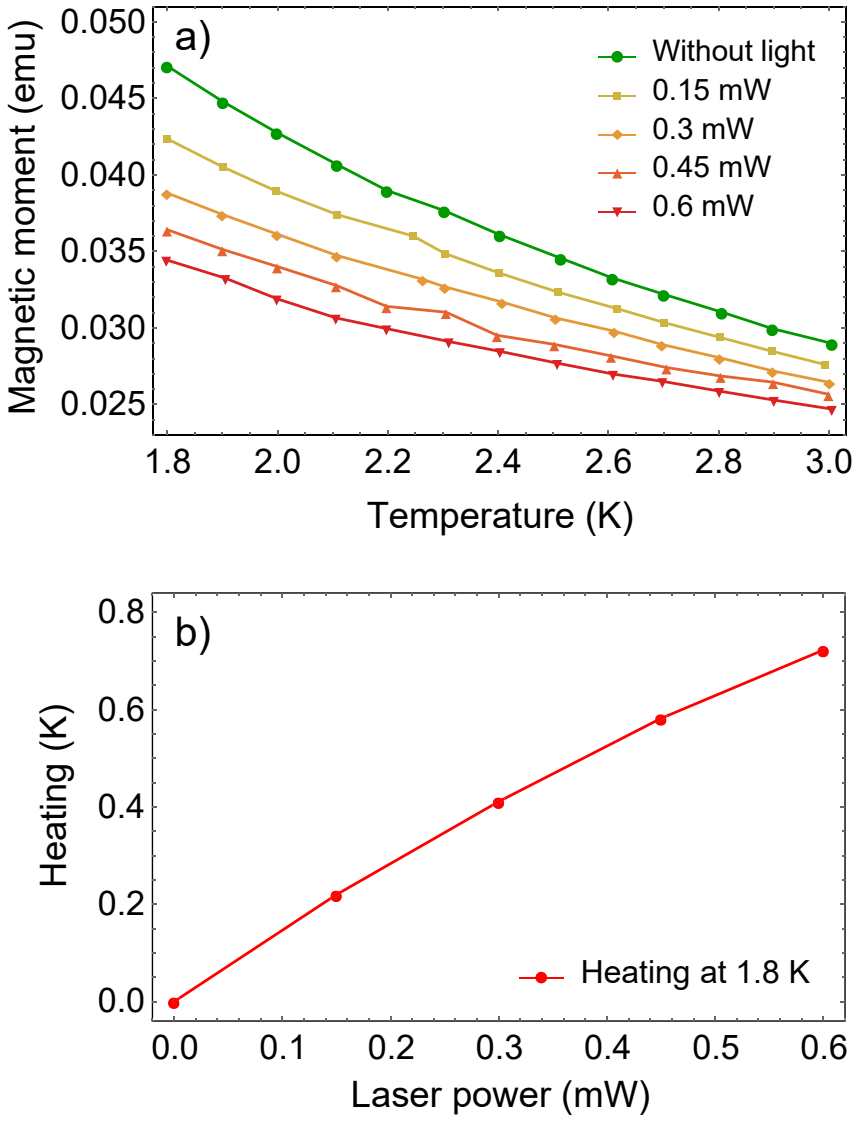

Fig. 5.9: Static magnetic moment of Fe_3Cr at different laser intensities. The measurements were performed on a thin, sub-mm pellet sample. (a) Although the spin state raises during irradiation, the magnetic moment decreases. Therefore, heating dominates over the SFT effect. The x-axis denotes the chamber, not the sample, temperature. (b) Extracted heating effect at a chamber temperature of 1.8 K. Illustrations created in collaboration with Eric Heintze [180].

5.4.2 Dynamic magnetometry

TDESR measurements indicate a lowered D-value in the photoexcited state. Since the anisotropy parameter determines the energy barrier for thermal relaxation, $U = |D|S^2$, we can use AC magnetometry to measure the slow relaxation of magnetisation, and from this we want to investigate whether we can deduce the existence of the photoexcited state. In AC magnetometry, we apply a small oscillating field of 3 Oe amplitude at frequencies between 0.1 Hz and 1500 Hz. When we apply a magnetic field, the paramagnetic spins become oriented along its direction. If we let the magnetic field oscillate below the blocking temperature, the magnetic sample will need more time to follow these field inversions. The magnetometer then returns two values: the in-phase magnetic moment m', which reflects the part that follows the field inversion, and the out-of-phase magnetic moment m'', which reflects the part that cannot keep up with the field inversions. This means that slow relaxation of magnetisation is present whenever we measure an out-of-phase component. A condition for the presence of slow relaxation is the existence of a doublet ground state [235], which is fulfilled in the case of Fe_3Cr.

It is reported that Fe_3Cr shows ground-state quantum tunnelling of magnetisation at zero magnetic field [224]. Hence, we added a static field of 1000 Oe so that relaxation becomes purely thermal. Larger fields, where the oscillation becomes small compared to the static magnetic field, yield worse SNRs and should be avoided. All measurements were carried out on the same pellet sample of sub-mm thickness. The fragility and brittleness of the pellet serve as hindrances to an accurate determination of its mass. Part of the sample may be lost upon insertion into the straw, leading to incorrect results. Therefore, the mass was estimated as 8.1 ± 0.5 mg by comparison with reference values from Ref. [224]. In any case, the determined susceptibilities will not be quantitatively analysed here.

Ground multiplet relaxation

We start with the description of measurements without light. A typical frequency dependence between 0.3 Hz and 1500 Hz for temperatures between 1.8 K and 3.0 K is shown in Fig. 5.10. The highest temperature at which measurable out-of-phase signals can be obtained is 3 K. Therefore, higher temperatures are neglected in this graph. As can be seen from Fig. 5.10a, the in-phase susceptibility decreases with increasing frequency. This behaviour indicates that the magnetic moment cannot follow the field oscillations at certain frequencies, leading to an out-of-phase magnetisation. The out-of-phase susceptibility shows two distinct features. First, a small peak around at 2 Hz arises. Second, a steep increase above 100 Hz. This indicates that two different relaxation behaviours are present, in agreement with measurements on a similar Fe_3Cr magnet [224]. Largest signals were obtained at 1.8 K due to Curie's law and the increasing remanence with falling temperature.

A better visualisation of AC data is obtained by plotting the out-of-phase susceptibility against the in-phase component, which, in literature, is also known as Argand representation. The isotemperature Argand diagram of our dataset is depicted in Fig. 5.11. In an isotemperature Argand diagram, every relaxing species appears as a half-circle. The maxima of those half-circles correspond to frequencies where $\omega_r^{-1} = \tau$, so that relaxation times τ can be directly extracted. When the characteristic frequencies ω_r of the different spin species are well separated from each other, this should, in principle, allow us to identify the two populated spin species Fe_3Cr with $S = 6$ and Fe_4 with $S = 5$. In fact, we can see one half-circle at lower, and one branch at higher, frequencies. By comparison with the reported value of ω_r of Fe_4 [224], we assign the smaller half-circle to Fe_4 contributions and the branch to Fe_3Cr. Due to experimental limitations, the full half-circle could not be resolved. Higher frequencies larger than 1.5 kHz are necessary. This makes the investigation of the photoeffect, when we eventually deal with three different spin species at the same time, challenging. In the following, we will show how we tackle this challenge and investigate whether we can obtain valuable information from light-excited spin states in Fe_3Cr via dynamic magnetometry.

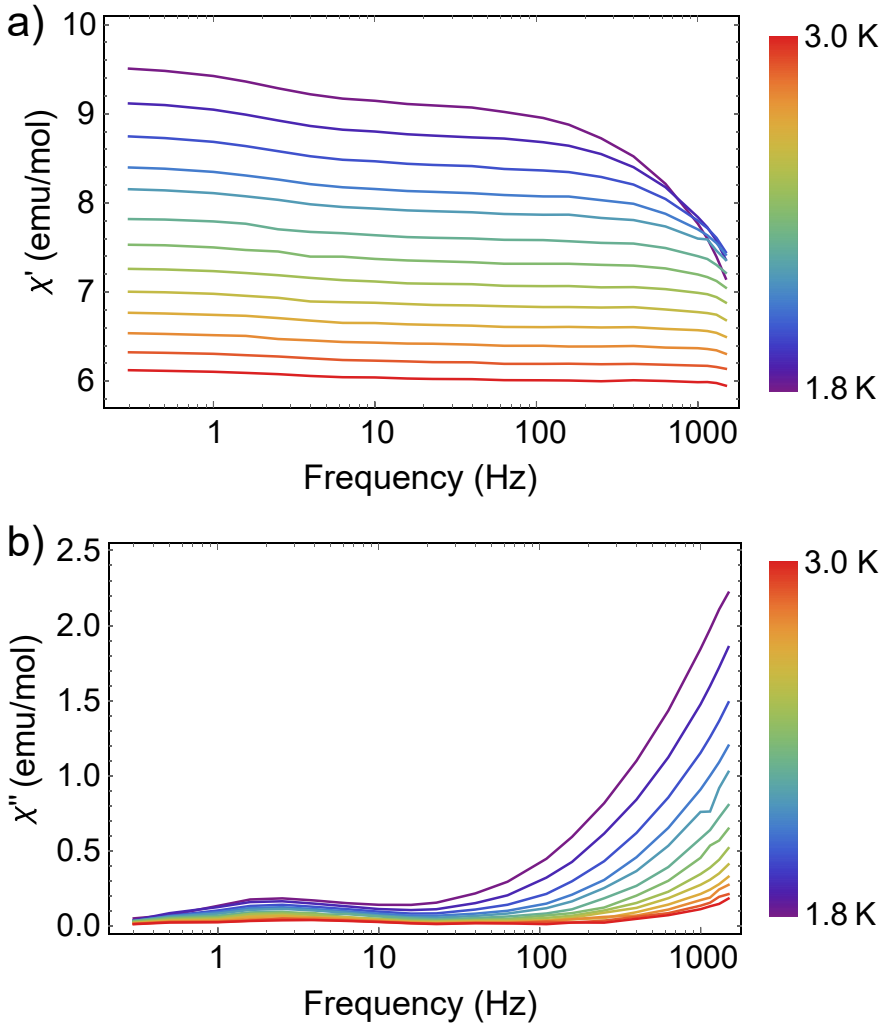

Fig. 5.10: In- and out-of-phase susceptibility of Fe_3Cr versus frequency and temperature. (a) The in-phase susceptibility decreases with increasing frequency. This behaviour indicates that the magnetic moment cannot follow the external field oscillations. The out-of-phase component (b) then increases. One resonance can be found around 2 Hz, while the second, indicated by a steep increase, appears at frequencies higher than accessible by the machine. The temperature increment is 0.1 K.

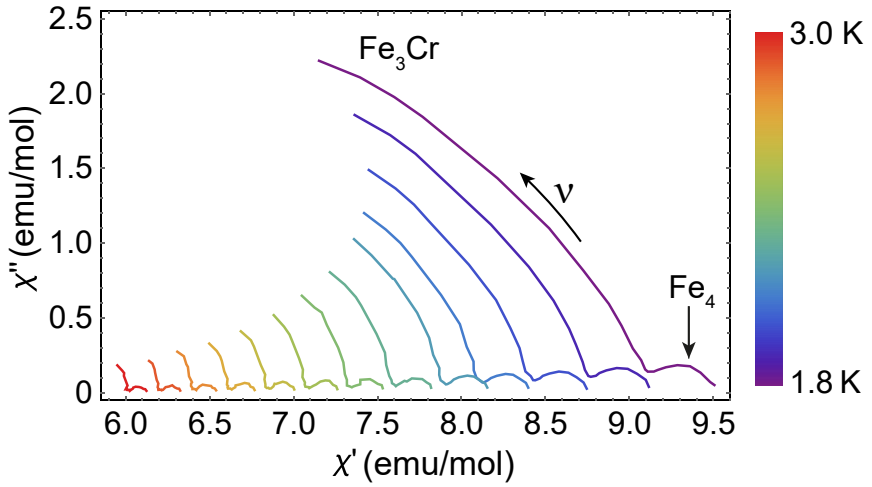

Fig. 5.11: Isothermal Argand plot of Fe_3Cr for different temperatures. Joined frequency data points of a distinct temperature form half-circles that correspond to different relaxing spin species. The direction of the frequency ν, i.e. from right to left, and the assignment of Fe_3Cr and Fe_4 are indicated. The temperature increment is 0.1 K.

AC magnetometry with light

The same experiment was performed under irradiation with light at different intensities up to 0.6 mW. Fig. 5.12 shows the isothermal Argand plots for 0.3 mW and 0.6 mW. In these graphs, the shown temperatures correspond to the chamber temperatures. The actual sample temperature can be obtained via Fig. 5.9b. At 0.3 mW, the sample gets heated up by approximately 0.4 K. Differences between the measurements can be seen in the slightly longer branches when performing the experiment under irradiation of light. For example, by comparing the 1.9 K measurement at 0.3 mW with the 2.3 K measurement without light, the branch is slightly elongated towards higher frequencies. This effect is stronger at 0.6 mW, but the higher laser power causes larger temperature fluctuations, as the cooling system of the SQUID has troubles countering the heating effect. Additionally, heating drives the sample further away from the blocking temperature, which decreases the AC signal. The best compromise between heating and AC signal was found at 0.3 mW.

Although the isothermal Argand representation is a common method to display and investigate AC signals, it makes more sense to take a closer look at the isofrequency spectrum, shown in Fig. 5.13. In contrast to the isothermal spectrum model, datapoints of the same frequency, rather than same temperature, are joined. To distinguish between the data sets, measurements without light are represented by thinner or dashed curves. However, the effect of light is relatively small. In order to visualise the light effects better, the figure shows zoom-ins. All curves obtained during irradiation appear slightly raised relative to the isofrequency curves without irradiation. This effect is stronger when using higher laser powers (Fig. 5.13b).

Nevertheless, the photoeffect is small, and additionally we are limited by the rather poor cooling power of the SQUID magnetometer at low temperatures. We could not apply more than 5% of the light intensity used in TDESR measurements. Consequently, only a fraction of the sample can be excited. Therefore,

a quantitative analysis is challenging, leading to large error bars and potential erroneous results. We will thus analyse the photoeffect in a more qualitative way. The characteristic frequency ω_r, where $\omega^{-1} = \tau$ (see Sec. 3.2.2), is related to the total anisotropy barrier $U = |D|S^2$ [7]. Using the TDESR simulation values, we find barriers of $U_6 = 6.4\,\mathrm{cm}^{-1}$ and $U_7 = 7.3\,\mathrm{cm}^{-1}$ for Fe_3Cr ground and photoexcited state, respectively, while $U_{Fe_4} = 10.6\,\mathrm{cm}^{-1}$ for Fe_4. Therefore, we expect the half-circle of the photoexcited state on the Argand plot to appear between the Fe_3Cr ground state one and the Fe_4 one. This also means that ω_r of the photoexcited state is lower than that of its ground state. Therefore, we can expect an increase of the main branch at lower frequencies, caused by a larger out-of-phase magnetic moment. This is accompanied by a decrease at higher frequencies, which are inaccessible by the SQUID. Since we are limited by the accessible frequencies and the cooling power of the SQUID, however, we only find a tiny increase of the out-of-phase component. It can be qualitatively understood via the reduced D value of the photoexcited state, which we could obtain from our TDESR results. A better understanding could be obtained when frequencies up to 10 kHz, and above, were accessible. Nevertheless, the heating of the sample also then makes an analysis challenging.

In contrast to TDESR, we cannot extract any quantitative information out of the data. Due to the small effect, sole information from AC magnetometry should be treated with caution, and can only support our TDESR results. Therefore, we give emphasis to understand what is happening in the photoexcited state to the TDESR data.

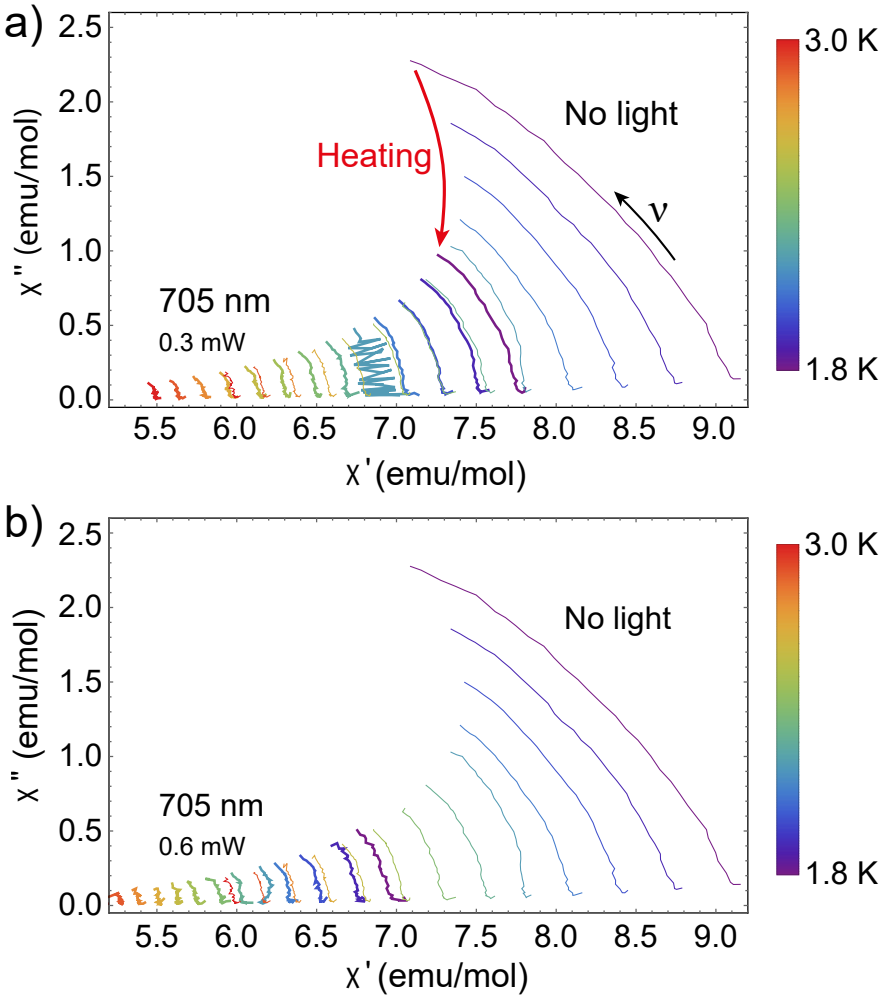

Fig. 5.12: Isothermal Argand diagram of Fe_3Cr under irradiation of light. The two Argand graphs show both cases before (thin curves) and during irradiation (thick curves) with 705 nm light at laser powers of 0.3 mW (a) and 0.6 mW (b). The indicated temperature legend corresponds to the chamber temperature. The sample temperature can be obtained via DC calibration measurements (Fig. 5.9). Illustrations created in collaboration with Eric Heintze [180].

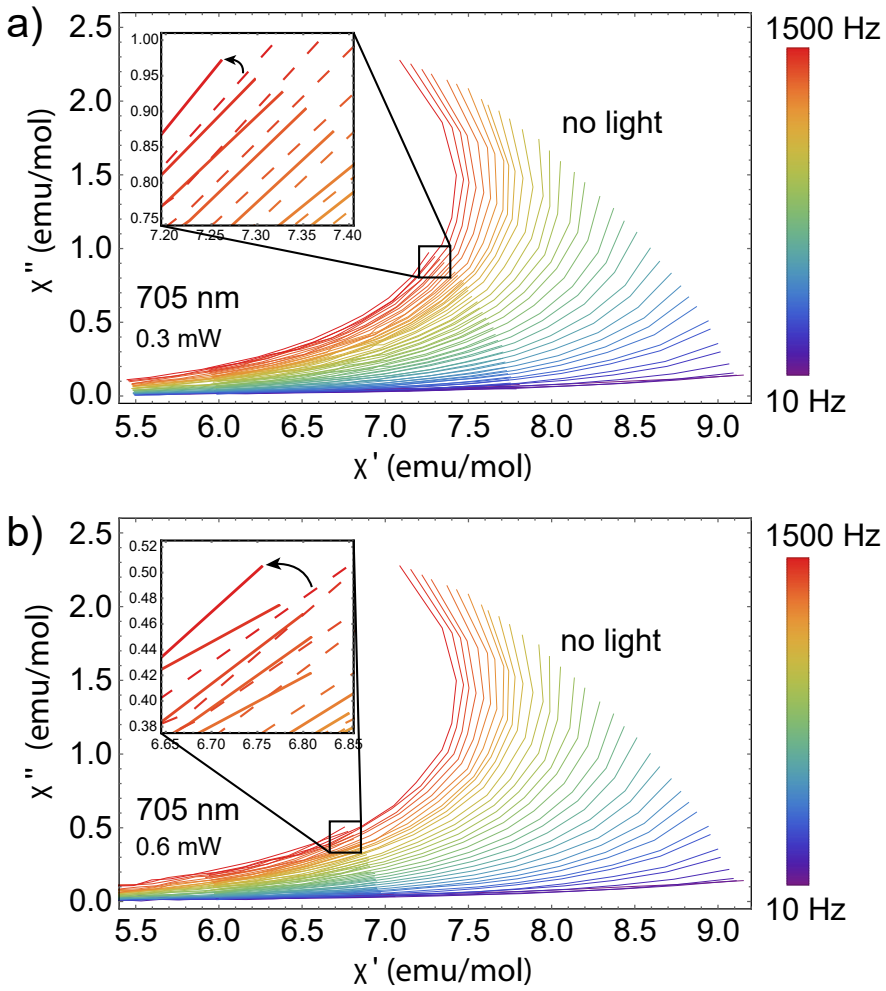

Fig. 5.13: Isofrequency Argand diagram of Fe_3Cr under irradiation of light. Graph (a) shows the comparison between 0.3 mW laser power and no light, while diagram (b) shows the case for 0.6 mW laser power. The zoom-ins, where the dashed lines correspond to the data without light, display the effect of light on the spectrum as indicated by the arrows. Overall, the out-of-phase susceptibility increases during irradiation at the given frequencies, which we ascribe to a population of the photoexcited state. Illustrations created in collaboration with Eric Heintze [180].

Fitting of the dynamic susceptibility

In order to obtain relaxation times, the susceptibility data needs to be fitted. The dynamic susceptibility is described by the following law [236, 237]:

$$\chi(\omega) = \chi_{S_N} + \sum_{n=1}^{N} \frac{\chi_{T_n} - \chi_{S_n}}{(1 + \mathrm{i}\omega\tau_n)^{1-\alpha_n}}\,, \tag{5.20}$$

with χ_S and χ_T the adiabatic and isothermal susceptibility, respectively, $\omega = 2\pi\nu$ the frequency, τ the relaxation time and α represents the distribution of relaxation times. The sum accounts for all relaxing subspecies N. By considering frequencies only above 10 Hz, we can neglect influences from Fe_4 and focus on the Fe_3Cr data. By fitting the imaginary part, we arrive at the relaxation times shown in Fig. 5.14. As can be seen, the relaxation time scale exponentially with the inverse temperatures, indicating Arrhenius behaviour. However, a kink in the data appears between 2.1 K and 2.2 K, which is probably a measurement artefact. By fitting

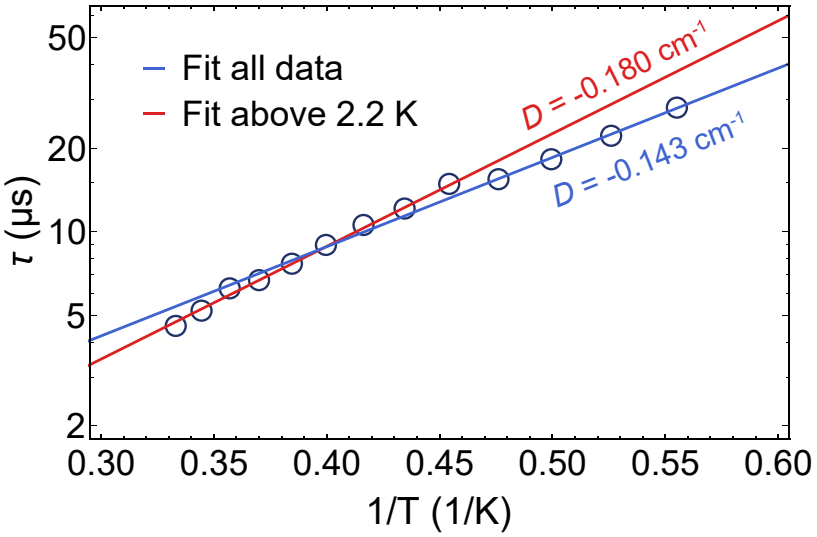

Fig. 5.14: Arrhenius fit of Fe_3Cr ground state relaxation. The datapoints, marked as blue open circles, were obtained by fitting Eq. 5.20 to the out-of-phase data. A kink appears around the lambda point of liquid helium, 2.2 K. This is likely a measurement artefact. The blue fit regards all data points, while the red fit only considers temperatures above 2.2 K. Illustration created in collaboration with Eric Heintze [180].

Eq. 5.2 to all our data, we find $D = -0.143 \pm 0.004\,\mathrm{cm}^{-1}$ (blue fit), which does not fall in line with our TDESR results. However, if we disregard datapoints below 2.2 K, where the kink happens, we find $D = -0.180 \pm 0.004\,\mathrm{cm}^{-1}$ (red fit), which is in agreement with our TDESR results and Ref. [224]. This indicates that the kink is likely a measurement artefact.

AC magnetometry with 532 nm light

By comparison with documentation on Fe-Cr complexes, the absorption of green light leads to double excitations of Fe^{III} and Cr^{III}-ions [227, 229]. To compare the efficiency of green light versus red light, AC magnetometry was performed under the same conditions. The results for 0.15 mW and 0.3 mW laser power are shown in Fig. 5.15. From the diagram, we notice a stronger heat generation at lower laser powers. The 0.3 mW measurement generates approximately as much heat as the 0.6 mW measurement at 705 nm light, whereas the effect of the photoexcited state is smaller. We explain this observation with the additional absorptions at 532 nm that compete with the SFT, which eventually induces heat and thus deteriorates the measurement.

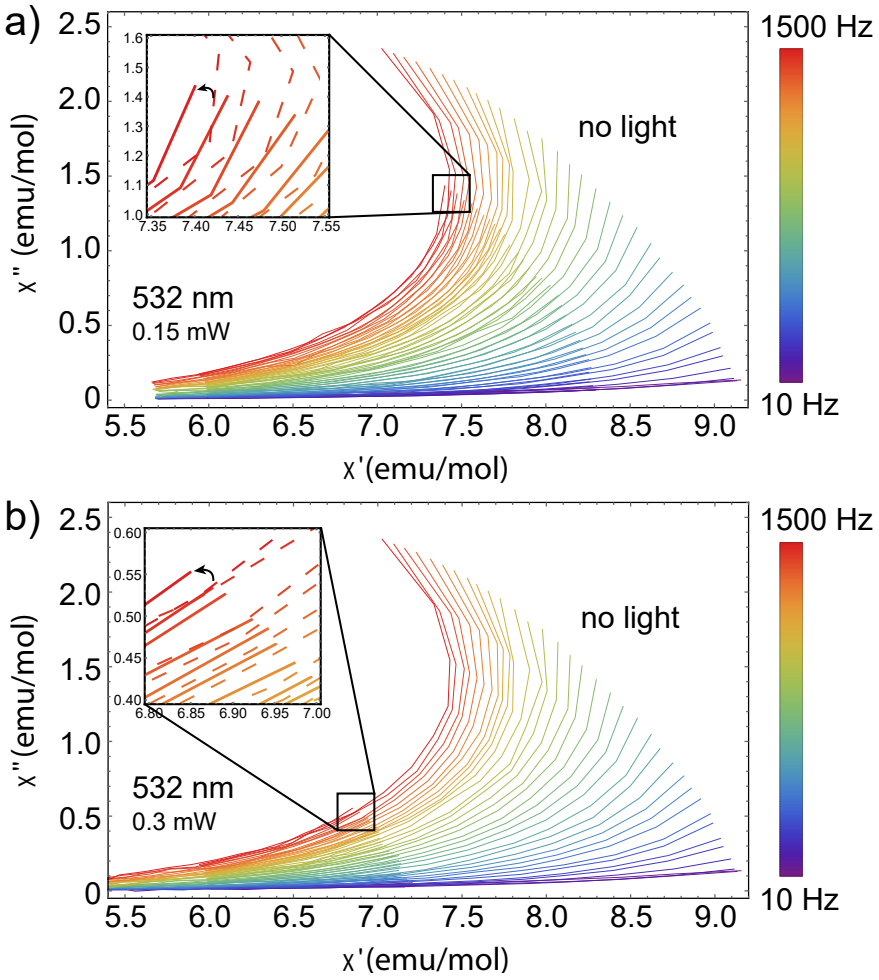

Fig. 5.15: Isofrequency Argand diagram of Fe_3Cr under irradiation of 532 nm light. Graph (a) shows the comparison between 0.15 mW laser power and no light, while diagram (b) shows the case for 0.3 mW laser power. The zoom-ins, where the dashed lines correspond to the data without light, display the effect of light on the spectrum as indicated by the arrows. Overall, the out-of-phase susceptibility increases at the given frequencies due to the population of the photoexcited state. Illustrations created in collaboration with Eric Heintze [180].

5.5 Outlook and perspectives

Experiments performed on the isostructural Fe_4-SMM grafted on surfaces revealed interesting phenomena [226], such as electrical control of magnetic anisotropy [12] or Franck-Condon blockade [238]. The molecule investigated here, Fe_3Cr, allows for the possibility of introducing two different states, in which the physical properties can be altered via light. In order to perform investigations on the nanoscale, we can take advantage of existing methods in SMM-based spintronics. In fact, it has been shown that Fe_3Cr can be grafted on surfaces, on which it retains its SMM-behaviour [231]. We furthermore expect that Fe_3Cr remains photoswitchable when grafted on a surface, since the photoswitching properties are linked to the Cr^{III}-ion rather than activated by metal-ligand interactions.

The precise direction of light towards SMMs could be achieved via plasmonic nanostructures. Plasmonic nanoantennas represent an interesting approach to distinctly addressing photoswitchable molecules at the sub-wavelength scale [239, 240]. As depicted in Fig. 5.16, plasmonic nanoantennas represent structures that collect light and transfer the energy to a receiver unit, and vice versa. For instance, such nanoantennas can be used to increase the performance of photovoltaic systems [241]. Furthermore, plasmonic structures can be shaped in a chiral way and driven with polarised light, which would allow one to excite distinct transitions in molecules [242]. An array of directed light could be achieved via photonic crystal structures, although sizes are restricted to the diffraction limit. A photonic crystal consists of a dielectric periodic structure with an array of materials with alternating indices of refraction [243]. The periodic structure allows light to propagate only in certain directions. Research on photonic crystals is often motivated by a desire to commission bio- or chemical sensors on chips [243, 244]. Combining photonic structures with photoswitchable SMMs creates fascinating possibilities, and could enable quantum operations in different Hilbert spaces within the same molecule.

In order to fulfill the basic requirements for quantum operations, it is important

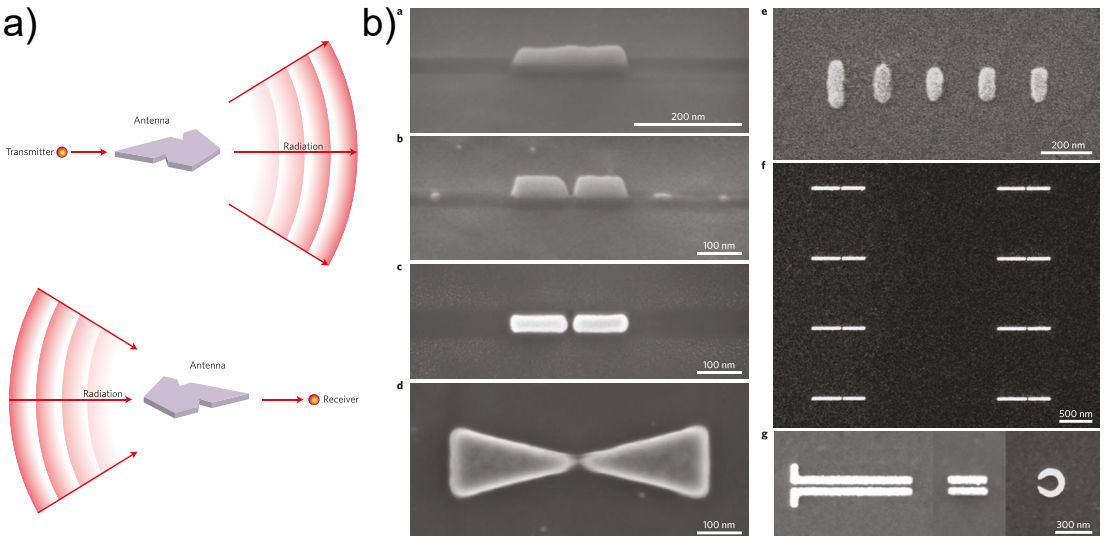

Fig. 5.16: Nanoantennas as possible building block for molecular spintronics. (a) Nanoantenna principle. The nanoantenna collects incoming light and direct the energy towards a receiver, and vice versa. (b) Structures of different kind of nanoantennes generated via electron-beam lithography and subsequent lift-off. Figures adapted from Ref. [239].

for the molecule to show sufficiently large coherence times, both in the ground, and in the photoexcited state. With a view to investigating coherence times of the photoexcited state, a pulsed laser with a pulse duration at the nanosecond scale is required. By combining such a laser with the ESR setup, spin dynamics of the photoexcited state can be investigated. This technique, often applied in solar cell research [245, 246] or in biochemical photosynthesis studies [247, 248], is also known as transient ESR. Finally, if coherence times are long enough, i.e. larger than hundreds of nanoseconds, Fe_3Cr can be used as a versatile qubit with a plethora of available states.

Further interesting candidates for photoswitchable nanodevices beyond SMMs are donor-acceptor (D-A) pairs, where light initiates an electron transfer from the donor to the acceptor group. One of the first theoretical attempts to integrate D-A_1-A_2 systems in molecular electronics was demonstrated in 1988 [249]. As reported eight years later, such molecular assemblies can be realised as shift registers [250], thus opening new avenues for nanodevices. This scheme motivated

the development of donor-bridge-acceptor systems (D-B-A), where a bridge delays recombination, and intramolecular electron transfers can be studied via ESR. Furthermore, the bridge can be functionalised, enabling distinct investigations of interactions with various possible attachments. An example of such a compound is a D-B-A-NIT-complex, where a nitronyl-nitroxide radical is attached to the bridge [100, 251], as shown in Fig. 2.10a. When grafted to a substrate, these compounds can be used as electron injectors in nanodevices. In contrast to systems where spintronic properties are investigated via electrodes, D-B-A systems represent an ultra-clean variant with a well-defined geometry, thus allowing for the thorough study of spin-spin interactions. Finally, results from these studies may lead to a novel generation of nanometre-sized field-effect transistors.

5.6 Summary

In this section, we have presented an in-depth analysis of the photoswitching properties of an Fe_3Cr-based SMM, where the SFT changes the spin state of the SMM from six to seven. We have seen that detection of the photoeffect requires sensitive instrumentation and a deep look into the theoretical treatment of the data. Compared to the Co-VT, the lifetime of the photoexcited state lies in the order of milliseconds. This is not necessarily a disadvantage, especially since Fe_3Cr shows SMM-behaviour. The smaller lifetime also allows for resetting the system on a convenient timescale.

One goal of this study was to show that Fe_3Cr is photoswitchable via the spin-forbidden transition of the Cr^{III}-ion. To prove this, TDESR measurements were combined with the possibility of photoexcitation in collaboration with the University of Stuttgart. The capacititve detection of ESR-transitions via magnetisation changes was sensitive enough to measure ESR-transitions within the photoexcited multiplet. Therefore, via simulation of the measured spectra, we were able to determine the axial crystal-field parameter D as $-0.148 \pm 0.004\,\mathrm{cm}^{-1}$, which is significantly lower than for the ground multiplet, determined as $-0.178 \pm 0.003\,\mathrm{cm}^{-1}$ in agreement with Ref. [224]. Using projection coefficients [224, 232, 234, 252], we could estimate a lowered D value of -0.138 cm^{-1} in the photoexcited state. The electrostatic environment around the spin centre could slightly change in the photoexcited state, which could explain the difference in the D-value we found in our TDESR experiment. In the fitting of the TDESR data we had to include all the different populated subspecies, and the identification of the photoexcited state might be hampered by overparameterisation. Since theoretical results support our TDESR findings, we are confident with our model.

In order to find a second proof for the chosen model, we then progressed with SQUID measurements under irradiation of light. In static measurements, light-induced magnetisation changes were mainly caused by the generation of heat. This enables us to treat the static moment as an internal temperature sensor

so as to calibrate the SQUID data. In AC SQUID measurements, application of a small oscillating field allows for an investigation of the relaxation dynamics. We identified the relaxation of Fe_4, and Fe_3Cr $S = 6$ species, in agreement with Ref. [224]. By adding light to the measurement, we noticed a relatively small shift of the Argand half-circles towards higher out-of-phase magnetisation. Although the small shift goes into the expected direction, which we deduced from the TDESR results and the lowered D value of -0.148 cm^{-1}, it is not sufficiently large to allow for a quantitative analysis. Main difficulties here are, on the one hand, the low cooling power of the SQUID magnetometer that cannot compensate for the heating effect by light irradiation, limitations in accessible AC frequencies, and, on the other hand, an insufficient change of the anisotropy barrier height in the photoexcited state. Therefore, we concluded that TDESR is superior to SQUID magnetometry when investigating the SFT in Fe_3Cr SMMs.

Finally, our results prove that we can use the SFT to switch the spin states of the molecule, offering interesting applications where quantum operations can be performed using different multiplets within the same molecule. However, without measurable coherence times, this concept falls. In order to verify coherence times, a pulsed laser source is required. This can be achieved by transient ESR, where a Hahn-echo sequence is followed by a laser flash, allowing for a direct access to phase-memory times.

6 Magnetic edge states and coherent manipulation in graphene nanoribbons

6.1 Overview of the project

In contrast to graphene, graphene nanoribbons represent quasi onedimensional semiconductors with a distinct band gap. As presented in Chapter 2.3, a vast effort has been made to describe, calculate and simulate the behaviour of GNRs from a theoretical point of view. One theory incorporates the existence of an additional magnetic edge state that is delocalised along the edges of zigzag-type GNRs [23, 253]. Theories predict the edge state also in modified structures, based on ZGNRs, such as cove-type GNRs [129]. However, experimental evidence for this effect is, at best, scarce [115, 254]. Being one of the most theoretically investigated nanosystems, the properties of the edge state remain chiefly unexplored on the experimental level. One of the difficulties experimentalists face is that nanoribbons often do not have the required atomically-precise edges. Furthermore, due to the radical character of the edges, zigzag-type GNRs show a strong reactivity that leads to deterioration [255]. Even when GNRs are fabricated under ultra-high vacuum conditions, they immediately degrade under exposition to air [256]. Altogether, a thorough experimental investigation of the edge state is often hindered.

We overcome these problems by using nitronyl-nitroxide radicals as spin injectors, which allows us to experimentally identify the edge state and investigate its magnetic properties. We took advantage of recent developments in bottom-up fabrication of GNRs [106, 257, 258], which enables nearly defect-free and almost scattering-free chemically-stable systems, onto which nitronyl-nitroxide radicals

can be grafted. Since in such systems all functionalities are well-defined, spin-spin interactions can be investigated and quantified, so that theoretical models of GNRs can be tested. To gain a comprehensive picture of the magnetic interactions, we use state-of-the-art continuous-wave and time-resolved electron spin resonance techniques throughout this work.

This chapter is organised as follows. First, it begins with a general definition of the structure of our samples and how these are fabricated. All samples were provided by collaborators from the Müllen group of the Max-Planck-Institute for Polymer Research in Mainz, Germany. Second, density functional theory (DFT) calculations, which were carried out by collaborators of the Lambert group from the University of Lancaster, were used to gain an estimate on the spin injection effect. Finally, in the main part we present an extensive investigation based on electron spin resonance spectroscopy, which eventually leads to the identification of the edge state. Many figures shown in this chapter have been published in Ref. [259], and are reprinted with permission.

6.2 Structure and synthesis

6.2.1 Bottom-up fabrication

The GNR samples produced for this project are depicted in Fig. 6.1a. The backbone represents a well-defined cove-type graphene nanoribbon with a width of seven carbon atoms. Nitronyl-nitroxide radicals (NIT) were grafted on the edges of the GNR-backbone, in which an electron is localised in a π-orbital along the O-N-C-N-O bond. Since this orbital partially overlaps with the π-orbitals of the GNR-backbone, spin density gets injected. We chose NIT-radicals as spin centres due to their chemical stability, and, more importantly, because their chemical structure enables grafting via covalent bonds, thus enabling spin injection into the GNR-backbone. Furthermore, various kinds of NIT-radicals have already been studied and characterised so that we can rely on reported properties [260, 261].

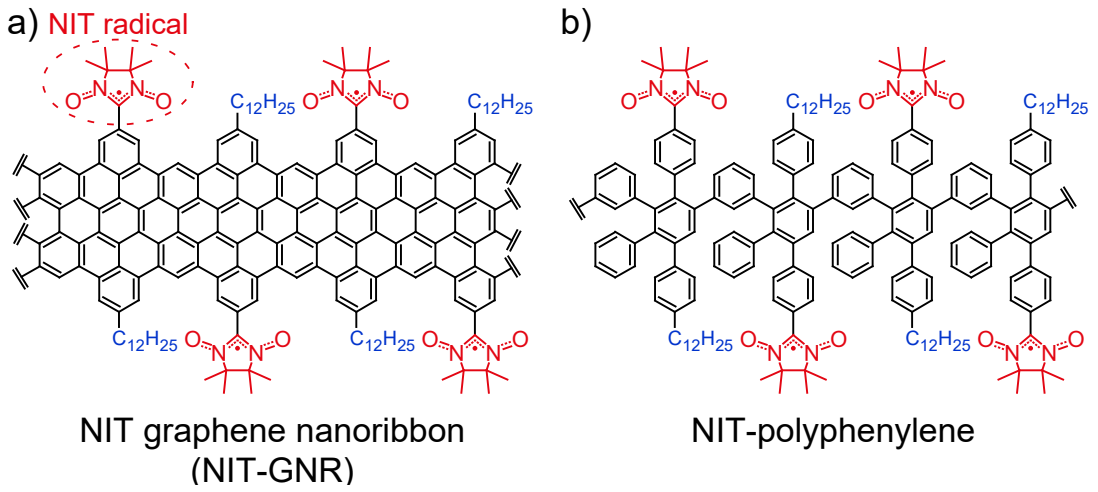

Fig. 6.1: Chemical structures of the samples used throughout this project. (a) Chemical structure of a nitronyl-nitroxide graphene nanoribbon (NIT-GNR). The nitronyl-nitroxide groups are labelled red. (b) Chemical structure of nitronyl-nitroxide polyphenylene (NIT-polyphenylene). In both cases, a periodic unit is shown. The actual mean length of the ribbons lies above 100 nm. $C_{12}H_{25}$-groups (blue) are employed to stabilise the compounds. Hydrogen atoms, which bond on the GNR edges, were omitted for clarity.

In order to study the effect of a possible edge state, a non-polymerised NIT-polyphenylene control sample was synthesised (Fig. 6.1b). Compared to NIT-GNR, NIT-polyphenylene lacks the delocalised electron system and thus no edge states can develop. This allows us to clearly identify the role of NIT-radicals, so that we can focus on how they manipulate the properties of the GNRs and how they promote the development of an edge state in the GNR.

All samples were fabricated using a bottom-up synthetic approach as explained in Fig. 6.2. A mean length of >100 nm was determined via size-exclusion chromatography of precursor **2** in Fig. 6.2. The bottom-up synthetic approach assures a well-defined structure of NIT-GNR and NIT-polyphenylene without the presence of magnetic impurities, which might derive from transition metal atoms [106]. However, we have to note that the radical substitution might be incomplete.

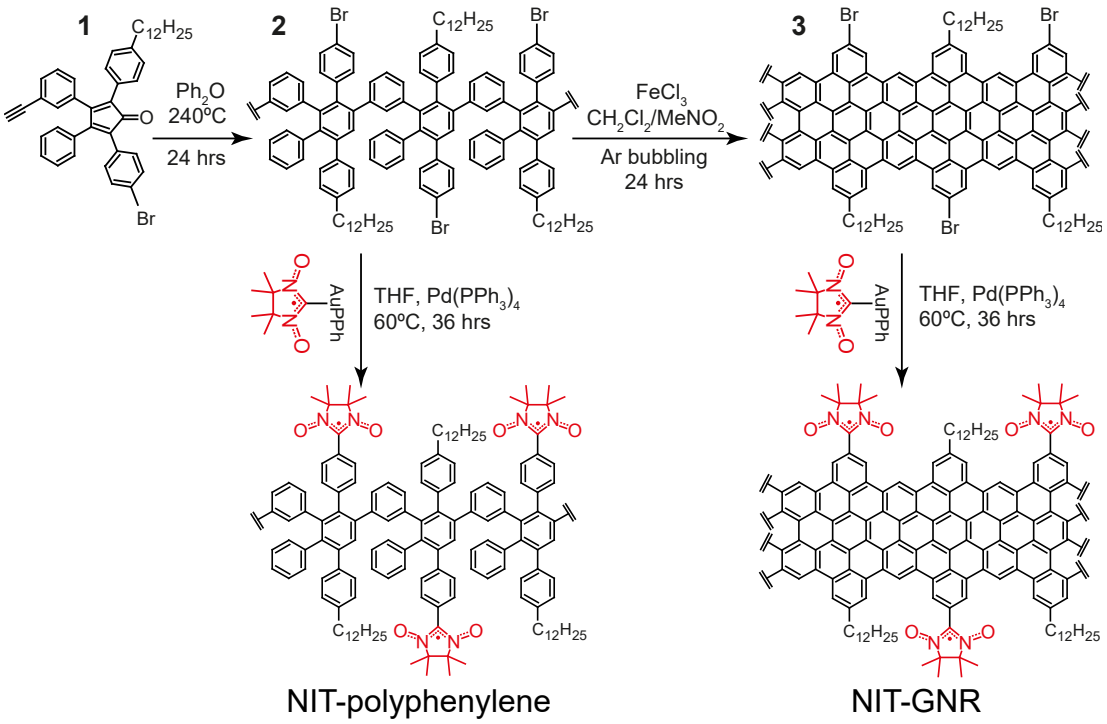

Fig. 6.2: Chemical synthesis of NIT-GNR and NIT-polyphenylene. The synthesis is based on the Diels-Alder polymerisation of bromo-functionalised tetraphenylcyclopentadienone-based monomers (**1** in Fig. 6.2). Via palladium-catalysed cross-coupling of the resulting bromo-substituted polymer **2** and triphenylphosphine-gold(I)-(nitronyl nitroxide-2-ide) [262], NIT-polyphenylene is obtained. By graphitisation of **2**, bromo-substituted GNRs (**3**) are produced, which can be turned into magnetically functionalised NIT-GNRs via palladium-catalysed cross-coupling.

6.2.2 Theoretical calculations on spin injection effects and band structure

DFT calculations represent a versatile technique to predict the electronic or magnetic behaviour of molecular materials. The calculations are based on electron densities of a material and are thus especially useful in the prediction of the orbital occupation in the system and the resulting band structure. Here, we used DFT calculations to gain an estimate on how spin density is injected from the radical sites into the GNR-backbone. For this project, DFT calculations were performed by collaborators from the Lambert group of the University of Lancaster. In

principle, spin Hamiltonian parameters described in the next section can also be predicted, but they are usually not as precise as those obtained from experiments, and, therefore, no calculations of these were carried out.

The results shown in this thesis are based on the following DFT methods. The Gaussian code [263] with unrestricted local-spin-density approximation (ULSDA), 6-311++g(d,p) basis set and XQC method for the self-consistent reaction field was employed. In the unrestricted local-spin-density approximation, electrons of opposite spin occupy different spatial orbitals. More details on the LSDA can be found in Ref. [264]. A generalised gradient approximation of the correlation and the exchange functional is used with the Perdew-Burke-Ernzerhof parametrisation with an energy cutoff of 150 Ry and a force tolerance smaller than 100 meV/nm. Band structures were calculated using the SIESTA [265] implementation. Structures were sampled by a $1 \times 1 \times 15$ Monkhorst-Pack k-point grid. Periodic boundary conditions have been applied. The repeated structure is depicted in Fig. 6.3.

The results are shown in Fig. 6.3. They indicate that band structures, given in energy in eV against normalised wavevector kl ranging from 0 to π, are completely different for the two materials. For NIT-polyphenylene, the bands are non-dispersive, i.e. the effective mass of electrons is close to zero. Therefore, the visualisation of the highest occupied orbitals displays a large localisation of the states in the nitronyl-nitroxide side groups. In contrast, the band structure of NIT-GNR shows both non-dispersive (blue) and magnetic dispersive (orange) states. In the non-dispersive state, electron density is mainly localised in the NIT-radicals, while the dispersive state is completely delocalised. Since we observe a state, which is largely delocalised along the edges and minorly at the NIT-radical sites, DFT hints at the existence of an edge state in our molecular NIT-GNR geometry.

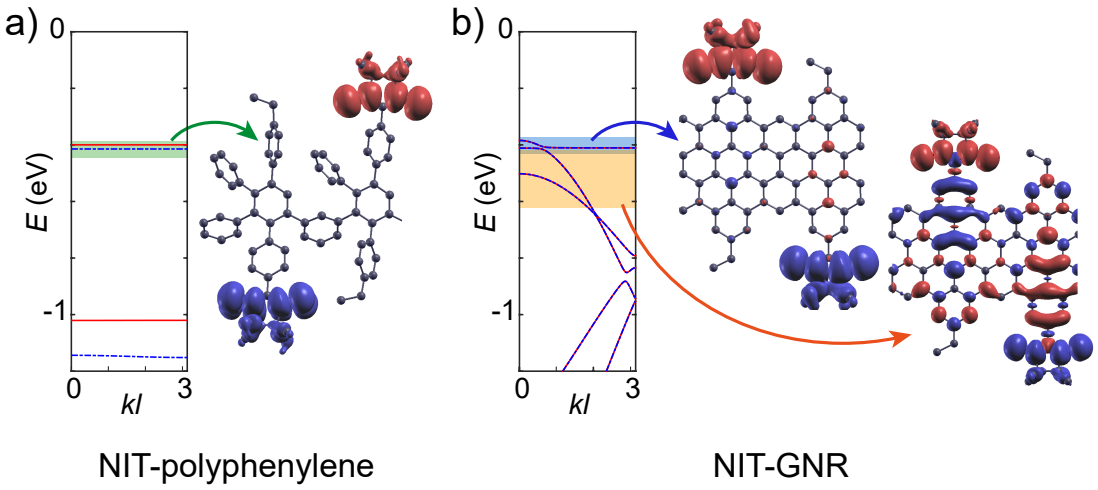

Fig. 6.3: DFT calculations on NIT-GNR and NIT-polyphenylene. (a) Band structure (energy, in eV, against the normalised wavevector kl) of NIT-polyphenylene. The visualisation of the highest occupied orbital (green arrow) shows that spin density is localised in the nitronyl-nitroxide. Different spin species are marked with different orbital colours. (b) Band structure of NIT-GNR. In contrast to NIT-polyphenylene, a localised state (blue) and a delocalised state (orange) can be observed.

6.3 Electron spin resonance characterisation

6.3.1 Spin Hamiltonian

The physics of magnetic systems are described and modelled with the spin Hamiltonian, which takes all relevant interactions into account. By fitting ESR spectra, these interaction parameters can be obtained with good confidence. The spin Hamiltonian for our system is given as:

$$\mathcal{H} = \underbrace{\sum_i \mu_B \boldsymbol{B}\mathbf{g}_i\boldsymbol{S}_i}_{\mathcal{H}_Z} + \underbrace{\sum_{i,n} \boldsymbol{S}_i\mathbf{A}_n I_n}_{\mathcal{H}_{\mathrm{HF}}} + \underbrace{\sum_{i\neq j} \boldsymbol{S}_i\mathbf{D}_{ij}\boldsymbol{S}_j}_{\mathcal{H}_d} + \underbrace{\sum_{i\neq j} J_{ij}\boldsymbol{S}_i\cdot\boldsymbol{S}_j}_{\mathcal{H}_{\mathrm{ex}}}, \tag{6.1}$$

where the single terms are explained in detail in Ch. 2.1.2. For the purposes of this project, the dipolar coupling tensor $\mathbf{D}_{ij}$ and the isotropic exchange coupling tensor $\mathbf{J}_{ij}$ are defined as

$$\mathbf{D}_{ij} = \frac{\mu_0\mu_B^2 g_i g_j}{4\pi r_{ij}^3}\begin{pmatrix} -1 & 0 & 0 \\ 0 & -1 & 0 \\ 0 & 0 & 2 \end{pmatrix} = d_{ij}\mathrm{diag}\left(-1,-1,2\right), \tag{6.2}$$

$$\mathbf{J}_{ij} = J_{ij}\mathrm{diag}\left(1,1,1\right), \tag{6.3}$$

where g_i and g_j are the g-values of spins i and j that are separated by the distance r_{ij}, μ_0 stands for the vacuum permeability and $\hbar$ represents the reduced Planck constant. Since both exchange (range usually smaller than 1.5 nm) and dipolar interactions ($\propto (-r_{ij})^{-3}$) decrease rapidly with distance [156, 266], only nearest neighbour interactions will be considered here. Therefore, the summation over the spins can be reduced to nearest neighbour interactions along the edges, called D_1 and J_1, and between opposite positions across the ribbon, named as D_2 and J_2, as depicted in Fig. 6.4. Consequently, this model takes three spins into account and each spin has two coupling partners, so that the interaction pattern is triangular. The spins along the ribbons are separated by ca. 1.5 nm, and nearest neighbours

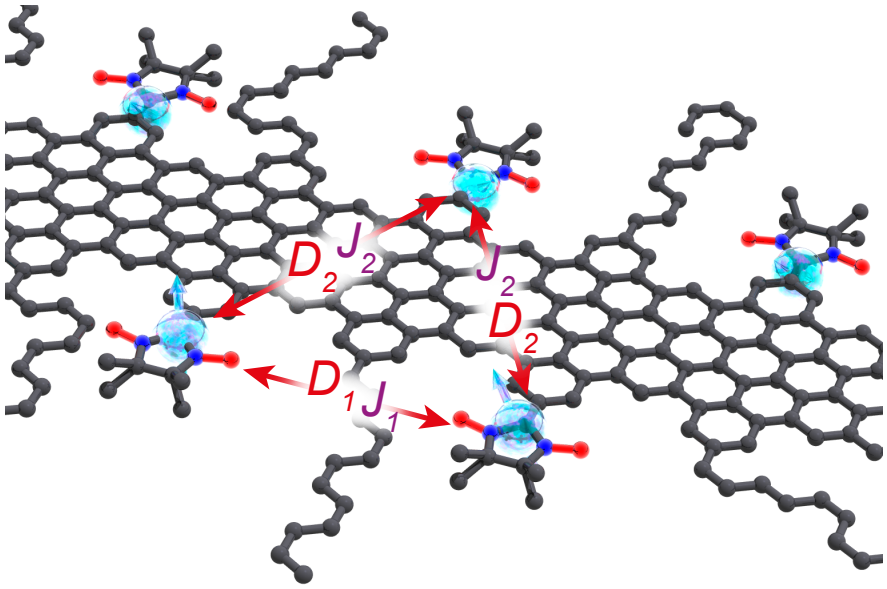

Fig. 6.4: Definition of the nearest neighbour interaction terms. For the samples used in this project, it is enough to consider nearest neighbour dipolar and exchange interactions along the edges, D_1 and J_1, and to opposite sides across the ribbon, D_2 and J_2.

across the ribbon are separated by about 1.6 nm. Those values can be either directly obtained from the structure, or by calculating from the carbon-carbon spacing of 0.142 nm. The next nearest neighbours are split by about 3.0 nm along and ca. 2.7 nm across the ribbon. Since their dipolar couplings are nearly one order of magnitude smaller compared to the dipolar coupling between the nearest neighbours, we restrict our model to three interacting spins. Furthermore, the dipolar coupling of spins separated by more than 2 nm cannot be resolved using continuous-wave ESR techniques [156], which justifies the use of the three-spin model herein.

The situation for NIT-polyphenylene is similar, except for the fact that exchange coupling is likely not strong enough to be mediated by the backbone. Therefore, exchange coupling will be neglected in the analysis of NIT-polyphenylene spectra.

6.3.2 CW and FID-detected ESR

In order to obtain the spin Hamiltonian parameters of Eq. 6.1, CW and FID-detected ESR on powder samples were carried out. These techniques are able to resolve dipolar interaction parameters for spin-spin distances between 1 nm and 2 nm [156] and thus ideal to quantify the nearest neighbour interactions. To reduce the errors, measurements were performed at three frequencies: ∼9.5 GHz (X-band, 293 K), ∼34 GHz (Q-band, 293 K) and ∼94 GHz (W-band, 85 K). The field-swept CW (X and Q-band) and FID-detected (W-band) spectra are shown in Fig. 6.5. Since the different frequencies require different magnetic fields, we shifted the spectra and defined a new field axis as indicated in Fig.6.5, so that we can display all spectra in one diagram. Simulations were performed using the Matlab package Easyspin [171].

We started by simulating the NIT-polyphenylene spectra. Assuming that the only possible signal arises from the localised NIT-radicals, we are able to fully reproduce the spectra using the parameters given in Tab. 6.1. The lineshapes are best described with Gaussians. We found that only hyperfine interactions with two nitrogen atoms play a role, and their tensors are tilted in-plane by $\varphi = 9°$ relative to the g-tensor frame, as indicated in Fig. 6.5b. Possible hyperfine interactions with ^{13}C or ^{1}H were not observed here. The best agreement between simulation and data was achieved for the W-band spectrum, where, owing to the use of higher fields, orientation-selective absorptions lines related to the g-anisotropy are widely separated.

The main source of uncertainty in the measurements is the presence of a strain in the applied magnetic field of the spectrometers. To minimise this source of error, all spectra were calibrated with samples resonating at a known field. In single-frequency measurements this would, however, remain an important source of uncertainty, but its impact is minimised here by our multi-frequency approach. We extract the set of parameters that best reproduces the data from three instruments, each one with an independent magnetic field strain. This is especially useful to

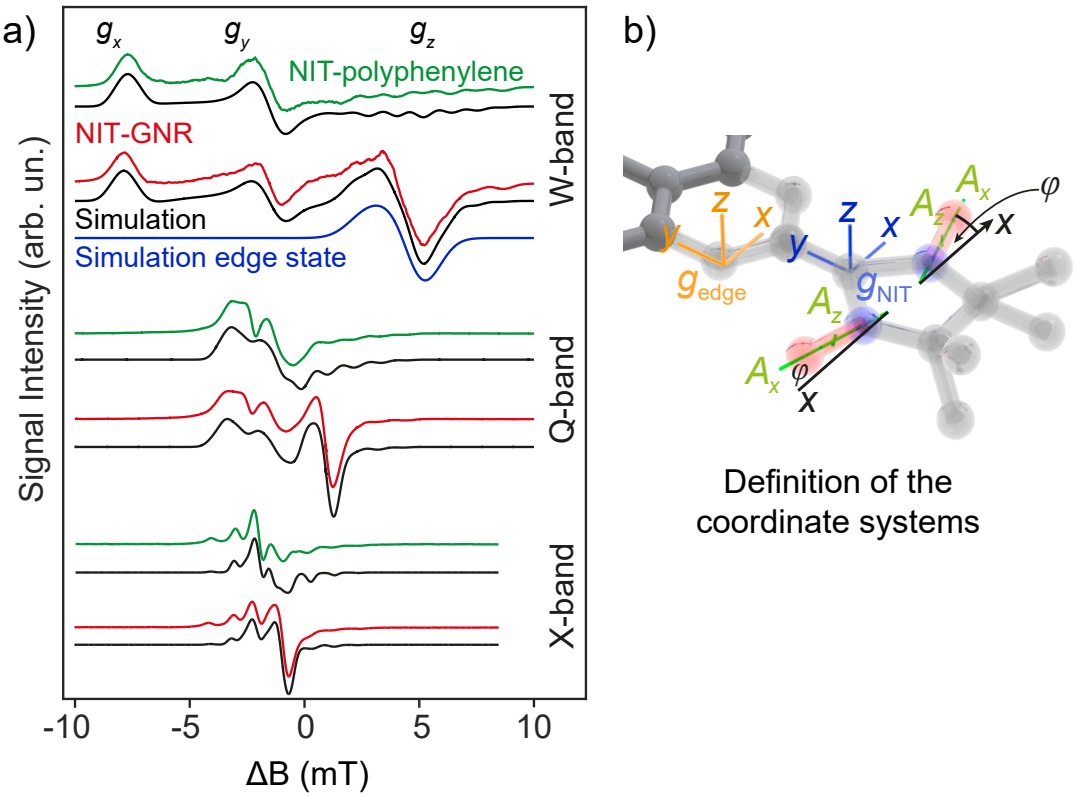

Fig. 6.5: X-, Q- and W-band ESR spectra of NIT-polyphenylene powder and NIT-GNR flakes. (a) A pair of NIT-polyphenylene (green) and NIT-GNR (red) spectra, obtained at 85 K and their simulations (black) are shown for 9.5 GHz, 34 GHz and 94 GHz, corresponding to X-, Q- and W-band frequencies, respectively. The g_x, g_y and g_z resonance lines are indicated at W-band frequency. The spectra have been shifted to enable a uniform axis ΔB, where the g_y resonances appear at the same field ΔB. The NIT-GNR spectra show a strong additional feature that can be best observed at W-band frequency between the g_y and g_z resonance, which we attribute to the edge state. To illustrate the contribution of the edge state to the overall NIT-GNR spectrum, its simulation is depicted via the blue curve at W-band frequency. (b) Definition of the coordinate systems for the different tensors in Eq. 6.1. While the coordinate systems of the different g distance are the same, the hyperfine tensors of the nitrogen nuclei are rotated in-plane by φ = 9°.

minimise the impact from the superconducting W-band magnet, whose hysteretic behaviour varies on the sweep rate and the field range, with maximum errors observed up to 1 mT in the vicinity of 3.3 T, i.e. 0.3 ‰. This error is significantly reduced in the X- and Q-band spectrometers, producing the errors in g estimated in Tab. 6.1 and 6.2.

As best shared set of parameters that contemporarily reproduces the three NIT-polyphenylene spectra, we found $g_{\mathrm{NIT}} = (2.0097(5), 2.0060(4), 2.0026(1))$, $A_N = (0, 3(2), 34(2))$ MHz, $D_1 = 11.0 \pm 2.0$ MHz and $D_2 = 8.5 \pm 2.0$ MHz. Exchange couplings could not be resolved and were disregaded. These results come close to reported values for similar nitronyl-nitroxide compounds [261], and the interaction strengths fall in line with distances at the order of 1.6 nm. In principle, one could extract the exact distances between the radical sites from the dipolar interaction energies. Due to the highly parameterised Hamiltonian, and the fact that we cannot completely exclude exchange interactions, a precise distance calculation from these values should not be expected. Almost the same results were obtained for the NIT-GNR (Tab. 6.2. We found $g_{\mathrm{NIT}} = (2.0098(5), 2.0059(4), 2.0026(1))$, $A_N = (0, 5(2), 34(2))$ MHz, $D_1 = 11.0 \pm 2.0$ MHz and $D_2 = 8.5 \pm 2.0$ MHz as best parameters to explain all data with one set. Additionally, we found exchange interactions of $J_1 = -25 \pm 5$ MHz and $J_2 = +15 \pm 5$ MHz.

The variation range of the coupling parameters was estimated from spectral calculations. Producing a fit of the spectra, instead of a simulation, is problematic. As it is in ESR spectroscopy, usually, simulations and not fits are the norm in the literature. One reason for this is that here, three electron spins couple mutually, and each electron spin is coupled to two nitrogen atoms, and the resulting computation of one spectrum requires the diagonalisation of a 72×72 matrix, i.e. 5184 elements. The spectrum cannot be simplified by fixing, for example, $g = 2$ because this is a parameter of interest here. Furthermore, nonlinear background effects may distort the spectra, which cannot be completely removed and overestimated by fits. As a consequence, we provide the uncertainty over the D_i, J_i and A_i values as calculated

not from a fitting of the whole spectrum but by considering an error interval where spectral features can be reproduced. This means that outside of the given error ranges, a calculated spectrum produces either satellite peaks that are not present in the experiment, or the spectral distances along the field-axis between distinct features no longer match the corresponding spectral distances in the measurement.

Role of exchange coupling

The found exchange interactions in NIT-GNRs show that the radical spins couple ferromagnetically along the edges of the GNR, and antiferromagnetically to radicals sitting on opposite sites, making NIT-GNRs interesting spin filters. The exact source of this behaviour cannot be extracted from ESR spectroscopy, and is thus a matter for theoreticians. We notice, however, that this behaviour agrees with predictions made by calculations of edge states using *ab initio* methods [111, 123]. We notice that this can be attributed to Rashba-type spin-orbit coupling effects discussed in Sec. 2.3.6, and agrees as well with the predictions made by the phenomenological and simple Goodenough-Kanamori rules that are widely employed in understanding the exchange interactions in aromatic systems functionalised with NIT-radicals [260, 267], as illustrated in Fig. 6.6. It is shown in detailed studies that nitronyl-nitroxide bi-, tri- and tetraradicals [268, 269], which are separated by aromatic spacers or carbon-carbon double-bonds or triple-bonds, couple antiferromagnetically to each neighbouring site. By following the through-space exchange pathway from one radical group to another other radical group, and assuming that antiferromagnetic coupling takes place between each neighbouring site, we arrive at the coupling scheme as depicted in Fig. 6.6. This scheme follows a pattern that is similar to Goodenough-Kanamori rules, although the Goodenough-Kanamori rules are usually applied to salts. We not, however, that the consideration of exchange coupling only slightly improves the quality of the simulated curves and consequently the error can be relatively large.

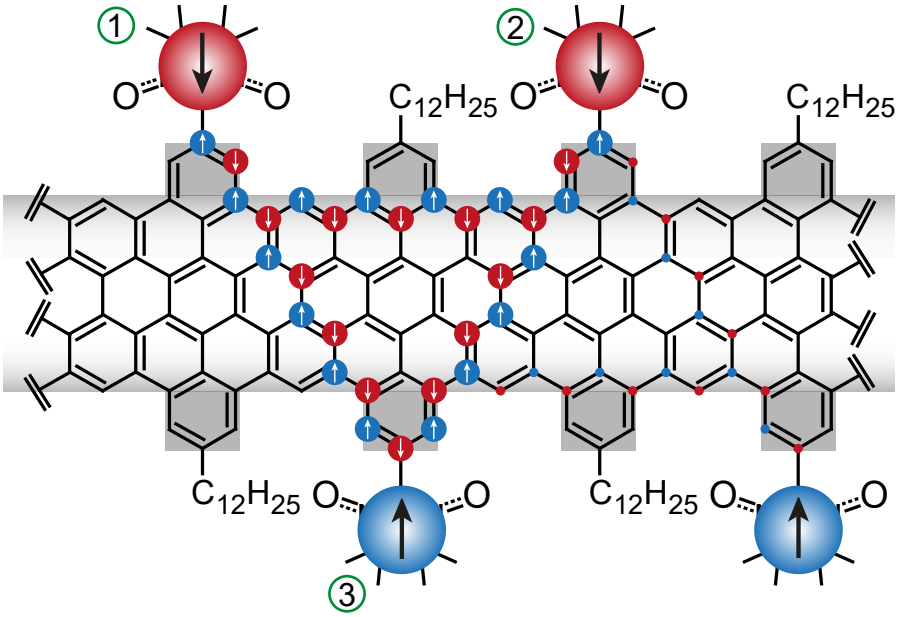

Fig. 6.6: Illustration of exchange coupling rules for aromatic systems. Electron spins couple antiferromagnetically on neighbouring sites in aromatic rings. In the NIT-GNR, ferromagnetic coupling is therefore expected along the edges of the GNR (NIT 1 and NIT 2). In contrast, NIT-radicals couple antiferromagnetically across the ribbon (NIT 1 and NIT 3). The grey shade illustrates the delocalisation of the edge state.

First hint of the edge state

In addition to the signals arising from the radicals, we can see an intense feature in between the g_y and g_z resonances in the NIT-GNR data. Because of its uniaxial symmetry, we attribute this signal to the resonance line of the edge state. Impurities caused by metal ions can be neglected, as these usually show broad spectra with linewidths of ∼10 mT. Instead, its linewidth of the order of 1 mT falls in line with radical states. The edge-state absorption does not show any kind of hyperfine coupling, which can be related to a delocalisation in the graphene backbone and the typically low natural abundance of ^{13}C. We found that the edge state is best described as spin $S = 1/2$ with a uniaxial g-tensor with values $g_{||} = 2.0024(3)$ and $g_{\perp} = 2.0041(2)$.

The obtained spectra give the first hint of the existence of an edge state in the

NIT-GNR. However, interactions between NIT-radicals and the edge state could not be resolved and thus require more sophisticated, time-resolved ESR methods such as DEER spectroscopy, which will be discussed in the following sections.

Tab. 6.1: Simulation parameters for the NIT-polyphenylene spectra. The dipolar couplings are given in tensor notation as multiples of diag(-1, -1, 2). The Gaussian linewidths are defined as full-width at half-maximum, FWHM.

	X-band	Q-band	W-band
g_x	2.0092(1)	2.0095(3)	2.01035(60)
g_y	2.0058(1)	2.0058(3)	2.0065(6)
g_z	2.0027(1)	2.0026(3)	2.0025(6)
A_x (MHz)	0	0	0
A_y (MHz)	3 ± 2	3 ± 2	4 ± 2
A_z (MHz)	31 ± 2	35 ± 2	35 ± 2
φ	9°	9°	9°
D_1 (MHz)	11.5 ± 2.0	11 ± 2	10.5 ± 2.0
D_2 (MHz)	8.5 ± 2.0	8 ± 2	9 ± 2
J_1 & J_2 (MHz)	0	0	0
Linewidth (mT)	0.37	0.65	0.8

Tab. 6.2: Simulation parameters for the NIT-GNR spectra. The first part of the table gives the parameters of the NIT-radicals, while the edge-state parameters are given in the second. The dipolar couplings are given in tensor notation as multiples of diag(-1, -1, 2). The Gaussian linewidths are defined as FWHM, and the spectral strength denotes the line intensity relative to the NIT-radicals.

	X-band	Q-band	W-band
g_x	2.0093(1)	2.0096(3)	2.01035(60)
g_y	2.0056(1)	2.0056(3)	2.00650(60)
g_z	2.0025(1)	2.0026(3)	2.00255(60)
A_x (MHz)	0	0	0
A_y (MHz)	6 ± 2	5 ± 2	5 ± 2
A_z (MHz)	32 ± 2	35 ± 2	35 ± 2
φ	9°	9°	9°
D_1 (MHz)	11 ± 2	11 ± 2	11 ± 2
D_2 (MHz)	8 ± 2	8.5 ± 2.0	9 ± 2
J_1 (MHz)	−25 ± 5	−25 ± 5	−25 ± 5
J_2 (MHz)	15 ± 5	15 ± 5	15 ± 5
Linewidth (mT)	0.40	0.65	0.82
$g_\perp$	2.0023(1)	2.0021(3)	2.0027(6)
$g_{\|\|}$	2.0044(1)	2.0040(3)	2.0040(6)
Linewidth (mT)	0.60	0.75	1.9
Spectral weight	3.5 : 1	3.15 : 1	3.4 : 1

6.3.3 Spin-orbit effects

From the g-anisotropy of the edge state we can estimate the energy scales of spin-orbit coupling. The parameters Δ_{SO} and Δ_R, defined in Eq. 2.15, describe the axial and transverse spin-orbit coupling, respectively. Using perturbation theory, one finds

$$|\Delta E\,(g_i - g_e)| = 2\Delta_i\,, \tag{6.4}$$

where ΔE describes the energy difference to a perturbing state, g_i the g-value of either parallel or perpendicular orientation, g_e the Dirac g-value of a free electron (2.0023) and Δ_i the spin-orbit coupling. From DFT calculations (Fig. 6.3b) the order of magnitude for ΔE is 0.1 eV. We therefore identify $\Delta_{SO} \sim 15\,\mu$eV and $\Delta_R \sim 1\,\mu$eV. These experimental values are smaller than expectations for carbon nanotubes, where curvature-induced spin-orbit coupling dominates. They confirm estimates from tight-binding models, which are still under discussion [132, 133, 270]. Therefore, the estimated values provide an interesting ground for future investigations.

6.3.4 Spin-lattice relaxation

Information on spin-lattice and spin-spin relaxation is of crucial importance to appraise the performance of the compounds. The spin-lattice relaxation time T_1 gives a typical timescale on how long a magnetisation can be retained by the spins in a phonon bath. It furthermore determines the optimal repetition rates to achieve best signal-to-noise-ratios (SNRs) in time-resolved ESR experiments. Because of its advantages over standard methods, we chose the Picket-Fence pulse sequence to determine T_1 (see Sec. 3.1.6). Measurements to determine T_1 were performed at X-band frequency. The field was set to drive the edge-state resonance for NIT-GNR, and the g_y-resonance of NIT-polyphenylene, as the largest absorptions were observed at those resonances in the field-swept FID-detected spectrum, shown in Fig. 6.7. This allows us to maximise signal-to-noise ratios. A discussion on the

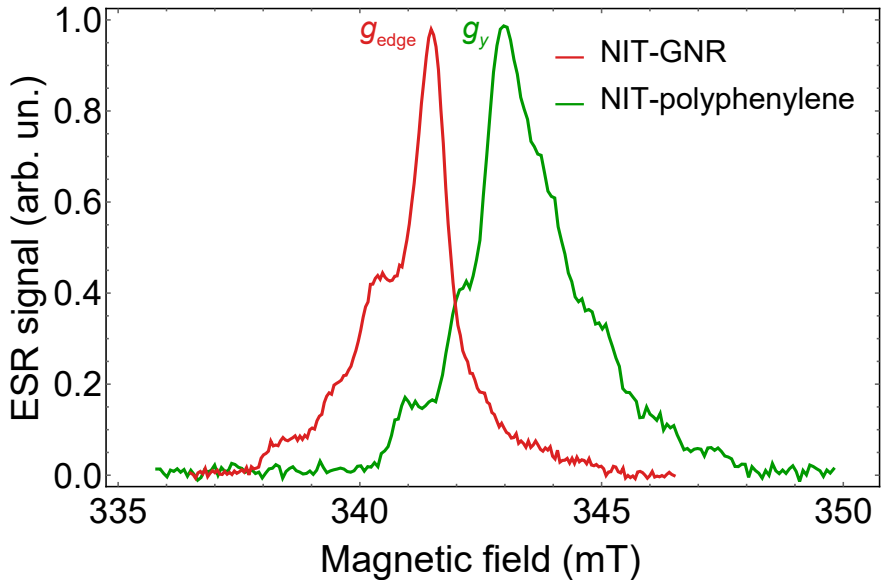

Fig. 6.7: Field-swept FID-detected spectrum obtained at X-band frequency and 85 K. The T_1 and later T_m times were measured at the point of highest absorption, about 341.5 mT for NIT-GNR and 343.0 mT for NIT-polyphenylene, to allow for highest SNRs. The two spectra appear shifted relative to each other because the frequencies were slightly different in the two experiments.

orientation-dependence and field-dependence is given at the end of the section.

A typical relaxation curve is shown in Fig. 6.8a. To account for residual spin diffusion processes, a double exponential function was fitted:

$$Y(t) = a_1 \mathrm{e}^{-b_1 t} + a_2 \mathrm{e}^{-b_2 t} + c\,, \tag{6.5}$$

where $Y(t)$ describes the ESR signal intensity, t the time, a_i the absolute signal intensity contributions, b_i the rate constants and c the saturation intensity. We identify the smaller contribution to the data, a_2, to be the one related to spin diffusion. Thus, the other contribution, a_1 is related to spin-lattice relaxation, and we find $1/b_1 = T_1$.

The temperature dependence of T_1 is displayed in Fig. 6.8b. The fitted values of 10^{-5} s at room temperature agree with theoretical expectations [271]. We identified three different relaxation regimes: direct relaxation A_{lin} below 25 K, Raman

relaxation A_{Ram} between 25 K and 200 K, and the excitation of local vibrational modes A_{loc} above 200 K. The function, describing the relaxation rate behaviour, is then given as [158, 162]

$$\frac{1}{T_1} = A_{\mathrm{lin}}T + A_{\mathrm{Ram}}\left(\frac{T}{\theta_D}\right)^9 \int_0^{\theta_D/T} \frac{x^8 \mathrm{e}^x \mathrm{dx}}{\left(\mathrm{e}^x - 1\right)^2} + A_{\mathrm{loc}}\left(\frac{\mathrm{e}^{\Delta_{\mathrm{loc}}/T}}{\left(\mathrm{e}^{\Delta_{\mathrm{loc}}/T} - 1\right)^2}\right), \qquad (6.6)$$

with A_{lin}, A_{Ram} and A_{loc} the rate constants for the different processes, θ_D the Debye-temperature, x an integration variable and Δ_{loc} the excitation energy of the corresponding vibrational mode. By simulating the behaviour around room temperature, we find the same parameters $A_{\mathrm{loc}} = (3.5 \pm 0.5) \cdot 10^7\,\mathrm{s}^{-1}$ and $\Delta_{\mathrm{loc}} = 1950\,\mathrm{K}$ ($1354\,\mathrm{cm}^{-1}$) for both NIT-GNR and NIT-polyphenylene. The determined value for Δ_{loc} matches with the N-O vibrational stretching energy in NIT-radicals [272] and is thus an important contributor at room temperature. Fixing these values in the subsequent fitting procedure helps to reduce the number of variables of the otherwise overparameterised equation. The other rate constants are similar for both compounds. We fitted $A_{\mathrm{lin}} = 17.1(2)\,\mathrm{s}^{-1}$, $A_{\mathrm{Ram}} = 3.25(15) \cdot 10^{-17}\,\mathrm{s}^{-1}$ and $\theta_D = 284.2\,\mathrm{K} \pm 5.0\,\mathrm{K}$ for NIT-polyphenylene, and $A_{\mathrm{lin}} = 62.0(2)\,\mathrm{s}^{-1}$, $A_{\mathrm{Ram}} = 1.70(11) \cdot 10^{-16}\,\mathrm{s}^{-1}$ and $\theta_D = 205.8\,\mathrm{K} \pm 5.0\,\mathrm{K}$ for NIT-GNR. We note that direct relaxation is present for all temperatures, while Raman relaxation is visible above 25 K and local vibrational modes above 200 K. The experimental error, especially in the case of NIT-polyphenylene, may be larger than the errors estimated via simulations and fits, as can be seen from the deviation of the fitted curve from the data points below 50 K. Furthermore, we found that direct relaxation dominates in a broad temperature regime. Theoretically, at temperatures below 10 K, contributions from Raman or local modes are negligible, compared to direct relaxation processes [273]. However, we found that direct relaxation dominates up to 25 K. This observation is likely due to the high concentration of spins in our sample [273]. It can be related to a slight measurement artefact, where a π-pulse in the pulse sequence may affect neighbouring

spins instead of observer spins.

The T_1-behaviour at low magnetic fields (about 0.1 T) and low temperatures (100 mK) can be, as for graphene quantum dots, explained by deformation-potential mechanisms for longitudinal-acoustic phonons, and bond-length-change mechanisms for both longitudinal- and transversal-acoustic phonons [133, 134, 271]. These seem to couple with NIT-radical spins. The reported calculations, under the assumption of Van Vleck cancellation [271], show a nearly field-independent T_1 at those low fields. It would be interesting to investigate and compare the T_1-behaviour using a dilution refrigerator, which is able to provide such low temperatures.

Magnetic field dependence

Since we observe the edge state in the NIT-GNRs spectra, it is interesting to investigate how it affects T_1. As displayed in Fig. 6.5, there is a partial overlap between the edge state resonance and the resonance lines of the NIT-radicals. We thus measured the field-dependence of T_1, shown in Fig. 6.9. This measurement was performed at Q-band frequency, where, due to the larger magnetic fields, the spectrum is wider split than at X-band frequency. The temperature was set to 85 K, which allows for a decent signal-to-noise ratio. Furthermore, at 85 K we can cool down our sample using liquid nitrogen, which represents a more economic way compared to liquid helium cooling.

The field dependence of T_1 does not reveal any particular feature of the edge state. It seems that T_1 of the edge state does not dominate, and is likely shorter than T_1 of the NIT-radicals. A shortened T_1 can be explained by the rather delocalised nature of the edge state, and possibly larger spin-phonon coupling. Moreover, the increase of T_1 at higher fields can be related to the different spin-phonon couplings of the different hyperfine-dipolar-coupled excited states. These spin-phonon couplings, however, go beyond the scope of this project, and require in-depth theoretical investigations.

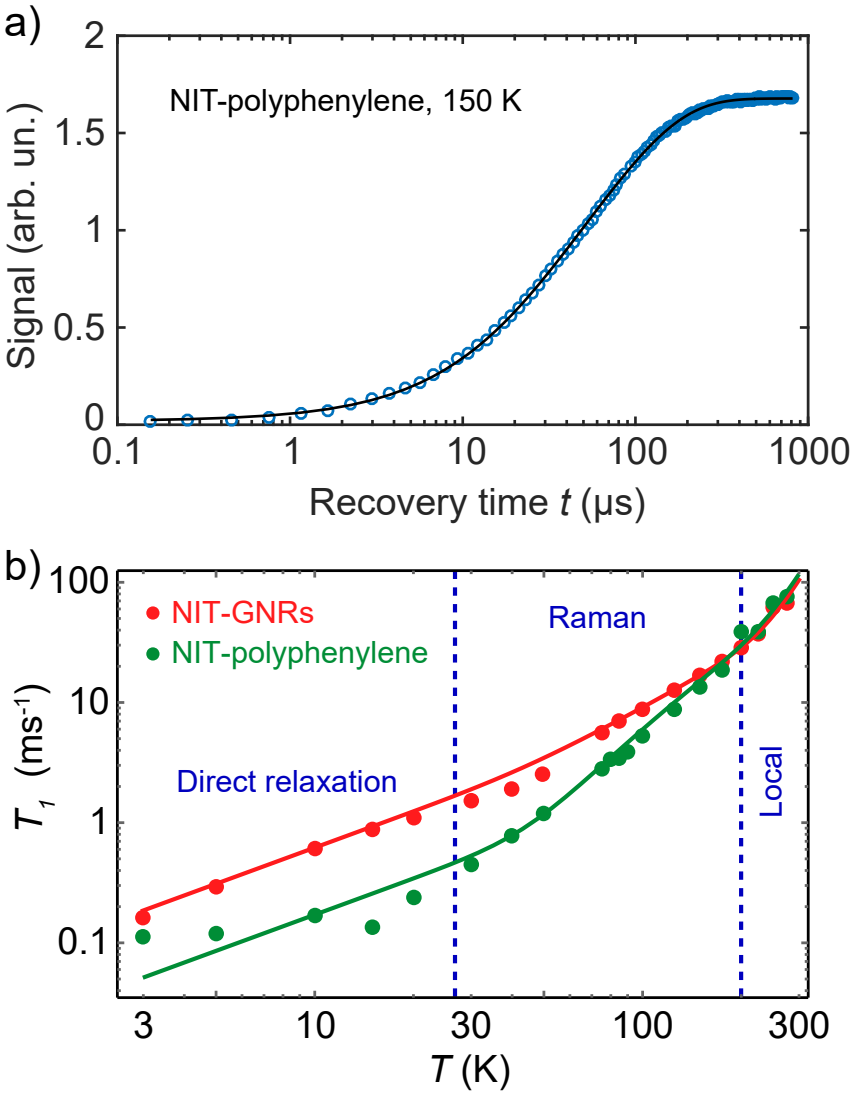

Fig. 6.8: Typical T_1 relaxation curve (a) and temperature dependence of T_1 times (b). (a) The relaxation data was fitted using a double exponential function to account for spectral diffusion. (b) We identified three different relaxation regimes denoted as direct relaxation, Raman relaxation and relaxation via excitation of local vibrational modes. The T_1-values range from 10^{-2} s at 3 K to 10^{-5} s at room temperature. The curves represent the best fit using Eq. 6.6 to the data points (full circles). All measurements were performed at X-band frequency. Fields were set to where maximum absorption occurs, shown in Fig. 6.7.

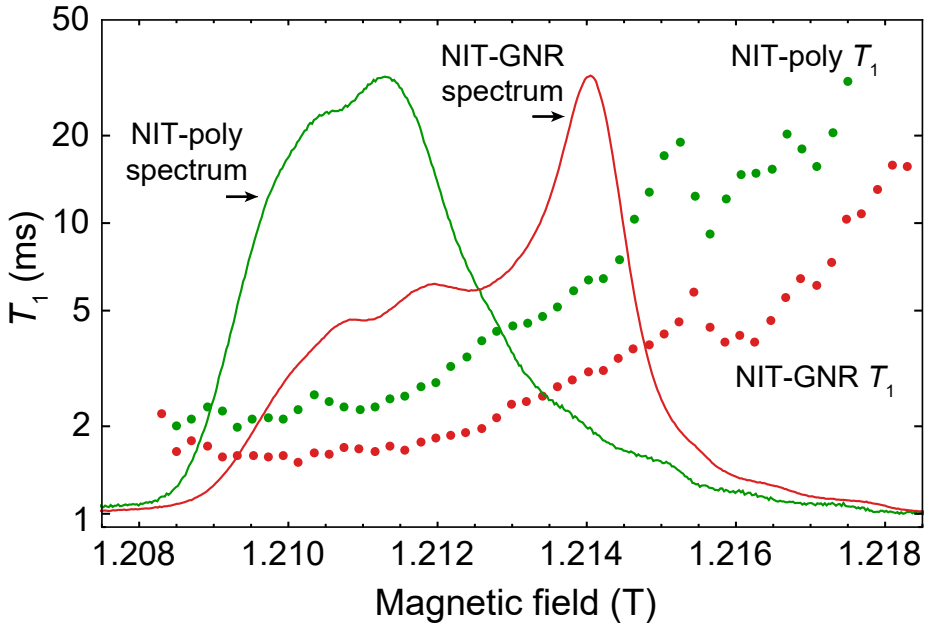

Fig. 6.9: Magnetic field dependence of T_1 at Q-band frequency and 85 K. The full circles represent the extracted T_1 times for NIT-polyphenylene (green) and NIT-GNRs (red). The Q-band FID-detected spectra are shown as solid curves in arbitrary units as reference. Here, the actual field axis as directly obtained from the experiment is shown, whereas in Fig. 6.5 we represented the data on a shifted field-axis ΔB, so that we could show all the data obtained at different frequencies in one diagram. The small relative shift between NIT-polyphenylene and NIT-GNR is related to the slightly different frequencies used in the two experiments. At higher fields, the data becomes noisier due to a lower absorption.

6.3.5 Spin-spin relaxation

The next important number to characterise our samples is the phase-memory time T_m, which can be obtained via a Hahn-echo sequence. Our results at X-band frequency are shown in Fig. 6.10. In the weak coupling limit, the echo-signal decay $Y(\tau)$ versus the precession time 2τ can be fitted, as it has been shown in Ref. [71], using the following formula

$$Y(\tau) = Y_0 \mathrm{e}^{-\left(\frac{2\tau}{T_M}\right)^x} \left[1 + k_1 \sin(2\omega\tau + \phi_1) + k_2 \sin(4\omega\tau + \phi_2)\right] + c\,. \tag{6.7}$$

The formula consists of an exponential decay part and a modulation part, where Y_0 describes the maximum signal amplitude. The exponential decay describes the loss of coherence over time, while the coupling between electrons and nuclear spins lead to a modulation of the spectrum, in literature also known as electron-spin-echo-envelope-modulation (ESEEM) [46, 71]. For example, the modulation can be caused by nuclear spin flips. Often, the decay does not follow a monoexponential law. Effects like nuclear spin diffusion yield a stretched decay, phenomenologically described with a stretch exponent x. In the weak coupling limit, the modulation is described by the nuclear frequency ω and its first harmonic 2ω [71], where k_1 and k_2 describe their modulation depths. Phase shifts are described by ϕ_1 and ϕ_2. In order to reduce the number of parameters, we do not consider the effect that the modulations may decay independently [71, 156]. In fact, the modulation with the frequency ω decays faster than the overall echo signal [156]. Since we are mainly interested in the determination of T_m, this approximation is justified. The parameter c corrects for a constant background and incomplete phase cycling.

A Hahn-echo decay, measured at X-band frequency at 85 K, is shown in Fig. 6.10a. Same as for the T_1 measurements, the field was set to where maximum absorption occurs (Fig. 6.7). Note that the actual field value may vary, depending on the temperature and calibration of the instrument. We found a significant modulation of the NIT-polyphenylene signal with a characteristic frequency of $\nu = \omega/2\pi = 3.46\,\mathrm{MHz}$ at a field of 342.9 mT. The same modulation frequency was found for NIT-GNRs, but with a significantly smaller modulation depth. Therefore, there seems to be a coupling mechanism in common that causes dephasing. In principle, one could remove this modulation by increasing the pulse duration. Since the coupling partners are of interest in this studies, we can deduce potential decoherence paths from these oscillations. Surprisingly, the modulation frequency matches with the ^{13}C nuclear resonance frequency at the chosen field, although its natural abundance is relatively low (ca. 1.1%). Deeper investigations on hyperfine couplings will be presented later in Sec. 6.3.6. Furthermore, we found that the

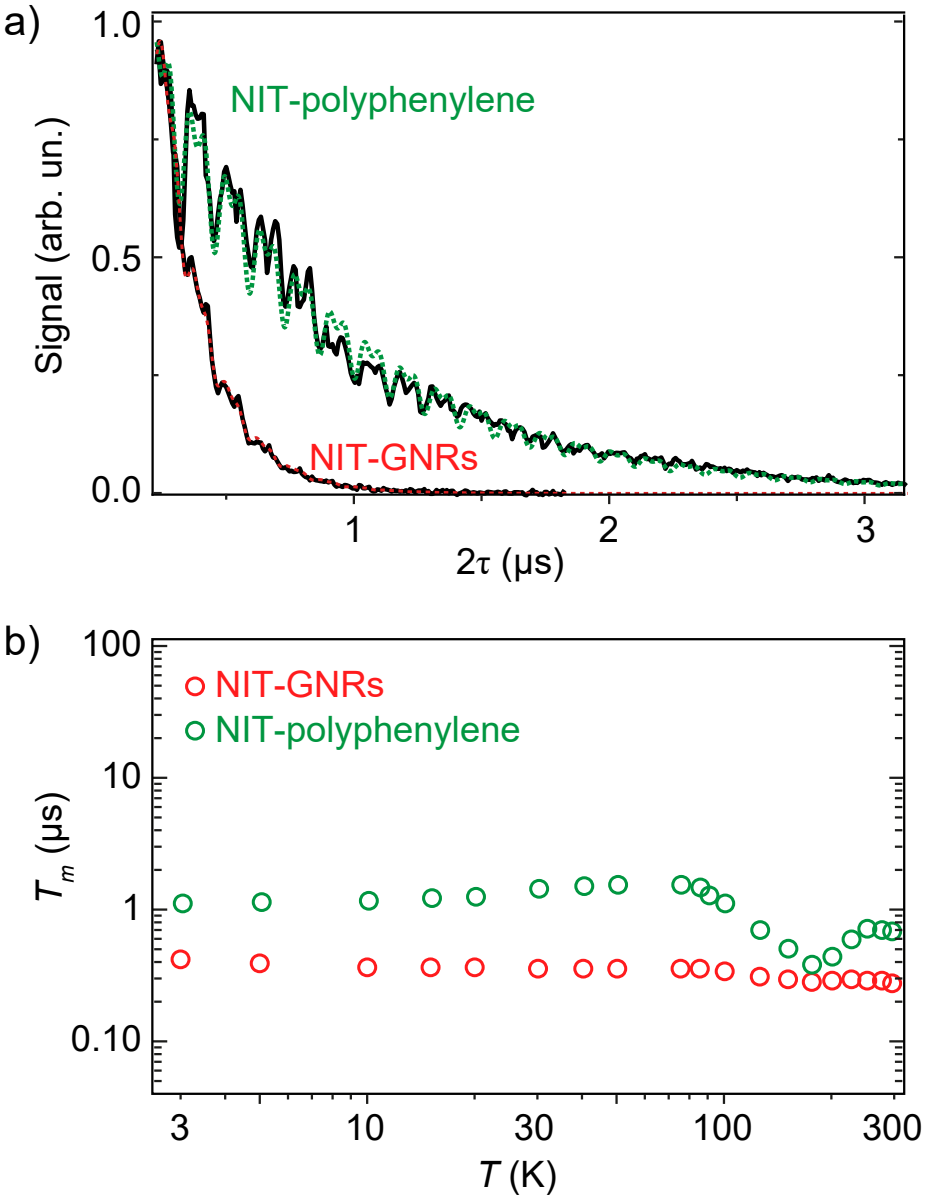

Fig. 6.10: Dephasing of excited spins at X-band frequency. (a) Measured spin-echo decay at 85 K using the Hahn-echo sequence. Same as for the T_1 measurements, the field was set to where maximum absorption occurs in Fig. 6.7. By increasing the free evolution time τ, excited spins dephase due to interactions with the environment. Both compounds show a notable modulation likely caused by nuclear spin flips. The dashed lines represent best fits using Eq. 6.7. (b) Temperature dependence of T_m. NIT-GNRs show an almost temperature-independent phase-memory time. NIT-polyphenylene shows a step change in T_m between 100 K and 200 K, which is likely related to dangling of bonds, since it does not represent a purely two-dimensional structure.

decay is best described by a monoexponential function. In this limit, where $x = 1$, successive events are not correlated, so that we can identify $T_m \approx T_2$ [274].

The temperature dependence of T_m is depicted in Fig. 6.10b. For NIT-GNRs, T_m increases slightly with decreasing temperature. A measurable phase-memory time is even retained at room temperature, with a typical value of about 300 ns. NIT-polyphenylene shows a minimum of T_m at 170 K followed by a maximum at around 60 K. We attribute this behaviour to a change of the physical structure, where movements of benzene-benzene σ-bonds in the polyphenylene-backbone are involved. In contrast to NIT-GNR, NIT-polyphenylene has a slightly twisted and non-rigid structure, with some extensions out of plane. The exact modelling of the temperature-dependence then requires simulations of the bonding dynamics, which we leave as a possible future task. Although the phase-memory times of NIT-polyphenylene are significantly higher, it does not show an edge state feature, and is thus less interesting for future applications. The shorter phase-memory times of NIT-GNR are likely due to interactions between the two spin species. It is actually the coexistence of NIT-radical states and the edge states which makes NIT-GNRs a promising material for quantum transport and quantum operations, and the determined phase-memory times are still large enough to fulfil these purposes. Moreover, with this material, several theories on GNRs can be verified. Although T_m is lower, we find that NIT-GNRs have more potential applications.

Using higher frequencies, T_m can even be enhanced. For NIT-GNR, we find values of about 0.7 µs at Q-band and 1.1 µs at W-band frequency at 85 K, which allows for advanced manipulation schemes such as DEER spectroscopy, shown in Sec. 3.1.7. The field dependence at Q-band and W-band frequencies is displayed in Fig. 6.11. Here, we use the actual field axis as directly obtained from the experiment, while in Fig. 6.5 we made use of a field axis ΔB so that we could show all the data obtained at different frequencies in one diagram. The field dependence of NIT-GNR shows no special signature of the edge state. Same as for the T_1 measurements, the T_m field-dependence of NIT-GNR shows no special

signature of the edge state. Consequently, the choice of the magnetic field does not have a significant effect on the coherence time, so that we can choose and compare orientations were maximum absorption occurs so as to provide best SNRs.

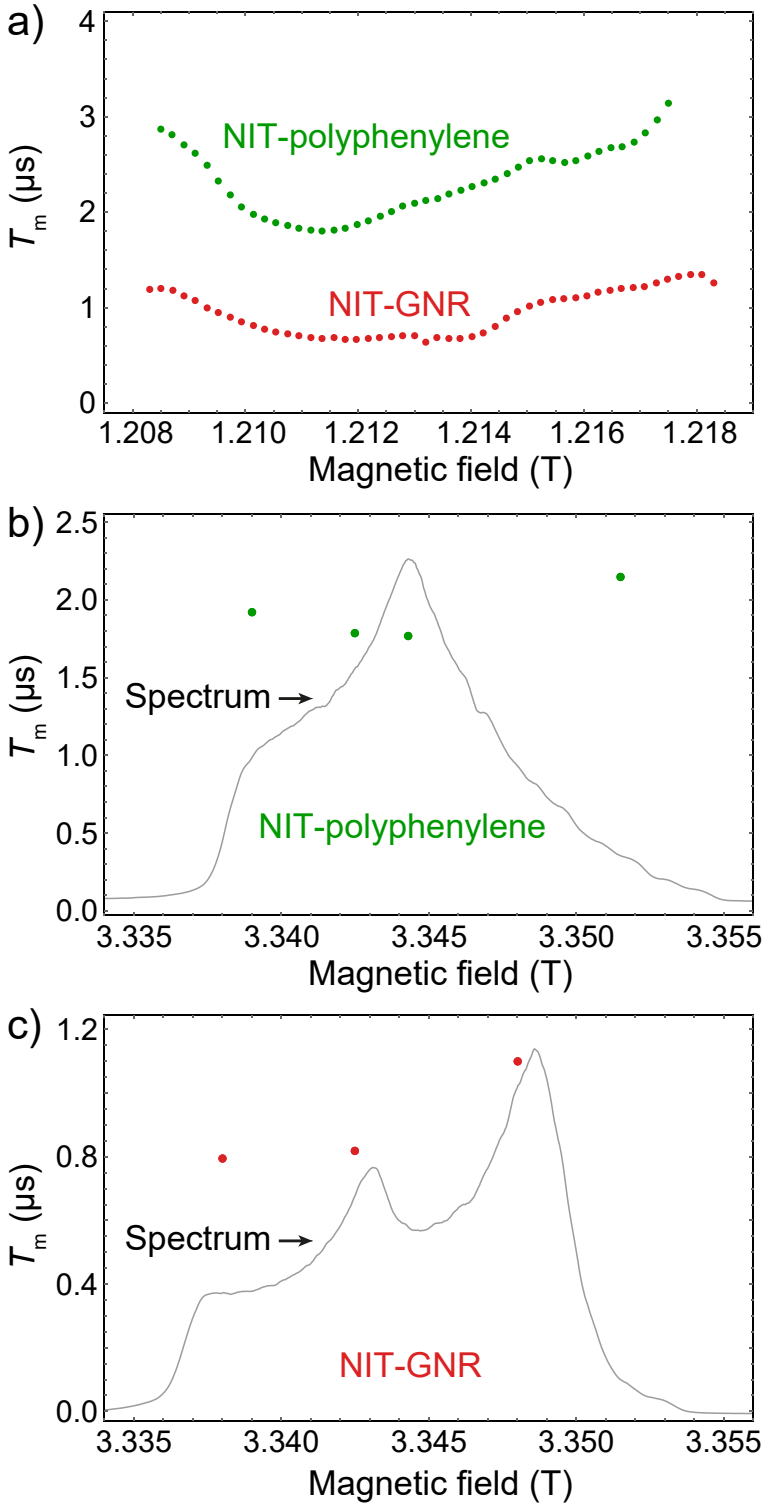

Fig. 6.11: Magnetic field and frequency dependence of T_m. Throughout all figures, red full circles correspond to NIT-GNR data and green ones to NIT-polyphenylene. The data were acquired at 85 K. (a) Field dependence of T_m at Q-band frequency. (b) and (c) show the field dependence of T_m at W-band frequency for NIT-polyphenylene and NIT-GNRs, respectively. The corresponding W-band spectra are shown in arbitrary units with a grey colour.

6.3.6 Investigation of hyperfine interactions

In the next step, we will have a look at the origin of the modulation observed in the Hahn-echo decay. As the source is common for both compounds, it cannot arise from interactions between the edge state and the NIT-radicals. Using EDNMR [167] and HYSCORE spectroscopy [170], explained in Sec. 3.1.8 and Sec. 3.1.9, hyperfine interactions can be unravelled [156, 273].

EDNMR

The EDNMR spectrum of NIT-GNRs, performed at Q-band frequency at 85 K, is shown in Fig. 6.12. In our case, it gives a qualitative insight into the coupling between the NIT-radical spin and the spin-bearing nuclei. The field dependence shows different coupling strengths depending on the observer spin orientation. We find strongest coupling with nitrogen atoms, where contributions of both isotopes ^{14}N and ^{15}N can be seen in the double quantum peak N DQ. The spin-forbidden double quantum transitions of the nitrogen nuclei are dominant, and even stronger than any spin-allowed single-quantum transition of other specimens. This can be explained by the fact that a large spin density is localised on the NO bonds. Therefore, we may conclude that coupling to nitrogen atoms represents an important decoherence mechanism. The weak coupling between the spins and any other spin-bearing nuclei can be analysed in more detail via HYSCORE spectroscopy.

HYSCORE

HYSCORE experiments were carried out at X-band and Q-band frequencies. The X-band data is used to resolve interactions with nuclei other than nitrogens. A higher resolution of hyperfine interactions with nitrogen atoms can be obtained at the higher Q-band frequencies. This is due to the fact that at Q-band frequency, larger magnetic fields are employed which better allow resolving nitrogen contributions in time-resolved spectra. The two-dimensional Fourier transforms of the

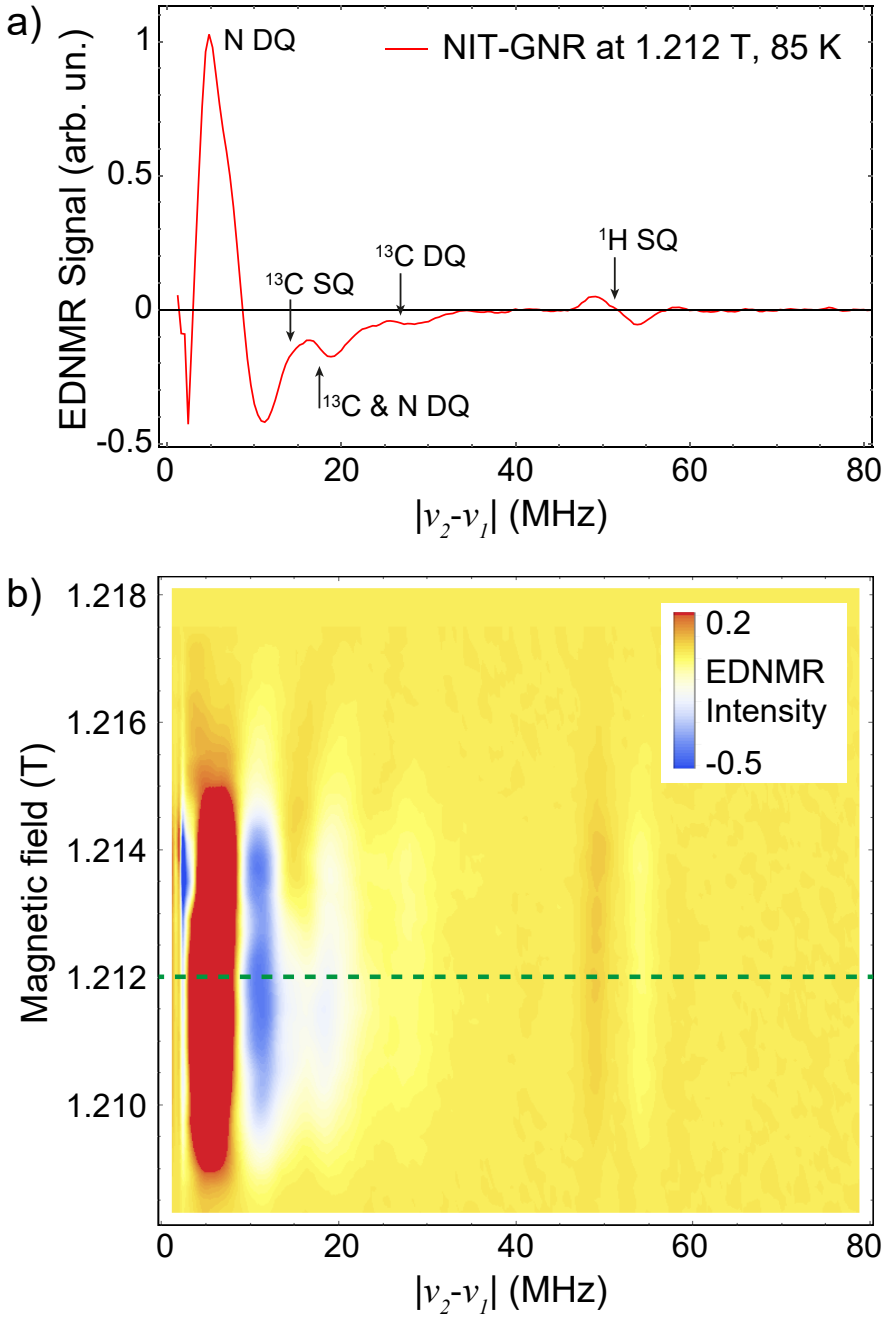

Fig. 6.12: EDNMR on NIT-GNRs taken at Q-band frequency at 85 K. (a) First-derivative EDNMR spectrum taken at 1.212 T. The different transitions are indicated as SQ (single quantum) and DQ (double quantum). A mixed transition with a combination frequency of carbon and nitrogen nuclei can be observed near 20 MHz. (b) Field-swept EDNMR spectrum. The extract in (a) is marked with a green dashed line the two-dimensional EDNMR diagram.

time-domain data sets are displayed in Fig. 6.13 and Fig. 6.14.

HYSCORE spectroscopy at the edge state resonance of NIT-GNR (Fig. 6.13a) at 5 K shows coupling to ^{1}H and to ^{13}C atoms, which appear at 14.5 MHz and 3.6 MHz, respectively. The coupling is likely to ^{13}C atoms of the backbone. For NIT-polyphenylene, contributions from ^{13}C are minimal. We attribute this finding to the delocalisation of the edge state in the GNR-backbone, which has a higher chance of interacting with a ^{13}C atom than the NIT-radicals. The ^{1}H atoms, to which the edge state is coupled, are localised on the edges and the alcane side-groups. Furthermore, the visible features from ^{1}H can also be attributed to the NIT-radicals, since there is a small spectral overlap of the edge state resonance field with the NIT-radical one. From the simulation, we obtain $\mathbf{A_H} = (2, 2, 6)$ MHz ± 0.5 MHz and $\mathbf{A_C} = (1.5, 1.5, 2.5)$ MHz ± 0.5 MHz as coupling energies. Furthermore, spectral details can be seen in the left quadrant, which are due to the strong coupling to nitrogen atoms. However, the resonance frequency of nitrogen atoms lies at 1.0 and 1.5 MHz for ^{14}N and ^{15}N, respectively, which is on the edge of the detection limit. Therefore, Q-band measurements were performed, where the resonance frequencies are at 3.1 MHz and 3.7 MHz for the two isotopes, respectively. Moreover, no significant temperature dependence was observed between 5 K and 75 K data.

The Q-band data at 85 K, displayed in Fig. 6.14a and 6.14b, show a similar peak pattern. Here we performed the measurement at the g_y resonance field of the NIT-radicals. The interesting pattern is almost solely related to the two nitrogen atoms present in the NIT-radical. Hydrogen and carbon contributions, observed at 51.7 MHz and 13.0 MHz, appear relatively sharp, so that reliable hyperfine interactions constants cannot be determined from these. A different value for τ (Fig. 3.12) might help to resolve this. By simulating a spectrum that considers both nitrogen atoms, shown in Fig. 6.14c and 6.14d, we can identify most of the observed peak positions. Interestingly, the determined hyperfine couplings from FID-detected and CW spectroscopy seem a bit too large, since a value of $A_z = 30$ MHz ± 2 MHz

better reproduces the spectrum. Likely, this value is more accurate, since the FID-detected and CW spectra might be slighty overparameterised, while HYSCORE spectra solely show hyperfine interactions.

The findings shown here are temperature and field stable. Several measurements at different temperatures and different fields yield similar spectra. However, the Q-band HYSCORE spectrum at the edge state resonance, displayed in Fig. 6.14e, yet needs to be understood. One can identify an oscillating pattern with a lowest frequency of about 3.3 MHz, and an additional peak at 26 MHz, which is half of the hydrogen nuclear resonance frequency. Since the spectrum at the edge state resonance changes entirely, the experiment shows that the edge state be separately excited from the NIT-radicals at Q-band frequency, which is favourable for DEER spectroscopy.

The determined coupling strength to the ^{13}C atoms of the graphene backbone is lower than the theoretically predicted 70 MHz for graphene quantum dots. In these systems, however, physical phenomena such as anisotropic, nuclei-orbital and Fermi-contact interactions contribute to the hyperfine coupling [134, 275]. Such strong couplings could be used for quantum computation processing [276]. Our system suggests radical-edge state pairs as coupled partners for this aim. Their interactions will be unravelled in the next section.

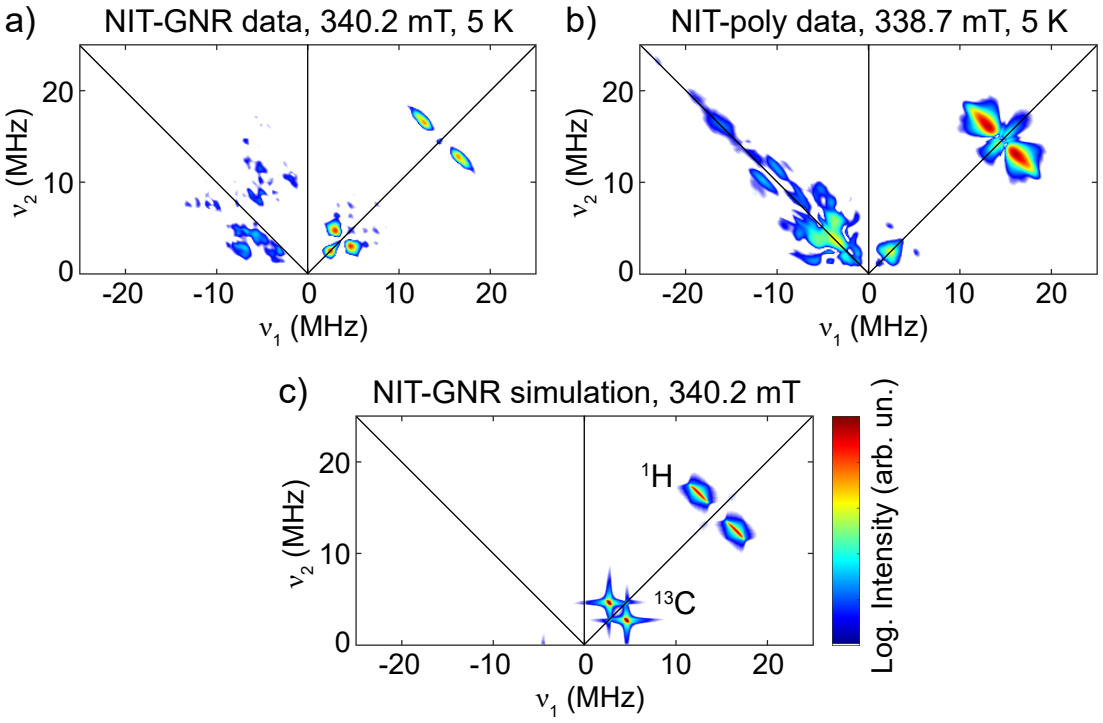

Fig. 6.13: HYSCORE results at X-band frequency. (a) The data set for NIT-GNRs was obtained at 340.2 mT (edge state resonance) and 5 K. The intensity map is given in logarithmic arbitrary units. (b) NIT-polyphenylene HYSCORE map at 338.7 mT (g_y resonance) and 5 K. (c) Easyspin simulation of the carbon and hydrogen contributions. The peak intensities were scaled to fit the experimental findings.

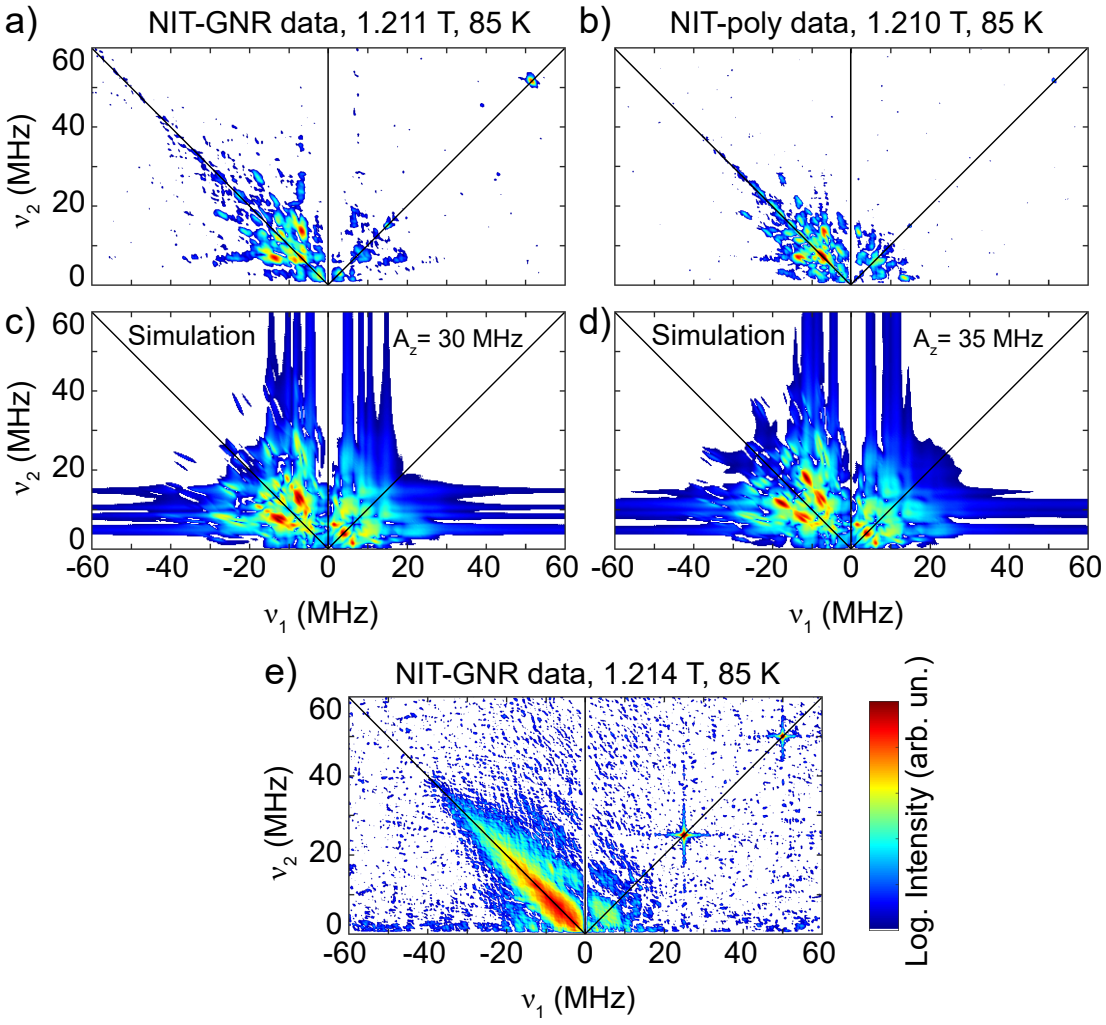

Fig. 6.14: HYSCORE results at Q-band frequency. (a) The shown data set for NIT-GNRs was obtained at 1.211 T (g_y resonance) and 85 K. The intensity map is given in logarithmic arbitrary units. (b) NIT-polyphenylene HYSCORE map at 1.210 mT (g_y resonance) and 85 K. (c) Easyspin simulation of the nitrogen contributions with $A_N = (0, 5, 30)$ MHz. (d) Easyspin simulation with $A_N = (0, 5, 35)$ MHz. (e) Measured NIT-GNR HYSCORE map at 1.214 mT, which corresponds to the edge state resonance, and 85 K.

6.3.7 Coherent manipulation using DEER spectroscopy

Using all the information gained on the material, we can finally progress to the exploration of couplings between NIT-radical spins and the edge state. We performed DEER spectroscopy, explained in Sec. 3.1.7, at Q-band frequency to investigate how the spin density on the NIT-radical sites are influenced by the spin orientation of the edge state. To achieve this goal, we decided to treat the NIT-radical spins as observer spins, which means that the pulse sequence under the frequency ν_1 is performed on these. Following a time-delay t after the primary sequence on the NIT-radicals, we applied a π-pulse on the edge state at frequency ν_2, which flips the edge state orientation and thus affects the precessions of the NIT-radical spins. By varying t, we expect a modulation of the echo amplitude, similar to what has been observed in Sec. 6.3.5. The frequencies and fields for this experiment were set as explained in Fig. 6.15.

All data were analysed using the Matlab package DeerAnalysis [165]. In our analysis, we solely use DeerAnalysis to remove the background of our DEER data and calculate the resulting time-domain and FFT data. Since dipolar couplings are possibly on the edge of the detection limit, and comparable to exchange couplings, we cannot calculate any distances between spins in our samples.

The normalised raw DEER data is shown in Fig. 6.16. Using DeerAnalysis, the background, which is proportional to $\exp(-kt^{D/3})$, with t the time, k the decay constant and D the dimensionality, was subtracted first. We found that the background is best described by $D = 3$, i.e. the background shows a monoexponential decay. Second, the resulting time-domain signal was normalised to its maximum and accounted for the nearest neighbouring spins, which finally leads to the signal shown in Fig. 6.17. The NIT-GNR spectrum shows a dip, which is part of a slow oscillation, superimposed with fast oscillations. We noticed that a change in the time constraints for the fitting of the background does not significantly change the nature of the oscillation itself. By fitting a smaller data set to the background, for example data between $0.4\,\mu s$-$0.6\,\mu s$, the oscillation amplitude becomes smaller,

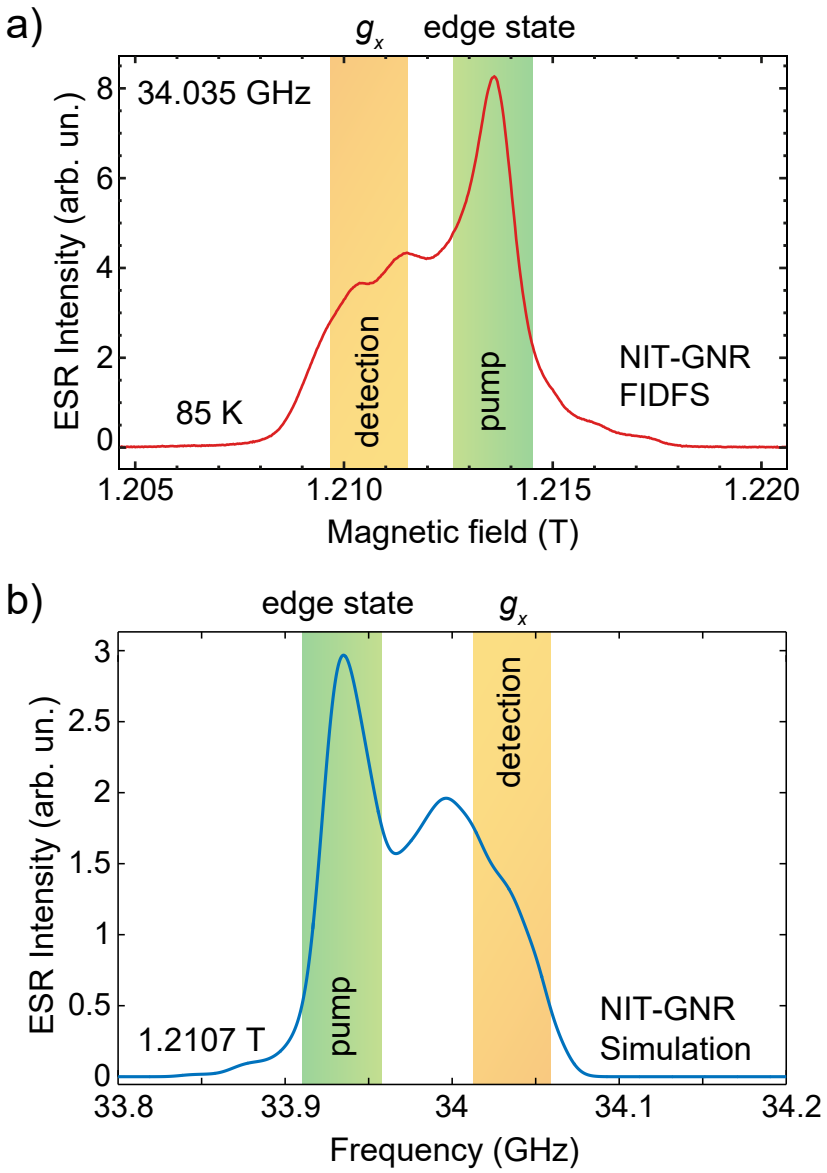

Fig. 6.15: Setup of frequencies for the DEER experiment. a) FID-detected field swept ESR spectrum of NIT-GNR at 85 K and Q-band frequency, 34.035 GHz. b) Simulated frequency-dependence ESR spectrum of NIT-GNR at 1.2107 T, using the parameters from Tab. 6.2. The spectral weight of the edge state was adjusted to fit the measured spectrum. The field was set to drive the g_x resonance (orange region in (a)). Therefore, the NIT-radical spins act as the detection (observer) spins for the DEER experiment. Using an additional frequency of -100 MHz offset, we pump on the edge state (green region). The magnetic field is kept fixed throughout the whole DEER experiment.

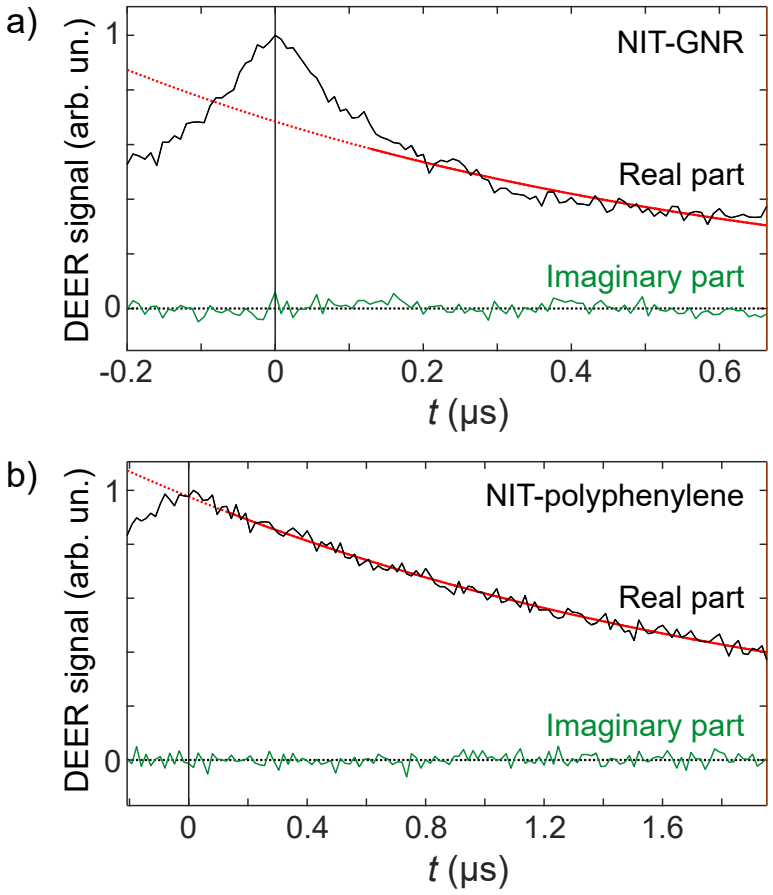

Fig. 6.16: Background correction via DeerAnalysis. (a) Normalised raw DEER signal of NIT-GNR. The black and green curve represent the real and imaginary part, respectively. The red curve denotes the three-dimensional background, which was subtracted later. b) Normalised raw DEER signal of NIT-polyphenylene.

but does not vanish. This indicates that the observed oscillations are not an artefact of the background correction. However, the experiment is limited by the coherence time, which is not long enough to observe a full oscillation of the slow oscillation, and to perform a background correction that relies on data that is not superimposed with oscillations.

The fast oscillations might originate from dipolar or exchange coupling between the NIT-radicals, which partially get excited by the pump pulse. Indeed, one can identify peak energies close to D_1 and D_2 in the fast Fourier transform, displayed in Fig.6.17b. However, these are rather small, since most of the microwaves are getting absorbed by the edge state. HYSCORE experiments at Q-band frequency

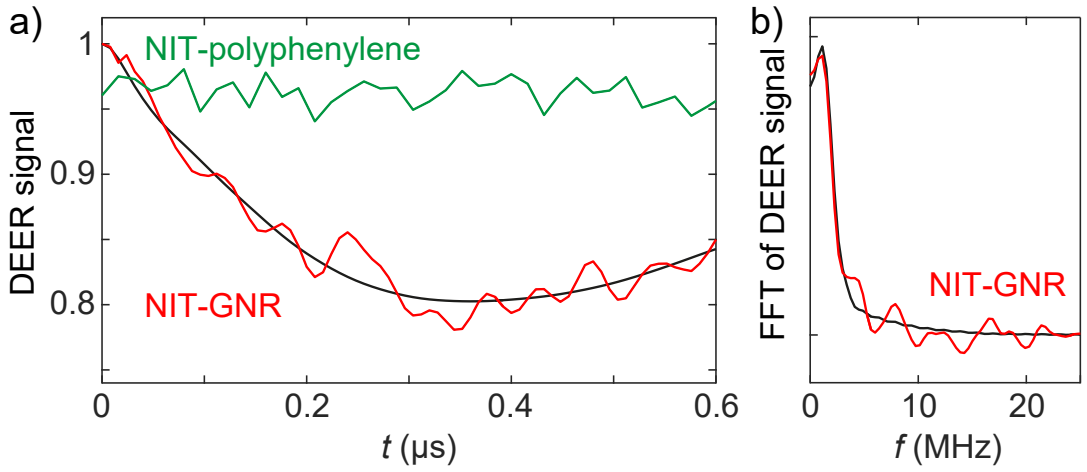

Fig. 6.17: DEER at Q-band frequency. (a) Time-domain spectrum of NIT-GNRs and NIT-polyphenylene. The data set was obtained at 85 K at Q-band frequency. The fields and frequencies were set as explained in Fig. 6.15. The data was filtered with a long-pass filter of 24 MHz so as to improve the visualisation of the data. (b) Frequency-domain DEER signal of NIT-GNR, obtained via fast Fourier transform (FFT) of the time-domain data. The black curves represent a strongly filtered line to the data.

indicated that this is happening, since the spectrum completely changes at the edge state resonance, compared to the HYSCORE spectra of the NIT-radicals. The dipolar interaction energies are possibly on the edge of the detection limit of the instrument. For this reason, we cannot exclude that noise contributes to the observed fast oscillations. Only in favorable cases, and when no exchange hinders the measurement, DEER spectroscopy is able to resolve spin distances down to 1.5 nm, which corresponds the length scale in our sample.

The slow oscillation goes through its first minimum at $T_e = 350$ ns, which corresponds to a frequency of 1.5 MHz. A comparable measurement with NIT-polyphenylene does not show any slow oscillating features. Therefore, taking all the previous results into account, we may conclude that this oscillation arises from the coupling between NIT-radical spins and the edge state. This measurement gives clear evidence that the edge state is preserved in the NIT-GNR molecular geometry, which opens up interesting possibilities. The first minimum in the time-

domain can be interpreted as the characteristic time-scale where the NIT-radical spin becomes inverted under the influence of the edge state. Since the edge-state radical-state inversion time T_e found here is much shorter than $T_m \approx 700\,\mathrm{ns}$, yet, at the same time, longer than typical ESR pulse durations, $\approx 10\,\mathrm{ns}$, the material requirements for a two-qubit phase gate are fulfilled. Thus, the theoretical sample requirements for coherent inversion operations and controlled entanglement are met [277].

The coupling energy of 1.5 MHz might seem relatively weak, significantly weaker than the intramolecular dipolar interactions between NIT-radicals obtained from the continuous-wave spectra. One reason for the low coupling energy could be the delocalised nature of the edge state, which shows a delocalisation over the whole ribbon backbone as illustrated in Fig. 6.3. Another reason could be an incomplete functionialisation of the edges, which we, however, expect to be majorly populated by the magnetic groups. Furthermore, the spin injection efficiency could play an important role here. It would be interesting to investigate different radical substituents. A big library of potential organic radicals is available [278], and the chemical synthesis of other radical-substituted GNRs is theoretically possible. Therefore, the spin injection effects, and how it influences the edge state properties and the coupling between radicals and the edge state, can be studied and compared. In this thesis, we have demonstrated how one can investigate the edge state spin dynamics in NIT-GNRs, and a similar analysis can be carried out for other radical-substituted GNRs.

6.4 Outlook and perspectives

The quasi-onedimensional nature and the advances in nanofabrication of molecular nanodevices potentially enable the integration of NIT-GNRs in nanodevices. Two-qubit operations could be, in principle, realised via single-electron transport [279], and the detection can be performed electrically [74]. Being a one-dimensional conductor, flowing electrons could potentially be used to transmit entanglement

through a series of spin centres, since we found a coupling of the NIT-radicals to the delocalised edge state [270, 280]. This could be achieved via scattering-free ballistic transport, which has been reported to happen in carbon nanotubes and graphene nanoribbons with well-defined edges [281–283]. Therefore, it would be interesting to investigate whether such ballistic transport can also happen in our systems. Thus, the next step would be the integration of NIT-GNRs in nanodevices.

In order to integrate NIT-GNRs in nanodevices, rigid substrates that preserve the NIT-GNR properties are of crucial importance. Preliminary DFT calculations show that hexagonal boron-nitride, h-BN, can be a suitable two-dimensional substrate. DFT calculations, shown in Fig. 6.18, predict that the spin density properties of NIT-GNRs are not largely altered when deposited on h-BN. This means that, in principle, one should be able to observe the coupling of the edge state to the NIT-radicals on h-BN, so that its fabrication is a favourable option. Nevertheless, possible environmental interactions such as between NIT-GNRs and the surface are yet unknown, and are thus an interesting future direction of research.

In this project we have demonstrated that NIT-GNRs can be used to test theories of graphene and graphene nanoribbons. Not only were we able to see the edge state character in electron spin resonance experiments, we also estimated spin-orbit and hyperfine coupling strengths, which are theoretically still under discussion. Instead of using quantum Hall effects at ultra-low temperatures [132, 133], which are accessible through complicated instruments such as dilution refrigerators, we were able to perform all the measurements at liquid-nitrogen temperatures. In fact, our systems show decent quantum coherence times even at room temperature, so that characterisations do not necessarily require extensive cooling, although it still helps to improve the SNR. These atomically-defined structures open the path to a quantitative analysis of further theories on graphene nanoribbons.

However, there is ample room to optimise the structure of the NIT-GNRs and to get a deeper understanding of the coupling between the radicals and the edge state.

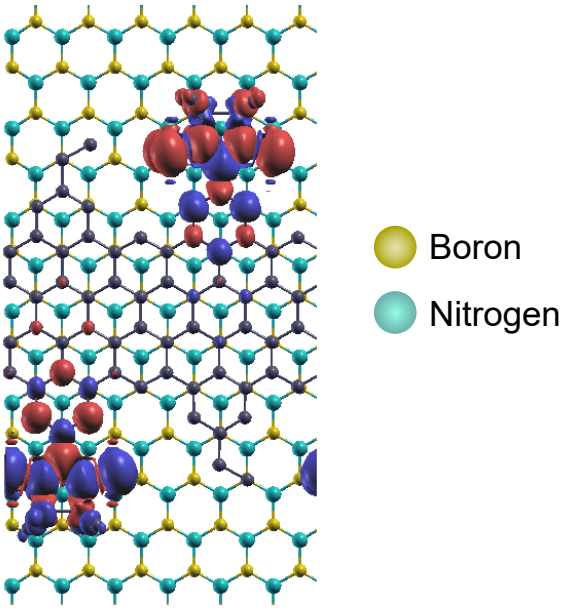

Fig. 6.18: DFT calculations for NIT-GNRs on a hexagonal boron-nitride (h-BN) surface. The different spins are depicted with blue and red orbitals, whereas boron and nitrogen atoms are marked with yellow and cyan colours. The entire spin density, shown via the blue and red orbitals, mainly remains on the NIT-GNR site. Therefore, the properties of GNR-NITs should not change in this geometry.

Probably, the nitrogen atoms of the NIT-radicals represent a dominant decoherence path, given their strong signal in HYSCORE spectroscopy. Using magnetic groups with the least nuclear-spin bearing nuclei as possible will likely help to improve the coherence properties. There are vast libraries of radicals that can potentially be grafted on the GNRs [260, 284]. As the synthetic and characterisation methods are set up, different molecular spin-injectors and, in addition, different GNR backbones, which probably modulate the spin coupling, can be investigated. Furthermore, to increase T_m, one can use either nuclear-spin-free isotopes such as deuterium or ^{12}C [285], or the possibilities of chemical engineering [286]. On the experimental side, special pulse sequences taking advantage of dynamic nuclear spin polarisation also help to increase T_m [287].

6.5 Summary

We have presented an in-depth investigation of a novel spin-bearing class of materials based on a GNR-backbone. Owing to state-of-the-art fabrication of atomically-precise GNR, spin-bearing NIT-radicals could be grafted onto the edges of the GNR-backbone, therefore creating a novel quasi-onedimensional magnetic system. Using DFT calculations, we were able to see a spin-injection effect induced by the NIT-radicals, which enables the formation of a magnetic edge state in the GNR backbone of our systems. Thus far, studies on the edge state were hampered by the strong reactivity of the edges, as well as imperfect fabrication methods. However, we were able to directly observe the edge state using electron spin resonance spectroscopy. We have shown a detailed ESR characterisation of the magnetic properties and could separate the roles of the NIT-radicals and the edge state. CW and FID-detected spectra were simulated to the experimental data, allowing for a quantification of the important interaction parameters such as hyperfine coupling to nitrogen atoms or dipolar coupling between the radicals. All values are listed in Tab. 6.1 and 6.2. There, we found a first hint of the edge state in NIT-GNRs, since in contrast to the NIT-polyphenylene analogue, an additional ESR signal with uniaxial g-anisotropy appeared. Using DEER spectroscopy, we could drive coherent manipulations on the spin systems, and directly observe the edge-state coupling to the NIT-radicals. By inverting the edge-state polarisation via a π-pulse, the spin orientation of NIT-radicals become inverted after about 350 ns, which corresponds to a coupling energy of about 1.5 MHz. The timescale lies between the phase-memory time at Q-band frequency, 700 ns, and the duration of a microwave pulse, 10 ns. Therefore, NIT-GNRs are a very promising material for the realisation of two-qubit gates. Additionally, we estimated the spin-orbit coupling by considering DFT calculations together with the g-anisotropy of the edge state, which agrees with discussions on theoretical expectations.

Furthermore, we have performed a full characterisation of the spin-lattice relaxation T_1 and phase-memory time T_m. We have presented a model to explain the

temperature dependence of T_1, where we identified three relaxation regimes: direct relaxation, Raman relaxation and relaxation via local N-O vibrations. We found T_m times of about 350 ns at X-band, 700 ns at Q-band and 1100 ns at W-band frequency at liquid nitrogen temperatures. There are large enough for potential qubit applications. Interestingly, no large temperature dependence has been found, as shown at X-band frequency, so that quantum coherence can even be observed at room temperature.

With the help of EDNMR and HYSCORE spectroscopy, we gained insight into the hyperfine couplings. While CW and FID-detected spectra were only able to resolve the nitrogen hyperfine structure, EDNMR and HYSCORE unravelled the interactions with ^{13}C and ^{1}H atoms. The edge state shows coupling to ^{13}C atoms in the HYSCORE experiment, although the natural abundance of ^{13}C is about 1.1 %, which is an indication for the delocalised nature of the edge state. In contrast to theoretical expectations, we found hyperfine couplings of about $A_C = (1.5, 1.5, 2.5)$ MHz ± 0.5 MHz, which might be due to the low abundance and strong delocalisation.

It is our hope that this project will lead to new approaches towards electrical control of magnetic states. The present work accords one technique for bringing the fields of molecular magnetism and graphene electronics together. The next step would be the integration of NIT-GNRs in nanodevices, and the first DFT studies on hexagonal boron nitride substrates yielded promising results. Since the GNR backbone is a quasi-onedimensional conductor, one could think of using electrons to control the coupling between the NIT-radicals and the edge state, which may finally lead to the realisation of a molecular spintronic two-qubit device.

7 Conclusion

The manipulation of the intra- and inter-coupling between electronic and spin degrees of freedom is one of the most basic and fundamental challenges of solid state physics today. In this thesis I have used visible light and microwave irradiation to shed light on this problem, using molecular systems as model testbeds. The results were both unexpected and intriguing, to me.

I explored three very different mechanisms: light-induced electron transfers that create a conformational change; light-induced spin-forbidden transitions; microwave-induced edge-localised spin perturbations in extended nanostructures. Observing these effects necessitates, in some regards, even completely opposite requirements, and I thus used three model systems.

The first was employed to explore how photons can create long-lived perturbations in spin centres, by affecting both the electronic and the vibrational states of a magnetic molecule. To this aim, I used a new cobalt valence-tautomer complex (Co-VT) exhibiting a long-lived photoexcited state at cryogenic temperatures. The results show that conversion efficiencies between the high- and low-spin transitions ($S = 5/2$ and $S = 1/2$, respectively) can reach 98%, owing to a home-built fibre-optic setup. When warming up from liquid helium temperature, we were able to keep the high-spin state below 68 K, considerably higher than similar Co-VT complexes. To find an explanation for the higher critical temperature, density functional theory calculations were taken into account. These show how the volume change of the unit cell during the low-spin to high-spin transition is of paramount importance to model these phenomena. The greater volume changes

result in a larger thermal relaxation barrier, which explains the higher critical temperature. Tests at different wavelengths showed that the compound cannot be switched back to its low-spin state, so that backswitching is restricted to thermal reversal or relaxation via quantum tunnelling. Our Co-VT represents a purely paramagnetic system, rather than a single-molecule magnet. They can be applied to the modern synthetic strategies of grafting Co-VTs onto known SMMs (where, via intramolecular exchange, magnetic states could be switched with light) or to charge transfer effects in other paramagnetic systems under irradiation such as magnetic graphene nanoribbons.

As the second system, I explored short-lived photoexcited states that are much more challenging to detect, implementing switching mechanisms that were proposed more than thirty years ago but had remained without validation. These mechanisms, although largely ignored at the time, are increasingly relevant today because they offer one of the rare possibilities to switch between different Hilbert spaces of a quantum system. To this purpose I investigated an Fe_3Cr-based single-molecule magnet and developed dedicated high sensitivity instrumentation and advanced data treatment.

A different route towards photoswitchable nanodevices is provided by the use of photoactive metal ions. In this work, we took advantage of the spin-forbidden transition (SFT) in chromium ions. We have shown that we can use the SFT in Fe_3Cr-SMMs to change the molecular spin state from $S = 6$ to $S = 7$. Due to the relatively small spin-state change, magnetic signals of the photoexcited state were approaching the detection limits of the experimental setups. Nevertheless, we were able to quantitatively simulate the torque-detected electron spin resonance spectra with good confidence. We determined a lowered anisotropy parameter of $D = -0.148\,\mathrm{cm}^{-1}$ in the photoexcited state, compared to $D = -0.178\,\mathrm{cm}^{-1}$ in the ground state. The total anisotropy barrier $|D|S^2$ decreases in the photoexcited state, which is supported by theoretical calculations. Although AC magnetometry under irradiation of light showed the expected trend, gaining quantitative results

on the photoexcited state was hindered by strong heating effects. In the next step, it remains essential to investigate quantum coherence properties. One idea is to use transient electron spin resonance, where access to phase-memory times is granted via a laser-pulse, followed by a Hahn-echo sequence.

Eventually I moved to the longstanding problem of magnetic edge states in graphene nanoribbons (GNRs). To this purpose I used molecular graphene systems, which have the advantage of perfectly defined edges, and time-resolved electron spin resonance (ESR) experiments.

This study is prompted by the fact that graphene nanoribbons represent an interesting semiconducting material for a potential new generation of nanotransistors. We have investigated how spin centres behave in GNRs. Our collaborators were able functionalise the GNRs with magnetic nitronyl-nitroxide radicals on their edges. Using a combination of continuous-wave and time-resolved ESR spectroscopy, we could resolve spin-spin interactions between the spin centres, and quantify hyperfine interactions. Quantum coherence times are of the order of a microsecond at 85 K and 94 GHz, which is long enough for potential quantum operations. More interestingly, however, the coupling of the radical spins with the GNR results in the formation of an additional magnetic state within the GNR-backbone, which is delocalised along the edges. In fact, this edge state was theoretically predicted, but never observed so far with such high confidence. Using double-electron-electron-resonance techniques, radical and edge-state spin interactions can be modulated, where we found two-qubit gate times of 350 ns. This brings our system in an interesting regime. The two-qubit time is larger than the single-qubit time (10 ns), but smaller than the quantum coherence time, thus meeting the fundamental material requirements for two-qubit operations. This knowledge can now be merged with the insight obtained in the previous systems for a purely optical control of coherent advanced magnetic materials.

7.1 Outlook

Being ultra-fast, light is an appealing method to manipulate spin states, and consequently their couplings. This is extremely appealing when thinking of spins sitting on different sites of a magnetic GNR and having microsecond coherence times. Both the long-lived and short-lived photon-spin interaction mechanisms could be used to manipulate the edge states of the magnetic GNRs, then using microwaves to control the side spins.

Additionally, the identification of several decoherence channels, including nuclear ones, allows using microwave-induced nuclear polarisation and control of nuclei to store and retrieve quantum information on these systems. Graphene nanoribbons not only give an additional spin degree of freedom via the edge state, but also intrinsically provide a conductive base, which can be conveniently attached to electrodes. In this respect, we hope to motivate further research devoted to the interactions of flowing electrons and spin centres, leading to a better understanding of coupling phenomena, and resulting in a new and improved generation of spintronic elements.

List of Figures

2.1 Selected structures of molecular magnets 7

2.2 Spherical representation of the crystal-field parameters. 9

2.3 Calculations of environmental effects on magnetic properties of a LnDOTA-complex 10

2.4 Slow relaxation of magnetisation 12

2.5 Splitting of SMM spin states in a magnetic field 14

2.6 Spin-crossover process 19

2.7 Tristability in an iron-based SMM 20

2.8 Photoswitching via charge-transfer 21

2.9 Photoswitching via isomerisation 22

2.10 Donor-bridge-acceptor nitronyl-nitroxides. 24

2.11 Graphene as base for other carbon materials. 26

2.12 Graphene and possible GNR structures. 28

2.13 AGNR band gaps and band structure. 29

2.14 Ferromagnetic and antiferromagnetic polarisation of the edge state. 31

2.15 Edge-state delocalisation of GNRs. 32

2.16 ZGNR band gaps and band structure. 33

2.17 Small selection of further GNR structures. 34

2.18 Rashba spin-orbit effects on the band structure of a ZGNR. . . . 37

2.19 Top-down fabrication of GNRs. 39

2.20 Bottom-up fabrication of GNRs. 40

3.1 Energy splitting of a spin-1/2-system in a magnetic field. 44

3.2 FID-detection pulse scheme 53
3.3 Hahn-echo pulse sequence 55
3.4 Saturation recovery sequences. 59
3.5 Picket-fence pulse sequence 60
3.6 DEER pulse sequence 61
3.7 Energy splitting of an $S = 1/2$, $I = 1/2$ system. 62
3.8 EDNMR pump and probe pulse setting for an $S = 1/2$, $I = 1/2$ system. 63
3.9 EDNMR pulse sequence 64
3.10 Example of a W-band EDNMR spectrum 65
3.11 Definition of the density matrix terms. 66
3.12 HYSCORE pulse sequence 67
3.13 Example spectrum of a HYSCORE experiment. 68
3.14 Schematic setup of a Bruker Elexsys system. 73
3.15 Schematic setup of the pulsed unit of the Bruker Elexsys system. 74
3.16 Schematic setup of a MPMS XL-7 SQUID magnetometer. 77
3.17 Function of the MPMS XL-7 SQUID magnetometer. 78
3.18 Frequency-dependence of the dynamic magnetic susceptibility. . . 80
3.19 Argand diagram of the dynamic magnetic susceptibility. 81
3.20 Fibre-coupling units. 84
3.21 SQUID sample holder for measurements under irradiation of light. 85
3.22 ESR EMX sample holder for measurements under irradiation of light. 86
3.23 Semiclassical vector-model for the spin orentiation. 89
3.24 TDESR setup. 93
3.25 Extension of the TDESR setup with a laser. 96

4.1 Oxidation states of the quinone ligand. 99
4.2 Numbering of the atoms in the Co-VT complex. 101
4.3 Valence tautomerism in Co(3,5-dbbq)$_2$(μ-bpym). 103
4.4 SQUID characterisation of Co(3,5-dbbq)$_2$(μ-bpym). 106

4.5 $\chi_m T$ for different sample preparations. 108
4.6 ESR spectra of the Co-VTs between 220 K and 3.7 K. 110
4.7 ESR-intensity temperature product against temperature. 111
4.8 Simulation of the Co-VT ESR spectrum at 80 K 112
4.9 Fitting of the Co-VT ESR spectrum at 80 K 113
4.10 Temperature dependence of the ESR signal intensity 114
4.11 Photomagnetic properties of the Co-VT complex 116
4.12 Photomagnetic properties of the pellet sample 120
4.13 ESR signal before and after irradiation 122
4.14 Normalised ESR signal strength during and after irradiation at 10 K and 532 nm 124
4.15 Relaxation behaviour of the photoexcited HS-staten 125
4.16 UV/Vis/NIR spectrum of our Co-VT complex. 127
4.17 Time evolution of the ESR signal with and without light at different wavelengths. 128
4.18 A Co-VT-SMM complex. 130

5.1 Fe_3Cr structure. 136
5.2 Intersystem crossing in Cr^{III}. 137
5.3 UV/vis absorption diagram of Fe_3Cr and Fe_4. 138
5.4 TDESR measurement data set and simulation for Fe_3Cr and 19.4 K. 140
5.5 Zeeman removal procedure. 141
5.6 Averaged TDESR-data on Fe_3Cr with and without light. 143
5.7 Populations of states obtained from the simulation of the TDESR data. 146
5.8 Fit of the TDESR data. 147
5.9 Static magnetic moment of Fe_3Cr at different laser intensities. . . 152
5.10 In- and out-of-phase susceptibility of Fe_3Cr versus frequency and temperature. 155
5.11 Isothermal Argand plot of Fe_3Cr. 156

5.12 Isothermal Argand diagram of Fe_3Cr under irradiation of light. . . 159
5.13 Isofrequency Argand diagram of Fe_3Cr under irradiation of light. . 160
5.14 Arrhenius fit of Fe_3Cr ground state relaxation. 161
5.15 Isofrequency Argand diagram of Fe_3Cr under irradiation of 532 nm light. 163
5.16 Nanoantennas as possible building block for nanoscale molecular spintronics. 165

6.1 Structure of NIT-GNR and NIT-polyphenylene 171
6.2 Chemical synthesis of NIT-GNR and NIT-polyphenylene 172
6.3 DFT calculations on NIT-GNR and NIT-polyphenylene 174
6.4 Definition of the nearest neighbour interaction terms 176
6.5 X-, Q- and W-band ESR spectra of NIT-polyphenylene powder and NIT-GNR flakes 178
6.6 Illustration of exchange coupling rules for aromatic systems 181
6.7 Field-swept FID-detected spectrum obtained at X-band frequency and 85 K 185
6.8 Temperature dependence of T_1 times 188
6.9 Magnetic field dependence of T_1 at Q-band frequency and 85 K. . 189
6.10 Dephasing of excited spins at X-band frequency 191
6.11 Magnetic field and frequency dependence of T_m 194
6.12 EDNMR on NIT-GNRs 196
6.13 HYSCORE on NIT-GNRs and NIT-polyphenylene at X-band frequency 199
6.14 HYSCORE on NIT-GNRs and NIT-polyphenylene at Q-band frequency 200
6.15 Setup of frequencies for the DEER experiment 202
6.16 Background correction via DeerAnalysis 203
6.17 DEER on NIT-GNR and NIT-polyphenylene at Q-band frequency 204
6.18 DFT calculations for NIT-GNRs on a h-BN surface 207

List of Tables

4.1 Bond lengths of LS-Co^{III} and HS-Co^{II} obtained from DFT calculations 101

5.1 Simulation parameters for the Fe_3Cr TDESR spectra 145

6.1 Simulation parameters for the NIT-polyphenylene spectra 182

6.2 Simulation parameters for the NIT-GNR spectra 183

Bibliography

[1] I. L. Markov. "Limits on fundamental limits to computation". *Nature*, 512, 147–154 (2014).

[2] S. Gao, M. Affronte, M. Baker, S. Blundell, L. Bogani, L. Chibotaru, R. Clérac, A. Cornia, C. Coulon, N. Domingo, M. Evangelisti, A. Ghirri, S. Hill, S.-D. Jiang, F. Luis, M. Mannini, C. Milios, V. Pianet, F. Troiani, M. Urdampilleta, R. E. P. Winpenny and B.-W. Wangl. Molecular Nanomagnets and Related Phenomena. Springer Verlag Berlin-Heidelberg (2014).

[3] H. B. Heersche, Z. de Groot, J. A. Folk, H. S. J. van der Zant, C. Romeike, M. R. Wegewijs, L. Zobbi, D. Barreca, E. Tondello and A. Cornia. "Electron Transport through Single Mn_{12} Molecular Magnets". *Phys. Rev. Lett.*, 96, 206801 (2006).

[4] J. A. Mol, C. S. Lau, W. J. M. Lewis, H. Sadeghi, C. Roche, A. Cnossen, J. H. Warner, C. J. Lambert, H. L. Anderson and G. A. D. Briggs. "Graphene-porphyrin single-molecule transistors". *Nanoscale*, 7, 13181–13185 (2015).

[5] S. Y. Quek, M. Kamenetska, M. L. Steigerwald, H. J. Choi, S. G. Louie, M. S. Hybertsen, J. B. Neaton and L. Venkataraman. "Mechanically controlled binary conductance switching of a single-molecule junction". *Nat. Nanotech.*, 4, 230–234 (2009).

[6] R. Vincent, S. Klyatskaya, M. Ruben, W. Wernsdorfer and F. Balestro. "Electronic read-out of a single nuclear spin using a molecular spin transistor". *Nature*, 488, 357–360 (2012).

[7] D. Gatteschi, R. Sessoli and J. Villain. Molecular Nanomagnets. Oxford University Press (2006).

[8] J. R. Friedman and M. P. Sarachik. "Single-Molecule Nanomagnets". *Annu. Rev. Condens. Matter Phys.*, 1, 109–128 (2010).

[9] R. Bircher, G. Chaboussant, C. Dobe, H. U. Güdel, S. T. Ochsenbein, A. Sieber and O. Waldmann. "Single-Molecule Magnets Under Pressure". *Adv. Funct. Mater.*, 16, 209–220 (2006).

[10] A. Sieber, D. Foguet-Albiol, O. Waldmann, S. T. Ochsenbein, G. Carver, H. Mutka, F. Fernandez-Alonso, M. Mezouar, H. P. Weber, G. Christou and H. U. Güdel. "Pressure dependence of the exchange interaction in the dimeric single-molecule magnet $[Mn_4O_3Cl_4(O_2CEt)_3(py)_3]_2$ from inelastic neutron scattering". *Phys. Rev. B*, 74, 024405 (2006).

[11] A. Caneschi, A. Dei, F. Fabrizi de Biani, P. Gütlich, V. Ksenofontov, G. Levchenko, A. Hoefer and F. Renz. "Pressure- and Temperature-Induced Valence Tautomeric Interconversion in a *o*-Dioxolene Adduct of a Cobalt–Tetraazamacrocycle Complex". *Chem. Eur. J.*, 7, 3926–3930 (2001).

[12] A. S. Zyazin, J. W. G. van den Berg, E. A. Osorio, H. S. J. van der Zant, N. P. Konstantinidis, M. Leijnse, M. R. Wegewijs, F. May, W. Hofstetter, C. Danieli and A. Cornia. "Electric Field Controlled Magnetic Anisotropy in a Single Molecule". *Nano Lett.*, 10, 3307–3311 (2010).

[13] J. Hu and R. Wu. "Control of the Magnetism and Magnetic Anisotropy of a Single-Molecule Magnet with an Electric Field". *Phys. Rev. Lett.*, 110, 097202 (2013).

[14] O. Sato, J. Tao and Y.-Z. Zhang. "Control of Magnetic Properties through External Stimuli". *Angew. Chem. Int. Ed.*, 46, 2152–2187 (2007).

[15] X. Feng, C. Mathonière, I.-R. Jeon, M. Rouzières, A. Ozarowski, M. L. Aubrey, M. I. Gonzalez, R. Clérac and J. R. Long. "Tristability in a Light-Actuated Single-Molecule Magnet". *J. Am. Chem. Soc.*, 135, 15880–15884 (2013).

[16] A. Droghetti and S. Sanvito. "Electric Field Control of Valence Tautomeric Interconversion in Cobalt Dioxolene". *Phys. Rev. Lett.*, 107, 047201 (2011).

[17] M. Mannini, P. Sainctavit, R. Sessoli, C. Cartier dit Moulin, F. Pineider, M.-A. Arrio, A. Cornia and D. Gatteschi. "XAS and XMCD Investigation of Mn_{12} Monolayers on Gold". *Chem. Eur. J.*, 14, 7530–7535 (2008).

[18] S. Kahle, Z. Deng, N. Malinowski, C. Tonnoir, A. Forment-Aliaga, N. Thontasen, G. Rinke, D. Le, V. Turkowski, T. S. Rahman, S. Rauschenbach, M. Ternes and K. Kern. "The Quantum Magnetism of Individual Manganese-12-Acetate Molecular Magnets Anchored at Surfaces". *Nano Lett.*, 12, 518–521 (2012).

[19] A. Cornia, M. Mannini, P. Sainctavit and R. Sessoli. "Chemical strategies and characterization tools for the organization of single molecule magnets on surfaces". *Chem. Soc. Rev.*, 40, 3076–3091 (2011).

[20] N. Domingo, E. Bellido and D. Ruiz-Molina. "Advances on structuring, integration and magnetic characterization of molecular nanomagnets on surfaces and devices". *Chem. Soc. Rev.*, 41, 258–302 (2012).

[21] A. K. Geim and K. S. Novoselov. "The rise of graphene". *Nat. Mater.*, 6, 183–191 (2007).

[22] J. van Slageren. "New Directions in Electron Paramagnetic Resonance Spectroscopy on Molecular Nanomagnets". *Top. Curr. Chem.*, 321, 199–234 (2012).

[23] K. Nakada, M. Fujita, G. Dresselhaus and M. S. Dresselhaus. "Edge state in graphene ribbons: Nanometer size effect and edge shape dependence". *Phys. Rev. B*, 54, 17954–17961 (1996).

[24] M. del Carmen Giménez-López, F. Moro, A. L. Torre, C. J. Gómez-García, P. D. Brown, J. van Slageren and A. N. Khlobystov. "Encapsulation of single-molecule magnets in carbon nanotubes". *Nat. Commun.*, 2, 407 (2011).

[25] L. Bogani and W. Wernsdorfer. "Molecular spintronics using single-molecule magnets". *Nat. Mater.*, 7, 179–186 (2008).

[26] M. N. Leuenberger and D. Loss. "Quantum computing in molecular magnets". *Nature*, 410, 789–793 (2001).

[27] J. M. D. Coey. Magnetism and Magnetic Materials. Cambridge University Press (2010).

[28] L. H. Reddy, J. L. Arias, J. Nicolas and P. Couvreur. "Magnetic Nanoparticles: Design and Characterization, Toxicity and Biocompatibility, Pharmaceutical and Biomedical Applications". *Chem. Rev.*, 112, 5818–5878 (2012).

[29] A.-H. Lu, E. L. Salabas and F. Schüth. "Magnetic Nanoparticles: Synthesis, Protection, Functionalization, and Application". *Angew. Chem. Int. Ed.*, 46, 1222–1244 (2007).

[30] R. Sessoli, H. L. Tsai, A. R. Schake, S. Wang, J. B. Vincent, K. Folting, D. Gatteschi, G. Christou and D. N. Hendrickson. "High-spin molecules: $[Mn_{12}O_{12}(O_2CR)_{16}(H_2O)_4]$". *J. Am. Chem. Soc.*, 115, 1804–1816 (1993).

[31] A. J. Tasiopoulos, A. Vinslava, W. Wernsdorfer, K. A. Abboud and G. Christou. "Giant Single-Molecule Magnets: A Mn_{84} Torus and Its Supramolecular Nanotubes". *Angew. Chem. Int. Ed.*, 43, 2117–2121 (2004).

[32] S. Accorsi, A.-L. Barra, A. Caneschi, G. Chastanet, A. Cornia, A. C. Fabretti, D. Gatteschi, C. Mortalò, E. Olivieri, F. Parenti, P. Rosa, R. Sessoli, L. Sorace, W. Wernsdorfer and L. Zobbi. "Tuning Anisotropy Barriers in a Family of Tetrairon(III) Single-Molecule Magnets with an S = 5 Ground State". *J. Am. Chem. Soc.*, 128, 4742–4755 (2006).

[33] D. N. Woodruff, R. E. P. Winpenny and R. A. Layfield. "Lanthanide Single-Molecule Magnets". *Chem. Rev.*, 113, 5110–5148 (2013).

[34] N. Ishikawa, M. Sugita, T. Ishikawa, S. ya Koshihara and Y. Kaizu. "Lanthanide Double-Decker Complexes Functioning as Magnets at the Single-Molecular Level". *J. Am. Chem. Soc.*, 125, 8694–8695 (2003).

[35] E. Heintze, F. E. Hallak, C. Clauß, A. Rettori, M. G. Pini, F. Totti, M. Dressel and L. Bogani. "Dynamic control of magnetic nanowires by light-induced domain-wall kickoffs". *Nat. Mater.*, 12, 202–206 (2013).

[36] R. Sessoli, D. Gatteschi, A. Caneschi and M. A. Novak. "Magnetic bistability in a metal-ion cluster". *Nature*, 365, 141–143 (1993).

[37] C. Görller-Walrand and K. Binnemans. "Rationalization of crystal-field parametrization". *Handbook on the Physics and Chemistry of Rare Earths*, 23, 121–283 (1996).

[38] C. Cervetti, E. Heintze and L. Bogani. "Interweaving spins with their environment: novel inorganic nanohybrids with controllable magnetic properties". *Dalton Trans.*, 43, 4220–4232 (2014).

[39] G. Cucinotta, M. Perfetti, J. Luzon, M. Etienne, P.-E. Car, A. Caneschi, G. Calvez, K. Bernot and R. Sessoli. "Magnetic Anisotropy in a Dysprosium/DOTA Single-Molecule Magnet: Beyond Simple Magneto-Structural Correlations". *Angew. Chem. Int. Ed.*, 51, 1606–1610 (2012).

[40] M.-E. Boulon, G. Cucinotta, J. Luzon, C. Degl'Innocenti, M. Perfetti, K. Bernot, G. Calvez, A. Caneschi and R. Sessoli. "Magnetic Anisotropy and Spin-Parity Effect Along the Series of Lanthanide Complexes with DOTA". *Angew. Chem. Int. Ed.*, 52, 350–354 (2013).

[41] A. Abragam and B. Bleaney. Electron Paramagnetic Resonance of Transition Ions. Oxford University Press (2012).

[42] H. Lueken. Magnetochemie. Teubner Stuttgart – Leipzig (1999).

[43] N. W. Ashcroft and N. D. Mermin. Solid State Physics. Cengage Learning, Inc (1976).

[44] I. Dzyaloshinsky. "A thermodynamic theory of "weak" ferromagnetism of antiferromagnetics". *J. Phys. Chem. Solids*, 4, 241 – 255 (1958).

[45] T. Moriya. "Anisotropic Superexchange Interaction and Weak Ferromagnetism". *Phys. Rev.*, 120, 91–98 (1960).

[46] D. Goldfarb. "Hyperfine Spectroscopy - ELDOR-detected NMR" in "EPR Spectroscopy: Fundamentals and Methods". Wiley-VCH Verlag GmbH & Co. KGaA (2018).

[47] A. Caneschi, D. Gatteschi, R. Sessoli, A. L. Barra, L. C. Brunel and M. Guillot. "Alternating current susceptibility, high field magnetization, and millimeter band EPR evidence for a ground S = 10 state in $[Mn_{12}O_{12}(Ch_3COO)_{16}(H_2O)_4]\cdot 2CH_3COOH\cdot 4H_2O$". *J. Am. Chem. Soc.*, 113, 5873–5874 (1991).

[48] J. R. Friedman, M. P. Sarachik, J. Tejada and R. Ziolo. "Macroscopic Measurement of Resonant Magnetization Tunneling in High-Spin Molecules". *Phys. Rev. Lett.*, 76, 3830–3833 (1996).

[49] A. M. Ako, I. J. Hewitt, V. Mereacre, R. Clérac, W. Wernsdorfer, C. E. Anson and A. K. Powell. "A Ferromagnetically Coupled Mn_{19} Aggregate with a Record S=83/2 Ground Spin State". *Angew. Chem. Int. Ed.*, 45, 4926–4929 (2006).

[50] J. D. Rinehart, M. Fang, W. J. Evans and J. R. Long. "A $N_2^{(3-)}$ Radical-Bridged Terbium Complex Exhibiting Magnetic Hysteresis at 14 K". *J. Am. Chem. Soc.*, 133, 14236–14239 (2011).

[51] Y.-S. Ding, N. F. Chilton, R. E. P. Winpenny and Y.-Z. Zheng. "On Approaching the Limit of Molecular Magnetic Anisotropy: A Near-Perfect Pentagonal Bipyramidal Dysprosium(III) Single-Molecule Magnet". *Angew. Chem. Int. Ed.*, 55, 16071–16074 (2016).

[52] C. A. P. Goodwin, F. Ortu, D. Reta, N. F. Chilton and D. P. Mills. "Molecular magnetic hysteresis at 60 Kelvin in dysprosocenium". *Nature*, 548, 439–442 (2017).

[53] M. A. Nielsen and I. L. Chuang. Quantum Computation and Quantum Information. Cambridge University Press (2000).

[54] C. Godfrin, A. Ferhat, R. Ballou, S. Klyatskaya, M. Ruben, W. Wernsdorfer and F. Balestro. "Operating Quantum States in Single Magnetic Molecules: Implementation of Grover's Quantum Algorithm". *Phys. Rev. Lett.*, 119, 187702 (2017).

[55] N. V. Prokof'ev and P. C. E. Stamp. "Theory of the spin bath". *Rep. Prog. Phys.*, 63, 669 (2000).

[56] A. Morello, P. C. E. Stamp and I. S. Tupitsyn. "Pairwise Decoherence in Coupled Spin Qubit Networks". *Phys. Rev. Lett.*, 97, 207206 (2006).

[57] "Intel Delivers 17-Qubit Superconducting Chip with Advanced Packaging to QuTech". *Intel Newsroom, retrieved on 30/12/2017.*

[58] "IBM Raises the Bar with a 50-Qubit Quantum Computer". *MIT Technology Review, retrieved on 30/12/2017.*

[59] P. J. J. O'Malley, R. Babbush, I. D. Kivlichan, J. Romero, J. R. McClean, R. Barends, J. Kelly, P. Roushan, A. Tranter, N. Ding, B. Campbell, Y. Chen, Z. Chen, B. Chiaro, A. Dunsworth, A. G. Fowler, E. Jeffrey, E. Lucero, A. Megrant, J. Y. Mutus, M. Neeley, C. Neill, C. Quintana, D. Sank, A. Vainsencher, J. Wenner, T. C. White, P. V. Coveney, P. J. Love, H. Neven, A. Aspuru-Guzik and J. M. Martinis. "Scalable Quantum Simulation of Molecular Energies". *Phys. Rev. X*, 6, 031007 (2016).

[60] A. Córcoles, E. Magesan, S. J. Srinivasan, A. W. Cross, M. Steffen, J. M. Gambetta and J. M. Chow. "Demonstration of a quantum error detection code using a square lattice of four superconducting qubits". *Nat. Commun.*, 6, 6979 (2016).

[61] F. Luis, F. L. Mettes, J. Tejada, D. Gatteschi and L. J. de Jongh. "Observation of Quantum Coherence in Mesoscopic Molecular Magnets". *Phys. Rev. Lett.*, 85, 4377–4380 (2000).

[62] S. Hill, R. S. Edwards, N. Aliaga-Alcalde and G. Christou. "Quantum Coherence in an Exchange-Coupled Dimer of Single-Molecule Magnets". *Science*, 302, 1015–1018 (2003).

[63] A. Ardavan, O. Rival, J. J. L. Morton, S. J. Blundell, A. M. Tyryshkin, G. A. Timco and R. E. P. Winpenny. "Will Spin-Relaxation Times in Molecular

Magnets Permit Quantum Information Processing?" *Phys. Rev. Lett.*, 98, 057201 (2007).

[64] S. Carretta, P. Santini, G. Amoretti, T. Guidi, J. R. D. Copley, Y. Qiu, R. Caciuffo, G. Timco and R. E. P. Winpenny. "Quantum Oscillations of the Total Spin in a Heterometallic Antiferromagnetic Ring: Evidence from Neutron Spectroscopy". *Phys. Rev. Lett.*, 98, 167401 (2007).

[65] C. Schlegel, J. van Slageren, M. Manoli, E. K. Brechin and M. Dressel. "Direct Observation of Quantum Coherence in Single-Molecule Magnets". *Phys. Rev. Lett.*, 101, 147203 (2008).

[66] G. Mitrikas, Y. Sanakis, C. P. Raptopoulou, G. Kordas and G. Papavassiliou. "Electron spin-lattice and spin-spin relaxation study of a trinuclear iron(III) complex and its relevance in quantum computing". *Phys. Chem. Chem. Phys.*, 10, 743–748 (2008).

[67] S. Bertaina, S. Gambarelli, T. Mitra, B. Tsukerblat, A. Müller and B. Barbara. "Quantum oscillations in a molecular magnet". *Nature*, 453, 203–206 (2008).

[68] S. Takahashi, J. van Tol, C. C. Beedle, D. N. Hendrickson, L.-C. Brunel and M. S. Sherwin. "Coherent Manipulation and Decoherence of $S = 10$ Single-Molecule Magnets". *Phys. Rev. Lett.*, 102, 087603 (2009).

[69] C. Schlegel, J. van Slageren, G. Timco, R. E. P. Winpenny and M. Dressel. "Origin of superhyperfine interactions in the antiferromagnetic ring Cr_7Ni". *Phys. Rev. B*, 83, 134407 (2011).

[70] C. J. Wedge, G. A. Timco, E. T. Spielberg, R. E. George, F. Tuna, S. Rigby, E. J. L. McInnes, R. E. P. Winpenny, S. J. Blundell and A. Ardavan. "Chemical Engineering of Molecular Qubits". *Phys. Rev. Lett.*, 108, 107204 (2012).

[71] D. Kaminski, A. L. Webber, C. J. Wedge, J. Liu, G. A. Timco, I. n. J. Vitorica-Yrezabal, E. J. L. McInnes, R. E. P. Winpenny and A. Ardavan. "Quantum spin coherence in halogen-modified Cr_7Ni molecular nanomagnets". *Phys. Rev. B*, 90, 184419 (2014).

[72] M. J. Martínez-Pérez, S. Cardona-Serra, C. Schlegel, F. Moro, P. J. Alonso, H. Prima-García, J. M. Clemente-Juan, M. Evangelisti, A. Gaita-Ariño, J. Sesé, J. van Slageren, E. Coronado and F. Luis. "Gd-Based Single-Ion Magnets with Tunable Magnetic Anisotropy: Molecular Design of Spin Qubits". *Phys. Rev. Lett.*, 108, 247213 (2012).

[73] D. Loss and D. P. DiVincenzo. "Quantum computation with quantum dots". *Phys. Rev. A*, 57, 120–126 (1998).

[74] J. R. Petta, A. C. Johnson, J. M. Taylor, E. A. Laird, A. Yacoby, M. D. Lukin, C. M. Marcus, M. P. Hanson and A. C. Gossard. "Coherent Manipulation of Coupled Electron Spins in Semiconductor Quantum Dots". *Science*, 309, 2180–2184 (2005).

[75] J. M. Elzerman, R. Hanson, L. H. W. van Beveren, S. Tarucha, L. M. K. Vandersypen and L. P. Kouwenhoven. "Semiconductor Few-Electron Quantum Dots as Spin Qubits". *Lect. Notes Phys.*, 667, 25–95 (2005).

[76] J. Clarke and F. K. Wilhelm. "Superconducting quantum bits". *Nature*, 453, 1031–1042 (2008).

[77] R. Blatt and D. Wineland. "Entangled states of trapped atomic ions". *Nature*, 453, 1008–1015 (2008).

[78] L. Childress and R. Hanson. "Diamond NV centers for quantum computing and quantum networks". *MRS Bulletin*, 38, 134–138 (2013).

[79] J. Wrachtrup, S. Y. Kilin and A. P. Nizovtsev. "Quantum computation using the ^{13}C nuclear spins near the single NV defect center in diamond". *Opt. Spectrosc.*, 91, 429–437 (2001).

[80] S. Nakazawa, S. Nishida, T. Ise, T. Yoshino, N. Mori, R. D. Rahimi, K. Sato, Y. Morita, K. Toyota, D. Shiomi, M. Kitagawa, H. Hara, P. Carl, P. Höfer and T. Takui. "A Synthetic Two-Spin Quantum Bit: g-Engineered Exchange-Coupled Biradical Designed for Controlled-NOT Gate Operations". *Angew. Chem. Int. Ed.*, 51, 9860–9864 (2012).

[81] O. Sato. "Dynamic molecular crystals with switchable physical properties". *Nat. Chem.*, 8, 644–650 (2016).

[82] O. Sato. "Switchable molecular magnets". *Proc. Jpn. Acad. Ser. B.*, 88, 213–225 (2012).

[83] J. Linares, E. Codjovi and Y. Garcia. "Pressure and Temperature Spin Crossover Sensors with Optical Detection". *Sensors*, 12, 4479–4492 (2012).

[84] J.-F. Létard, P. Guionneau, L. Rabardel, J. A. K. Howard, A. E. Goeta, D. Chasseau and O. Kahn. "Structural, Magnetic, and Photomagnetic Studies of a Mononuclear Iron(II) Derivative Exhibiting an Exceptionally Abrupt Spin Transition. Light-Induced Thermal Hysteresis Phenomenon". *Inorg. Chem.*, 37, 4432–4441 (1998).

[85] S. Decurtins, P. Gütlich, C. Köhler, H. Spiering and A. Hauser. "Light-induced excited spin state trapping in a transition-metal complex: The hexa-1-propyltetrazole-iron (II) tetrafluoroborate spin-crossover system". *Chem. Phys. Lett.*, 105, 1 – 4 (1984).

[86] S. Hayami, Z.-z. Gu, M. Shiro, Y. Einaga, A. Fujishima and O. Sato. "First Observation of Light-Induced Excited Spin State Trapping for an Iron(III) Complex". *J. Am. Chem. Soc.*, 122, 7126–7127 (2000).

[87] P. Gütlich, A. Hauser and H. Spiering. "Thermal and Optical Switching of Iron(II) Complexes". *Angew. Chem. Int. Ed. Engl.*, 33, 2024–2054 (1994).

[88] H. J. Shepherd, I. A. Gural'skiy, C. M. Quintero, S. Tricard, L. Salmon, G. Molnár and A. Bousseksou. "Molecular actuators driven by cooperative spin-state switching". *Nat. Commun.*, 4, 2607 (2013).

[89] C. Mathonière, H.-J. Lin, D. Siretanu, R. Clérac and J. M. Smith. "Photoinduced Single-Molecule Magnet Properties in a Four-Coordinate Iron(II) Spin Crossover Complex". *J. Am. Chem. Soc.*, 135, 19083–19086 (2013).

[90] W. Bao, M. Melli, N. Caselli, F. Riboli, D. S. Wiersma, M. Staffaroni, H. Choo, D. F. Ogletree, S. Aloni, J. Bokor, S. Cabrini, F. Intonti, M. B. Salmeron, E. Yablonovitch, P. J. Schuck and A. Weber-Bargioni. "Mapping Local Charge Recombination Heterogeneity by Multidimensional Nanospectroscopic Imaging". *Science*, 338, 1317–1321 (2012).

[91] T. Tezgerevska, K. G. Alley and C. Boskovic. "Valence tautomerism in metal complexes: Stimulated and reversible intramolecular electron transfer between metal centers and organic ligands". *Coord. Chem. Rev.*, 268, 23–40 (2014).

[92] C. G. Pierpont. "Studies on charge distribution and valence tautomerism in transition metal complexes of catecholate and semiquinonate ligands". *Coord. Chem. Rev.*, 216-217, 99 – 125 (2001).

[93] M. Nihei, Y. Okamoto, Y. Sekine, N. Hoshino, T. Shiga, I. P.-C. Liu and H. Oshio. "A Light-Induced Phase Exhibiting Slow Magnetic Relaxation in a Cyanide-Bridged [Fe4Co2] Complex". *Angew. Chem. Int. Ed.*, 51, 6361–6364 (2012).

[94] S. Thies, H. Sell, C. Schütt, C. Bornholdt, C. Näther, F. Tuczek and R. Herges. "Light-Induced Spin Change by Photodissociable External Ligands: A New Principle for Magnetic Switching of Molecules". *J. Am. Chem. Soc.*, 133, 16243–16250 (2011).

[95] M. Irie, T. Fukaminato, K. Matsuda and S. Kobatake. "Photochromism of Diarylethene Molecules and Crystals: Memories, Switches, and Actuators". *Chem. Rev.*, 114, 12174–12277 (2014).

[96] M. Morimoto, H. Miyasaka, M. Yamashita and M. Irie. "Coordination Assemblies of [Mn4] Single-Molecule Magnets Linked by Photochromic Ligands: Photochemical Control of the Magnetic Properties". *J. Am. Chem. Soc.*, 131, 9823–9835 (2009).

[97] H. Phan, K. Lekin, S. M. Winter, R. T. Oakley and M. Shatruk. "Photoinduced Solid State Conversion of a Radical σ-Dimer to a π-Radical Pair". *J. Am. Chem. Soc.*, 135, 15674–15677 (2013).

[98] L. S. Forster. "Excited state relaxation of Cr(III) in oxygen environments". *Coord. Chem. Rev.*, 248, 261 – 272 (2004).

[99] B. L. Feringa, W. R. Browne and *et al.* Molecular Switches. Wiley-VCH (2001).

[100] E. T. Chernick, Q. Mi, R. F. Kelley, E. A. Weiss, B. A. Jones, T. J. Marks, M. A. Ratner and M. R. Wasielewski. "Electron Donor–Bridge–Acceptor Molecules with Bridging Nitronyl Nitroxide Radicals: Influence of a Third Spin on Charge- and Spin-Transfer Dynamics". *J. Am. Chem. Soc.*, 128, 4356–4364 (2006).

[101] T. Yu, F. Wang, Y. Xu, L. Ma, X. Pi and D. Yang. "Graphene Coupled with Silicon Quantum Dots for High-Performance Bulk-Silicon-Based Schottky-Junction Photodetectors". *Adv. Mater.*, 28, 4912–4919 (2016).

[102] G. Lalwani, A. M. Henslee, B. Farshid, L. Lin, F. K. Kasper, Y.-X. Qin, A. G. Mikos and B. Sitharaman. "Two-Dimensional Nanostructure-Reinforced Biodegradable Polymeric Nanocomposites for Bone Tissue Engineering". *Biomacromolecules*, 14, 900–909 (2013).

[103] M. Xu, D. Fujita and N. Hanagata. "Perspectives and Challenges of Emerging Single-Molecule DNA Sequencing Technologies". *Small*, 5, 2638–2649 (2009).

[104] X. Li, W. Chen, S. Zhang, Z. Wu, P. Wang, Z. Xu, H. Chen, W. Yin, H. Zhong and S. Lin. "18.5% efficient graphene/GaAs van der Waals heterostructure solar cell". *Nano Energy*, 16, 310 – 319 (2015).

[105] S. Stankovich, D. A. Dikin, G. H. B. Dommett, K. M. Kohlhaas, E. J. Zimney, E. A. Stach, R. D. Piner, S. T. Nguyen and R. S. Ruoff. "Graphene-based composite materials". *Nature*, 442, 282–286 (2006).

[106] A. Narita, X. Feng, Y. Hernandez, S. A. Jensen, M. Bonn, H. Yang, I. A. Verzhbitskiy, C. Casiraghi, M. R. Hansen, A. H. R. Koch, G. Fytas, O. Ivasenko, B. Li, K. S. Mali, T. Balandina, S. Mahesh, S. D. Feyter and K. Müllen. "Synthesis of structurally well-defined and liquid-phase-processable graphene nanoribbons". *Nat. Chem.*, 6, 126–132 (2014).

[107] Y.-C. Chen, D. G. de Oteyza, Z. Pedramrazi, C. Chen, F. R. Fischer and M. F. Crommie. "Tuning the Band Gap of Graphene Nanoribbons Synthesized from Molecular Precursors". *ACS Nano*, 7, 6123–6128 (2013).

[108] A. Konishi, Y. Hirao, H. Kurata and T. Kubo. "Investigating the edge state of graphene nanoribbons by a chemical approach: Synthesis and magnetic properties of zigzag-edged nanographene molecules". *Solid State Commun.*, 175-176, 62–70 (2013).

[109] C. Lee, X. Wei, J. W. Kysar and J. Hone. "Measurement of the Elastic Properties and Intrinsic Strength of Monolayer Graphene". *Science*, 321, 385–388 (2008).

[110] G. S. Painter and D. E. Ellis. "Electronic Band Structure and Optical Properties of Graphite from a Variational Approach". *Phys. Rev. B*, 1, 4747–4752 (1970).

[111] Y.-W. Son, M. L. Cohen and S. G. Louie. "Energy Gaps in Graphene Nanoribbons". *Phys. Rev. Lett.*, 97, 216803 (2006).

[112] S. Dutta and S. K. Pati. "Novel properties of graphene nanoribbons: a review". *J. Mater. Chem.*, 20, 8207–8223 (2010).

[113] A. Kimouche, M. M. Ervasti, R. Drost, S. Halonen, A. Harju, P. M. Joensuu, J. Sainio and P. Liljeroth. "Ultra-narrow metallic armchair graphene nanoribbons". *Nat. Comm.*, 6, 10177 (2015).

[114] M. Fujita, K. Wakabayashi, K. Nakada and K. Kusakabe. "Peculiar Localized State at Zigzag Graphite Edge". *J. Phys. Soc. Jpn.*, 65, 1920–1923 (1996).

[115] C. Tao, L. Jiao, O. V. Yazyev, Y.-C. Chen, J. Feng, X. Zhang, R. B. Capaz, J. M. Tour, A. Zettl, S. G. Louie, H. Dai and M. F. Crommie. "Spatially resolving edge states of chiral graphene nanoribbons". *Nat. Phys.*, 7, 616–620 (2011).

[116] D. Pesin and A. H. MacDonald. "Spintronics and pseudospintronics in graphene and topological insulators". *Nat. Mater.*, 11, 409–416 (2012).

[117] M. Wimmer, İ. Adagideli, S. Berber, D. Tománek and K. Richter. "Spin Currents in Rough Graphene Nanoribbons: Universal Fluctuations and Spin Injection". *Phys. Rev. Lett.*, 100, 177207 (2008).

[118] K. Wakabayashi, M. Sigrist and M. Fujita. "Spin Wave Mode of Edge-Localized Magnetic States in Nanographite Zigzag Ribbons". *J. Phys. Soc. Jpn.*, 67, 2089–2093 (1998).

[119] J. Jung and A. H. MacDonald. "Carrier density and magnetism in graphene zigzag nanoribbons". *Phys. Rev. B*, 79, 235433 (2009).

[120] O. V. Yazyev, R. B. Capaz and S. G. Louie. "Theory of magnetic edge states in chiral graphene nanoribbons". *Phys. Rev. B*, 84, 115406 (2011).

[121] H. Lee, Y.-W. Son, N. Park, S. Han and J. Yu. "Magnetic ordering at the edges of graphitic fragments: Magnetic tail interactions between the edge-localized states". *Phys. Rev. B*, 72, 174431 (2005).

[122] M. J. Schmidt, M. Golor, T. C. Lang and S. Wessel. "Effective models for strong correlations and edge magnetism in graphene". *Phys. Rev. B*, 87, 245431 (2013).

[123] M. Golor, S. Wessel and M. J. Schmidt. "Quantum Nature of Edge Magnetism in Graphene". *Phys. Rev. Lett.*, 112, 046601 (2014).

[124] S. Dutta and S. K. Pati. "Half-Metallicity in Undoped and Boron Doped Graphene Nanoribbons in the Presence of Semilocal Exchange-Correlation Interactions". *J. Phys. Chem. B*, 112, 1333–1335 (2008).

[125] C. L. Kane and E. J. Mele. "Z_2 Topological Order and the Quantum Spin Hall Effect". *Phys. Rev. Lett.*, 95, 146802 (2005).

[126] P. Han, K. Akagi, F. F. Canova, H. Mutoh, S. Shiraki, K. Iwaya, P. S. Weiss, N. Asao and T. Hitosugi. "Bottom-Up Graphene-Nanoribbon Fabrication Reveals Chiral Edges and Enantioselectivity". *ACS Nano*, 8, 9181–9187 (2014).

[127] T. H. Vo, M. Shekhirev, D. A. Kunkel, M. D. Morton, E. Berglund, L. Kong, P. M. Wilson, P. A. Dowben, A. Enders and A. Sinitskii. "Large-scale solution synthesis of narrow graphene nanoribbons". *Nat. Commun.*, 5, 3189 (2014).

[128] A. Narita, X.-Y. Wang, X. Feng and K. Müllen. "New advances in nanographene chemistry". *Chem. Soc. Rev.*, 44, 6616–6643 (2015).

[129] W. Jaskólski, A. Ayuela, M. Pelc, H. Santos and L. Chico. "Edge states and flat bands in graphene nanoribbons with arbitrary geometries". *Phys. Rev. B*, 83, 235424 (2011).

[130] J. Liu, B.-W. Li, Y.-Z. Tan, A. Giannakopoulos, C. Sanchez-Sanchez, D. Beljonne, P. Ruffieux, R. Fasel, X. Feng and K. Müllen. "Toward Cove-Edged Low Band Gap Graphene Nanoribbons". *J. Am. Chem. Soc.*, 137, 6097–6103 (2015).

[131] D. Huertas-Hernando, F. Guinea and A. Brataas. "Spin-orbit coupling in curved graphene, fullerenes, nanotubes, and nanotube caps". *Phys. Rev. B*, 74, 155426 (2006).

[132] C. L. Kane and E. J. Mele. "Z_2 Topological Order and the Quantum Spin Hall Effect". *Phys. Rev. Lett.*, 95, 146802 (2005).

[133] H. Min, J. E. Hill, N. A. Sinitsyn, B. R. Sahu, L. Kleinman and A. H. MacDonald. "Intrinsic and Rashba spin-orbit interactions in graphene sheets". *Phys. Rev. B*, 74, 165310 (2006).

[134] P. Recher and B. Trauzettel. "Quantum dots and spin qubits in graphene". *Nanotechnology*, 21, 302001 (2010).

[135] P. L. McEuen, M. Bockrath, D. H. Cobden, Y.-G. Yoon and S. G. Louie. "Disorder, Pseudospins, and Backscattering in Carbon Nanotubes". *Phys. Rev. Lett.*, 83, 5098–5101 (1999).

[136] Y. A. Bychkov and E. I. Rashba. "Oscillatory effects and the magnetic susceptibility of carriers in inversion layers". *J. Phys. C: Solid State Phys.*, 17, 6039 (1984).

[137] M. Zarea and N. Sandler. "Rashba spin-orbit interaction in graphene and zigzag nanoribbons". *Phys. Rev. B*, 79, 165442 (2009).

[138] M. Zarea, C. Büsser and N. Sandler. "Unscreened Coulomb Interactions and the Quantum Spin Hall Phase in Neutral Zigzag Graphene Ribbons". *Phys. Rev. Lett.*, 101, 196804 (2008).

[139] A. Celis, M. N. Nair, A. Taleb-Ibrahimi, E. H. Conrad, C. Berger, W. A. de Heer and A. Tejeda. "Graphene nanoribbons: fabrication, properties and devices". *Journal of Physics D: Applied Physics*, 49, 143001 (2016).

[140] J. Bai, X. Duan and Y. Huang. "Rational Fabrication of Graphene Nanoribbons Using a Nanowire Etch Mask". *Nano Lett.*, 9, 2083–2087 (2009).

[141] G. Liu, Y. Wu, Y.-M. Lin, D. B. Farmer, J. A. Ott, J. Bruley, A. Grill, P. Avouris, D. Pfeiffer, A. A. Balandin and C. Dimitrakopoulos. "Epitaxial Graphene Nanoribbon Array Fabrication Using BCP-Assisted Nanolithography". *ACS Nano*, 6, 6786–6792 (2012).

[142] D. V. Kosynkin, A. L. Higginbotham, A. Sinitskii, J. R. Lomeda, A. Dimiev, B. K. Price and J. M. Tour. "Longitudinal unzipping of carbon nanotubes to form graphene nanoribbons". *Nano Lett.*, 9, 2600–2604 (2009).

[143] L. C. Campos, V. R. Manfrinato, J. D. Sanchez-Yamagishi, J. Kong and P. Jarillo-Herrero. "Anisotropic Etching and Nanoribbon Formation in Single-Layer Graphene". *Nano Lett.*, 9, 2600–2604 (2009).

[144] J. Cai, P. Ruffieux, R. Jaafar, M. Bieri, T. Braun, S. Blankenburg, M. Muoth, A. P. Seitsonen, X. F. Moussa Saleh, K. Müllen and R. Fasel. "Atomically precise bottom-up fabrication of graphene nanoribbons". *Nature*, 466, 470–473 (2010).

[145] A. N. Abbas, G. Liu, A. Narita, M. Orosco, X. Feng, K. Müllen and C. Zhou. "Deposition, Characterization, and Thin-Film-Based Chemical Sensing of Ultra-long Chemically Synthesized Graphene Nanoribbons". *J. Am. Chem. Soc.*, 136, 7555–7558 (2014).

[146] S. Linden, D. Zhong, A. Timmer, N. Aghdassi, J. H. Franke, H. Zhang, X. Feng, K. Müllen, H. Fuchs, L. Chi and H. Zacharias. "Electronic Structure of Spatially Aligned Graphene Nanoribbons on Au(788)". *Phys. Rev. Lett.*, 108, 216801 (2012).

[147] C. Bronner, S. Stremlau, M. Gille, F. Braußе, A. Haase, S. Hecht and P. Tegeder. "Aligning the Band Gap of Graphene Nanoribbons by Monomer Doping". *Angew. Chem. Int. Ed.*, 52, 4422–4425 (2013).

[148] H. Sakaguchi, Y. Kawagoe, Y. Hirano, T. Iruka, M. Yano and T. Nakae. "Width-Controlled Sub-Nanometer Graphene Nanoribbon Films Synthesized by Radical-Polymerized Chemical Vapor Deposition". *Adv. Mater.*, 26, 4134–4138 (2014).

[149] T. Kato and R. Hatakeyama. "Site- and alignment-controlled growth of graphene nanoribbons from nickel nanobars". *Nat. Nanotech.*, 7, 651–656 (2012).

[150] A. V. Talyzin, I. V. Anoshkin, A. V. Krasheninnikov, R. M. Nieminen, A. G. Nasibulin, H. Jiang and E. I. Kauppinen. "Synthesis of Graphene Nanoribbons Encapsulated in Single-Walled Carbon Nanotubes". *Nano Lett.*, 11, 4352–4356 (2011).

[151] A. Chuvilin, E. Bichoutskaia, M. C. Gimenez-Lopez, T. W. Chamberlain, G. A. Rance, N. Kuganathan, J. Biskupek, U. Kaiser and A. N. Khlobystov. "Self-assembly of a sulphur-terminated graphene nanoribbon within a single-walled carbon nanotube". *Nat. Mater.*, 10, 687–692 (2014).

[152] I. Palacio, A. Celis, M. N. Nair, A. Gloter, A. Zobelli, M. Sicot, D. Malterre, M. S. Nevius, W. A. de Heer, C. Berger, E. H. Conrad, A. Taleb-Ibrahimi and A. Tejeda. "Atomic Structure of Epitaxial Graphene Sidewall Nanoribbons: Flat Graphene, Miniribbons, and the Confinement Gap". *Nano Lett.*, 15, 182–189 (2015).

[153] C. Görller-Walrand and K. Binnemans. "Spectral intensities of f-f transitions". *Handbook on the Physics and Chemistry of Rare Earths*, 25, 101–264 (1998).

[154] P. Atkins and R. Friedman. Molecular Quantum Mechanics. Oxford University Press (2005).

[155] J. J. Jiang, R. T. Weber, A. H. Heiss and D. P. Barr. EleXsys E500 User's Manual - Basic Operations. Bruker Instruments, Inc. (2001).

[156] A. Schweiger and G. Jeschke. Principles of Pulse Electron Paramagnetic Resonance. Oxford University Press (2001).

[157] T. Wacker, G. A. Sierra and A. Schweiger. "The Concept of FID-detected Hole-burning in Pulsed EPR Spectroscopy". *Isr. J. Chem.*, 32, 305–322 (1992).

[158] L. J. Berliner, G. R. Eaton and S. R. Eaton. "Distance Measurements in Biological Systems by EPR". *Biol. Magn. Reson.*, 19 (2002).

[159] S. R. Eaton, G. R. Eaton and L. J. Berliner. "Biomedical EPR, Part B: Methodology, Instrumentation, and Dynamics". *Biol. Magn. Reson.*, 24 (2005).

[160] J.-J. Yin and J. S. Hyde. "Spin label saturation-recovery electron spin resonance measurements of oxygen transport in membranes". *Z. Phys. Chem. Neue Folge*, 153, 57–65 (1987).

[161] J. S. Hyde, L. Kevan and R. N. Schwartz. "Saturation recovery methodology", in "Time Domain Electron Spin Resonance". Wiley-Interscience, New York (1979).

[162] S. K. Misra. "Relaxation of Paramagnetic Spins" in "Multifrequency Electron Paramagnetic Resonance: Theory and Applications". Wiley-VCH Verlag GmbH & Co. KGaA (2011).

[163] G. Jeschke. "DEER Distance Measurements on Proteins". *Annu. Rev. Phys. Chem.*, 63, 419–446 (2012).

[164] G. W. Reginsson and O. Schiemann. "Pulsed electron–electron double resonance: beyond nanometre distance measurements on biomacromolecules". *Biochem. J.*, 434, 353–363 (2011).

[165] G. Jeschke, V. Chechik, P. Ionita, A. Godt, H. Zimmermann, J. Banham, C. R. Timmel, D. Hilger and H. Jung. "DeerAnalysis2006—a comprehensive software package for analyzing pulsed ELDOR data". *Appl. Magn. Reson.*, 30, 473–498 (2006).

[166] N. Cox, W. Lubitz and A. Savitsky. "W-band ELDOR-detected NMR (EDNMR) spectroscopy as a versatile technique for the characterisation of transition metal-ligand interactions". *Mol. Phys.*, 111, 2788–2808 (2013).

[167] N. Cox, A. Nalepa, W. Lubitz and A. Savitsky. "ELDOR-detected NMR: A general and robust method for electron-nuclear hyperfine spectroscopy?" *J. Magn. Reson.*, 280, 63 – 78 (2017).

[168] I. Kaminker, T. D. Wilson, M. G. Savelieff, Y. Hovav, H. Zimmermann, Y. Lu and D. Goldfarb. "Correlating nuclear frequencies by two-dimensional ELDOR-detected NMR spectroscopy". *J. Magn. Reson.*, 240, 77 – 89 (2014).

[169] S. van Doorslaer. "Hyperfine Spectroscopy - ESEEM" in "EPR Spectroscopy: Fundamentals and Methods". Wiley-VCH Verlag GmbH & Co. KGaA (2018).

[170] P. Höfer, A. Grupp, H. Nebenführ and M. Mehring. "Hyperfine sublevel correlation (hyscore) spectroscopy: a 2D ESR investigation of the squaric acid radical". *Chem. Phys. Lett.*, 132, 279 – 282 (1986).

[171] S. Stoll and A. Schweiger. "EasySpin, a comprehensive software package for spectral simulation and analysis in EPR". *J. Magn. Reson.*, 178, 42 – 55 (2006).

[172] A. Ponti and A. Schweiger. "Nuclear coherence-transfer echoes in pulsed EPR". *J. Chem. Phys.*, 102, 5207–5219 (1995).

[173] R. T. Weber. E 580 Pulse EPR Course. Bruker BioSpin Manual (2005).

[174] R. L. Fagaly. "Superconducting quantum interference device instruments and applications". *Rev. Sci. Instrum.*, 77, 101101 (2006).

[175] Magnetic Property Measurement System (MPMS) Hardware Reference Manual. Quantum Design, San Diego (2005).

[176] H. Casimir and F. du Pré. "Note on the thermodynamic interpretation of paramagnetic relaxation phenomena". *Physica*, 5, 507 – 511 (1938).

[177] K. S. Cole and R. H. Cole. "Dispersion and Absorption in Dielectrics I. Alternating Current Characteristics". *J. Chem. Phys.*, 9, 341–351 (1941).

[178] O. Kahn. Molecular Magnetism. VCH Publishers, Inc. (1993).

[179] F. E. Hallak. "Magnetic Anisotropy of Molecular Nanomagnets". Ph.D. thesis, University of Stuttgart (2009).

[180] E. Heintze. "Optical control of molecular high spin states via spin-forbidden transitions". Ph.D. thesis, University of Stuttgart (2016).

[181] S. Demir, I.-R. Jeon, J. R. Long and T. D. Harris. "Radical ligand-containing single-molecule magnets". *Coord. Chem. Rev.*, 289-290, 149–176 (2015).

[182] Z. Sun, D. N. Hendrickson, Z. Sun, C. M. Grant, S. L. Castro and G. Christou. "Single-molecule magnets: out-of-phase ac susceptibility signals from tetranuclear vanadium(III) complexes with an S = 3 ground state". *Chem. Commun.*, 721–722 (1998).

[183] S. L. Castro, Z. Sun, C. M. Grant, J. C. Bollinger, D. N. Hendrickson and G. Christou. "Single-Molecule Magnets: Tetranuclear Vanadium(III) Complexes with a Butterfly Structure and an S = 3 Ground State". *J. Am. Chem. Soc.*, 120, 2365–2375 (1998).

[184] W. Chu, Q. Sun, X. Yao, P. Yan, G. An and G. Li. "Luminescent single molecule magnets of a series of β-diketone dysprosium complexes". *RSC Adv.*, 5, 94802–94808 (2015).

[185] M. Affronte, A. Beni, A. Dei and L. Sorace. "Valence tautomerism interconversion triggers transition to stable charge distribution in solid polymeric cobalt-polyoxolene complexes". *Dalton Trans.*, 5253–5259 (2007).

[186] A. Witt, F. W. Heinemann, S. Sproules and M. M. Khusniyarov. "Modulation of Magnetic Properties at Room Temperature: Coordination-Induced Valence Tautomerism in a Cobalt Dioxolene Complex". *Chem. Eur. J.*, 20, 11149–11162 (2014).

[187] J. Dai, S. Kanegawa, Z. Li, S. Kang and O. Sato. "A Switchable Complex Ligand Exhibiting Photoinduced Valence Tautomerism". *Eur. J. Inorg. Chem.*, 2013, 4150–4153 (2013).

[188] R. D. Schmidt, D. A. Shultz, J. D. Martin and P. D. Boyle. "Goldilocks Effect in Magnetic Bistability: Remote Substituent Modulation and Lattice Control of Photoinduced Valence Tautomerism and Light-Induced Thermal Hysteresis". *J. Am. Chem. Soc.*, 132, 6261–6273 (2010).

[189] X.-Y. Chen, R.-J. Wei, L.-S. Zheng and J. Tao. "Valence Tautomeric Transitions of Three One-Dimensional Cobalt Complexes". *Inorg. Chem.*, 53, 13212–13219 (2014).

[190] A. Tashiro, S. Kanegawa, O. Sato and Y. Teki. "ESR study of light-induced valence tautomerism of a Co mononuclear complex: [Co(phen)(3,5-DTBSQ)(3,5-DTBCat)]". *Polyhedron*, 66, 167 – 170 (2013).

[191] Y. Teki, M. Shirokoshi, S. Kanegawa and O. Sato. "ESR Study of Light-Induced Valence Tautomerism of a Dinuclear Co Complex". *Eur. J. Inorg. Chem.*, 2011, 3761–3767 (2011).

[192] H. S. Das, F. Weisser, D. Schweinfurth, C.-Y. Su, L. Bogani, J. Fiedler and B. Sarkar. "Straightforward Synthesis of Substituted p-Quinones: Isolation of a Key Intermediate and Use as a Bridging Ligand in a Diruthenium Complex". *Chem. Eur. J.*, 16, 2977–2981 (2010).

[193] P. L. Gentili, L. Bussotti, R. Righini, A. Beni, L. Bogani and A. Dei. "Time-resolved spectroscopic characterization of photo-induced valence tautomerism for a cobalt-dioxolene complex". *Chem. Phys.*, 314, 9 – 17 (2005).

[194] M. Slota, M. Blankenhorn, E. Heintze, M. Vu, R. Hübner and L. Bogani. "Photoswitchable stable charge-distributed states in a new cobalt complex exhibiting photo-induced valence tautomerism". *Faraday Discuss.*, 185, 347–359 (2015).

[195] J. Ok-Sang, J. D. Hwan, L. Young-A, C. H. Kwon and S. Y. Soo. "Charge Distribution Dependent on the Chelating Ratio. [Co(μ-bpym)(dbbq)$_2$] vs. [{ Co(dbbq)$_2$ }$_2$(μ-bpym)] (bpym = 2,2'-bipyrimidine; dbbq = 3,6-di-t-butyl-1,2-benzoquinone)". *Bull. Chem. Soc. Jpn.*, 69, 2211–2214 (1996).

[196] W. Kohn, A. D. Becke and R. G. Parr. "Density Functional Theory of Electronic Structure". *J. Phys. Chem.*, 100, 12974–12980 (1996).

[197] Y. Shao *et al.* "Advances in methods and algorithms in a modern quantum chemistry program package". *Phys. Chem. Chem. Phys.*, 8, 3172–3191 (2006).

[198] J. M. Recio, J. M. Menendez and A. O. de la Roza. An Introduction to High-Pressure Science and Technology. CRC Press (2015).

[199] M. Reiher, O. Salomon and B. Artur Hess. "Reparameterization of hybrid functionals based on energy differences of states of different multiplicity". *Theor. Chem. Acc.*, 107, 48–55 (2001).

[200] B. Pinter, A. Chankisjijev, P. Geerlings, J. N. Harvey and F. D. Proft. "Conceptual Insights into DFT Spin-State Energetics of Octahedral Transition-Metal Complexes through a Density Difference Analysis". *Chem. Eur. J.*, 24, 5281–5292 (2018).

[201] A. Caneschi, D. Gatteschi, N. Lalioti, R. Sessoli, L. Sorace, V. Tangoulis and A. Vindigni. "Ising-Type Magnetic Anisotropy in a Cobalt(II) Nitronyl Nitroxide Compound: A Key to Understanding the Formation of Molecular Magnetic Nanowires". *Chem. Eur. J.*, 8, 286–292 (2001).

[202] A. Pezeshk. "Newly resolved ESR spectrum of a low-spin cobalt(II) macrocyclic complex in 3-methylpyridine". *Inorg. Chem.*, 31, 2282–2284 (1992).

[203] D. M. Jenkins, A. J. Di Bilio, M. J. Allen, T. A. Betley and J. C. Peters. "Elucidation of a Low Spin Cobalt(II) System in a Distorted Tetrahedral Geometry". *J. Am. Chem. Soc.*, 124, 15336–15350 (2002). PMID: 12487609.

[204] I. Krivokapic, M. Zerara, M. L. Daku, A. Vargas, C. Enachescu, C. Ambrus, P. Tregenna-Piggott, N. Amstutz, E. Krausz and A. Hauser. "Spin-crossover in cobalt(II) imine complexes". *Coord. Chem. Rev.*, 251, 364 – 378 (2007). A Special Issue Highlighting the Many Aspects of the Electronic Spectrosocpy of Inorganic Compounds.

[205] K. Farmery, N. K. Kildahl and D. H. Busch. "Axial Coordination in cobalt(II) complexes of two synthetic macrocyclic ligands containing the bidentate α-diimine group". *J. Coord. Chem.*, 10, 85–100 (1980).

[206] M. C. Symons, T. Taiwo, A. M. Sargeson, M. M. Ali and A. S. Tabl. "EPR spectra for high- and low-spin CoII encapsulated complexes". *Inorg. Chim. Acta*, 241, 5 – 8 (1996).

[207] F. Lloret, M. Julve, J. Cano, R. Ruiz-García and E. Pardo. "Magnetic properties of six-coordinated high-spin cobalt(II) complexes: Theoretical

background and its application". *Inorganica Chim. Acta*, 361, 3432 – 3445 (2008).

[208] J. P. S. Walsh, G. Bowling, A.-M. Ariciu, N. F. M. Jailani, N. F. Chilton, P. G. Waddell, D. Collison, F. Tuna and L. J. Higham. "Evidence of Slow Magnetic Relaxation in $Co(AcO)_2(py)_2(H_2O)_2$". *Magnetochemistry*, 2 (2016).

[209] W. Low. "Paramagnetic and Optical Spectra of Divalent Cobalt in Cubic Crystalline Fields". *Phys. Rev.*, 109, 256–265 (1958).

[210] Y. Mulyana, G. Poneti, B. Moubaraki, K. S. Murray, B. F. Abrahams, L. Sorace and C. Boskovic. "Solvation effects on the valence tautomeric transition of a cobalt complex in the solid state". *Dalton Trans.*, 39, 4757–4767 (2010).

[211] E. Evangelio, C. Rodriguez-Blanco, Y. Coppel, D. N. Hendrickson, J. P. Sutter, J. Campo and D. Ruiz-Molina. "Solvent effects on valence tautomerism: A comparison between the interconversion in solution and solid state". *Solid State Sci.*, 11, 793 – 800 (2009).

[212] D. M. Adams and D. N. Hendrickson. "Pulsed Laser Photolysis and Thermodynamics Studies of Intramolecular Electron Transfer in Valence Tautomeric Cobalt σ-Quinone Complexes". *J. Am. Chem. Soc.*, 118, 11515–11528 (1996).

[213] G. R. Eaton, S. S. Eaton, D. P. Barr and R. T. Weber. Quantitative EPR. Springer Verlag Wien - New York (2010).

[214] S. Hill, S. Datta, J. Liu, R. Inglis, C. J. Milios, P. L. Feng, J. J. Henderson, E. del Barco, E. K. Brechin and D. N. Hendrickson. "Magnetic quantum tunneling: insights from simple molecule-based magnets". *Dalton Trans.*, 39, 4693–4707 (2010).

[215] J.-F. Létard, L. Capes, G. Chastanet, N. Moliner, S. Létard, J.-A. Real and O. Kahn. "Critical temperature of the LIESST effect in iron(II) spin crossover compounds". *Chem. Phys. Lett.*, 313, 115–120 (1999).

[216] C. Carbonera, A. Dei, C. Sangregorio and J.-F. Létard. "Optically switchable behaviour of a dioxolene adduct of a cobalt-macrocycle complex". *Chem. Phys. Lett.*, 396, 198–201 (2004).

[217] A. Beni, A. Dei, D. A. Shultz and L. Sorace. "Ligand design modulates photoinduced properties of cobalt-dioxolene valence tautomers". *Chem. Phys. Lett.*, 428, 400–404 (2006).

[218] C. Carbonera, A. Dei, J.-F. Létard, C. Sangregorio and L. Sorace. "Relaxation dynamics of a photoinduced di-cobalt-tetraoxolene valence tautomer". *Inorg. Chim. Acta*, 360, 3825 – 3828 (2007).

[219] C. Sangregorio, T. Ohm, C. Paulsen, R. Sessoli and D. Gatteschi. "Quantum Tunneling of the Magnetization in an Iron Cluster Nanomagnet". *Phys. Rev. Lett.*, 78, 4645–4648 (1997).

[220] R. V. Chamberlin, G. Mozurkewich and R. Orbach. "Time Decay of the Remanent Magnetization in Spin-Glasses". *Phys. Rev. Lett.*, 52, 867–870 (1984).

[221] A. Cui, K. Takahashi, A. Fujishima and O. Sato. "Mechanism and relaxation kinetics of photo-induced valence tautomerism of [Co(phen)(3,5-DBSQ)2]·C6H5Cl". *J. Photochem. Photobiol. A*, 167, 69 – 73 (2004).

[222] L. Bogani. "Experiments on Molecular Magnetsfor Molecular Spintronics" in "Molecular Nanomagnets and Related Phenomena" by Song Gao. Springer Verlag Berlin-Heidelberg (2014).

[223] M. Mannini, F. Pineider, P. Sainctavit, L. Joly, A. Fraile-Rodríguez, M.-A. Cartier dit Arrio, C. Moulin, W. Wernsdorfer, A. Cornia, D. Gatteschi and R. Sessoli. "Magnetic Materials: X-Ray Magnetic Circular Dichroism Picks out Single-Molecule Magnets Suitable for Nanodevices". *Adv. Mater.*, 21, 167–171 (2009).

[224] E. Tancini, M. J. Rodriguez-Douton, L. Sorace, A.-L. Barra, R. Sessoli and A. Cornia. "Slow Magnetic Relaxation from Hard-Axis Metal Ions in Tetranuclear Single-Molecule Magnets". *Chem. Eur. J.*, 16, 10482–10493 (2010).

[225] P. Totaro, K. C. M. Westrup, M.-E. Boulon, G. G. Nunes, D. F. Back, A. Barison, S. Ciattini, M. Mannini, L. Sorace, J. F. Soares, A. Cornia and R. Sessoli. "A new approach to the synthesis of heteronuclear propeller-like single molecule magnets". *Dalton Trans.*, 42, 4416–4426 (2013).

[226] A. Cornia and M. Mannini. "Single-Molecule Magnets on Surfaces" in "Molecular Nanomagnets and Related Phenomena" by Song Gao. Springer Berlin-Heidelberg, Berlin, Heidelberg (2014).

[227] M. Milos, S. Kairouani, S. Rabaste and A. Hauser. "Energy migration within the ^{2}E state of Cr^{3+}". *Coord. Chem. Rev.*, 252, 2540–2551 (2008).

[228] M. Milos and A. Hauser. ""Chromium(III)-trisoxalate, a versatile building block for luminescent materials"". *J. Lumin.*, 133, 15 – 20 (2013).

[229] L. S. Forster. "Intersystem crossing in transition metal complexes". *Coord. Chem. Rev.*, 250, 2023 – 2033 (2006).

[230] T. D. Ladd, F. Jelezko, R. Laflamme, Y. Nakamura, C. Monroe and J. L. O'Brien. "Quantum computers". *Nature*, 464, 45–53 (2010).

[231] M. Mannini, E. Tancini, L. Sorace, P. Sainctavit, M.-A. Arrio, Y. Qian, E. Otero, D. Chiappe, L. Margheriti, J. C. Cezar, R. Sessoli and A. Cornia. "Spin Structure of Surface-Supported Single-Molecule Magnets from Isomorphous Replacement and X-ray Magnetic Circular Dichroism". *Inorg. Chem.*, 50, 2911–2917 (2011).

[232] L. Sorace, M.-E. Boulon, P. Totaro, A. Cornia, J. Fernandes-Soares and R. Sessoli. "Origin and spectroscopic determination of trigonal anisotropy in a heteronuclear single-molecule magnet". *Phys. Rev. B*, 88, 104407 (2013).

[233] A. L. Barra, A. Caneschi, A. Cornia, F. Fabrizi de Biani, D. Gatteschi, C. Sangregorio, R. Sessoli and L. Sorace. "Single-Molecule Magnet Behavior of a Tetranuclear Iron(III) Complex. The Origin of Slow Magnetic Relaxation in Iron(III) Clusters". *J. Am. Chem. Soc.*, 121, 5302–5310 (1999).

[234] A. Bencini and D. Gatteschi. EPR of Exchange Coupled Systems. Dover Books on Chemistry Series. Dover Publications, Incorporated (2012).

[235] M. Sugita, N. Ishikawa, T. Ishikawa, S.-y. Koshihara and Y. Kaizu. "Static Magnetic-Field-Induced Phase Lag in the Magnetization Response of Tris(dipicolinato)lanthanides". *Inorg. Chem.*, 45, 1299–1304 (2006).

[236] M. Grahl, J. Kötzler and I. Seßler. "Correlation between domain-wall dynamics and spin-spin relaxation in uniaxial ferromagnets". *J. Magn. Magn. Mater.*, 90-91, 187 – 188 (1990).

[237] V. Tkáč, A. Orendáčová, R. Tarasenko, E. Čižmár, M. Orendáč, K. Tibenská, A. G. Anders, S. Gao, V. Pavlík and A. Feher. "Multiple-timescale relaxation dynamics in $CsGd(MoO_4)_2$ – a dipolar magnet with a highly anisotropic layered crystal structure". *J. Phys. Condens. Matter*, 25, 506001 (2013).

[238] E. Burzurí, Y. Yamamoto, M. Warnock, X. Zhong, K. Park, A. Cornia and H. S. J. van der Zant. "Franck-Condon Blockade in a Single-Molecule Transistor". *Nano Lett.*, 14, 3191–3196 (2014).

[239] L. Novotny and N. van Hulst. "Antennas for light". *Nat. Photonics*, 5, 83–90 (2011).

[240] G. Malheiros-Silveira, L. Gabrielli, C. Chang-Hasnain and H. Hernandez-Figueroa. "Breakthroughs in Photonics 2013: Advances in Nanoantennas". *IEEE Photon. J.*, 6, 1–6 (2014).

[241] L. Tang, S. E. Kocabas, S. Latif, A. K. Okyay, D.-S. Ly-Gagnon, K. C. Saraswat and D. A. B. Miller. "Nanometre-scale germanium photodetector enhanced by a near-infrared dipole antenna". *Nat. Photon.*, 2, 226–229 (2008).

[242] M. Hentschel, M. Schäferling, B. Metzger and H. Giessen. "Plasmonic Diastereomers: Adding up Chiral Centers". *Nano Lett.*, 13, 600–606 (2013).

[243] J. E. Baker, R. Sriram and B. L. Miller. "Two-dimensional photonic crystals for sensitive microscale chemical and biochemical sensing". *Lab Chip*, 15, 971–990 (2015).

[244] B. T. Cunningham, M. Zhang, Y. Zhuo, L. Kwon and C. Race. "Recent Advances in Biosensing With Photonic Crystal Surfaces: A Review". *IEEE Sens. J.*, 16, 3349–3366 (2016).

[245] F. Kraffert, R. Steyrleuthner, S. Albrecht, D. Neher, M. C. Scharber, R. Bittl and J. Behrends. "Charge Separation in PCPDTBT:PCBM Blends from an EPR Perspective". *J. Phys. Chem. C*, 118, 28482–28493 (2014).

[246] A. Rao, P. C. Y. Chow, S. Gelinas, C. W. Schlenker, C.-Z. Li, H.-L. Yip, A. K.-Y. Jen, D. S. Ginger and R. H. Friend. "The role of spin in the kinetic control of recombination in organic photovoltaics". *Nature*, 500, 435–440 (2013).

[247] M. Kammel, J. Kern, W. Lubitz and R. Bittl. "Photosystem II single crystals studied by transient EPR: the light-induced triplet state". *Biochim. Biophys. Acta - Bioenergetics*, 1605, 47–54 (2003).

[248] Y. Kodera, K. Takura and A. Kawamori. "Distance of P680 from the manganese complex in Photosystem II studied by time resolved EPR". *Biochim. et Biophys. Acta - Bioenergetics*, 1101, 23–32 (1992).

[249] J. J. Hopfield, J. N. Onuchic and D. N. Beratan. "A Molecular Shift Register Based on Electron Transfer". *Science*, 241, 817–820 (1988).

[250] M. P. Debreczeny, W. A. Svec, E. M. Marsh and M. R. Wasielewski. "Femtosecond Optical Control of Charge Shift within Electron Donor-Acceptor Arrays: An Approach to Molecular Switches". *J. Am. Chem. Soc.*, 118, 8174–8175 (1996).

[251] V. F. Tarasov, S. S. M. Islam, Y. Ohba, M. D. E. Forbes and S. Yamauchi. "Multifrequency TREPR Investigation of Excited-State ZnTPP Nitroxide Radical Complexes". *Appl. Magn. Reson.*, 41, 175–193 (2011).

[252] A. Bencini and D. Gatteschi. "EPR of Exchange-coupled Systems". *Springer-Verlag Berlin* (1990).

[253] V. Meunier, A. G. Souza Filho, E. B. Barros and M. S. Dresselhaus. "Physical properties of low-dimensional sp^2-based carbon nanostructures". *Rev. Mod. Phys.*, 88, 025005 (2016).

[254] S. S. Rao, S. N. Jammalamadaka, A. Stesmans, V. V. Moshchalkov, J. v. Tol, D. V. Kosynkin, A. Higginbotham-Duque and J. M. Tour. "Ferromagnetism in Graphene Nanoribbons: Split versus Oxidative Unzipped Ribbons". *Nano Lett.*, 12, 1210–1217 (2012).

[255] De-en Jiang, B. G. Sumpter and S. Dai. "Unique chemical reactivity of a graphene nanoribbon's zigzag edge". *J. Chem. Phys.*, 126, 134701 (2007).

[256] P. Ruffieux, S. Wang, B. Yang, C. Sánchez-Sánchez, J. Liu, T. Dienel, L. Talirz, P. Shinde, C. A. Pignedoli, D. Passerone, T. Dumslaff, X. Feng, K. Müllen and R. Fasel. "On-surface synthesis of graphene nanoribbons with zigzag edge topology". *Nature*, 531, 489–498 (2016).

[257] L. Dössel, L. Gherghel, X. Feng and K. Müllen. "Graphene Nanoribbons by Chemists: Nanometer-Sized, Soluble, and Defect-Free". *Angew. Chem. Int. Ed.*, 50, 2540–2543 (2011).

[258] Z. Chen, W. Zhang, C.-A. Palma, A. Lodi Rizzini, B. Liu, A. Abbas, N. Richter, L. Martini, X.-Y. Wang, N. Cavani, H. Lu, N. Mishra, C. Coletti, R. Berger, F. Klappenberger, M. Kläui, A. Candini, M. Affronte, C. Zhou,

V. De Renzi, U. del Pennino, J. V. Barth, H. J. Ráder, A. Narita, X. Feng and K. Müllen. "Synthesis of Graphene Nanoribbons by Ambient-Pressure Chemical Vapor Deposition and Device Integration". *J. Am. Chem. Soc.*, 138, 15488–15496 (2016).

[259] M. Slota, A. Keerthi, W. K. Myers, E. Tretyakov, M. Baumgarten, A. Ardavan, H. Sadeghi, C. J. Lambert, A. Narita, K. Müllen and L. Bogani. "Magnetic edge states and coherent manipulation of graphene nanoribbons". *Nature*, 557, 691–695 (2018).

[260] D. Luneau and P. Rey. "Magnetism of metal-nitroxide compounds involving bis-chelating imidazole and benzimidazole substituted nitronyl nitroxide free radicals". *Coord. Chem. Rev.*, 249, 2591 – 2611 (2005).

[261] A. Collauto, M. Mannini, L. Sorace, A. Barbon, M. Brustolon and D. Gatteschi. "A slow relaxing species for molecular spin devices: EPR characterization of static and dynamic magnetic properties of a nitronyl nitroxide radical". *J. Mater. Chem.*, 22, 22272–22281 (2012).

[262] T. Ryu, S. Shuichi, K. Masatoshi and O. Keiji. "Nitronyl Nitroxide as a Coupling Partner: Pd-Mediated Cross-coupling of (Nitronyl nitroxide-2-ido)(triphenylphosphine)gold(I) with Aryl Halides". *Chem. Lett.*, 43, 678–680 (2014).

[263] Gaussian 09, Revision A.02, Gaussian, Inc. Wallingford CT (2006).

[264] C. Fiolhais, F. Nogueira, M. A. Marques and *et al.* A primer in density functional theory. Springer Science & Business Media (2003).

[265] J. M. Soler, E. Artacho, J. D. Gale, A. García, J. Junquera, P. Ordejón and D. Sánchez-Portal. "The SIESTA method for ab initio order-N materials simulation". *J. Phys. Condens. Matter*, 14, 2745 (2002).

[266] G. Jeschke. "Determination of the Nanostructure of Polymer Materials by Electron Paramagnetic Resonance Spectroscopy". *Macromol. Rapid Commun.*, 23, 227–246 (2002).

[267] A. Caneschi, D. Gatteschi and P. Rey. "The Chemistry and Magnetic Properties of Metal Nitronyl Nitroxide Complexes" in "Progress in Inorganic Chemistry 38". John Wiley & Sons, Inc. (2007).

[268] L. Catala, J. Le Moigne, N. Kyritsakas, P. Rey, J. J. Novoa and P. Turek. "Towards a Better Understanding of the Magnetic Interactions within m-Phenylene α-Nitronyl Imino Nitroxide Based Biradicals". *Chem. Eur. J.*, 7, 2466–2480 (2001).

[269] L. Catala, J. Le Moigne, N. Gruber, J. J. Novoa, P. Rabu, E. Belorizky and P. Turek. "Towards a Better Understanding of Magnetic Interactions within m-Phenylene α-Nitronyl Nitroxide and Imino Nitroxide Based Radicals, Part III: Magnetic Exchange in a Series of Triradicals and Tetraradicals Based on the Phenyl Acetylene and Biphenyl Coupling Units". *Chem. Eur. J.*, 11, 2440–2454 (2005).

[270] B. Trauzettel, D. V. Bulaev, D. Loss and G. Burkard. "Spin qubits in graphene quantum dots". *Nat. Phys.*, 3, 192–196 (2007).

[271] P. R. Struck and G. Burkard. "Effective time-reversal symmetry breaking in the spin relaxation in a graphene quantum dot". *Phys. Rev. B*, 82, 125401 (2010).

[272] L. Rintoul, A. Micallef and S. Bottle. "The vibrational group frequency of the N-O stretching band of nitroxide stable free radicals". *Spectrochim. Acta A*, 70, 713 – 717 (2008).

[273] G. R. Eaton and S. S. Eaton. "Multifrequency Electron Spin-Relaxation Times" in "Multifrequency Electron Paramagnetic Resonance: Theory and Applications". Wiley-VCH Verlag GmbH & Co. KGaA (2011).

[274] J. R. Klauder and P. W. Anderson. "Spectral Diffusion Decay in Spin Resonance Experiments". *Phys. Rev.*, 125, 912–932 (1962).

[275] J. Fischer, B. Trauzettel and D. Loss. "Hyperfine interaction and electron-spin decoherence in graphene and carbon nanotube quantum dots". *Phys. Rev. B*, 80, 155401 (2009).

[276] M. V. G. Dutt, L. Childress, L. Jiang, E. Togan, J. Maze, F. Jelezko, A. S. Zibrov, P. R. Hemmer and M. D. Lukin. "Quantum Register Based on Individual Electronic and Nuclear Spin Qubits in Diamond". *Science*, 316, 1312–1316 (2007).

[277] A. Ardavan, A. M. Bowen, A. Fernandez, A. J. Fielding, D. Kaminski, F. Moro, C. A. Muryn, M. D. Wise, A. Ruggi, E. J. L. McInnes, K. Severin, G. A. Timco, C. R. Timmel, F. Tuna, G. F. S. Whitehead and R. E. P. Winpenny. "Engineering coherent interactions in molecular nanomagnet dimers". *npj Quantum Inf.*, 1, 15012 (2015).

[278] I. Ratera and J. Veciana. ""Playing with organic radicals as building blocks for functional molecular materials"". *Chem. Soc. Rev.*, 41, 303–349 (2012).

[279] R. Hanson, L. P. Kouwenhoven, J. R. Petta, S. Tarucha and L. M. K. Vandersypen. "Spins in few-electron quantum dots". *Rev. Mod. Phys.*, 79, 1217–1265 (2007).

[280] A. Rycerz, J. Tworzydło and C. W. J. Beenakker1. "Valley filter and valley valve in graphene". *Nat. Phys.*, 3, 172–175 (2007).

[281] M. Koch, F. Ample, C. Joachim and L. Grill. "Voltage-dependent conductance of a single graphene nanoribbon". *Nat. Nanotech.*, 7, 713–717 (2012).

[282] J. Baringhaus, M. Ruan, F. Edler, A. Tejeda, M. Sicot, A. Taleb-Ibrahimi, A.-P. Li, Z. Jiang, E. H. Conrad, C. Berger, C. Tegenkamp and W. A. de Heer. "Exceptional ballistic transport in epitaxial graphene nanoribbons". *Nature*, 506, 349–354 (2014).

[283] N. Dotti. "Electronic Transport in Magnetic Materials at Different Dimensionalities". Ph.D. thesis, University of Oxford (submitted in 2018).

[284] S. Kumar, Y. Kumar, S. K. Keshri and P. Mukhopadhyay. "Recent Advances in Organic Radicals and Their Magnetism". *Magnetochemistry*, 2 (2016).

[285] G. Balasubramanian, P. Neumann, D. Twitchen, M. Markham, R. Kolesov, N. Mizuochi, J. Isoya, J. Achard, J. Beck1, J. Tissler, V. Jacques, P. R. Hemmer, F. Jelezko1 and J. Wrachtrup. "Ultralong spin coherence time in isotopically engineered diamond". *Nat. Mater.*, 8, 383–387 (2009).

[286] M. Shiddiq, D. Komijani, Y. Duan, A. Gaita-Ariño, E. Coronado and S. Hill. "Enhancing coherence in molecular spin qubits via atomic clock transitions". *Nature*, 531, 348–351 (2016).

[287] S. Foletti, H. Bluhm, D. Mahalu, V. Umansky and A. Yacoby. "Universal quantum control of two-electron spin quantum bits using dynamic nuclear polarization". *Nat. Phys.*, 5, 903–908 (2009).

Acknowledgement

My thesis would not have been possible without the great help of many people. This last chapter is dedicated to them.

First of all, I want to thank Prof. Lapo Bogani for his excellent supervision. I appreciate your help in all matters, great support and feedback throughout my studies. You encouraged me in all scientific matters and always provided the information I needed to proceed with my projects. You showed me how to become an independent scientist and shared important knowledge with me. Thank you for allowing me to join your group and enjoy a friendly atmosphere, both at the University of Oxford, and formerly at the University of Stuttgart. You provided an environment that motivated me.

I want to thank Prof. Arzhang Ardavan for all the scientific discussions on my topic. The knowledge on ESR you shared with me helped me greatly in my research projects. With your help I was able to perform and understand the experiments that led to exciting results presented in this work. I appreciate your important inputs, which always advanced the research in a fruitful way.

All the ESR experiments at CAESR would not have been possible without the help of Dr. Will Myers. You taught me how to run state-of-the-art ESR experiments and provided help whenever I needed. I thank you and Prof. Christiane Timmel for the welcoming atmosphere at CAESR. I also thank all my collaborators from the Müllen group at the Max-Planck-Institute for Polymer Research in Mainz, from the Lambert group at the University of Lancaster, and Andrea Cornia from the University of Florence, who altogether contributed to the research outcomes.

Special thanks go to my office and lab colleagues, in particular Nicola Dotti for the great time in the office and welcoming attitude in any matters. I thank Dr. Jennifer LeRoy for answering all my questions about Chemistry. Furthermore, I want to thank all new students in our group, who altogether created a great atmosphere in our new office.

Big thanks go to my former collaborators from the University of Stuttgart, with whom I could spend a great time. I want to thank Dr. Eric Heintze, who introduced me into the world of science and showing me how to plan and carry out scientific experiments. You shared a lot of your knowledge with me, and managed to motivate and support me both in my studies as in personal decisions. Furthermore, I thank Dr. Ralph Hübner and Marian Blankenhorn for the friendly atmosphere and scientific exchanges.

My work would not have been possible without the support of my friends outside the lab, and my family. Time spent with you invariably empowered me. In particular, I thank Alina Valsan for proofreading. You always built me up. My biggest thanks goes to my parents and siblings. Without your continuous help throughout my entire life, and encouragements in good as in difficult times, I would have never arrived at the point where I am now.

Declaration of Authorship

I, Michael Christian Slota, hereby declare that I have authored this thesis, entitled "Manipulating the Coupling between Electronic and Spin Degrees of Freedom in Molecules", independently under the supervision of Prof. Lapo Bogani and advisory co-supervision of Prof. Arzhang Ardavan, and used no other sources and aids than the stated ones. In particular I declare that:

* The thesis I am submitting is entirely my own work except where otherwise indicated.
* Where any part of this thesis is based on work by others or jointly in collaborations, I have made clear exactly what was done by myself and what was done by collaborators.
* I have clearly indicated the presence of all material I have quoted from other sources, including any diagrams, charts, tables or graphs.
* Where any part of the thesis has been submitted by someone else to the University of Oxford or any other institution, this has been clearly stated.
* This thesis has not been submitted, either partially or in full, either for this Honour School or qualification or for another Honour School or qualification of this University (except where the Special Regulations for the subject permit this), or for a qualification at any other institution.
* I have given all sources to quotes.
* I have acknowledged any assistance or help.

Oxford, 11 January 2018